PDE-based vs. Variational Methods for Perspective Shape from Shading

Von der Fakultät für Informatik, Elektrotechnik und Informationstechnik der
Universität Stuttgart zur Erlangung der Würde eines Doktors der
Naturwissenschaften (Dr. rer. nat.) genehmigte Abhandlung

Vorgelegt von

Yong Chul Ju

aus Seoul, Südkorea

Hauptberichter: Prof. Dr. Andrés Bruhn

Mitberichter: Prof. Dr. Michael Breuß

Tag der mündlichen Prüfung: 30.01.2017

Institut für Visualisierung und Interaktive Systeme (VIS)
der Universität Stuttgart

2017

ACKNOWLEDGEMENTS

This thesis could not have been possible without the contributions from many people in one way or another during my Ph.D. journey from Saarbrücken to Stuttgart via Cottbus in Germany. Since I have actually had a rare privilege to receive timely support wherever I went, it is my great pleasure to have a chance to express my heartfelt gratitude.

Above all, I am deeply indebted to my thesis advisor Prof. Andrés Bruhn at University of Stuttgart who gave me the opportunity to work in his group and whose valuable advice and constant support guide me throughout my Ph.D. period. Large part of this thesis is based on the outcome of our fruitful discussions that we had over years. What I have learned from his deep insight and enthusiasm will undoubtedly influence on my future career.

Moreover, Prof. Michael Breuß at BTU Cottbus-Senftenberg has earned him my profound gratitude for sharing his extensive expertise especially on hyperbolic partial differential equations upon which not only the first part of this thesis but also my master's thesis relied. I also thank him for giving me the opportunity to work on the joint project with Prof. Andrés Bruhn.

In addition, I also want to thank both Prof. Andrés Bruhn and Prof. Michael Breuß for reviewing this thesis.

Furthermore, I wish to express my sincere gratitude to Prof. Joachim Weickert from the Mathematical Image Analysis (MIA) group at Saarland University for his hospitality and support during the period in Saarbrücken. He is the one who actually made all this possible in the first place because I was able to meet many great people through the graduate program that he had started.

I would also like to thank all my wonderful colleagues from Computer Vision and Intelligent System group at University of Stuttgart for the pleasant working atmosphere and the great time we had. In particular, I wish to thank Daniel Maurer who shares not only the office but also the same goal with the Suzanne as well as the Stanford Bunny. I also thank the former office mates, Michael Stoll who makes me laugh with his foreign language skills and Sebastian Volz who also shares some part of my journey from Saarbrücken to Stuttgart. I sincerely wish them all the best for their remaining Ph.D. period as well as future endeavour.

I owe an enormous debt of gratitude to Prof. Michael Breuß, Prof. Andrés Bruhn, Daniel Maurer, and Michael Stoll for proofreading the drafts of this thesis and giving me invaluable feedback.

Besides, I also thank system administrators, Anton Malina and Martin Schmid, for taking care of computer related problems and secretaries, Margot Roubicek and Christine Schütz, for helping me to save a lot of time to handle administrative matters. Moreover, my heartfelt thanks should go to Sophie Schroth as well for providing the professional assistance to deal with German bureaucratic matters.

I am also grateful to all MIA members at Saarland University that I have met while I was staying in Saarbrücken for the kindness and great working atmosphere: Dr. Oliver Demetz, Silvano Galliani, Gabriela Ghimpeteanu, Dr. Sven Grewenig, Dr. Pascal Gwosdek, Kai Hagenburg, Dr. Laurent Hoeltgen, Sebastian Hoffmann, Dr. Markus Mainberger, Dr. Nico Persch, Dr. Christian Schmaltz, Dr. Christopher Schroers, Dr. Simon Setzer, Dr. Levi Valgaerts, Dr. Henning Zimmer. In particular, I thank Prof. Martin Welk for the detailed comments on my presentation at Lège-Cap-Ferret and Dr. Oliver Vogel for sharing his code, respectively. The former system administrator Marcus Hargarter and the secretary Ellen Wintringer have always helped me with technical problems and tedious paperwork, respectively.

In the same context, I also thank all the nice people that I have met in Cottbus: Prof. Georg Bader, Prof. Peter Osterrieder, Dr. Romain Gengler. In particular, I thank PD Dr. Friedemann Kemm for sharing his broad knowledge not only on mathematics but also on many different areas and Dr. Andreas Kleefeld for the effective collaboration, respectively. I also have received the big aid from the system administrator Silke Büttner and the secretary Sigrid Schenk. Besides, I appreciate the kindness and the warmth as well from the family of Prof. Michael Breuß (Doris, Sonja, Johannes, Christian, Jonathan, Dominik) during my stay in Cottbus.

I would also like to give my special thanks to Prof. Thomas Ertl from Institute for Visualization and Interactive System (VIS) at University of Stuttgart for the hospitality during my period in Stuttgart. Moreover, I also deeply thank all VIS members for bringing up various topics over lunch at the canteen which sometimes lead to interesting and informative discussions: Martin Baumann, Tanja Blascheck, Dr. Harald Bosch, Dr. Florian Haag, Qi Han, Dr. Florian Heimerl, Dominik Herr, Markus John, Dr. Steffen Koch, Robert Krüger, Kuno Kurzhals, Dr. Steffen Lohmann, Dr. Alexandros Panagiotidis, Hermann Pflüger, Dr. Michael Raschke, Dr. Bernhard Schmitz, Dr. Dennis Thom, Dr. Michael Wörner.

I also gratefully acknowledge that this research has been financially supported in part by German Research Foundation (DFG), which makes my Ph.D. work possible.

Last but not the least, I would like to thank my family, my father who is still alive in my heart, my mother and my brother as well as his wife and son for their unconditional support not only throughout my Ph.D. work but also my whole life in general.

CONTENTS

Nomenclature ix

German Abstract - Zusammenfassung xi

Abstract xiii

1 Introduction 1
- 1.1 Perspective Shape from Shading: An Overview . . . 2
  - 1.1.1 PDE-based Methods . . . 2
  - 1.1.2 Variational Methods . . . 5
- 1.2 Contributions . . . 9
  - 1.2.1 PDE-based Methods . . . 9
  - 1.2.2 Variational Methods . . . 10
- 1.3 Outline . . . 12

I PDE-based Approaches 17

2 Mathematical Background on PDE-based Approaches 19
- 2.1 Hamilton-Jacobi Equations . . . 19
  - 2.1.1 Partial Differential Equations . . . 20
- 2.2 Well-Posedness and Notions of Solutions . . . 23
  - 2.2.1 Vanishing Viscosity Method . . . 26
  - 2.2.2 One-Sided Differentials . . . 32
  - 2.2.3 Viscosity Solutions . . . 38
- 2.3 Fast Marching Methods . . . 44
  - 2.3.1 A Motivational Example . . . 44
  - 2.3.2 Approximation by an Upwind Scheme . . . 46
  - 2.3.3 The Fast Marching Algorithm . . . 55
- 2.4 Summary . . . 58

3 PDE-based Shape from Shading Models 59

3.1 Modelling Components . . . 59
    3.1.1 Camera Model . . . 59
    3.1.2 Basics on Radiometry . . . 62
    3.1.3 Surface Reflectance . . . 63
    3.1.4 Brightness Equation with Light Attenuation Term . . . 70
3.2 Perspective Lambertian SfS Model . . . 71
    3.2.1 Surface Parametrisation under Perspective Projection . . . 72
    3.2.2 Brightness Equation with Lambertian Reflectance . . . 72
    3.2.3 Hamiltonian for the Perspective Lambertian SfS . . . 75
3.3 Perspective Phong SfS Model . . . 76
    3.3.1 Brightness Equation with Phong Reflectance . . . 76
    3.3.2 Hamiltonian for the Perspective Phong SfS . . . 77
3.4 Perspective Oren-Nayar SfS Model . . . 78
    3.4.1 Brightness Equation with Oren-Nayar Reflectance . . . 79
    3.4.2 Hamiltonian for the Perspective Oren-Nayar SfS . . . 79
3.5 Properties of PDE-based SfS Models . . . 82
    3.5.1 Types of Hamiltonians . . . 82
    3.5.2 Fast Marching Methods for PDE-based SfS Models . . . 83
    3.5.3 Ambiguities . . . 88
3.6 Summary . . . 91

4 Generalised Perspective Shape from Shading Models 93

4.1 Surface Parametrisation for Arbitrary Light Source Positions . . . 94
    4.1.1 Surface Representation in Spherical Coordinates . . . 94
4.2 Lambertian SfS Model in Spherical Coordinates . . . 100
    4.2.1 Generalised Lambertian Brightness Equation . . . 101
4.3 Oren-Nayar SfS in Spherical Coordinates . . . 102
    4.3.1 Generalised Oren-Nayar Brightness Equation . . . 103
4.4 Adapted Fast Marching Scheme for Spherical Coordinates . . . 111
    4.4.1 Initialisation . . . 111
    4.4.2 Update Process in Fast Marching Scheme . . . 112
    4.4.3 Benefits of Adapted Fast Marching Method . . . 112
4.5 Experimental Evaluation . . . 113
    4.5.1 Lambertian Surface . . . 113
    4.5.2 Oren-Nayar Surface . . . 115
4.6 Summary . . . 118

II Variational Methods 119

5 Variational Perspective Shape from Shading 121
- 5.1 Mathematical Background on Variational Methods 122
  - 5.1.1 Calculus of Variations 122
  - 5.1.2 Regularisation by Smoothness Terms 127
- 5.2 Variational Shape from Shading Models 129
  - 5.2.1 Shortcomings of Existing Models for Variational SfS 129
  - 5.2.2 Variational Perspective SfS Model 130
- 5.3 Minimisation 133
  - 5.3.1 The Base Case 133
  - 5.3.2 The Extension Cases 136
  - 5.3.3 Discretisation 138
  - 5.3.4 Numerical Solution 144
- 5.4 Experimental Results 145
  - 5.4.1 Influence of Regularisations 145
  - 5.4.2 Influence of Confidence Function 146
  - 5.4.3 Robustness with Respect to Noise 148
- 5.5 Summary 149

6 Variational Perspective SfS with Cartesian Depth Parametrisation 153
- 6.1 PDE-based Model with Cartesian Depth Parametrisation 154
  - 6.1.1 Cartesian Depth Parametrisation of the Surface 154
  - 6.1.2 Brightness Equation with Cartesian Depth Parametrisation . . 156
- 6.2 Variational Model with Cartesian Depth Parametrisation 159
  - 6.2.1 Variational Model 159
  - 6.2.2 Model Properties 159
- 6.3 Minimisation 161
  - 6.3.1 Euler-Lagrange Equations 162
  - 6.3.2 Approximation of Spatial Derivative for Data Term 165
  - 6.3.3 Euler-Lagrange Equation with Approximate Energy 166
  - 6.3.4 Discretisation 173
- 6.4 Experimental Evaluation 184
  - 6.4.1 Test Images and Evaluation Metrics 185
  - 6.4.2 Results on Synthetic Test Images 186
  - 6.4.3 Results on Real World Images 196
- 6.5 Summary 196

7 An Efficient Linearisation Approach 199
- 7.1 Hyperbolic Warping Strategy 200
  - 7.1.1 Fixed Point Iteration 200
  - 7.1.2 Incremental Computation and Linearisation 201

7.1.3 Coarse-to-fine Scheme 208
7.1.4 Computation Method 210
7.2 Experimental Evaluation 212
7.2.1 Impact of the Smoothness Term 212
7.2.2 Comparison with Other Methods 213
7.2.3 Reconstruction with Inpainting 215
7.2.4 High-resolution Image 215
7.3 Summary 216

8 Summary & Outlook **219**
8.1 Summary of Contributions 219
8.1.1 PDE-based Methods 219
8.1.2 Variational Methods 220
8.2 Outlook 222

References **225**

Appendix A Intrinsic Parameters **247**
A.1 Coordinate Transformation 248
A.2 Standard PDE-based Models in Pixel Coordinates 248
A.3 Variational Models in Pixel Coordinates 249
A.4 Euler-Lagrange Equations in Pixel Coordinates 250

Appendix B Publications **253**
B.1 Book Chapters 253
B.2 Conference Proceedings 253

NOMENCLATURE

Acronyms / Abbreviations

BRDF	bidirectional reflectance distribution function
DBC	Dirichlet boundary condition
FM	fast marching
GBR	generalised bas-relief
GNC	graduated non-convexity
HJBE	Hamilton-Jacobi-Bellman equation
HJE	Hamilton-Jacobi equation
LDFPI	lagged diffusivity fixed point iteration
NBC	Neumann boundary condition
ODE	ordinary differential equation
PDE	partial differential equation
PSfS	perspective Shape from Shading
SfS	Shape from Shading

GERMAN ABSTRACT - ZUSAMMENFASSUNG

Das Ziel von Shape from Shading (SfS) ist die Rekonstruktion der 3-D Oberflächentiefe innerhalb einer Szene durch die Verwendung der Intensitätsvariationen aus einem einzelnen 2-D Eingabebild, wobei Informationen über die Oberflächenreflexion, Beleuchtungs- und Kamerabedingungen gegeben sind. Für dieses klassische Problem in Computer Vision wurden im wesentlichen zwei Klassen von Ansätzen entwickelt: eine Klasse basiert auf partiellen Differentialgleichungen (PDGls) während die andere sich auf Variationsansätze stützt.

Im allgemeinen beinhalten PDGl-basierte Ansätze fortgeschrittenere Modellannahmen wie etwa die perspektivische Projektion oder weitergehende Reflexion. Sie reagieren allerdings empfindlicher auf Bildrauschen und fehlende Information. Darüberhinaus wurde bis jetzt – trotz des Fortschritts hinsichtlich weitergehenderer Modellannahmen – *kein* Verfahren vorgestellt, welches allgemeine Beleuchtungsszenarien im Hinblick auf die Position der Lichtquelle berücksichtigt.

Im Gegensatz zu PDGl-basierten Ansätzen beinhalten Variationsansätze für gewöhnlich eher einfache Modellannahmen wie etwa die orthografische Projektion oder Lambertsche Reflexion. Andererseits sind sie durch ihren Glattheitsterm robust unter Bildrauschen und fehlender Information.

Die Hauptdefizite von bestehenden Variationsansätzen setzen sich zusammen aus: (i) Einige Methoden verwenden *approximierte* Oberflächennormalen für perspektivisches SfS (PSfS), indem sie sich der Normalen aus der orthografischen Projektion bedienen. (ii) Weiterhin dominieren *indirekte* Strategien: im ersten Schritt werden die Oberflächennormalen unter Verwendung von Hilfsvariablen gewonnen. Anschließend wird die Tiefe durch die Integration der Normalen mit Hilfe der Integrierbarkeits-Nebenbedingung rekonstruiert.

In Anbetracht der Haupteigenschaften und Defizite beider Klassen von Ansätzen liefert die vorliegende Arbeit Beiträge *sowohl* zu PDGl-basierten Verfahren *als auch* zu Variationsansätzen, jeweils im Hinblick auf Aspekte der Modellierung und der Numerik.

Bei den PDGl-basierten Ansätzen stellen wir ein neues PSfS-Modell basierend auf *allgemeinen Beleuchtungsgleichungen* (ABGls) vor, das durch Hamilton-Jacobi Gleichungen (HJGls) beschrieben wird. Anders als bisherige Modelle kann unser vorgestelltes Modell tatsächlich mit allgemeinen Beleuchtungsszenarien im Hinblick auf die Position einer Lichtquelle umgehen. Zusätzlich erweitern wir das Modell so, dass es auch mit nicht-Lambertschen Objekten zurechtkommt. Abgesehen von der Modellierungsseite entwickeln wir ein numerisches Schema, das auf der Fast-Marching-Methode (FM) aufbaut, welche als eine der effizientesten Methoden zu Lösung der HJGls gilt. Unser Schema erlaubt es uns, auf effiziente Weise Lösungen für die vorgestellten ABGls zu erhalten, indem die zu Beginn der Berechnung gegebene Information an kritischen Punkten auf die verbleibenden, d.h. die noch zu berechnenden Bereiche, ausgebreitet wird.

Im Bereich der Variationsansätze setzen wir unser Energiefunktional für PSfS unter Verwendung einer direkten Tiefenparametrisierung und eines kanten-erhaltenden Regularisierers zusammen. Unsere Methode ist ein *voll* perspektivischer und *direkter* Ansatz: die verwendeten Oberflächennormalen werden aus der perspektivischen Projektion hergeleitet anstatt sie den orthografischen Modellen zu entlehnen. Da unsere Modelle direkt unter Verwendung der Tiefe optimiert werden, können wir darüber hinaus auf zusätzliche Schritte wie etwa die Integration von Gradientenfeldern und zusätzliche Terme wie etwa die Integrabilitätsbedingung verzichten – im Gegensatz zu existierenden Variationsansätzen. Auf der Seite der Numerik stellen wir für die Optimierung ein alternierendes explizites Schema vor, um mit den hyperbolischen Eigenschaften des Datenterms, welcher auf Grund der hochgradig nicht-konvexen Energie in eine grob-nach-fein Strategie eingebettet ist, umzugehen. Weiterhin entwickeln wir ein hyperbolisches Warping-Schema, um die Beschränkungen der Zeitschrittweite und die starke Nichtlinearität des vorgenannten expliziten Schemas zu überwinden, indem wir einen Linearisierungsansatz, welcher auf einem verzögerten Upwind-Schema und einer verzögerten Diffusivitätsmethode fußt, in einen Gauß-Newton-artigen grob-nach-fein Löser einbetten. Unser Schema erzielt nicht nur einen signifikanten Geschwindigkeitsschub, sondern bietet verglichen mit traditionellen expliziten Lösern auch einen substantiellen Nutzen im Falle starker Regularisierung oder hochauflösender Bilddaten.

Abstract

Shape from Shading (SfS) aims at reconstructing the 3-D surface depth in a scene using intensity variations from a single 2-D input image with information given on surface reflectance, illumination and camera conditions. For this classical problem in computer vision, mainly two classes of approaches have been developed in the field: One is based on partial differential equations (PDEs) and the other relies on variational methods.

In general, PDE-based methods have more advanced model assumptions such as the perspective projection and advanced reflectance. However, they are more sensitive to noise and missing information. Moreover, despite the progress with the advanced model assumptions *no* model has been proposed so far to consider general illumination scenarios in terms of the position of a light source.

In contrast to PDE-based approaches, variational methods usually make relatively simple model assumptions such as the orthographic projection and Lambertian reflectance. But they are robust with respect to noise and missing information because of the smoothness term. The main shortcomings of existing variational methods are: (i) Some methods use *approximated* surface normals for perspective SfS (PSfS) by borrowing normals from orthographic models. (ii) In addition, *indirect* strategies are dominant: As a first step, surface normals are obtained using auxiliary variables. Then, as a subsequent step the depth is reconstructed by integrating the normals with the integrability constraint.

Being aware of these main properties and shortcomings of each approach, the present thesis makes contributions to *both* PDE-based *and* variational approaches, each of which with respect to modelling and numerical aspects.

For PDE-based approaches, we propose a novel PSfS model called *generalised brightness equations* (GBEs) described by Hamilton-Jacobi equations (HJEs). In contrast to existing models, our proposed model can actually handle general illumination scenarios in terms of the position of a light source. Furthermore, we extend the model in a way that it can also manage non-Lambertian objects. Apart from the modelling side, we develop a numerical scheme based on the fast marching (FM) method which is known to be one of the most efficient methods for solving HJEs. Our scheme allows to obtain solutions efficiently to the proposed GBEs by propagating the initial information at critical points to the remaining computational domain.

For variational methods, we construct our energy functional for PSfS by making use of a direct depth parametrisation and an edge-preserving regulariser. Our method is a *full* perspective and *direct* approach: The employed surface normals in our models are derived from the perspective projection instead of borrowing from orthographic models. Moreover, since our models are optimised with respect to the depth directly, neither a subsequent step such as the integration of gradient fields nor an additional term such as integrability constraint is required in contrast to most existing variational methods. On the numerical side, we propose an alternating explicit scheme as an optimisation strategy to deal with the hyperbolic properties of the data term, which is embedded into a coarse-to-fine framework due to highly non-convex energy. Furthermore, we develop a hyperbolic warping scheme to overcome the time step size constraint and the strong nonlinearity of the aforementioned explicit-type scheme by embedding a linearisation approach based on a lagged upwind scheme and lagged diffusivity method into a Gauß-Newton type coarse-to-fine solver. Our scheme not only achieves a significant speedup but also offers a substantial benefit for a large amount of regularisations as well as high resolution images compared to traditional explicit solvers.

CHAPTER 1

INTRODUCTION

The world that we live in consists of numerous objects, each of which has its own shape. In daily life, we encounter many situations where we have to interact with these objects via our visual system by looking at them, by recognising them and by responding to them accordingly, e.g. when observing the surface of the moon through a telescope. One can note that during the detection and recognition of an object our brain has actually demonstrated the capability of implicitly inferring the 3-D surface shape of an object from a 2-D retinal image without making any serious efforts. This type of perception is, however, still by no means trivial for computers despite all sophistications with considerable technological advancement [99]. Therefore, a clear understanding of this process constitutes an integral part for enhancing the quality of computer vision systems.

The aforementioned inference process is known as *Shape from Shading* (SfS) and aims at extracting the 3-D depth information of an object (shape) relying on the light intensity variations from a single 2-D grey value image (shading), provided that the information on the surface reflectance, the camera and the illumination conditions is available, see Figure 1.1. During the recovery process, only the shading plays a crucial role as a cue upon the typical assumption that a surface patch facing towards the light source in a scene receives more energy and thereby appears brighter than the one facing away from the source.

Given the fact that this monocular cue based strategy, unlike other 3-D reconstruction methods such as stereo or multi-view, does not depend on texture information, it can be an appealing alternative, particularly when the setup of two or multiple cameras is not allowed possibly due to space constraints or a wide baseline. This distinct advantage leads naturally to an enormous diversity of applications in a wide variety of fields, ranging from large scale problems like astronomy [102, 214] and terrain analysis [40, 183, 205, 266] to small scale ones including, but not limited to, dentistry [3], endoscopy [167, 171, 237, 270], document restoration [60, 278, 279, 280], reconstruction of archaeological finds [84], and quality control in manufacturing industry [74, 81, 169]. Consequently, SfS has been one of the fundamental problems in computer vision for almost a half-century [79, 87, 234, 281].

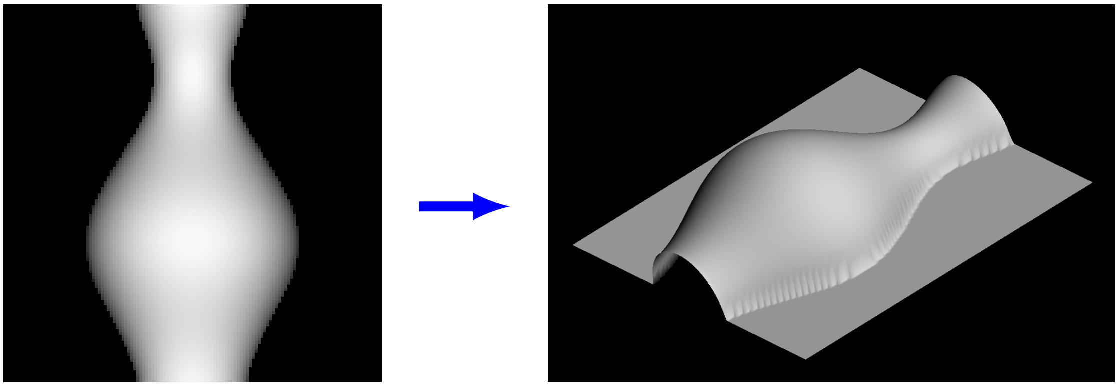
(a) Input: Shading. (b) Output: Shape.

Figure 1.1. The Shape from Shading (SfS) problem.

1.1 Perspective Shape from Shading: An Overview

In this section, we provide a brief overview of approaches to solve the problem and how they have made progress with special emphasis on modelling assumptions. To this end, we focus mainly on two classes of approaches following the classification in [281]: One approach is to make use of partial differential equations (PDEs), the other one is the usage of variational methods. For both classes, we are particularly interested in *perspective* SfS (PSfS) methods which correspond to relatively modern and realistic approaches [79].

1.1.1 PDE-based Methods

This section gives an insight into PDE-based SfS methods by having a look at the most important related work in the field.

Basic Idea of PDE-based Methods

Typically, the SfS problem is formulated by the so-called brightness equation (or image irradiance equation) [116] which describes the relationship between the obtained grey value image and the surface profiles of an object by incorporating the surface normal vectors in consideration of illumination conditions. Since the 1970's when Horn had proposed to solve the image irradiance equation by propagating the depth information at brightest points of an input image to the rest of the computational domain [116], most PDE-based methods have followed the same fundamental principle for reconstruction [79, 281]. On this account, PDE-based methods are also called *propagation* methods despite all the differences in each model. The points with maximal grey value called singular points (or critical points) are of great importance in this approach not only from a theoretical viewpoint, e.g. for an ambiguity analysis [44, 78, 172] or for mathematical concepts such as viscosity solutions [63, 64], but also for the development of efficient algorithms, e.g. the fast marching (FM) algorithm [230].

Related Work

Classical PDE-based Methods. According to [79], it was the Dutch astronomer Van Diggelen who first attempted to use photometric cues for surface reconstruction in the 1950's [250]. Rindfleisch, then, proposed the first solution in the 1960's, where he used photometric properties of a surface to extract the profile of lunar topography [214]. Subsequently, Horn coined the term "Shape from Shading" for this problem, and formulated the problem as nonlinear first-order PDEs [116, 117] by generalising the solution by Rindfleisch based on so-called characteristic strips expansions [79, 116, 281]. Since most approaches in this period had been designed for applications in astronomy [1] [120, 127, 185, 265], the following simplified assumptions have been dominant for almost three decades [79, 281]: (i) The camera performs a simple *orthographic* projection, (ii) a light source is placed at *infinity*, and (iii) the object under consideration has *Lambertian* surface.

PDE-based Perspective Shape from Shading. As stated in [281], the reconstruction results of orthographic SfS models were still not compelling until the end of the 1990's, even if novel notions such as viscosity solutions [219] and level set formulations [136, 139] were introduced to resolve inherent difficulties of the problem, e.g. the existence and the uniqueness of solutions.

However, the situation has been entirely turned around when a realistic *perspective* camera projection became the *de facto* standard in the modelling process around the late 1990's and early 2000's [60, 71, 171, 194, 236]. The perspective projection offers a clear advantage when an object is relatively close to the camera, e.g. in endoscopy or dentistry. Since a traditional orthographic camera model cannot capture the perspective effects appropriately in such cases, it constitutes the primary source of errors in the reconstruction as Tankus and his colleagues have shown in [235, 236, 238].

Aside from the perspective projection, Deguchi and Okatani have considered two more factors for a realistic modelling in endoscopy: the position of a light source at *the projection centre of a camera* and *the light attenuation term* [71, 171]. In view of the relatively small size of an endoscope head, the light source position was approximated by the optical centre of a camera. Furthermore, the employed physics motivating a quadratic fall-off term provided a good description of a scenario when a camera flash is turned on in mostly dark surroundings. The solution to the resulting image irradiance equation was obtained by the extended method of

---

[1] SfS is sometimes known as "photoclinometry" outside computer vision community.

Kimmel *et al.* [139] which is based on a level set approach [182]. By taking advantage of the same modelling assumptions as in [71, 171], Prados and Faugeras, afterwards, have obtained a brightness equation described by a hyperbolic type of PDE, where the solution was attained by propagating the initial depth on critical points with the efficient fast marching algorithm [195]. As discussed in [193, 195], the light attenuation term from the inverse square law plays a significant role in resolving the convex/concave ambiguity to a large extent, although some ambiguities are still present [44]. The work of Prados and Faugeras [195] has been further extended by incorporating advanced *non-Lambertian* reflectance models such as Oren-Nayar [178, 179, 180, 181] or the Phong reflectance [189].

Apart from considering advanced reflection models, there have been other aspects of investigations as well. For instance, Bruvoll and Reimers have used a radial parametrisation for describing a surface in Cartesian coordinates by considering the light attenuation term [49]. In this case, the solution was obtained in triangular meshes using the extended FM method of Kimmel and Sethian [137].

Table 1.1. An overview of progress in PDE-based SfS models.

camera projection	position of a light source	surface reflectance	light attenuation	references
orthographic	infinity	Lambertian [148]	–	[116, 194, 196, 219]
orthographic	infinity	Oren-Nayar [178]	–	[203, 204, 223]
orthographic	infinity	Wolff [267, 268]	–	[203, 204]
orthographic	infinity	Wolf-Nayar-Oren [269]	–	[203, 204]
orthographic	infinity	Ward [263]	–	[7]
perspective	infinity	Lambertian [148]	–	[60, 194, 196, 236]
perspective	optical centre	Lambertian [148]	✓	[49, 71, 171, 195]
perspective	optical centre	Oren-Nayar [178]	✓	[6]
perspective	optical centre	Wolf-Nayar-Oren [269]	✓	[7]
perspective	optical centre	Phong [189]	✓	[258]
perspective	*not* optical centre	Lambertian [148]	✓	this work [93]
perspective	*not* optical centre	Oren-Nayar [178]	✓	this work [130]

Shortcomings of Existing PDE-based Methods

For an overview, we have summarised the current status of PDE-based SfS methods in Table 1.1. While considerable progress has been made by combining a realistic perspective camera model, advanced reflectance models as well as the light attenuation term, there have been *no* attempts so far to consider general illumination scenarios in terms of the position of a light source, i.e. a point light source *not* being at the optical centre of the camera:

(i) When it comes to the modelling side, the standard assumption of recent PSfS on the position of a light source *cannot* hold per construction, e.g. a flash attached to a digital camera cannot be in the optical centre.

(ii) Apart from the modelling side, an *efficient* numerical strategy is required to propagate the information at singular points in the general scenario.

This suggests that it is highly desirable to construct a new model by relaxing the current PSfS assumptions as well as to develop an associated numerical algorithm.

1.1.2 Variational Methods

As in the case of PDE-based methods, we now present a brief review of variational PSfS methods by paying close attention to recent developments in the field.

Basic Idea of Variational Methods

While PDE-based methods aim to determine the solution of the brightness equation directly, the solution of variational methods is obtained as the minimiser of an associated energy functional. This functional typically comprises a data term and a smoothness term: The brightness constraint formulated by the image irradiance equation is contained in the data term, which ensures the similarity between the input image and the reprojected solution. The role of the smoothness term is to impose regularity constraints on the solution candidates attained from the data term by retrieving information from the neighbourhood, so that the final reconstruction reveals the desired properties. The main strength of variational methods lies in their robustness and their adaptability: Even though some noise is present or some piece of information is missing in the input data, variational methods show robustness by taking advantage of the neighbouring information due to the smoothness term [131, 132, 160]. Moreover, in contrast to PDE-based methods no information at singular points is required for initialisation [79, 270]. Hence, variational methods can be applied to most general cases [79]. Besides, the entire optimisation framework can be adjusted accordingly for different situations, e.g. when further constraints such as integrability on solutions are required to be enforced [89], which is sometimes even infeasible for PDE-based methods.

Related Work

Classical Variational Methods. Although Horn had proposed the solution strategy to the brightness equation by means of PDE-based methods [116], these approaches were not very common for over two decades [281]. The main reasons for this situation were: On the one hand, the classical mathematical framework cannot handle appropriately the brightness equation formulated by nonlinear first order PDEs [14], e.g. existence and uniqueness of solutions. On the other hand, another difficulty comes from the selection of unknowns and the parametrisations of surfaces in brightness equations. As in [89, 119], the gradient field related to the surface normal vectors had been selected as unknowns in most early work. This leads necessarily to an underdetermined system because there are two unknowns (the gradient entries) for one grey value. Since the depth is not computed directly, the variables for the gradient are typically called auxiliary variables [281]. In order to overcome the difficulty of being underdetermined, variational methods became an appealing alternative framework to using PDE-based methods. Although several methods had been proposed since the first variational model of Ikeuchi and Horn [125], the employed modelling assumptions had still remained to be simple as in the case of PDE-based approaches: an *orthographic* camera projection, a *distant* light source at infinity and the *Lambertian* reflectance model. The focus was rather on enforcing meaningful constraints such as integrability [89] instead of formulating appropriate brightness equations relying on more realistic assumptions such as a perspective camera projection. Moreover, the smoothness term had typically regularised the surface normals instead of the depth itself due to the selection of unknowns. There had also been methods for *direct* reconstruction which require no integration of surface normals as a subsequent step for final depth recovery, e.g. Leclerc and Bobick [149] by considering a discrete formulation and a conjugate gradient and Vogel *et al.* [257] by making use of a second order smoothness term. However, all these methods have been restricted to the orthogonal camera model. Not surprisingly, results were often rather limited in terms of quality or approaches even failed in practice, which is not different from the case of PDE-based methods [281].

Variational Perspective Shape from Shading. For exploiting the strengths of both the perspective projection and variational methods, researches have recently considered approaches which embed PSfS models into an appropriate variational framework. However, only few works can be found in literature based on this recent idea. They may be classified into two groups: indirect and direct estimation methods.

In [278], Zhang and colleagues have formulated the model by means of the brightness equation with Cartesian parametrisation using auxiliary variables and imposed smoothness and integrability constraints. Since the light source is assumed to be far away from the scene, the light attenuation term is not taken into account. The solution was only obtained for gradient fields, which need to be further integrated. Moreover, initialisation of the algorithm relied actually on that of PDE-based methods. Afterwards, Wu *et al.* have proposed a model using a Cartesian parametrisation in view of the light attenuation term assuming that two point light sources are close to the projection centre of a camera [270]. The solution strategy also relied on indirect methods by repeatedly integrating surface normals during the minimisation process. Furthermore, both approaches have utilised their surface normals from orthographic projection based methods relying on the work of Horn and Brooks [119]. Hence, this makes the resulting models only applicable as long as only weak perspective effects are dominant.

In contrast, Abdelrahim *et al.* have adopted an approach [1], where the Cartesian surface depth has been directly reconstructed by penalising the surface normals using initialisation based on PDE-based methods and the homogeneous smoothness term that does not allow to retain edge structures of an object. This necessarily entails the integrability constraint as an additional term in the model.

Linearisation Methods. In the class of variational methods, there exists a strategy which makes use of linear approximations for the brightness equations containing reflectance functions. This strategy refers to linearisation methods [281] and is primarily focused on the numerical aspect. However, in contrast to PDE-based or other variational approaches this strategy has not been preferred since the results had already been unsatisfactory without linearisation [281].

The first approach using this strategy dates back to the late 1980's by Pentland [186], where he applied a linear approximation to the reflectance function with respect to the surface gradient and obtained a solution by means of the Fourier transform of the linearised function. Afterwards, Tsai and Shah had first discretised the gradient fields and then approximated the brightness equation by applying the discretised gradient as well as the Taylor expansion with respect to the depth [247], where the solution was attained by the Jacobi iteration method. Recently, Barron and Malik have proposed a method [22] that jointly estimates shape, illumination and albedo using a linearisation as well as the statistics of natural images [86, 123] within a stochastic optimisation framework. Nevertheless, all these approaches were developed in the context of an orthogonal projection.

The only two works that considered a linearisation approach for perspective SfS were proposed by Lee and Kuo [150, 151]. However, these two methods are specifically designed for a surface approximated by triangular elements and no explicit regularisation was reported. Moreover, none of the aforementioned methods has respected the hyperbolic nature of the brightness equation by employing appropriate upwind type schemes such as [219] for discretising the occurring gradient field. However, it is well known that such schemes are particularly important for developing a stable numerical method [229].

Table 1.2. Comparison of variational models for Shape from Shading.

	Ikeuchi *et al.* [125]	Brooks *et al.* [45]	Frankot *et al.* [89]	Zhang *et al.* [278]	Vogel *et al.* [258]	Wu *et al.* [270]	Abdelrahim *et al.* [1]	this work [131]	this work [132]
assumptions									
camera projection	orthographic	orthographic	orthographic	perspective	orthographic	perspective	perspective	perspective	perspective
surface type	Lambertian	Lambertian	Lambertian	Lambertian	Lambertian	Lambertian	Lambertian	Lambertian	Lambertian
light source position	distant	distant	distant	distant	distant	close to optical centre	distant	optical centre	optical centre
features									
selection of unknowns	stereographic functions [2]	Cartesian surface normals	Cartesian surface normals	Cartesian depth	Cartesian depth	Cartesian depth	Cartesian depth	radial depth	Cartesian depth
parametrisation	stereographic functions [2]	Cartesian surface normals	Cartesian surface normals	Cartesian depth	Cartesian depth	Cartesian depth	Cartesian depth	radial depth	Cartesian depth
reprojection error as data term	✓	✓	✓	✓	✓	✓	✓	–	✓
regularisation	stereographic functions [2]	Cartesian surface normals	Cartesian surface normals	Cartesian depth	Cartesian depth	Cartesian depth	Cartesian surface normal	radial depth	Cartesian depth
light attenuation factor	–	–	–	–	–	✓	✓[5]	✓	✓
correct surface normal	✓	✓	✓	–	✓	–	✓[6]	✓	✓
no auxiliary variables	–	–	–	–	✓	–	✓	✓	✓
no integrability term	–[3]	–[3]	–	–	✓	–[4]	–	✓	✓
direct estimation[1]	–	–	–	–	✓	–	✓	✓	✓
edge preservation	–	–	–	–	–	–	–	✓	✓

[1] depth is computed without using extra variable for surface normals
[2] represents Cartesian surface normals by means of stereographic projection
[3] no integrability constraint considered
[4] integrability constraint realised through repeated integration of surface normals
[5] factor not explicitly formulated in terms of the Cartesian depth
[6] based on the derivation in [2]

Shortcomings of Existing Variational Methods

As we have conducted for PDE-based methods, we compile the features of existing variational SfS models in Table 1.2 to identify shortcomings:

(i) From a modelling standpoint, *no* single model contains *all* useful features listed in Table 1.2. For instance, the work of Wu *et al.* [270] had considered general illumination scenarios in terms of the position of a light source but an *orthographic* surface normal was used for the perspective model. Besides, most approaches belong to the class of *indirect* methods that require a subsequent step for reconstruction. Moreover, an *edge-preserving* smoothness term has *not* even been mentioned for PSfS in the literature.

(ii) From an algorithmic side, *no* scheme has been proposed to handle both *non-convex models* and the *hyperbolic properties* of the data term. Moreover, concerning the initialisation some approaches still rely on PDE-based methods [1, 278]. However, this, in fact, is obviously against the spirit of variational framework, which states that the optimisation approach is applicable to most general cases according to [79].

Therefore, it is desirable to design a unified variational model for PSfS that can reconstruct the parametrised depth *directly* without requiring the explicit integrability constraint or repeated integration steps. When it comes to the numerical side, an efficient optimisation scheme should be developed which can deal with the underlying non-convex model as well as the hyperbolic data term. Moreover, the scheme should *not* be susceptible to any specific initialisation such as the one from the PDE-based methods as in [1, 278] and should *not* require any relatively accurate initial depth for meaningful results at the same time.

1.2 Contributions

The main goal of this thesis is to establish a mathematical model and to provide an appropriate algorithmic solution in the field of perspective Shape from Shading by taking the current state-of-the-art into account with respect to each of the two types of methods in Section 1.1: PDE-based approaches and variational methods. In this section, we state our contributions of this thesis which have been presented at conferences or have appeared in form of a book chapter: [93] and [130] as well as [129] for PDE-based methods, [131], [132] and [160] for variational methods.

1.2.1 PDE-based Methods

Our contributions to PDE-based approaches are twofold: One is for the modelling side and the other is for the numerical one.

Modelling Aspect

On the modelling side of PDE-based methods, in consideration of a quadratic light attenuation factor we first construct our mathematical model in a spherical coordinate system based on the Lambertian reflectance supposing that a point light source is *not* at the optical centre of a camera. Moreover, we further advance the field by *successfully merging* the two paths of research – advanced reflectance models *and* an arbitrary light position. This finally allows *flexibility* to handle general illumination scenarios with non-Lambertian objects. The resulting mathematical model is delineated by a set of *Hamilton-Jacobi equations* (HJEs) belonging to a special class of PDEs whose solution should be understood in the viscosity sense [63, 64]. We call the derived novel image irradiance equations *generalised brightness equations* (GBEs).

Aside from our novel model, by investigating the Oren-Nayar based standard PSfS model of Ahmed and Farag [6] with respect to Osher's criterion [182, 200, 248] we provide a theoretical justification in terms of the safe range of the roughness parameter for applying the FM method to the model, which has been chosen so far only on a purely heuristic basis; see [256].

Numerical Aspect

On the numerical side of PDE-based methods, we design an *adapted* fast marching scheme which is a specifically tailored variant of the FM for the derived model. This algorithm extends the usual FM method in such a way that it can handle the general-type HJEs in a spherical coordinate system for the Cartesian input data by an iterative correction step as well as the bilinear interpolation and it can also find a solution in the viscosity sense at the same time.

1.2.2 Variational Methods

For variational methods, we also have made contributions to the field regarding both modelling and numerical aspects.

Modelling Aspect

On the modelling side, we first consider a variational model for perspective SfS using a radial depth parametrisation based on the PDE-based model of Prados and Faugeras [195]. Subsequently, we construct another variational model by changing the parametrisation from a radial depth to a Cartesian one. Both models incorporate an edge-preserving smoothness term which has *not* been applied to variational PSfS so far as well as a correct surface normal which is, in some models, *not* the case, e.g. the work of Zhang *et al.* [278] and Wu *et al.* [270], see Table 1.2. Moreover, both approaches are full *direct* methods for reconstruction since the unknown in each of our model is the depth itself and all actions are directly taken on the depth. This suggests that our methods do not yield gradient fields that need to be integrated in a subsequent step as in [45, 89, 125]. Furthermore, in contrast to [1, 278] no integrability constraints are required in the model because the condition is already contained in the smoothness term, cf. Table 1.2. Besides, our models are equipped with a mechanism to exclude unreliable regions such as noise or missing information through a confidence function, where the smoothness term takes the control and fills in information retrieved from the neighbourhood. One of the main advantages by changing the parametrisation from the radial depth to the Cartesian one is that the Cartesian depth based model allows a *geometrically* more meaningful interpretation of the smoothness induced by the regulariser since an object of constant depth describes a plane instead of a sphere on which the radial depth based model rely. In addition, the Cartesian depth based model has the potential to be combined with different cues such as stereo [216], multi-view stereo [271, 273], or scene flow [24, 25], where the depth is typically described in the same way.

Numerical Aspect

On the numerical side, we propose a novel optimisation scheme based on a hierarchical graduated optimisation strategy [9, 10, 211]. In order to deal with the arising *non-convex* energy, we embed an alternating explicit scheme based on the upwind discretisation [219] into a coarse-to-fine minimisation framework, where the employed alternating explicit scheme achieves considerable speedup compared with the traditional explicit scheme. Furthermore, this approach brings another advantage on the initialisation such that our method does *not* necessarily rely on a specific initialisation strategy any more, e.g. on PDE-based methods as the SfS approaches in [1, 278].

Linearisation Methods. Regarding linearisation methods, we develop a *hyperbolic warping scheme*, i.e. an efficient numerical algorithm based on our variational PSfS model that can resolve not only *nonlinearity* but also *non-convexity*. To obtain a linear approximation, we introduce an incremental computation as in [48, 254] and apply different methods to each term in view of structures at hand: For the data term, we make use of the Taylor approximation after employing the lagged upwind type discretisation [219] by respecting the hyperbolic nature of the data term, which is typically not the case for usual linearisation methods such as [247]. To resolve the nonlinearity in the smoothness term which actually arises in the argument of a function, we utilise the lagged diffusivity method [48, 51, 253, 254] that deals with a nonlinear problem as a series of linear ones by means of a fixed point iteration. For the non-convexity of the problem, we embed the derived lagged upwind discretisation scheme into a Gauß-Newton type multi-resolution optimisation framework as in our variational approach. The resulting scheme achieves a speedup by more than three orders of magnitude compared with the aforementioned alternating explicit scheme, which thereby allows our algorithm to handle considerably larger image sizes efficiently. Aside from the efficiency, the essential feature that distinguishes our hyperbolic warping scheme from other explicit methods lies in the feasibility of a large amount of regularisation without being affected by time step constraints. This makes our algorithm more robust with respect to corrupt data with noise or missing information in an effective way. Moreover, we propose a method to compute the arising derivatives of the reflectance function in the data term numerically during the linearisation process. Evidently, the proposed method has the full potential to be extended in a straightforward way to more advanced reflection models such as the Oren-Nayar model for the rough surfaces [178] or the Phong model for specular reflections [189]. This demonstrates the high versatility of our hyperbolic warping scheme: it can be applied to other existing variational SfS models which typically utilise the *explicit* schemes as the *de facto* standard, or it can be extended to the aforementioned advanced reflectance models as well as it can be integrated as a module for a joint work with different depth cues such as stereo or multi-view due to the Cartesian depth based parametrisation. A recent variational method that combines SfS and stereo already makes use of our hyperbolic warping strategy [161]. Hence, the proposed numerical scheme is a promising candidate for a standard tool in variational perspective SfS.

1.3 Outline

Let us now provide a synopsis of this thesis that consists of two parts by covering the main subjects of each chapter: Part I is pertinent to PDE-based methods and Part II is germane to variational methods, each of which contains three chapters, see Figure 1.2 for the structure of the work. As we proceed, we also indicate our other contributions to which no attention has been drawn yet in Section 1.2. Moreover, the complete publication list is compiled in Chapter B that also contains works not considered in this thesis.

Part I begins with Chapter 2 which lays the foundation of the mathematical background that is imperative for understanding modern PDE-based PSfS methods including this work. The central topic of Chapter 2 consists of the Hamilton-Jacobi equations since they are the ones that describe brightness equations for PSfS in PDE-based methods. Since this special type of PDEs, in general, does not admit a solution in the classical sense, we consider a notion of solutions different from the classical one which is called viscosity solutions [63, 64]. Within this mathematical framework, we also look into upwind schemes [219] which form the basis of the fast marching (FM) method [110, 226, 249] – one of the most efficient numerical solvers for HJEs – and which are used throughout the work not only in the PDE-based methods but also in variational methods.

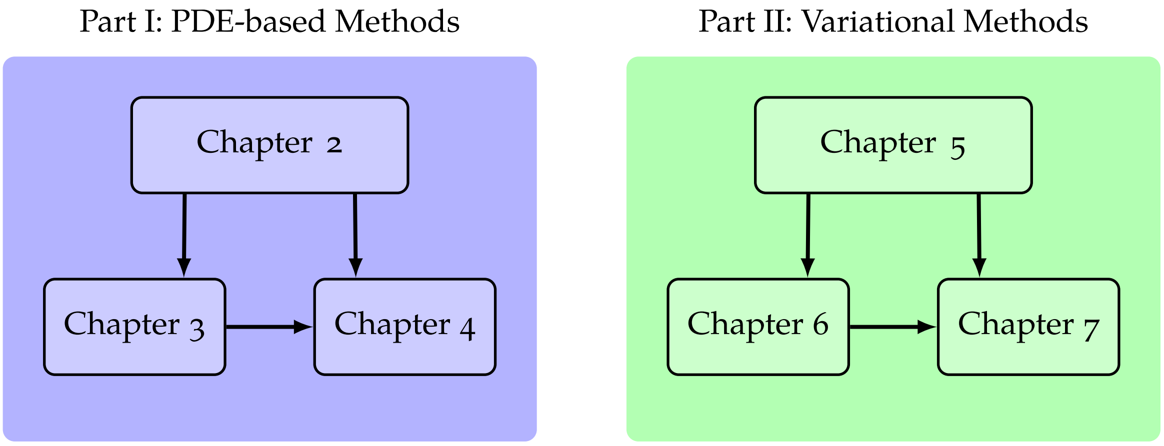

Figure 1.2. Structure of present work: The dependency graph type notation is used in "Chapter A → Chapter B" which denotes that the notions or parts of contents in Chapter A are helpful for comprehending the ones in Chapter B.

Chapter 3 concerns three important modern PSfS models: One is that of Prados and Faugeras [195] using the Lambertian surface model [148], another is that of Ahmed and Farag [6] incorporating the Oren-Nayar reflectance model [178], and the other is that of Vogel *et al.* [258] employing the Phong reflectance assumption [189]. Except for the designated reflectance functions, all three models make the same following assumptions on modelling the brightness equations: a perspective camera projection, a point light source being at the optical centre of a camera, and the light attenuation term following the inverse square law. After reviewing the basics of modelling components, we derive all three models in the form of HJEs and discuss important properties of the derived models. This mainly encompasses the role of the employed light attenuation term which is linked to the types of Hamiltonian, the discussion of convex/concave ambiguities and the significance of critical points w.r.t. both theoretical and practical aspects including the initialisation method for applying FM methods. In this respect, we carry out an in-depth analysis with respect to critical points for the Phong PSfS model [258] in [42], which shows how the model behaves around the critical points and how the model convexity is affected that plays a role for the application of the FM method. Furthermore, we investigate the Oren-Nayar PSfS model [6] in [129] by analysing the model with respect to the Osher's criterion [182, 200, 248] along with the roughness parameter. This gives a theoretical justification for the appropriate range of the roughness parameter for the use of the FM method, which was selected so far on a purely empirical basis; see [256].

Subsequently in Chapter 4, we construct our two generalised PSfS models [93, 130] that were presented at the International Conference on Scale Space and Variational Methods (SSVM) and the British Machine Vision Conference (BMVC) by making use of the spherical surface parametrisation along with the light fall-off term. The

Lambertian surface is employed for the former model and the Oren-Nayar reflectance for the latter one, both of which can handle general illumination scenarios even when a point light source is not at the optical centre. Apart from the generalised models, we account for our customised FM algorithm: how the algorithm should be initialised by taking advantage of the spherical coordinate system and how the update process in the algorithm should be realised for dealing with Cartesian input data in the spherical coordinate system.

Turning to Part II, we focus on a novel variational method for PSfS under the standard assumptions: the Lambertian surface and a light source being at the optical centre of a camera as well as the light attenuation factor. This approach is based on our work [131] that was presented at the International Conference on Scale Space and Variational Methods. The main goal of Chapter 5 is to provide fundamentals of variational methods on which the pertinent chapters can rely and to establish a basis model for variational PSfS for further development. To this end, we first elaborate on the calculus of variations covering Euler-Lagrange equations which are the key ingredients for optimising established variational PSfS models. Then, we build our radial depth based variational PSfS model. The data term of this model incorporates the brightness equation of Prados and Faugeras [195] that we have introduced in Chapter 3. On top of that, the noticeable properties of this model come from the smoothness term that has the capability: (i) to preserve an edge by means of the subquadratic penaliser, (ii) to deal with the noise or missing information with the help of a confidence function, and (iii) to require no additional term in the model to respect the integrability constraint.

In contrast to Chapter 5, the next two chapters are involved with the Cartesian depth based PSfS instead of the radial depth based one. In Chapter 6 which is based on work that has been published as a book chapter [132], we derive a variational PSfS model in terms of the Cartesian depth and develop an appropriate optimisation algorithm via a coarse-to-fine strategy in order to deal with the arising non-convex energy. By still retaining all the desirable properties from the radial depth based model [131], e.g. robustness against corrupt data due to noise or missing information, our Cartesian depth based model has another attractive feature, i.e. the parametrisation in terms of the Cartesian depth, which can be shared with other methods such as stereo for building a joint framework. Moreover, using an alternating explicit scheme brings a considerable speedup compared with the standard explicit scheme. Apart from the speedup, our novel scheme is *not* affected by a specific type of initialisation methods since it uses a multi-resolution optimisation framework as stated in Section 1.2.2.

Although the numerical method presented in Chapter 6 can deal with the non-convexity of the energy, the difficulty of the nonlinearity has not been resolved yet. In Chapter 7, we therefore consider our hyperbolic warping scheme [160] that has been presented at the German Conference on Pattern Recognition (GCPR). By introducing incremental computations, the nonlinearity is handled by applying an upwind type Taylor approximation to the data term and the lagged diffusivity method [48, 51, 253, 254] to the smoothness term, respectively. Hence, the resulting novel scheme, on the one hand, allows a speedup of more than three orders of magnitude in comparison to the alternating explicit scheme. On the other hand, a large amount of regularisations becomes feasible because the presented algorithm is *not* affected by the time step size any more. This makes it possible to deal with high-resolution images in contrast to a rather slow alternating explicit scheme.

Finally, Chapter 8 closes this work by summarising contents and giving some comments along with an outlook on potential improvements.

Part I

PDE-based Approaches

CHAPTER 2

MATHEMATICAL BACKGROUND ON PDE-BASED APPROACHES

Partial differential equations are one of the common tools when it comes to the modelling of recent state-of-the-art methods for perspective Shape from Shading [6, 49, 93, 130, 195, 236, 259]. However, in general, it is not so trivial to find a solution of such PDEs. In particular, PDEs called Hamilton-Jacobi equations do not have a solution in the classical sense [14]. Furthermore, when looking for a weak solution from an extended solution candidate set to resolve the problem of existence, the uniqueness of the solution becomes another issue [14, 142]. All this requires a solid theoretical framework that can deal with such difficulties.

In this chapter, we provide the essential mathematical background for solving PDE-based SfS models. To this end, we focus on the notion of viscosity solutions [63, 64] with the help of a 1-D eikonal equation. This modern notion of solutions not only allows to obtain the desired properties of the solutions but it also lays the foundation for developing a special numerical algorithm: the fast marching method. This method is known to be the most efficient approach for solving the considered type of Hamilton-Jacobi equations in the viscosity sense [229].

This chapter is organised as follows: In Section 2.1, we first describe Hamilton-Jacobi equations for SfS in the context of PDEs by extracting their main features. Afterwards, in Section 2.2 we introduce modern notions of viscosity solutions for HJEs with respect to well-posedness and we compare them with other notions of solutions including vanishing viscosity solutions. Finally, we elaborate on the basic idea of fast marching methods in Section 2.3.

2.1 Hamilton-Jacobi Equations

PDEs arise in many areas of physical science, since they are extremely useful mathematical tools for modelling physical phenomena. Hamilton-Jacobi equations belong to the family of PDEs and are also pervasive, especially in classical mechanics and geometrical optics. In this context, it is not surprising that there are several ways to define, derive, and interpret HJEs. As an example, one way to interpret HJEs is considering them as a special case of Hamilton-Jacobi-Bellman equations (HJBEs) that are central to optimal control theory [16].

Among others, we follow the approach in [12] by defining HJEs as a special type of PDEs: *first*[1] order *nonlinear* PDEs. To understand the terminology, let us first define PDEs according to [82].

2.1.1 Partial Differential Equations

A *partial differential equation* is, in general, defined as an equation which describes the relationship between an unknown function of two or more variables and some of its partial derivatives [82].

Definition 2.1.1 (Partial Differential Equations). For a fixed integer $k \geq 1$ and an open subset Ω of $\mathbb{R}^n$, a k-th order partial differential equation is an expression of the form

$$F\left(x, u(x), D\,u(x), \ldots, D^{k-1}\,u(x), D^k\,u(x)\right) = 0\,, \tag{2.1}$$

where

$$F : \Omega \times \mathbb{R} \times \mathbb{R}^n \times \ldots \times \mathbb{R}^{n^{k-1}} \times \mathbb{R}^{n^k} \tag{2.2}$$

is given and

$$u : \Omega \to \mathbb{R} \tag{2.3}$$

is the *unknown* function.

The *order* of the PDE (2.1) in Definition 2.1.1 refers to the order of the highest-order derivative being present in the equation. The notation $D^k u(x)$ in (2.1) is used in terms of multi-index [82, 209, 222]. This means that $D^k u(x)$ with a non-negative integer k is the set of all partial derivatives of order k and is thereby defined as

$$D^k\,u(x) := \{D^\gamma\,u(x)\,; |\gamma| = k\}\,, \tag{2.4}$$

where

$$D^\gamma := \frac{\partial^{\gamma_1}}{\partial x_1^{\gamma_1}} \cdots \frac{\partial^{\gamma_n}}{\partial x_n^{\gamma_n}} = \frac{\partial^{|\gamma|}}{\partial x_1^{\gamma_1} \cdots \partial x_n^{\gamma_n}} =: \partial x_1^{\gamma_1} \cdots \partial x_n^{\gamma_n}\,. \tag{2.5}$$

The multi-index γ in (2.5) has the form of n-tuple

$$\gamma = (\gamma_1, \ldots, \gamma_n) \tag{2.6}$$

and each component γ_i in (2.6) is a non-negative integer. Moreover, the order $|\gamma|$ is defined by

$$|\gamma| = \gamma_1 + \cdots + \gamma_n\,. \tag{2.7}$$

---

[1] While there also exist second order HJEs in literature, e.g. [100, 101], we restrict ourselves to the first order case in this thesis. This approach is based on, e.g. [16, 63, 64, 155].

Let us have a look at a more concrete example with $k = 1$. In this case, we can possibly have n different multi-indices as follows:

$$\begin{aligned} \gamma = &\quad (1,0,0,\dots,0) \\ \gamma = &\quad (0,1,0,\dots,0) \\ &\quad\vdots \\ \gamma = &\quad (0,0,0,\dots,1)\,. \end{aligned} \tag{2.8}$$

Moreover, by plugging (2.8) into (2.5) one can obtain

$$\left(D^{(1,0,0,\dots,0)}, D^{(0,1,0,\dots,0)}, \dots, D^{(0,0,0,\dots,1)}\right) \overset{(2.5)}{=} \left(\frac{\partial}{\partial x_1}, \frac{\partial}{\partial x_2}, \dots, \frac{\partial}{\partial x_n}\right). \tag{2.9}$$

Then, applying the result (2.9) to the function u and arranging as a vector yields a gradient vector Du

$$Du\,(x) = \left(\frac{\partial u}{\partial x_1}, \dots, \frac{\partial u}{\partial x_n}\right)^\top . \tag{2.10}$$

At this point, one can realise that HJEs are related to (2.10) since they are first order. In a similar way, for $k = 2$ one can obtain the Hessian matrix

$$D^2u\,(x) = \begin{bmatrix} \dfrac{\partial^2 u}{\partial x_1\,\partial x_1} & \cdots & \dfrac{\partial^2 u}{\partial x_1\,\partial x_n} \\ \vdots & \ddots & \vdots \\ \dfrac{\partial^2 u}{\partial x_n\,\partial x_1} & \cdots & \dfrac{\partial^2 u}{\partial x_n\,\partial x_n} \end{bmatrix} \in \mathbb{R}^{n\times n}\,. \tag{2.11}$$

This can be further extended in a straightforward way for the case of higher dimensions. For compact notations, we often abbreviate $\frac{\partial u}{\partial x_i}$ as u_{x_i}.

As mentioned previously, another characterisation of HJEs are nonlinear PDEs. To this end, we introduce the definition of *linear* PDEs from [82] before discussing nonlinear PDEs.

Definition 2.1.2 (Linear Partial Differential Equations). The PDE in (2.1) is called *linear* if it has the form

$$\sum_{|\gamma|\leqslant k} a_\gamma(x)\,D^\gamma u(x) = f(x) \tag{2.12}$$

for given functions a_γ with $|\gamma| \leqslant k$ and f. The linear PDE is called *homogeneous* if $f = 0$, and *inhomogeneous* if $f \neq 0$.

One should note that for the expressions of the form (2.12) the following properties of linearity hold [190, 231]

$$\mathcal{D}(u+v) = \mathcal{D}u + \mathcal{D}v \quad \text{and} \quad \mathcal{D}(c\,u) = c\,\mathcal{D}u\,, \tag{2.13}$$

where u and v denote unknown functions, $c \in \mathbb{R}$ is a constant, and the differential operator $\mathcal{D}$ has the form of

$$\mathcal{D} = \sum_{|\gamma| \leqslant k} a_\gamma(x)\, D^\gamma\,. \tag{2.14}$$

One famous example of linear PDEs is the Laplace's equation (heat equation) [82]

$$\Delta u = \sum_{i=1}^{n} u_{x_i\,x_i} = 0\,. \tag{2.15}$$

Let us have a look how this PDE follows the linearity in terms of Definition 2.1.2. If we restrict ourselves to the 2-D case of (2.15) for simplicity, i.e. $n = 2$, three cases of order are involved to write (2.15) in terms of (2.12), i.e. $k = 2$, $k = 1$, and $k = 0$. As we have performed in (2.9), by (2.4) and (2.5) we can obtain

$$\begin{array}{lll} \gamma = (2,0)\,, & a_{(2,0)} = 1\,, & D^{(2,0)} \overset{(2.5)}{=} \partial x_1^2 \\ \gamma = (1,1)\,, & a_{(1,1)} = 0\,, & D^{(1,1)} \overset{(2.5)}{=} \partial x_1\, \partial x_2 \\ \gamma = (0,2)\,, & a_{(0,2)} = 1\,, & D^{(0,2)} \overset{(2.5)}{=} \partial x_2^2 \end{array} \tag{2.16}$$

for $k = 2$. In the same way, we have

$$\begin{array}{lll} \gamma = (1,0)\,, & a_{(1,0)} = 0\,, & D^{(1,0)} \overset{(2.5)}{=} \partial x_1 \\ \gamma = (0,1)\,, & a_{(0,1)} = 0\,, & D^{(0,1)} \overset{(2.5)}{=} \partial x_2 \end{array} \tag{2.17}$$

for $k = 1$ and

$$\gamma = (0,0)\,, \quad a_{(0,0)} = 0 \tag{2.18}$$

for $k = 0$, respectively. Therefore, by putting all cases together the Laplace's equation (2.15) has the form of

$$\left(\partial x_1^2 + \partial x_2^2\right) u\,(x) = 0\,, \tag{2.19}$$

and it is a linear PDE according to the Definition 2.1.2. Moreover, one can also note that the form (2.19) satisfies the linear properties in (2.13).

In this context, one may consider, in a natural way, nonlinear PDEs as PDEs that do not have the form of (2.12). Since the size of the class of nonlinear PDEs is enormous, the k-th order PDE (2.1) is, among others, called *fully nonlinear* if it depends nonlinearly upon the highest-order derivatives of u [82].

A famous example of a fully nonlinear PDE is the eikonal[2] equation [82] from geometrical optics, which is a special case of HJEs,

$$|Du| = 1\,. \tag{2.20}$$

Since there is no way to express (2.20) in the form of (2.12) based on the property of the Euclidean norm

$$|Du| = \sqrt{(Du)^\top Du} \tag{2.21}$$

and the first order derivatives behave nonlinearly with respect to (2.13), one can confirm that (2.20) is fully nonlinear PDE. With the same line of reasoning, one can find another example, the minimal surface equation [82]

$$\operatorname{div}\left(\frac{Du}{(1+|Du|^2)^{1/2}}\right) = 0 \tag{2.22}$$

to be a fully nonlinear PDE as well.

So far, we have seen the characterisations of HJEs: first order and fully nonlinear PDEs. Furthermore, one classifies HJEs into two types: eikonal-type and general-type HJEs.

HJEs of eikonal-type depend only on Du. Based on the fact that Du in (2.20) denotes a gradient vector as indicated in (2.10), the eikonal equation (2.20) takes the form

$$H(\boldsymbol{x}, \nabla u(\boldsymbol{x})) = 0\,, \tag{2.23}$$

where $H : \Omega \times \mathbb{R}^n \to \mathbb{R}$ with $\Omega \subset \mathbb{R}^n$ and H is called *eikonal*-type *Hamiltonian*.

In this context, the Hamiltonian of general-type HJEs relies not only on ∇u but also on u and hence has the form of

$$H(\boldsymbol{x}, u(\boldsymbol{x}), \nabla u(\boldsymbol{x})) = 0\,, \tag{2.24}$$

where $H : \Omega \times \mathbb{R} \times \mathbb{R}^n \to \mathbb{R}$ with $\Omega \subset \mathbb{R}^n$ is called *general*-type *Hamiltonian*.

2.2 Well-Posedness and Notions of Solutions

So far, we have classified HJEs as PDEs that are nonlinear and of first order. However, it still is, in general, a difficult task to actually find solutions of problems described by PDEs, even when they are restricted to HJEs.

In this context, to specify the meaning of “finding a solution of a PDE” and to provide a guidance for the study of PDEs by asking fundamental theoretical questions, the French mathematician Hadamard introduced the concept of *well-*

---

[2] The term “eikonal” stems from the Greek word “$\varepsilon\iota\kappa\omega\nu$” which means image.

posedness [104, 105]. A mathematical problem is called *well-posed* if it fulfils the following conditions:

Definition 2.2.1 (Well-Posedness).

(i) There exists a solution of the problem;

(ii) There is at most one solution of the problem;

(iii) The solution depends continuously on the given data;

If one or more of these conditions do not hold, the problem is called *ill-posed*.

The first condition concerns the existence of solutions and deals with regularity requirements i.e. differentiability (or smoothness) of solutions [82, 142]. These requirements can actually provide us important information when looking for a solution, i.e. the search space of a function class. Moreover, an answer to the existence of solutions may be different depending on the degree of regularity, e.g. if a continuous solution $u \in C^0$ is sufficient or if an infinitely many times differentiable solution $u \in C^\infty$ is necessary.

With respect to this matter, we consider a simple 1-D eikonal equation with Dirichlet boundary condition (DBC) from geometrical optics as an example. It is given by

$$\begin{cases} |u'(x)| = 1 & \text{in} \quad \Omega\,, \\ u(x) = 0 & \text{on} \quad \partial\Omega\,, \end{cases} \tag{2.25}$$

where $u' := \frac{du}{dx}$, $\Omega = (-1, 1)$ and $\partial\Omega = \{\pm 1\}$.

When one tries to find a solution to (2.25) at least in the class C^1, all efforts being made turn out to be in vain because such solution does not exist. To show the validity of the statement, i.e. the non-existence of solutions in C^1, one can make use of "proof by contradiction" [14]. We, therefore, assume for the time being that at least one such solution exists. Since the solution is assumed to be in C^1, it must satisfy Rolle's theorem in calculus [11]. This basically states that a one-time continuously differentiable real-valued function attaining the same values at two different points, i.e. $u(\pm 1) = 0$ for (2.25), must have a critical point (or a stationary point), i.e. a point where the first derivative disappears and thereby the slope of the tangent line at the point is equal to 0, somewhere in-between these two distinct points, i.e. $(-1, 1)$. Such points, however, cannot exist on the grounds that the first derivative in that interval is already given by the problem (2.25). This contradiction justifies the original assertion that a solution belonging to the class C^1 does not exist.

Since a solution does not exist in C^1, we expand the search space from C^1 to C^0. Then, one can find infinitely many solution candidates to (2.25) including all possible sawtooth-shaped functions that are composed of lines whose slopes are either 1, -1, or both of them, as shown in Figure 2.1. One may, therefore, realise that the existence of solution candidates can be achieved by allowing solutions that are less regular. These solution candidates are called *weak* or *generalised solutions* [82, 142, 152].

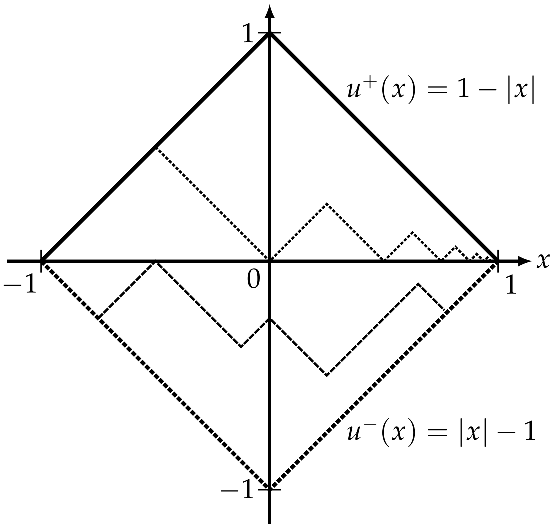

Figure 2.1. Solution candidates for the 1-D eikonal equation (2.25).

However, as can be observed in Figure 2.1 weak solutions come usually with the issue of uniqueness. Therefore, to single out a meaningful solution more information is needed or more conditions have to be imposed on the problem: e.g. when one needs to find a "distance" from the boundary points, from either 1 or -1, the proper solution to (2.25) can be attained as [142]

$$u(x) = \operatorname{dist}(x, \partial\Omega) := \inf_{y \in \partial\Omega} |x - y| = 1 - |x| \,. \tag{2.26}$$

Concerning the third component in Definition 2.2.1, it basically states that the behaviour of solutions depends continuously on the initial conditions or input data. In other words, a small change in the data or in the conditions results in a small change in the solution as well. This property is of great importance in practice: e.g. one expects to compute a robust solution, albeit the input data can be perturbed with noise.

As a consequence, each component of well-posedness in Definition 2.2.1 is useful to provide a strategy how one can solve a PDE. In this respect, the modern notion of viscosity solutions proposed by Crandall and Lions plays a significant role in the context of HJEs [63, 64, 65] and second order PDEs [66].

Since "viscosity solutions" are actually obtained as limits of the "vanishing viscosity method" [18], we first have a look at "vanishing viscosity solutions" in the next section before we go into "viscosity solutions" in Section 2.2.3. This approach is also helpful to distinguish how qualitatively different they are from each other.

2.2.1 Vanishing Viscosity Method

The idea behind the vanishing viscosity method [16, 64, 82, 142, 155] is actually based on a technique first proposed in hydrodynamics [260]. Since, in general, a first order nonlinear PDE does not have a classical solution as previously shown, one tries to find a weak solution of a slightly modified problem by introducing an artificial viscosity term into the original formulation.

There are two advantages of this approach: On the one hand, the modified problem can be turned into the original one when the weight parameter ε of the viscosity term becomes 0. On the other hand, a sufficiently smooth and unique solution to the modified problem may be attained for each $\varepsilon \neq 0$.

Since this method is not only helpful for understanding the general definitions of "viscosity solutions" in [63] but also one of the reasons that "viscosity solutions" are called as such, we look into how the idea is realised by applying the method to the 1-D eikonal equation. To this end, instead of applying the vanishing viscosity method directly to (2.25) we deal with the following equivalent but differentiable formulation as in [142]

$$\begin{cases} (u'(x))^2 = 1 & \text{in} \quad \Omega\,, \\ u(x) = 0 & \text{on} \quad \partial\Omega\,, \end{cases} \tag{2.27}$$

where $\Omega = (-1, 1)$ and $\partial\Omega = \{\pm 1\}$.

There are two possibilities to add an artificial viscosity term $\varepsilon u_\varepsilon''(x)$ with $0 < \varepsilon \ll 1$ to (2.27): One is a positive one $+\varepsilon u_\varepsilon''(x)$ and the other is a negative one $-\varepsilon u_\varepsilon''(x)$. Therefore, one can obtain the following expressions:

$$\begin{cases} (u_\varepsilon'(x))^2 - 1 = \varepsilon\, u_\varepsilon''(x) & \text{in} \quad \Omega\,, \\ u_\varepsilon(x) = 0 & \text{on} \quad \partial\Omega\,, \end{cases} \tag{2.28}$$

and

$$\begin{cases} (u_\varepsilon'(x))^2 - 1 = -\varepsilon\, u_\varepsilon''(x) & \text{in} \quad \Omega\,, \\ u_\varepsilon(x) = 0 & \text{on} \quad \partial\Omega\,, \end{cases} \tag{2.29}$$

where $\Omega = (-1, 1)$ and $\partial\Omega = \{\pm 1\}$.

As shown in [224] based on the theory presented in [98], there exists a classical solution for the problem (2.28) and the solution is unique. Obviously, this statement also holds for (2.29) because of the structure of the formulation. In the next section, we will find these unique vanishing viscosity solutions for (2.28) and (2.29) which we call u_ε^+ and u_ε^-, respectively.

Vanishing Viscosity Solution u_ε^+

The solution u_ε^+ to (2.28) can be obtained by applying the change of variable $v_\varepsilon(x) = u'_\varepsilon(x)$. In order to achieve that, one may first suppose $u'_\varepsilon(0) = 0$ by respecting the symmetric structure of (2.28) as suggested in [142]. This leads to

$$\begin{cases} (v_\varepsilon(x))^2 - 1 = \varepsilon\, v'_\varepsilon(x)\,, & x \in (-1,1) \\ v_\varepsilon(x) = 0\,, & x \in \{0\}\,. \end{cases} \tag{2.30}$$

In (2.30), one can observe that $v_\varepsilon(x)$ cannot be 1 or -1 owing to $\varepsilon \neq 0$. Moreover, based on $v_\varepsilon(0) = 0$ in (2.30), one may further assume that

$$v_\varepsilon(x) \in (-1,1)\,. \tag{2.31}$$

At this moment, we are in a position to proceed to find a solution. In what follows, we drop the dependence of x in (2.30) for a compact presentation.

First, we rearrange (2.30) as

$$-\,\varepsilon\, v'_\varepsilon = 1 - v_\varepsilon^2\,. \tag{2.32}$$

Then, by replacing v'_ε in (2.32) with $\frac{dv_\varepsilon}{dx}$ and utilising the method of separation of variables, one is able to obtain

$$-\,\varepsilon\, v'_\varepsilon = -\varepsilon\,\frac{dv_\varepsilon}{dx} = 1 - v_\varepsilon^2 \;\Leftrightarrow\; \frac{dv_\varepsilon}{1 - v_\varepsilon^2} = -\frac{1}{\varepsilon}\,dx\,. \tag{2.33}$$

Applying the partial fraction decomposition to (2.33) further leads to

$$\frac{dv_\varepsilon}{1 - v_\varepsilon^2} = \frac{dv_\varepsilon}{(1 - v_\varepsilon)(1 + v_\varepsilon)} = -\frac{1}{\varepsilon}\,dx \;\Leftrightarrow\; \frac{1}{2}\left(\frac{1}{1 - v_\varepsilon} + \frac{1}{1 + v_\varepsilon}\right) dv_\varepsilon = -\frac{1}{\varepsilon}\,dx\,. \tag{2.34}$$

When integrating both sides of (2.34) with the assumption (2.31), one can attain

$$\frac{1}{2}\int \left(\frac{1}{1 - v_\varepsilon} + \frac{1}{1 + v_\varepsilon}\right) dv_\varepsilon = \int -\frac{1}{\varepsilon}\,dx \;\Leftrightarrow\; \frac{1}{2}\ln\left(\frac{1 + v_\varepsilon}{1 - v_\varepsilon}\right) = -\frac{1}{\varepsilon}\,x + c_1\,, \tag{2.35}$$

where $c_1 \in \mathbb{R}^+$ denotes a constant. The constant c_1 can be determined by plugging $v_\varepsilon(0) = 0$ from (2.30) into (2.35), which gives us

$$c_1 = 0\,. \tag{2.36}$$

As a consequence, (2.35) becomes

$$\frac{1}{2}\ln\left(\frac{1 + v_\varepsilon}{1 - v_\varepsilon}\right) = -\frac{1}{\varepsilon}\,x \;\Leftrightarrow\; \ln\left(\frac{1 + v_\varepsilon}{1 - v_\varepsilon}\right) = -\frac{2}{\varepsilon}\,x \;\Leftrightarrow\; \frac{1 + v_\varepsilon}{1 - v_\varepsilon} = e^{-\frac{2x}{\varepsilon}}\,. \tag{2.37}$$

Rearranging (2.37) with respect to v_ε then leads to

$$v_\varepsilon = \frac{-1+e^{-\frac{2x}{\varepsilon}}}{1+e^{-\frac{2x}{\varepsilon}}} = \frac{e^{\frac{x}{\varepsilon}}\,(-1+e^{-\frac{2x}{\varepsilon}})}{e^{\frac{x}{\varepsilon}}\,(1+e^{-\frac{2x}{\varepsilon}})} = \frac{-e^{\frac{x}{\varepsilon}}+e^{-\frac{x}{\varepsilon}}}{e^{\frac{x}{\varepsilon}}+e^{-\frac{x}{\varepsilon}}} = -\frac{e^{\frac{x}{\varepsilon}}-e^{-\frac{x}{\varepsilon}}}{e^{\frac{x}{\varepsilon}}+e^{-\frac{x}{\varepsilon}}}\,. \tag{2.38}$$

With the hyperbolic functions

$$\sinh x = \frac{e^x - e^{-x}}{2} \quad \text{and} \quad \cosh x = \frac{e^x + e^{-x}}{2}\,, \tag{2.39}$$

the result of (2.38) can be further simplified to

$$v_\varepsilon(x) = -\frac{e^{\frac{x}{\varepsilon}}-e^{-\frac{x}{\varepsilon}}}{e^{\frac{x}{\varepsilon}}+e^{-\frac{x}{\varepsilon}}} = -\frac{\left(\frac{e^{\frac{x}{\varepsilon}}-e^{-\frac{x}{\varepsilon}}}{2}\right)}{\left(\frac{e^{\frac{x}{\varepsilon}}+e^{-\frac{x}{\varepsilon}}}{2}\right)} = -\frac{\sinh\left(\frac{x}{\varepsilon}\right)}{\cosh\left(\frac{x}{\varepsilon}\right)} = -\tanh\left(\frac{x}{\varepsilon}\right)\,. \tag{2.40}$$

In order to calculate u_ε from (2.40), we replace u'_ε with $\frac{du_\varepsilon}{dx}$ and apply the separation of variables to (2.40) as in (2.33). This leads to

$$u'_\varepsilon = -\tanh\left(\frac{x}{\varepsilon}\right) \Leftrightarrow \frac{du_\varepsilon}{dx} = -\frac{\sinh\left(\frac{x}{\varepsilon}\right)}{\cosh\left(\frac{x}{\varepsilon}\right)} \Leftrightarrow du_\varepsilon = -\frac{\sinh\left(\frac{x}{\varepsilon}\right)}{\cosh\left(\frac{x}{\varepsilon}\right)}\,dx \tag{2.41}$$

Since $\cosh\left(\frac{x}{\varepsilon}\right)$ is an even function and $\cosh\left(\frac{x}{\varepsilon}\right) > 0$ in $(-1,1)$, integrating both sides of (2.41) results in

$$\int du_\varepsilon = -\int \frac{\sinh\left(\frac{x}{\varepsilon}\right)}{\cosh\left(\frac{x}{\varepsilon}\right)}\,dx \Leftrightarrow u_\varepsilon = -\varepsilon \ln\left(\cosh\left(\frac{x}{\varepsilon}\right)\right) + c_2\,. \tag{2.42}$$

Moreover, the boundary condition in (2.28) delivers the information about the arbitrary constant of integration c_2 in (2.42). Therefore, one can attain

$$u_\varepsilon(\pm 1) \overset{(2.28)}{=} 0 = -\varepsilon \ln\left(\cosh\left(\frac{1}{\varepsilon}\right)\right) + c_2 \Leftrightarrow c_2 = \varepsilon \ln\left(\cosh\left(\frac{1}{\varepsilon}\right)\right)\,. \tag{2.43}$$

By putting together the result of (2.42) as well as that of (2.43), one can eventually find a solution $u_\varepsilon^+ \in C(\overline{\Omega}) \cap C^2(\Omega)$ to the problem (2.28) as

$$\begin{aligned} u_\varepsilon^+(x) &= -\varepsilon \ln\left(\cosh\left(\frac{x}{\varepsilon}\right)\right) + \varepsilon \ln\left(\cosh\left(\frac{1}{\varepsilon}\right)\right) = -\varepsilon\left(\ln\left(\cosh\left(\frac{x}{\varepsilon}\right)\right) - \ln\left(\cosh\left(\frac{1}{\varepsilon}\right)\right)\right) \\ &= -\varepsilon \ln\left(\frac{\cosh\left(\frac{x}{\varepsilon}\right)}{\cosh\left(\frac{1}{\varepsilon}\right)}\right) \overset{(2.39)}{=} -\varepsilon \ln\left(\frac{\frac{e^{\frac{x}{\varepsilon}}+e^{-\frac{x}{\varepsilon}}}{2}}{\frac{e^{\frac{1}{\varepsilon}}+e^{-\frac{1}{\varepsilon}}}{2}}\right) = -\varepsilon \ln\left(\frac{e^{\frac{x}{\varepsilon}}+e^{-\frac{x}{\varepsilon}}}{e^{\frac{1}{\varepsilon}}+e^{-\frac{1}{\varepsilon}}}\right)\,. \end{aligned} \tag{2.44}$$

Limiting Process of Vanishing Viscosity Solution u_ε^+. Let us now have a look how the obtained solution u_ε^+ behaves as $\varepsilon \to 0$. To this end, we first consider the case if $x \in (0,1)$ and reformulate the solution (2.44) as

$$\begin{aligned} u_\varepsilon^+(x) &= -\varepsilon \ln\left(\frac{e^{\frac{x}{\varepsilon}} + e^{-\frac{x}{\varepsilon}}}{e^{\frac{1}{\varepsilon}} + e^{-\frac{1}{\varepsilon}}}\right) = -\varepsilon \ln\left(\frac{e^{\frac{x}{\varepsilon}}\left(1 + e^{-\frac{2x}{\varepsilon}}\right)}{e^{\frac{1}{\varepsilon}}\left(1 + e^{-\frac{2}{\varepsilon}}\right)}\right) = -\frac{1}{\left(\frac{1}{\varepsilon}\right)} \ln\left(e^{\frac{x-1}{\varepsilon}}\left(\frac{1 + e^{-\frac{2x}{\varepsilon}}}{1 + e^{-\frac{2}{\varepsilon}}}\right)\right) \\ &= -\frac{1}{\left(\frac{1}{\varepsilon}\right)}\left(\ln e^{\frac{x-1}{\varepsilon}} + \ln\left(\frac{1 + e^{-\frac{2x}{\varepsilon}}}{1 + e^{-\frac{2}{\varepsilon}}}\right)\right) = -\frac{1}{\left(\frac{1}{\varepsilon}\right)}\left(\frac{x-1}{\varepsilon} + \ln\left(\frac{1 + e^{-\frac{2x}{\varepsilon}}}{1 + e^{-\frac{2}{\varepsilon}}}\right)\right) \\ &= (1-x) - \frac{1}{\left(\frac{1}{\varepsilon}\right)} \ln\left(\frac{1 + e^{-\frac{2x}{\varepsilon}}}{1 + e^{-\frac{2}{\varepsilon}}}\right). \end{aligned} \tag{2.45}$$

Then, the limiting process of (2.45) yields

$$\begin{aligned} \lim_{\varepsilon\to 0} u_\varepsilon^+(x) &\overset{(2.45)}{=} \lim_{\varepsilon\to 0}\left((1-x) - \frac{1}{\left(\frac{1}{\varepsilon}\right)} \ln\left(\frac{1 + e^{-\frac{2x}{\varepsilon}}}{1 + e^{-\frac{2}{\varepsilon}}}\right)\right) = (1-x) - \underbrace{\lim_{\varepsilon\to 0}\left(\frac{1}{\left(\frac{1}{\varepsilon}\right)} \ln\left(\frac{1 + e^{-\frac{2x}{\varepsilon}}}{1 + e^{-\frac{2}{\varepsilon}}}\right)\right)}_{\to 0} \\ &= 1 - x\,. \end{aligned} \tag{2.46}$$

The case when $x \in (-1,0)$ can be handled in an analogous way. By keeping the negative x in mind, we rewrite the solution (2.44) as

$$\begin{aligned} u_\varepsilon^+(x) &= -\varepsilon \ln\left(\frac{e^{\frac{x}{\varepsilon}} + e^{-\frac{x}{\varepsilon}}}{e^{\frac{1}{\varepsilon}} + e^{-\frac{1}{\varepsilon}}}\right) = -\varepsilon \ln\left(\frac{e^{-\frac{x}{\varepsilon}}\left(e^{\frac{2x}{\varepsilon}} + 1\right)}{e^{\frac{1}{\varepsilon}}\left(1 + e^{-\frac{2}{\varepsilon}}\right)}\right) = -\frac{1}{\left(\frac{1}{\varepsilon}\right)} \ln\left(e^{-\frac{x+1}{\varepsilon}}\left(\frac{e^{\frac{2x}{\varepsilon}} + 1}{1 + e^{-\frac{2}{\varepsilon}}}\right)\right) \\ &= (x+1) - \frac{1}{\left(\frac{1}{\varepsilon}\right)} \ln\left(\frac{e^{\frac{2x}{\varepsilon}} + 1}{1 + e^{-\frac{2}{\varepsilon}}}\right). \end{aligned} \tag{2.47}$$

This gives the limiting process

$$\lim_{\varepsilon\to 0} u_\varepsilon^+(x) \overset{(2.47)}{=} (x+1) - \underbrace{\lim_{\varepsilon\to 0}\left(\frac{1}{\left(\frac{1}{\varepsilon}\right)} \ln\left(\frac{e^{\frac{2x}{\varepsilon}} + 1}{1 + e^{-\frac{2}{\varepsilon}}}\right)\right)}_{\to 0} = x + 1\,. \tag{2.48}$$

In case of $x = 0$, both (2.46) and (2.48) converge to the same value 1.

In Figure 2.2(a), we have plotted the graph of u_ε^+ depending on the several values of ε. This shows that the behaviour of the approximate solution (2.44) is in full accordance with our analysis of the limiting process, cf. (2.46) and (2.48). Since the artificial viscosity term $\varepsilon u_\varepsilon''(x)$ in (2.28) introduces small diffusion around 0, i.e. in the interval x_ε depending on ε shown in Figure 2.2(b), one can observe a smoothing effect in this region. As a consequence, one obtains a difference around 0 between the desired solution $u^+(x)$ and the vanishing viscosity solution $u_\varepsilon^+(x)$, see Figure 2.2(b). However, as ε decreases to 0, it can be observed that the interval x_ε is reduced to 0 and the approximate solution $u_\varepsilon^+(x)$ approaches $u^+(x)$, see Figure 2.2(a).

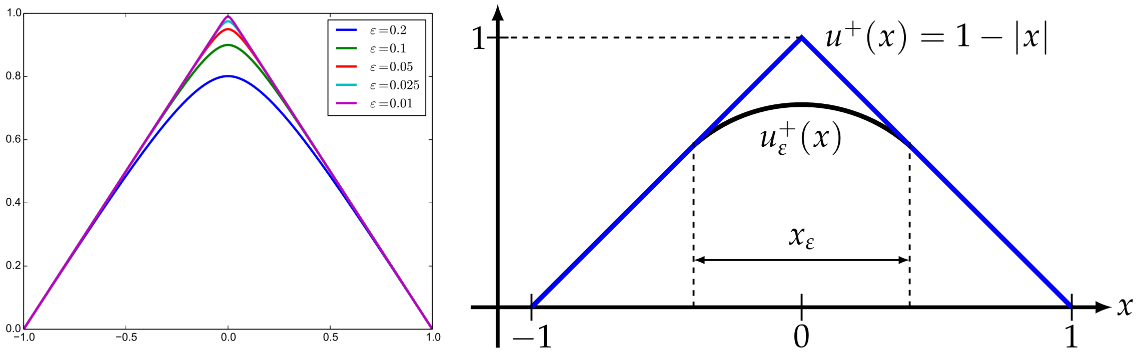

(a) Graphs of $u_\varepsilon^+(x)$ depending on ε.

(b) Graphs of $u_\varepsilon^+(x)$ and $u^+(x)$.

Figure 2.2. The vanishing viscosity method for the problem (2.30).

Vanishing Viscosity Solution u_ε^-

From the structure of the solution u_ε^+, one can also note that the vanishing viscosity solution u_ε^+ for the problem (2.28) becomes invalid when the sign of the artificial viscosity term in (2.28) is modified from $\varepsilon\, u_\varepsilon''(x)$ to $-\varepsilon\, u_\varepsilon''(x)$, i.e. if one considers (2.29). As we have carried out for the problem (2.28), it can be verified that the solution u_ε^- to the problem (2.29) is given by

$$u_\varepsilon^-(x) = \varepsilon \ln\left(\frac{e^{\frac{x}{\varepsilon}} + e^{-\frac{x}{\varepsilon}}}{e^{\frac{1}{\varepsilon}} + e^{-\frac{1}{\varepsilon}}}\right). \tag{2.49}$$

Limiting Process of Vanishing Viscosity Solution u_ε^-. As $\varepsilon \to 0$, the analysis of u_ε^- can be performed in a straightforward way, since the solution u_ε^- is only different up to a sign when compared with u_ε^+, cf. (2.44) and (2.49). This yields

$$u_\varepsilon^-(x) = (x-1) - \frac{1}{\left(\frac{1}{\varepsilon}\right)} \ln\left(\frac{1 + e^{-\frac{2x}{\varepsilon}}}{1 + e^{-\frac{2}{\varepsilon}}}\right) \quad \Rightarrow \quad \lim_{\varepsilon \to 0} u_\varepsilon^-(x) = x - 1 \tag{2.50}$$

for $x \in (0,1)$ and

$$u_\varepsilon^-(x) = -(x+1) - \frac{1}{\left(\frac{1}{\varepsilon}\right)} \ln\left(\frac{e^{\frac{2x}{\varepsilon}} + 1}{1 + e^{-\frac{2}{\varepsilon}}}\right) \quad \Rightarrow \quad \lim_{\varepsilon \to 0} u_\varepsilon^-(x) = -(x+1) \tag{2.51}$$

for $x \in (-1, 0)$, respectively. Moreover, both (2.50) and (2.51) converge to the same value -1 if $x = 0$. The corresponding graph of u_ε^- with several values of ε and the limit of the vanishing viscosity solution, i.e. u^-, are shown in Figure 2.3(a) and 2.3(b), respectively.

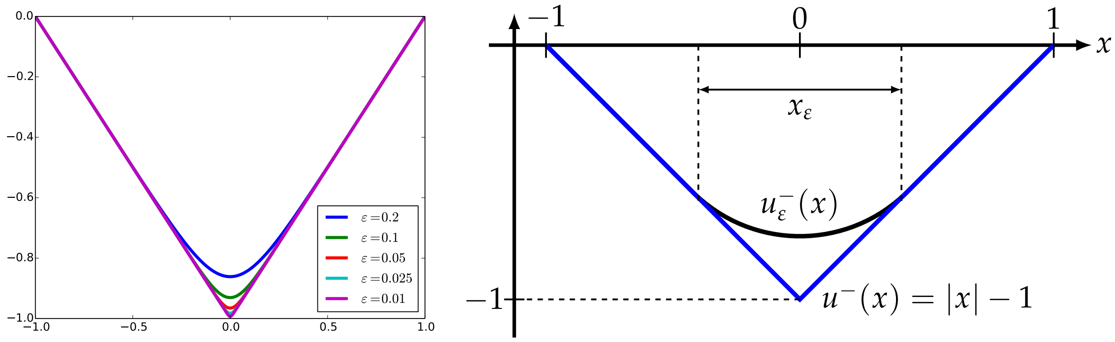

(a) Graphs of $u_\varepsilon^-(x)$ depending on ε.

(b) Graphs of $u_\varepsilon^-(x)$ and $u^-(x)$.

Figure 2.3. The vanishing viscosity method for the problem (2.29).

Important Properties of Vanishing Viscosity Solutions

So far we have studied the vanishing viscosity method using the 1-D eikonal equation. Based on our analysis one can note that there is a distinct feature in this method: Changing the sign of the artificial viscosity term in the problem leads to a different solution. This feature can be explained from the viewpoint of local extrema. In this respect, the important observation suggests that the solution to the problem (2.28) admits no local minima in the interval $(-1, 1)$. In a symmetric way, the solution to the problem (2.29) accepts no local maxima in the same interval.

In order to verify the former statement, we suppose for the time being that u_ε^0 is a solution to the problem (2.28) and it attains a local minimum at x_ε^0. Then, for every $\varepsilon > 0$ in view of the first- and second-order optimality conditions with respect to the local minimum, we obtain the following relationship

$$\left.\frac{du_\varepsilon^0(x)}{dx}\right|_{x=x_\varepsilon^0} = 0 \quad \text{and} \quad \left.\frac{d^2u_\varepsilon^0(x)}{dx^2}\right|_{x=x_\varepsilon^0} > 0\,. \tag{2.52}$$

Plugging this condition into the problem (2.28) leads to the contradiction

$$0 - 1 = -1 \neq \varepsilon \left.\frac{d^2u_\varepsilon^0(x)}{dx^2}\right|_{x=x_\varepsilon^0} > 0\,. \tag{2.53}$$

As a consequence, one can confirm that the solution to the problem (2.28) does not admit any local minimum. Moreover, this fact is also supported by the solution in

(2.44) that we have computed for the same problem. Furthermore, it is clear that using the analogous line of reasoning one can also validate the latter statement, i.e. the problem (2.29) does not accept any local maximum.

In fact, the same feature, i.e. that changing the sign of the problem leads to a different solution and solutions do not admit local maxima or minima depending on the problem, also appears in viscosity solutions with different characterisations, as we shall discuss in Section 2.2.3.

2.2.2 One-Sided Differentials

For viscosity solutions [63, 65], one needs a mathematical framework that should have the capability of dealing with non-differentiable points. To this end, instead of going directly into definitions of viscosity solutions, we introduce definitions of one-sided differentials [16, 17, 65] (or sometimes called semi-differentials) which are composed of super- and subdifferentials.

Definition 2.2.2 (One-sided Differentials). For a scalar function $u : \Omega \subset \mathbb{R}^n \to \mathbb{R}$,

(i) the *superdifferential* D^+u at a point $\boldsymbol{x}$ is defined as

$$D^+u(\boldsymbol{x}) = \left\{ \boldsymbol{p} \in \mathbb{R}^n : \limsup_{\boldsymbol{y}\to\boldsymbol{x}} \frac{u(\boldsymbol{y}) - u(\boldsymbol{x}) - \boldsymbol{p}\cdot(\boldsymbol{y}-\boldsymbol{x})}{|\boldsymbol{y}-\boldsymbol{x}|} \leqslant 0 \right\} \tag{2.54}$$

and analogously

(ii) the *subdifferential* D^-u at a point $\boldsymbol{x}$ is defined as

$$D^-u(\boldsymbol{x}) = \left\{ \boldsymbol{q} \in \mathbb{R}^n : \liminf_{\boldsymbol{y}\to\boldsymbol{x}} \frac{u(\boldsymbol{y}) - u(\boldsymbol{x}) - \boldsymbol{q}\cdot(\boldsymbol{y}-\boldsymbol{x})}{|\boldsymbol{y}-\boldsymbol{x}|} \geqslant 0 \right\} . \tag{2.55}$$

From a geometrical point of view, the vector $\boldsymbol{p} \in \mathbb{R}^n$ defined in (2.54) is called a superdifferential when a hyperplane $\boldsymbol{y} \mapsto u(\boldsymbol{x}) + \boldsymbol{p}\cdot(\boldsymbol{y}-\boldsymbol{x})$ touches the graph of u from above at a point $\boldsymbol{x}$ [41, 142]. In Figure 2.4(a) the possible superdifferential set p at $x = 0$ is illustrated for the non-differentiable 1-D function $u(x) = 1 - |x|$. Since the hyperplane corresponds to a line in 1-D, the vector $\boldsymbol{p}$ in (2.54) represents the slope of the line in this case. In a similar way, the vector $\boldsymbol{q} \in \mathbb{R}^n$ defined in (2.55) is called a subdifferential when a hyperplane $\boldsymbol{y} \mapsto u(\boldsymbol{x}) + \boldsymbol{q}\cdot(\boldsymbol{y}-\boldsymbol{x})$ touches the graph of u from below at a point $\boldsymbol{x}$, see Figure 2.4(b). One can note that one-sided differentials are defined even if functions contain a non-differentiable point $x = 0$.

Superdifferential of $u(x) = 1 - |x|$. In order to comprehend how the one-sided differentials in Definition 2.2.2 can handle a non-differentiable function, we first

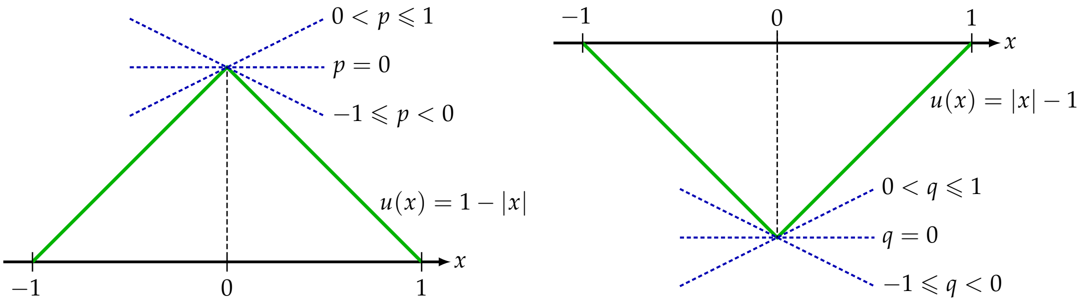

(a) Superdifferential of $u(x) = 1 - |x|$ at $x = 0$. (b) Subdifferential of $u(x) = |x| - 1$ at $x = 0$.

Figure 2.4. Geometrical interpretations of one-sided differentials for non-differentiable functions in 1-D.

apply the definition of the superdifferential (2.54) to the non-differentiable function $u(x) = 1 - |x|$. To this end, we reformulate the function $u(x) = 1 - |x|$ as

$$u(x) = \begin{cases} x + 1\,, & x < 0\,, \\ -x + 1\,, & x \geqslant 0\,, \end{cases} \tag{2.56}$$

and proceed with case distinctions: i.e. $x = 0$, $x > 0$ and $x < 0$.

The first case we consider is $x = 0$. If $x = 0$, there are two options for y to approach $x = 0$, i.e. either from the right side, $y > 0$, or from the left side, $y < 0$.

For $y > 0$ and $x = 0$, we arrive at

$$\begin{aligned} & \limsup_{y \to x} \frac{u(y) - u(0) - p\,(y - 0)}{|y - 0|} \leqslant 0 \quad \overset{(2.56)}{\Longleftrightarrow} \quad \limsup_{y \to x} \frac{-y - p\,y}{y} \leqslant 0 \\ \Leftrightarrow \quad & \limsup_{y \to x} \frac{-(1 + p)\,y}{y} \leqslant 0 \quad \Leftrightarrow \quad -(1 + p) \leqslant 0 \quad \Leftrightarrow \quad p \geqslant -1\,. \end{aligned} \tag{2.57}$$

For $y < 0$ and $x = 0$, we come to

$$\begin{aligned} & \limsup_{y \to x} \frac{u(y) - u(0) - p\,(y - 0)}{|y - 0|} \leqslant 0 \quad \overset{(2.56)}{\Longleftrightarrow} \quad \limsup_{y \to x} \frac{y - p\,y}{-y} \leqslant 0 \\ \Leftrightarrow \quad & \limsup_{y \to x} \frac{(1 - p)\,y}{-y} \leqslant 0 \quad \Leftrightarrow \quad -(1 - p) \leqslant 0 \quad \Leftrightarrow \quad p \leqslant 1\,. \end{aligned} \tag{2.58}$$

As a consequence, from the results (2.57) and (2.58) we can obtain the superdifferential $p \in [-1, 1]$ if $x = 0$ for the non-differentiable function $u(x) = 1 - |x|$. This suggests that the slope of the tangent plane at $x = 0$ touching from above can vary in the range from -1 to 1, which exactly corresponds to the geometric interpretation shown in Figure 2.4(a).

We turn our attention to the case $x > 0$. If $x > 0$, there are still two choices when y approaches x: either from right ($x < y$) or from left ($y < x$).

Taking the case $0 < x < y \Leftrightarrow y - x > 0$ into consideration gives

$$\begin{aligned}
&\limsup_{y\to x} \frac{u(y) - u(x) - p\,(y-x)}{|y-x|} \leqslant 0 \quad \overset{(2.56)}{\Longleftrightarrow} \quad \limsup_{y\to x} \frac{-y + x - p\,(y-x)}{(y-x)} \leqslant 0 \\
\Leftrightarrow \quad &\limsup_{y\to x} \frac{-(1+p)\,(y-x)}{(y-x)} \leqslant 0 \quad \Leftrightarrow \quad -(1+p) \leqslant 0 \quad \Leftrightarrow \quad p \geqslant -1\,. \qquad (2.59)
\end{aligned}$$

For $0 < y < x \Leftrightarrow -(y-x) > 0$, we have

$$\begin{aligned}
&\limsup_{y\to x} \frac{u(y) - u(x) - p\,(y-x)}{|y-x|} \leqslant 0 \quad \overset{(2.56)}{\Longleftrightarrow} \quad \limsup_{y\to x} \frac{-y + x - p\,(y-x)}{-(y-x)} \leqslant 0 \\
\Leftrightarrow \quad &\limsup_{y\to x} \frac{-(1+p)\,(y-x)}{-(y-x)} \leqslant 0 \quad \Leftrightarrow \quad (1+p) \leqslant 0 \quad \Leftrightarrow \quad p \leqslant -1\,. \qquad (2.60)
\end{aligned}$$

From the results (2.59) and (2.60), it follows that the superdifferential is $p = \{-1\}$ if $x > 0$ for the function (2.56). Since the function (2.56) is differentiable for $x > 0$, the result of the superdifferential coincides with that of the classical derivative.

As with the case $x > 0$, we move on to the case $x < 0$. If $x < 0$, there are two possibilities when y moves closer to x, either from right ($x < y$) or from left ($y < x$).

In consideration of the case $x < y < 0 \Leftrightarrow y - x > 0$ we arrive at

$$\begin{aligned}
&\limsup_{y\to x} \frac{u(y) - u(x) - p\,(y-x)}{|y-x|} \leqslant 0 \quad \overset{(2.56)}{\Longleftrightarrow} \quad \limsup_{y\to x} \frac{y - x - p\,(y-x)}{(y-x)} \leqslant 0 \\
\Leftrightarrow \quad &\limsup_{y\to x} \frac{(1-p)\,(y-x)}{(y-x)} \leqslant 0 \quad \Leftrightarrow \quad (1-p) \leqslant 0 \quad \Leftrightarrow \quad p \geqslant 1\,. \qquad (2.61)
\end{aligned}$$

The case of $y < x < 0 \Leftrightarrow -(y-x) > 0$ allows us to obtain

$$\begin{aligned}
&\limsup_{y\to x} \frac{u(y) - u(x) - p\,(y-x)}{|y-x|} \leqslant 0 \quad \overset{(2.56)}{\Longleftrightarrow} \quad \limsup_{y\to x} \frac{y - x - p\,(y-x)}{-(y-x)} \leqslant 0 \\
\Leftrightarrow \quad &\limsup_{y\to x} \frac{(1-p)\,(y-x)}{-(y-x)} \leqslant 0 \quad \Leftrightarrow \quad -(1-p) \leqslant 0 \quad \Leftrightarrow \quad p \leqslant 1\,. \qquad (2.62)
\end{aligned}$$

In view of (2.61) and (2.62), we thus receive the superdifferential $p = \{1\}$ when $x < 0$ for the function (2.56). As in the case of $x > 0$, the superdifferential is a singleton since the function (2.56) is also differentiable when $x < 0$.

By taking all the cases into account, we can summarise the result of the superdifferential for the non-differentiable function (2.56) as

$$D^+u(x) = \begin{cases} 1\,, & x < 0\,, \\ [-1,1]\,, & x = 0\,, \\ -1\,, & x > 0\,. \end{cases} \tag{2.63}$$

The graph of (2.63) is displayed in Figure 2.5(a). As can be observed in Figure 2.5(a), the superdifferential of the function (2.56) is actually in accordance with the classical derivatives when the function is differentiable. However, the difference is made when the function is not differentiable, i.e. at the point $x = 0$, by admitting set-valued derivatives although there does not exist a derivative in the classical sense.

Subdifferential of $u(x) = 1 - |x|$**.** As we have carried out for the superdifferential (2.54), the definition of the subdifferential (2.55) is applied to the non-differentiable function (2.56) by making use of case distinctions: i.e. $x = 0$, $x > 0$ and $x < 0$.

The first case we consider is when $x = 0$. If $x = 0$, there are two options for y to approach $x = 0$, i.e. either from the right side ($y > 0$) or from the left side ($y < 0$).

For $y > 0$ and $x = 0$, we obtain

$$\begin{aligned} &\liminf_{y\to x} \frac{u(y) - u(0) - q\,(y-0)}{|y-0|} \geqslant 0 \quad \overset{(2.56)}{\iff} \quad \liminf_{y\to x} \frac{-y - q\,y}{y} \geqslant 0 \\ \Leftrightarrow \quad &\liminf_{y\to x} \frac{-(1+q)\,y}{y} \geqslant 0 \quad \Leftrightarrow \quad -(1+q) \geqslant 0 \quad \Leftrightarrow \quad q \leqslant -1\,. \end{aligned} \tag{2.64}$$

For $y < 0$ and $x = 0$, we have

$$\begin{aligned} &\liminf_{y\to x} \frac{u(y) - u(0) - q\,(y-0)}{|y-0|} \geqslant 0 \quad \overset{(2.56)}{\iff} \quad \liminf_{y\to x} \frac{y - q\,y}{-y} \geqslant 0 \\ \Leftrightarrow \quad &\liminf_{y\to x} \frac{(1-q)\,y}{-y} \geqslant 0 \quad \Leftrightarrow \quad -(1-q) \geqslant 0 \quad \Leftrightarrow \quad q \geqslant 1\,. \end{aligned} \tag{2.65}$$

As a consequence, from the results (2.64) and (2.65) we can obtain the superdifferential $q = \varnothing$ if $x = 0$ for the non-differentiable function $u(x) = 1 - |x|$. In contrast to the superdifferential (2.63), one can notice that the subdifferential (2.55) does not admit any values for the function (2.56) at $x = 0$. This is because, as indicated previously, a subdifferential exists when a hyperplane is tangent from below to the graph of the function (2.56) at a point $x = 0$. However, as can be seen from Figure 2.4(a), this is not possible. Since the function (2.56) does not accept any local minimum, this can also be explained in terms of local extrema, which states that a local minimum is characterised by a subdifferential and a local maximum is described by a superdifferential [16, 41, 63]. Subdifferentials, subderivatives, and subgradients that generalise the concept of classical derivatives are extensively investigated in convex analysis literature such as [112, 113, 114, 217].

Let us continue with the case $x > 0$. As in the case of the superdifferential, there are two cases to consider: $0 < x < y$ and $0 < y < x$.

For $0 < x < y \Leftrightarrow y - x > 0$, we obtain

$$\begin{aligned} &\liminf_{y\to x} \frac{u(y) - u(x) - q\,(y-x)}{|y-x|} \geqslant 0 \quad \overset{(2.56)}{\Longleftrightarrow} \quad \liminf_{y\to x} \frac{-y + x - q\,(y-x)}{(y-x)} \geqslant 0 \\ \Leftrightarrow \quad &\liminf_{y\to x} \frac{-(1+q)\,(y-x)}{(y-x)} \geqslant 0 \quad \Leftrightarrow \quad -(1+q) \geqslant 0 \quad \Leftrightarrow \quad q \leqslant -1\,. \end{aligned} \tag{2.66}$$

For $0 < y < x \Leftrightarrow -(y - x) > 0$, we attain

$$\begin{aligned} &\liminf_{y\to x} \frac{u(y) - u(x) - q\,(y-x)}{|y-x|} \geqslant 0 \quad \overset{(2.56)}{\Longleftrightarrow} \quad \liminf_{y\to x} \frac{-y + x - q\,(y-x)}{-(y-x)} \geqslant 0 \\ \Leftrightarrow \quad &\liminf_{y\to x} \frac{-(1+q)\,(y-x)}{-(y-x)} \geqslant 0 \quad \Leftrightarrow \quad (1+q) \geqslant 0 \quad \Leftrightarrow \quad q \geqslant -1\,. \end{aligned} \tag{2.67}$$

From the results (2.66) and (2.67), one can confirm that the superdifferential is given by $q = \{-1\}$ for the function (2.56) for $x > 0$. Since the function (2.56) is differentiable for $x > 0$, the result is not different from the classical derivatives and that of the superdifferential given in (2.63).

As with the case $x > 0$, we proceed with the case $x < 0$. If $x < 0$, there are still two possibilities when y approaches x, either from right ($x < y$) or from left ($y < x$).

For $x < y < 0 \Leftrightarrow y - x > 0$, we reach

$$\begin{aligned} &\liminf_{y\to x} \frac{u(y) - u(x) - q\,(y-x)}{|y-x|} \geqslant 0 \quad \overset{(2.56)}{\Longleftrightarrow} \quad \liminf_{y\to x} \frac{y - x - q\,(y-x)}{(y-x)} \geqslant 0 \\ \Leftrightarrow \quad &\liminf_{y\to x} \frac{(1-q)\,(y-x)}{(y-x)} \geqslant 0 \quad \Leftrightarrow \quad (1-q) \geqslant 0 \quad \Leftrightarrow \quad q \leqslant 1\,. \end{aligned} \tag{2.68}$$

Taking the case $y < x < 0 \Leftrightarrow -(y - x) > 0$ into consideration yields

$$\begin{aligned} &\limsup_{y\to x} \frac{u(y) - u(x) - q\,(y-x)}{|y-x|} \geqslant 0 \quad \overset{(2.56)}{\Longleftrightarrow} \quad \limsup_{y\to x} \frac{y - x - q\,(y-x)}{-(y-x)} \geqslant 0 \\ \Leftrightarrow \quad &\limsup_{y\to x} \frac{(1-q)\,(y-x)}{-(y-x)} \geqslant 0 \quad \Leftrightarrow \quad -(1-q) \geqslant 0 \quad \Leftrightarrow \quad q \geqslant 1\,. \end{aligned} \tag{2.69}$$

Therefore, one can observe that the superdifferential is given by $q = \{1\}$ if $x < 0$ for the function (2.56) by virtue of (2.68) and (2.69). In an analogous way, one can find the subdifferential for the same function (2.56) for $x > 0$, i.e. $q = \{-1\}$.

By putting all the cases together, one can finally obtain the subdifferential for the non-differentiable function (2.56) as

$$D^{-}u(x) = \begin{cases} 1\,, & x < 0\,, \\ \varnothing\,, & x = 0\,, \\ -1\,, & x > 0\,. \end{cases} \tag{2.70}$$

The graph of (2.70) is displayed in Figure 2.5(b). As mentioned already, the important property of a subdifferential characterising a local minima explains the empty set at $x = 0$ in (2.70). Except the point at $x = 0$, the result of the subdifferential is equivalent to that of the superdifferential (2.63) and that of the classical derivative, as one may expect.

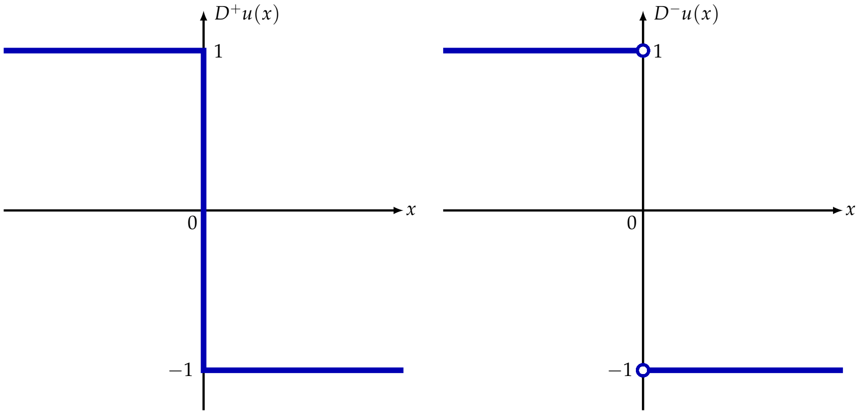

(a) Superdifferential $D^{+}u(x)$.   (b) Subdifferential $D^{-}u(x)$.

Figure 2.5. One-sided differentials for the non-differentiable function $u(x) = 1 - |x|$.

So far, we have performed the computations of one-sided differentials for the non-differentiable function $u(x) = |x| - 1$ which is shown in Figure 2.4(a). If we carry out the same procedure for the non-differentiable function $u(x) = |x| - 1$ that is shown in Figure 2.4(b), the following subdifferential

$$D^{-}u(x) = \begin{cases} -1\,, & x < 0\,, \\ [-1, 1]\,, & x = 0\,, \\ 1\,, & x > 0\,, \end{cases} \tag{2.71}$$

as well as the following superdifferential

$$D^{+}u(x) = \begin{cases} -1\,, & x < 0\,, \\ \varnothing\,, & x = 0\,, \\ 1\,, & x > 0\,. \end{cases} \tag{2.72}$$

are obtained. The graph of the result in (2.71) and (2.72) is displayed in Figure 2.6(a) and 2.6(b), respectively. Since the non-differentiable convex function $u(x) = |x| - 1$ admits a local minimum at $x = 0$ it is not surprising to end up with the empty set for the superdifferential.

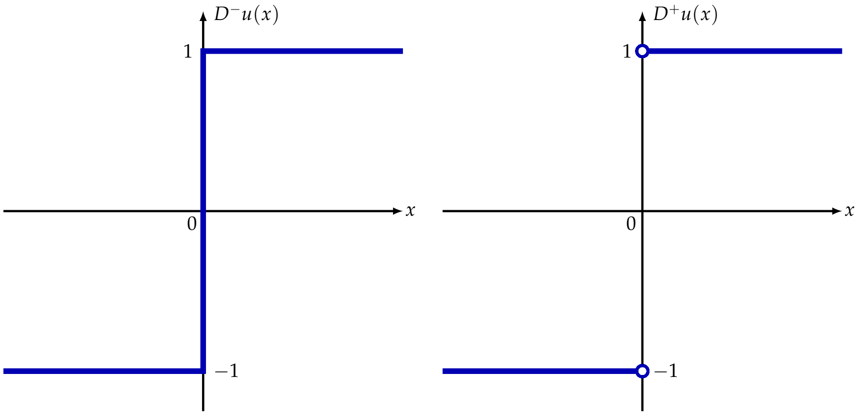

(a) Subdifferential $D^{-}u(x)$. (b) Superdifferential $D^{+}u(x)$.

Figure 2.6. One-sided differentials for the non-differentiable function $u(x) = |x| - 1$.

We have so far explored the important attributes of one-sided differentials by investigating non-differentiable functions in 1-D. However, as shown in [16] these main properties still hold in higher dimensions as well: For a function $u \in C^{0}(\Omega)$ with $x \in \Omega$, (i) super- and subdifferential are closed (possibly empty) subsets of $\mathbb{R}^{n}$; (ii) if u is differentiable at x, then both super- and subdifferential are equivalent to the classical derivative; (iii) if for some x both super- and subdifferential are non-empty sets, then u is differentiable at x; (iv) for some non-differentiable points x, a subdifferential characterises a local minimum while a superdifferential admits only a local maximum.

2.2.3 Viscosity Solutions

As we have previously encountered in the case of the 1-D eikonal equation (2.25), it is well known that HJEs, in general, do not admit classical solutions and thus are ill-posed in the sense of Hadamard [105]. Hence, in an attempt to tackle the difficulties of existence and uniqueness, serious effort was made before the notion of viscosity solutions by Crandall and Lions [62, 63, 65] was introduced in the early 1980s.

In this context, it should still be worth mentioning an important work to appreciate the mathematical advances in those times. In 1975, the Russian mathematician Kružkov has acquired generalised solutions and established the existence and uniqueness results for eikonal-type HJEs by imposing constraints on weak solutions relying upon Fermat's and Huygens' principles from geometrical optics [146]. In fact, as we shall discuss in Section 2.3, it turns out that these physical principles play the fundamental role even in developing an efficient numerical method such as the fast marching algorithm [226]. This suggests that physically meaningful constraints can help to find weak solutions not only for problems themselves but also for relaxed formulations.

In this section, we look into definitions of viscosity solutions by one-sided differentials from the previous section and investigate what properties they have and how they are useful especially when functions have points that are not differentiable in the classical sense by applying them to the 1-D eikonal equation (2.25). The key difference between viscosity solutions [63, 65] and vanishing viscosity solutions lies in the fact that viscosity solutions do not require solutions to be everywhere differentiable but only to be continuous, i.e. C^0, in contrast to the case of vanishing viscosity solutions as shown in Section 2.2.1.

For a given eikonal-type Hamilton-Jacobi equation with DBC

$$\begin{cases} H(\boldsymbol{x}, \nabla u(\boldsymbol{x})) = 0 & \text{in} \quad \Omega \\ u(\boldsymbol{x}) = \varphi(\boldsymbol{x}) & \text{on} \quad \partial\Omega\,, \end{cases} \tag{2.73}$$

a continuous viscosity solution $u \in C^0$ to (2.73) is defined as follows.

Definition 2.2.3 (Continuous Viscosity Solution). A continuous function $u \in C^0$ is a *continuous viscosity solution* of the equation (2.84) in Ω if the following conditions are satisfied:

(i) **(Viscosity subsolution)** $H(\boldsymbol{x}, \boldsymbol{p}) \leqslant 0 \quad \forall\, \boldsymbol{x} \in \mathbb{R}^n, \quad \forall \boldsymbol{p} \in D^+u,$

(ii) **(Viscosity supersolution)** $H(\boldsymbol{x}, \boldsymbol{q}) \geqslant 0 \quad \forall\, \boldsymbol{x} \in \mathbb{R}^n, \quad \forall \boldsymbol{q} \in D^-u,$

where D^+ and D^- denote the super- and subdifferential in (2.54) and (2.55), respectively.

In Definition 2.2.3, one can notice that continuous viscosity solutions extend the concept of a gradient in (2.73) from the classical sense to the more general one that can handle non-differentiable problems. In order to grasp how continuous viscosity solutions are selected from solution candidates shown in Figure 2.1, we find a solution to the 1-D eikonal equation (2.25) in the viscosity sense by applying the above definition.

Viscosity Solution for the Hamiltonian $H(x, \nabla u(x)) = 1 - |\nabla u(x)|$

To this end, we first make use of the following Hamiltonian

$$H(x, D^{\pm}u(x)) = 1 - |D^{\pm}u(x)|\,, \tag{2.74}$$

where $D^{\pm}u(x)$ denotes the one-sided differentials at a point x, i.e. $D^{+}u(x)$ for the superdifferential in (2.54) and $D^{-}u(x)$ for the subdifferential in (2.55), respectively.

While there are infinitely many solution candidates for the problem (2.25) as shown in Figure 2.1, it turns out within this mathematical framework that the pointwise minimum solution candidate

$$u^{-}(x) = |x| - 1 \tag{2.75}$$

is the only viscosity solution to (2.25) with the Hamiltonian (2.74).

Viscosity Subsolution. To validate this statement, we examine if (2.75) satisfies the criterion of the viscosity subsolution in Definition 2.2.3. From (2.72), which is the superdifferential of (2.75), one can infer

$$0 \geqslant 1 - \left|D^{+}u^{-}(x)\right| = \begin{cases} 0\,, & x < 0\,, \\ \varnothing\,, & x = 0\,, \\ 0\,, & x > 0\,. \end{cases} \tag{2.76}$$

This confirms that (2.75) fulfils the requirement for the viscosity subsolution in the interval $(-1, 1) \setminus \{0\}$.

Viscosity Supersolution. As a next step, we check whether (2.75) meets the condition for the viscosity supersolution in Definition 2.2.3. Since the viscosity supersolution incorporates the subdifferential, the equation (2.71), i.e. the subdifferential of (2.75), brings us to

$$0 \leqslant 1 - |D^{-}u^{-}(x)| = \begin{cases} 0\,, & x < 0\,, \\ [0,1]\,, & x = 0\,, \\ 0\,, & x > 0\,. \end{cases} \tag{2.77}$$

Based on the fact that a viscosity solution must satisfy both requirements for the viscosity subsolution and the viscosity supersolution according to Definition 2.2.3, one can conclude that (2.75) is a viscosity solution in the interval $(-1, 0) \cup (0, 1)$, given the results in (2.76) and (2.77). From this fact, it can also be noticed that viscosity solutions are not required to be defined everywhere but they are actually defined "almost everywhere" in mathematical terms [35, 107, 264]. The graph of the viscosity solution to (2.75) with the Hamiltonian (2.74) is shown in Figure 2.7, which illustrates the almost everywhere solution not being defined at $x = 0$.

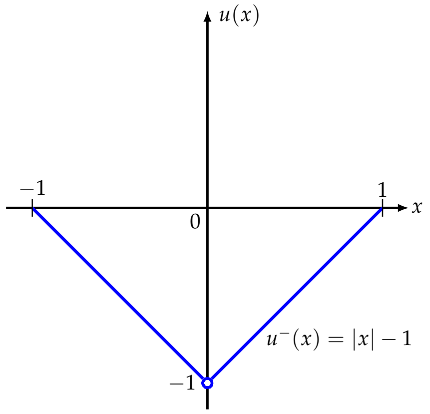

Figure 2.7. A viscosity solution to (2.25) with the Hamiltonian (2.74).

Uniqueness of a Solution. To verify the uniqueness of the solution (2.75) to the 1-D eikonal equation (2.25) with the Hamiltonian (2.74), we inspect whether the pointwise maximum solution candidate

$$u^{+}(x) = 1 - |x| \tag{2.78}$$

complies with the Definition 2.2.3.

To see if (2.78) qualifies for the viscosity subsolution, we proceed as carried out for (2.76) but this time with the different superdifferential (2.63), which is the superdifferential of (2.78). Then, we can attain

$$0 \ngeq 1 - \left|D^{+}u^{+}(x)\right| = \begin{cases} 0\,, & x < 0\,, \\ [0,1]\,, & x = 0\,, \\ 0\,, & x > 0\,. \end{cases} \tag{2.79}$$

The result (2.79) shows that the solution candidate (2.78) fails to be a viscosity subsolution at the point $x = 0$ on account of Definition 2.2.3. Therefore, it cannot be a viscosity solution regardless of the fulfilment of the supersolution criterion. Moreover, it can be observed that a viscosity solution to (2.25) with the Hamiltonian (2.74) does not admit local maxima by the properties of superdifferential discussed in Section 2.2.2. Whenever a solution candidate has at least one local maximum, e.g. those with dashed lines in Figure 2.1, these solution candidates are filtered out by the requirement for the viscosity supersolution as shown here. As a consequence, this procedure leaves only one solution candidate (2.75) from Figure 2.1, which is actually the only viscosity solution to the 1-D eikonal equation (2.25) with the

Hamiltonian (2.74). Since we have mainly focused here on elaborating the idea of the uniqueness of viscosity solutions by means of an example problem, we refer to [16, 17, 126, 142, 155] and the references therein for mathematically more rigorous treatment.

Viscosity Solution for the Hamiltonian $H(x, \nabla u(x)) = |\nabla u(x)| - 1$

To solve (2.25), one may realise that there is an alternative to use the Hamiltonian (2.74). We, therefore, turn our attention to investigate whether the viscosity solution (2.75) is preserved when we utilise the different Hamiltonian

$$H(x, D^{\pm}u(x)) = |D^{\pm}u(x)| - 1\,. \tag{2.80}$$

It turns out that the equation (2.75) is not a viscosity solution any more when the different Hamiltonian is used. To justify this, we simply check the condition for the viscosity supersolution. When we incorporate (2.71), i.e. the subdifferential of (2.75), we can observe the expected result

$$0 \nleqslant |D^{-}u^{-}(x)| - 1 = \begin{cases} 0\,, & x < 0\,, \\ [-1, 0]\,, & x = 0\,, \\ 0\,, & x > 0\,. \end{cases} \tag{2.81}$$

By the previous discussion, this suggests that a viscosity solution with the Hamiltonian (2.80) does not accept local minima. Then, it can be expected that the pointwise maximum solution candidate (2.78) should be singled out from the solution set portrayed in Figure 2.1 since other solution candidates are rejected by the requirement for the viscosity supersolution. By validating (2.78) to be both a viscosity subsolution and a viscosity supersolution, we can attest that (2.78) is a viscosity solution.

Viscosity Subsolution. To justify that (2.78) is a viscosity subsolution, we show from (2.63), i.e. the superdifferential of (2.78), that (2.78) is in accordance with the definition of viscosity subsolution

$$0 \geqslant \left|D^{+}u^{+}(x)\right| - 1 = \begin{cases} 0\,, & x < 0\,, \\ [-1, 0]\,, & x = 0\,, \\ 0\,, & x > 0\,. \end{cases} \tag{2.82}$$

Viscosity Supersolution. In a similar way, by (2.70), i.e. the subdifferential of (2.78), one confirms that (2.78) is a viscosity supersolution

$$0 \leqslant \left|D^- u^+(x)\right| - 1 = \begin{cases} 0\,, & x < 0\,, \\ \varnothing\,, & x = 0\,, \\ 0\,, & x > 0\,. \end{cases} \tag{2.83}$$

As a result, (2.78) is a viscosity solution in the interval $(-1, 0) \cup (0, 1)$ and thereby the assertion follows. The graph of the viscosity solution for the 1-D eikonal equation (2.25) with the Hamiltonian (2.80) is shown in Figure 2.8. When the Hamiltonian (2.80) is incorporated, it can be noted that the viscosity solution in Figure 2.8 coincides with the distance function (2.26) except one point $x = 0$, see $u^+(x) = 1 - |x|$ displayed in Figure 2.1.

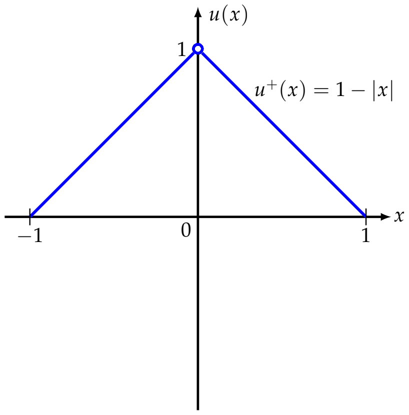

Figure 2.8. A viscosity solution to (2.25) with the Hamiltonian (2.80).

In what follows, we summarise some important attributes of viscosity solutions that are usually different in the classical sense: (i) Making use of the different Hamiltonian for the same problem leads, in general, to different viscosity solutions. In other words, viscosity solutions are generally not preserved with a different Hamiltonian. (ii) As can be noticed in Figure 2.7 and 2.8, viscosity solutions do *not* need be defined everywhere but almost everywhere, possibly except for some points. (iii) Since the framework of viscosity solutions is capable of handling non-differentiable points by one-sided differentials, viscosity solutions do not require solutions to be everywhere differentiable but only to be continuous almost everywhere. When comparing the quality from the vanishing viscosity solutions with those from the viscosity solutions, there is a big difference especially around the point $x = 0$ (see Figure 2.2 and 2.3 for vanishing viscosity solutions and Figure 2.7 and 2.8 for viscosity solutions, respectively). Concerning the role of the point $x = 0$, where solutions are not defined, we defer the matter to Section 3.5.3.

Finally, this framework can also be extended to the general-type Hamiltonian (2.24). For a given general-type Hamilton-Jacobi equation with DBC

$$\begin{cases} H(x, u(x), \nabla u(x)) = 0 & \text{in} \quad \Omega \\ u(x) = \varphi(x) & \text{on} \quad \partial\Omega, \end{cases} \tag{2.84}$$

a continuous viscosity solution $u \in C^0$ to an equation (2.84) is defined as follows.

Definition 2.2.4 (Continuous Viscosity Solution). A continuous function $u \in C^0$ is a *continuous viscosity solution* of the equation (2.84) in Ω if the following conditions are satisfied:

(i) **(Viscosity subsolution)** $H(x, u(x), \boldsymbol{p}) \leqslant 0 \quad \forall\, x \in \Omega, \quad \forall \boldsymbol{p} \in D^+u,$

(ii) **(Viscosity supersolution)** $H(x, u(x), \boldsymbol{q}) \geqslant 0 \quad \forall\, x \in \Omega, \quad \forall \boldsymbol{q} \in D^-u,$

where D^+ and D^- denote the super- and subdifferential in (2.54) and (2.55), respectively.

2.3 Fast Marching Methods

In many scientific areas, e.g. geophysics, electrodynamics and optics, estimating the arrival time of a wavefront described by an eikonal equation based on Fermat's and Huygens' principle [39, 115] plays a significant role. For finding a solution to an eikonal equation there are mainly two categories of strategies, namely time-consuming iterative algorithms, e.g. [219], and efficient non-iterative ones. In this section, we focus on efficient non-iterative approaches. For this type of methods, among others, Tsitsiklis proposed an optimal control based approach [249] which makes use of the Dijkstra's shortest path algorithm [73]. Helmsen *et al.* [110] and Sethian [226] derived the same idea in a different way by utilising the upwind discretisation of Rouy and Tourin [219]. The term "fast marching" method [226, 229, 230] was coined by Sethian and it refers to a specifically designed efficient numerical algorithm to solve an eikonal equation in the viscosity sense with an upwind scheme [219] by tracking the propagation of a wavefront in a systematic way and exploiting a heap data structure [225] for speedup.

2.3.1 A Motivational Example

In order to understand the basic idea of the FM method, we consider the following concrete scenario: Suppose that a company plans to begin broadcasting a local radio programme in a flat area and wants to know where to place how many signal amplification systems in order to synchronise with the original signal before it officially starts a business. To this end, a test signal, which is assumed to be a plane wave, is sent out with a constant speed from its station and thereby a wavefront of the electromagnetic wave is spreading out in the normal direction to the wavefront. In addition, receiving antenna systems are placed at regular grid points to measure the first arrival time of the wavefront of the original signal. The situation is illustrated in Figure 2.9.

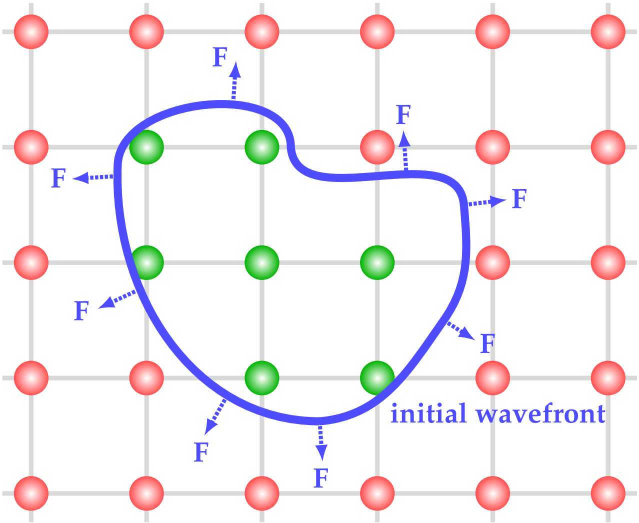

Figure 2.9. An illustration of the concrete example. A transmitted wavefront of an initial signal expands outwards with a constant speed $F > 0$. Assuming that a broadcasting station is located at green nodes and the arrival time inside the wavefront is already known to be 0. However, the arrival time at the red nodes is yet unknown.

As discussed in [229], the aforementioned scenario can be formulated by the basic relationship of a moving object in classical mechanics [85]. In 1-D, this reads as

$$dx = F\,dT \quad \Leftrightarrow \quad 1 = F\,\frac{dT}{dx}\,, \quad T(x_0) = 0 \tag{2.85}$$

where dx denotes a travelled distance, $F \in \mathbb{R}^+$ stands for a constant speed, x_0 an initial location of a wavefront, and dT amounts to be the elapsed time. In 2-D, the equation (2.85) is extended to

$$\begin{cases} |\nabla T|\,F = 1 & \text{in} \quad \Omega \setminus \Gamma_0 \\ T = 0 & \text{on} \quad \Gamma_0 \end{cases}, \tag{2.86}$$

where $T : \boldsymbol{x} \in \Omega \subset \mathbb{R}^2 \to \mathbb{R}^+$ is the elapsed time between the first arrival of the wavefront at grid node $\boldsymbol{x}$ and sending out at the signal at the station, $F : \mathbb{R}^2 \to \mathbb{R}^+$ stands for a constant speed at the grid point $\boldsymbol{x}$, and $\Gamma_0 \subset \mathbb{R}^2$ denotes the initial location of the wavefront. Although we rather focus on the 2-D case for the example, the same procedure may be applied to higher dimensional problems as well. As a result, the arrival time T of the front motion is described by a solution to the eikonal equation (2.86), which is also a boundary value problem [229].

2.3.2 Approximation by an Upwind Scheme

As previously mentioned, for a numerical approximation of (2.86), there are mainly two approaches of work: an iterative method such as [219] and a non-iterative one, e.g. [138, 227, 282]. In spite of some differences in detail, all these methods actually share one important principle: they strive to select the proper direction from which the wavefront is coming by retrieving information from those grid points where the wavefront has just been shortly before. Having this in mind, we first investigate the main properties of the method by Rouy and Tourin [219] and thereby may have an insight into other approaches such as [138, 227, 282].

For the discretisation we may define a grid point $\boldsymbol{x_i}$ in terms of an index set $\boldsymbol{i}$ and grid size $\boldsymbol{h}$ as

$$\boldsymbol{x_i} := \left(x_i, y_j\right)^\top = \left(i \cdot h_1, j \cdot h_2\right)^\top , \tag{2.87}$$

where $\boldsymbol{x_i} \in \Omega_{\boldsymbol{h}} \subset \Omega \subset \mathbb{R}^2$, $\boldsymbol{i} := (i, j)^\top \subset \mathbb{Z}^2$, $\boldsymbol{h} := (h_1, h_2)^\top \subset \mathbb{R}^{2+}$ with fixed grid sizes h_1 and h_2 in x- and y-direction, respectively. Since the grid size $\boldsymbol{h}$ is constant in each direction, a grid point $\boldsymbol{x_i}$ can be determined by an index $\boldsymbol{i}$ by assuming that the index $\boldsymbol{i}$ is well-defined in the computational domain $\Omega_{\boldsymbol{h}}$.

In this respect, one discretisation for the eikonal equation (2.86) can be realised by a first-order upwind scheme as in [219]. This reads

$$\sqrt{\widehat{T}_x^2 + \widehat{T}_y^2} = \frac{1}{F_{i,j}} , \tag{2.88}$$

where $\widehat{T}_x$ and $\widehat{T}_x$ represent the upwind discretisation in x- and y-direction that are defined by

$$\widehat{T}_x = \max\left(D_{i,j}^{-x} T, -D_{i,j}^{+x} T, 0\right) \tag{2.89}$$

and

$$\widehat{T}_y = \max\left(D_{i,j}^{-y} T, -D_{i,j}^{+y} T, 0\right) , \tag{2.90}$$

respectively. The term $D_{i,j}^{-x}\, T$ in (2.89) denotes a backward difference approximation at $(i, j)^\top$ in x-direction with a grid size h_1

$$D_{i,j}^{-x}\, T = \frac{T_{i,j} - T_{i-1,j}}{h_1} . \tag{2.91}$$

Analogously, $D^{+x}_{i,j}\,T$ in (2.89) stands for a forward difference

$$D^{+x}_{i,j}\,T = \frac{T_{i+1,j} - T_{i,j}}{h_1}\,. \tag{2.92}$$

In a similar way, for the y-direction the same notations are applied with a grid size h_2. Therefore, a backward difference $D^{-y}_{i,j}\,T$ in (2.90) is given by

$$D^{-y}_{i,j}\,T = \frac{T_{i,j} - T_{i,j-1}}{h_2} \tag{2.93}$$

and a forward difference $D^{+y}_{i,j}\,T$ in (2.90) is denoted by

$$D^{+y}_{i,j}\,T = \frac{T_{i,j+1} - T_{i,j}}{h_2}\,, \tag{2.94}$$

respectively. In what follows, we provide the underlying rationale for this specific type of numerical scheme in both 1-D and 2-D.

1-D case

Let us have a look on some properties of the employed scheme (2.88) in 1-D, i.e. (2.89) with (2.91) and (2.92). To this end, suppose $T_{i,j}$ is an unknown approximate solution and consider how one can select a proper upwind scheme by means of two neighbours in x-direction. In view of two adjacent nodes of $(i,j)^\top$, one needs to deal with three arrival times, i.e. $T_{i-1,j}$, $T_{i,j}$ and $T_{i+1,j}$. When one sorts these in an ascending order, the following six cases may occur:

$$\begin{aligned}
&\text{(i)} \quad T_{i-1,j} < T_{i,j} < T_{i+1,j}\,, && \text{(ii)} \quad T_{i-1,j} < T_{i+1,j} < T_{i,j}\,,\\
&\text{(iii)} \quad T_{i,j} < T_{i-1,j} < T_{i+1,j}\,, && \text{(iv)} \quad T_{i,j} < T_{i+1,j} < T_{i-1,j}\,,\\
&\text{(v)} \quad T_{i+1,j} < T_{i,j} < T_{i-1,j}\,, && \text{(vi)} \quad T_{i+1,j} < T_{i-1,j} < T_{i,j}\,.
\end{aligned}$$

Case (i) and (v). The case (i) represents the situation that a wavefront reaches the grid point $(i-1,j)^\top$ first then moves towards $(i+1,j)^\top$ through $(i,j)^\top$. Hence, the front motion propagates from left to right and thereby the backward difference $D^{-x}_{i,j}$ of (2.91) is the proper selection, see Figure 2.10(a). This means that the discrete eikonal equation (2.88) is reduced to

$$\sqrt{\left(D^{-x}_{i,j}T\right)^2} = \frac{1}{F_{i,j}} \tag{2.95}$$

and a physically meaningful solution to (2.95) satisfies the condition described in the case of (i). The detailed analysis with a geometric interpretation for this case is deferred to the discussion of the complete 2-D case. With the same logic but the opposite direction, the case (v) gives the forward difference $D^{+x}_{i,j}$ as a proper decision, see Figure 2.10(b).

Case (ii) and (vi). For the case (ii) and (vi), i.e. when both $T_{i-1,j}$ and $T_{i+1,j}$ are less than $T_{i,j}$, the smaller value is selected as an upwind direction, see Figure 2.10(c). Therefore, the case (ii) corresponds to the first argument in (2.89) since

$$
\begin{array}{cccccc}
 & T_{i-1,j} & < & T_{i+1,j} & < & T_{i,j} \\
\iff & T_{i-1,j} - T_{i,j} & < & T_{i+1,j} - T_{i,j} & < & 0 \\
\iff & \dfrac{T_{i-1,j} - T_{i,j}}{h_1} & < & \dfrac{T_{i+1,j} - T_{i,j}}{h_1} & < & 0 \\
\iff & \dfrac{T_{i,j} - T_{i-1,j}}{h_1} & > & -\left(\dfrac{T_{i+1,j} - T_{i,j}}{h_1}\right) & > & 0 \\
\overset{(2.91)}{\underset{(2.92)}{\iff}} & D^{-x}_{i,j}T & > & -D^{+x}_{i,j}T & > & 0\,.
\end{array}
\tag{2.96}
$$

Analogously, the case (vi) corresponds to the second argument in (2.89) because

$$
\begin{array}{cccccc}
 & T_{i+1,j} & < & T_{i-1,j} & < & T_{i,j} \\
\iff & T_{i+1,j} - T_{i,j} & < & T_{i-1,j} - T_{i,j} & < & 0 \\
\iff & \dfrac{T_{i+1,j} - T_{i,j}}{h_1} & < & \dfrac{T_{i-1,j} - T_{i,j}}{h_1} & < & 0 \\
\iff & \dfrac{T_{i+1,j} - T_{i,j}}{h_1} & < & -\left(\dfrac{T_{i,j} - T_{i-1,j}}{h_1}\right) & < & 0 \\
\overset{(2.91)}{\underset{(2.92)}{\iff}} & D^{+x}_{i,j}T & < & -D^{-x}_{i,j}T & < & 0 \\
\iff & -D^{+x}_{i,j}T & > & D^{-x}_{i,j}T & > & 0\,.
\end{array}
\tag{2.97}
$$

Especially in this case, one may notice that the actual difference is $D^{+x}_{i,j}T$, see the slope between $T_{i,j}$ and $T_{i+1,j}$ in Figure 2.10(c). This suggests that the role of the *max* operator in (2.89) is to select a correct direction for the upwind discretisation [43, 44, 132]. However, one should note that the original sign must be restored if the forward direction is selected. This corresponds to

$$
T_x \approx \begin{cases} D^{+x}_{i,j}T & \text{if} \quad \widehat{T}_x = -D^{+x}_{i,j}T\,, \\ \widehat{T}_x & \text{otherwise}\,, \end{cases}
\tag{2.98}
$$

and

$$T_y \approx \begin{cases} D^{+y}_{i,j}\,T & \text{if} \quad \widehat{T}_y = -D^{+y}_{i,j}\,T\,, \\ \widehat{T}_y & \text{otherwise}\,, \end{cases} \tag{2.99}$$

respectively.

Case (iii) and (iv). The cases (iii) and (iv) describe the situation that a wavefront passed by a node $(i,j)^\top$ earlier than $(i-1,j)^\top$ or $(i+1,j)^\top$. However, this does not make sense since a solution at $(i,j)^\top$ is already given before a decision for an upwind direction is made by neighbouring nodes. Furthermore, one may notice that the max operator in (2.88) does not accept locally convex solutions, see Figure 2.10(d).

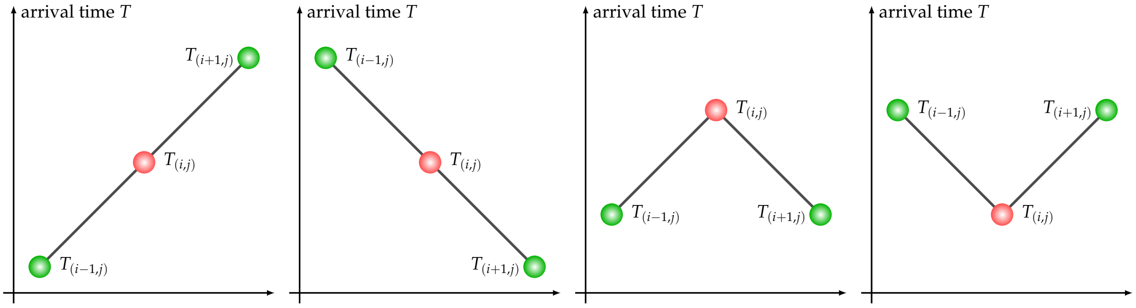

(a) Case (i). (b) Case (v). (c) Case (ii) and (vi). (d) Case (iii) and (iv).

Figure 2.10. Arrival time T at $(i-1,j)^\top$, $(i,j)^\top$ and $(i+1,j)^\top$. The arrival time of green nodes are known but that of red ones are not.

As a consequence, this type of an upwind scheme satisfies the causality [229, 230, 231], which means that a new arrival time computed only by already known upwind values from neighbours must be greater than the ones of adjacent nodes. Moreover, the presented 3-point based upwind scheme is stable since it does not introduce new local extrema during computations. This property of the scheme is called monotone [38, 92, 152, 153, 229].

2-D Case

Let us turn our attention to the 2-D case. To this end, as in [154] we provide a geometric interpretation to the solutions of (2.88) by constructing it with an upwind scheme [219]. Since there are four neighbouring nodes to consider in the 2-D case, we limit ourselves to the left half-plane with respect to $(i,j)^\top$ for the sake of simplicity. Nevertheless, the other half can be handled in a similar way.

First, one simple scenario occurs when the wavefront is approaching $(i,j)^\top$ in solely one direction as in 1-D. If this is the case, there are three possibilities for an upwind direction as shown in Figure 2.11. By the discussion in 1-D, the following decisions can be made: $D_{i,j}^{-x}$ for the case in Figure 2.11(a), $-D_{i,j}^{+y}$ for the case in Figure 2.11(b), and $D_{i,j}^{-y}$ for the case in Figure 2.11(c).

Since the case of Figure 2.11(a) actually corresponds to the case (i) in 1-D, from (2.95) one can obtain the following relationship

$$\sqrt{\left(D_{i,j}^{-x}\,T\right)^2} = \frac{1}{F_{i,j}} \overset{(2.91)}{\Longrightarrow} \left(\frac{T_{i,j}-T_{i-1,j}}{h_1}\right)^2 = \frac{1}{F_{i,j}^2} \Longleftrightarrow T_{i,j} = T_{i-1,j} \pm \frac{h_1}{F_{i,j}} \,. \tag{2.100}$$

However, in view of the geometry in Figure 2.11(a), the arrival time of the wavefront at $(i,j)^\top$ can be obtained by

$$T_{i,j} = T_{i-1,j} + \frac{h_1}{F_{i,j}} \,, \tag{2.101}$$

with the grid distance h_1 in x-direction and the constant speed $F_{i,j}$. At this point, one can observe that the solution $T_{i,j} = T_{i-1,j} - \frac{h_1}{F_{i,j}}$ in (2.100) is physically unfeasible based on the causality and thereby excluded from the solution.

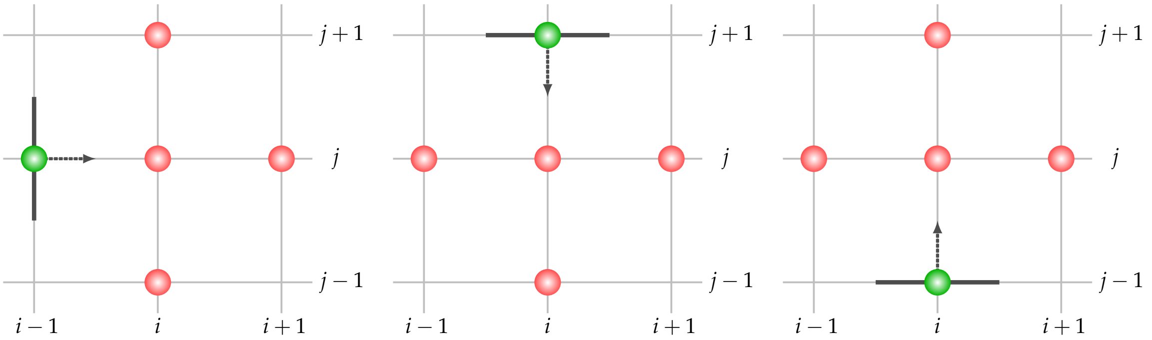

(a) $T_{i-1,j} < T_{i,j}$. (b) $T_{i,j+1} < T_{i,j}$. (c) $T_{i,j-1} < T_{i,j}$.

Figure 2.11. Upwind directions for one-direction movement of the wavefront (pure horizontal or vertical movement). The solid line denotes the planar wavefront and the dashed arrow corresponds to the direction of the movement. The arrival time of green nodes are known but that of red ones are not.

If the motion of the wavefront involves two directions for an upwind side, we have to make case distinctions for an analysis. To begin with, we investigate the situation that the planar wavefront is coming to $(i,j)^\top$ from the northwest direction. In this case, the wavefront can take three feasible routes in the quadrant, see Figure 2.12(a), 2.12(b) and 2.12(c). Since the correct decisions on upwind directions for the northwest quadrant are $D_{i,j}^{-x}$ and $-D_{i,j}^{+y}$, the discrete eikonal equation (2.88) is reduced to

$$\begin{aligned} \left(D^{-x}_{i,j}\,T\right)^2 + \left(-D^{+y}_{i,j}\,T\right)^2 &= \frac{1}{F^2_{i,j}} \\ \overset{(2.91)}{\underset{(2.94)}{\Longleftrightarrow}} \left(\frac{T_{i,j}-T_{i-1,j}}{h_1}\right)^2 + \left(-\frac{T_{i,j+1}-T_{i,j}}{h_2}\right)^2 &= \frac{1}{F^2_{i,j}}\,. \end{aligned} \tag{2.102}$$

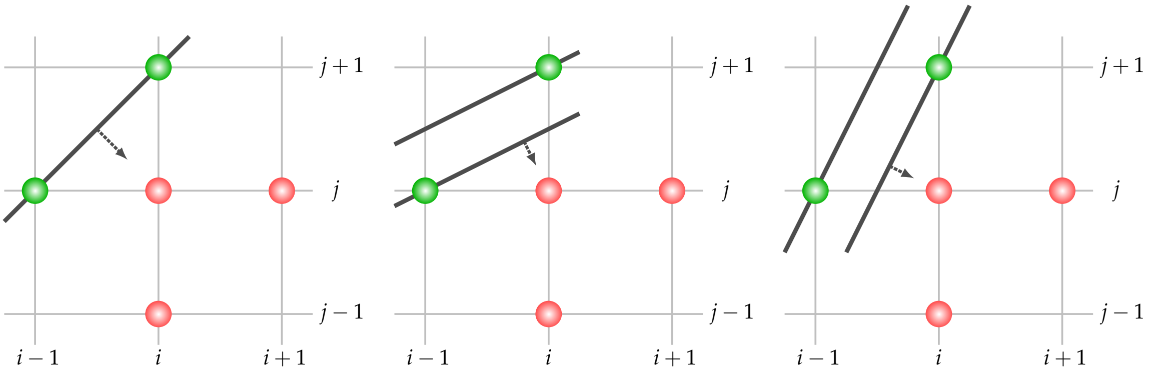

(a) $T_{i-1,j} = T_{i,j+1} < T_{i,j}$. (b) $T_{i,j+1} < T_{i-1,j} < T_{i,j}$. (c) $T_{i-1,j} < T_{i,j+1} < T_{i,j}$.

Figure 2.12. Different cases of the arrival time T at $(i-1,j)^\top$, $(i,j)^\top$ and $(i,j+1)^\top$ when the movement of the wavefront are not purely vertical or horizontal.

For the case of $T_{i-1,j} = T_{i,j+1} < T_{i,j}$ as in Figure 2.12(a), one can compute the arrival time as

$$T_{i,j} = T_{i-1,j} + \frac{|AC|}{F_{i,j}}\,, \tag{2.103}$$

where $|AC|$ denotes the shortest length between the planar wavefront and $(i,j)^\top$ depicted in Figure 2.13(a). Based on the area of the triangle, the distance $|AC|$ can be computed by

$$h_1\,h_2 = |AC|\sqrt{h_1^2+h_2^2} \quad\Leftrightarrow\quad |AC| = \frac{h_1\,h_2}{\sqrt{h_1^2+h_2^2}}\,. \tag{2.104}$$

For the case of $T_{i,j+1} < T_{i-1,j} < T_{i,j}$ as shown in Figure 2.12(b), one can draw the following connections: The elapsed time of the wavefront for the line segment $\overline{AC}$ in Figure 2.13(b) amounts to be

$$T_{i,j} = T_{i,j+1} + \frac{h_2\,\cos\beta}{F_{i,j}} \Leftrightarrow \frac{T_{i,j}-T_{i,j+1}}{h_2}\,F_{i,j} = \cos\beta\,. \tag{2.105}$$

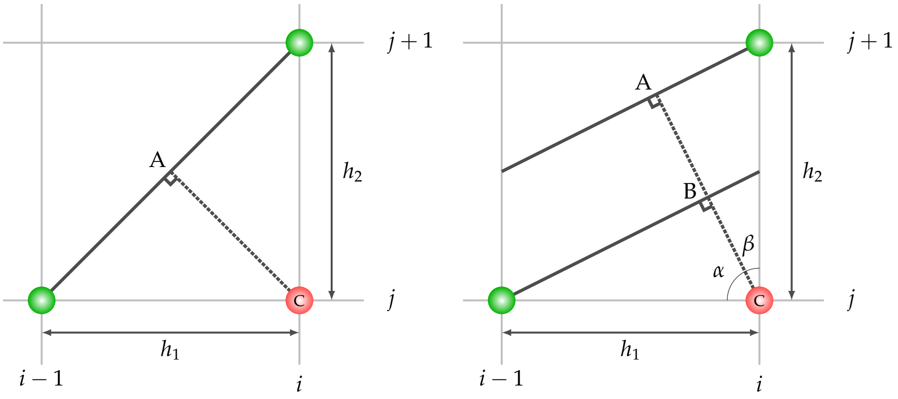

(a) Figure 2.12(a). (b) Figure 2.12(b).

Figure 2.13. The close-up view for the northwest quadrant in Figure 2.12.

In an analogous way, the travel time for $|BC|$ corresponds to

$$T_{i,j} = T_{i-1,j} + \frac{h_1 \cos\alpha}{F_{i,j}} \Leftrightarrow \frac{T_{i,j} - T_{i-1,j}}{h_1} F_{i,j} = \cos\alpha \,. \tag{2.106}$$

Then, based on the trigonometric identity

$$\cos\beta = \cos\left(\frac{\pi}{2} - \alpha\right) = \sin\alpha \tag{2.107}$$

as well as

$$\sin^2\alpha + \cos^2\alpha = 1 \,, \tag{2.108}$$

plugging (2.105) and (2.106) into (2.108) yields the exact same quadratic equation (2.102) whose solution can be expressed in an analytic form. Rearranging (2.102) with respect to the unknown $T_{(i,j)}$ leads to

$$a\, T_{i,j}^2 + b\, T_{i,j} + c = 0 \,, \tag{2.109}$$

where

$$a := h_1^2 + h_2^2 \,, \tag{2.110}$$

$$b := -2\left(T_{i-1,j}\, h_2^2 + T_{i,j+1}\, h_1^2\right) \,, \tag{2.111}$$

$$c := h_2^2\, T_{i-1,j}^2 + h_1^2\, T_{i,j+1}^2 - \frac{h_1^2\, h_2^2}{F_{i,j}^2} \,. \tag{2.112}$$

Since the discriminant D of (2.109) is given by

$$
\begin{aligned}
D &= b^2 - 4\,a\,c \\
&\overset{(2.110)}{\underset{(2.111)}{=}} 4\left(T_{i-1,j}\,h_2^2 + T_{i,j+1}\,h_1^2\right)^2 - 4\left(h_1^2 + h_2^2\right)\left(h_2^2\,T_{i-1,j}^2 + h_1^2\,T_{i,j+1}^2 - \frac{h_1^2\,h_2^2}{F_{i,j}^2}\right) \\
&= 4\,\left(T_{i-1,j}^2\,h_2^4 + 2\,T_{i-1,j}\,T_{i,j+1}\,h_1^2\,h_2^2 + T_{i,j+1}^2\,h_1^4\right) \\
&\quad - 4\left(h_1^2\,h_2^2\,T_{i-1,j}^2 + h_1^4\,T_{i,j+1}^2 - \frac{h_1^4\,h_2^2}{F_{i,j}^2} + h_1^2\,h_2^2\,T_{i,j+1}^2 + h_2^4\,T_{i-1,j}^2 - \frac{h_1^2\,h_2^4}{F_{i,j}^2}\right) \\
&= 4\left(\frac{h_1^2\,h_2^2\,\left(h_1^2 + h_2^2\right)}{F_{i,j}^2} - h_1^2\,h_2^2\,\left(T_{i-1,j} - T_{i,j+1}\right)^2\right) \\
&= 4\,h_1^2\,h_2^2\left(\frac{h_1^2 + h_2^2}{F_{i,j}^2} - \left(T_{i-1,j} - T_{i,j+1}\right)^2\right), \qquad (2.113)
\end{aligned}
$$

the real solution of (2.109) does not exist when the following condition holds true

$$
\begin{aligned}
&D < 0 \overset{(2.113)}{\iff} 4\,\underbrace{h_1^2\,h_2^2}_{>0}\left(\frac{h_1^2 + h_2^2}{F_{i,j}^2} - \left(T_{i-1,j} - T_{i,j+1}\right)^2\right) < 0 \\
&\Leftrightarrow \left(\frac{h_1^2 + h_2^2}{F_{i,j}^2} - \left|T_{i-1,j} - T_{i,j+1}\right|^2\right) < 0 \\
&\Leftrightarrow \underbrace{\left(\frac{\sqrt{h_1^2 + h_2^2}}{F_{i,j}} + \left|T_{i-1,j} - T_{i,j+1}\right|\right)}_{>0}\left(\frac{\sqrt{h_1^2 + h_2^2}}{F_{i,j}} - \left|T_{i-1,j} - T_{i,j+1}\right|\right) < 0 \\
&\Leftrightarrow \frac{\sqrt{h_1^2 + h_2^2}}{F_{i,j}} - \left|T_{i-1,j} - T_{i,j+1}\right| < 0 \quad \Leftrightarrow \quad \frac{\sqrt{h_1^2 + h_2^2}}{F_{i,j}} < \left|T_{i-1,j} - T_{i,j+1}\right| \\
&\text{(since it is unknown which one is larger than the other between } T_{i-1,j} \text{ and } T_{i,j+1}) \\
&\Rightarrow T_{i-1,j} = +\infty \quad \text{or} \quad T_{i,j+1} = +\infty\,. \qquad (2.114)
\end{aligned}
$$

Therefore, a solution of (2.109) has the form of

$$T_{i,j} = \begin{cases} T_{i-1,j} + \dfrac{h_1}{F_{i,j}}\,, & \text{if} \quad T_{i-1,j} < T_{i,j+1} \quad \text{and} \quad D < 0\,, \\ T_{i,j+1} + \dfrac{h_2}{F_{i,j}}\,, & \text{if} \quad T_{i-1,j} > T_{i,j+1} \quad \text{and} \quad D < 0\,, \\ \dfrac{-b + \sqrt{D}}{2\,a}\,, & D > 0\,, \\ (2.103)\,, & D = 0 \quad \text{(for the special case } T_{i-1,j} = T_{i,j+1})\,, \end{cases} \tag{2.115}$$

where a and b are referred to (2.110) and (2.111), respectively. It can be noticed that the condition for non-existence of real solutions given in (2.114) actually points out either purely horizontal or vertical movement of the wavefront, see (2.101) and Figure 2.11. It is, furthermore, clear that this procedure can be applied to other quadrants as well as to the case of Figure 2.12(c) in a straightforward way.

To present a solution, we first rewrite (2.88), for the purpose of compact notations, as

$$\sum_{n=1}^{2} \max\left(\frac{T - T_n}{h_n}, 0\right)^2 = \frac{1}{F^2}\,, \tag{2.116}$$

where $T := T_{i,j}$, $F := F_{i,j}$,

$$T_1 = \min\left(T_{i-1,j}, T_{i+1,j}\right)\,, \tag{2.117}$$

and

$$T_2 = \min\left(T_{i,j-1}, T_{i,j+1}\right)\,. \tag{2.118}$$

Then, one can formulate a solution for the whole quadrants by making case distinctions. Although there are the following six cases to handle in total

$$\begin{array}{llllll} \text{(i)} & T > T_1 > T_2\,, & \text{(ii)} & T > T_2 > T_1\,, & \text{(iii)} & T_1 > T > T_2\,, \\ \text{(iv)} & T_2 > T > T_1\,, & \text{(v)} & T_1 > T_2 > T\,, & \text{(vi)} & T_2 > T_1 > T\,, \end{array}$$

one does not need to deal with the cases (v) and (vi) on the grounds that they are physically infeasible as discussed in the 1-D case, see Figure 2.10.

For the case $T > \max(T_1, T_2)$ which represents both (i) and (ii), the larger solution of the quadratic equation

$$\sum_{n=1}^{2} \left(\frac{T - T_n}{h_n}, 0\right)^2 = \frac{1}{F^2} \tag{2.119}$$

is the desired solution. It is given by

$$T = \frac{b_{\text{FM}} + \sqrt{D_{\text{FM}}}}{a_{\text{FM}}}\,, \tag{2.120}$$

where

$$a_{\text{FM}} = \frac{1}{h_1^2} + \frac{1}{h_2^2}\,, \quad b_{\text{FM}} = \frac{T_1}{h_1^2} + \frac{T_2}{h_2^2}\,, \quad c_{\text{FM}} = \frac{T_1^2}{h_1^2} + \frac{T_2^2}{h_2^2} - \frac{1}{F^2}\,, \quad D_{\text{FM}} = b_{\text{FM}}^2 - a_{\text{FM}}\,c_{\text{FM}}\,. \tag{2.121}$$

Besides, the case (iii) $T_1 > T > T_2$ yields the solution

$$T = T_2 + \frac{h_2}{F} \tag{2.122}$$

and the case (iv) $T_2 > T > T_1$ suggests

$$T = T_1 + \frac{h_1}{F}\,. \tag{2.123}$$

One can note that the solutions (2.122) and (2.123) cover purely vertical and horizontal wavefronts, respectively. According similar formulations that are only valid for special cases, i.e. $h_1 = h_2 = 1$ or $h_1 = h_2 = h$, are described in [138, 282] and extended to higher dimensions in [282].

So far we have seen that the upwind scheme by Rouy and Tourin [219] fulfils the causality condition which plays a prime role in the FM algorithm. At this moment, we are in a position to proceed with the algorithm itself.

2.3.3 The Fast Marching Algorithm

The main idea behind the FM algorithm is to provide a specific way of traversing grid points once by classifying them into three classes, i.e. *known*, *trial* and *far*. Since a one-sided upwind-type scheme is employed during the computation, the causal relationship is secured at the same time. The algorithm is composed of mainly two parts: One part is the initialisation of the algorithm and the other part is the marching of the wavefront.

Initialisation

We begin with the initialisation part which is performed in three steps [229]: As a first step, all initial points are labelled as *known* and the value is fixed with $T_{(i,j)} = 0$. The initial points refer to the locations where the information of the arrival time is available. In the aforementioned concrete example, these coincide with the grid points where stations are placed, see the green points in Figure 2.9. The label *known* is flagged as green in Figure 2.14(a) and denoted as set $\mathcal{G}$ in Algorithm 2.1.

In the second step, all neighbours of *known* points are tagged as *trial* unless their states are *known*. The neighbours of a grid point $\boldsymbol{x_0} := (x_{i_0}, y_{j_0})^\top$ are defined as

$$\mathcal{N}(\boldsymbol{x_0}) := \{(x_{i_0-1}, y_{j_0})^\top, (x_{i_0+1}, y_{j_0})^\top, (x_{i_0}, y_{j_0-1})^\top, (x_{i_0}, y_{j_0+1})^\top\}\,. \tag{2.124}$$

The label *trial* is indicated by the blue points in Figure 2.14(a). They are denoted as set $\mathcal{B}$ in Algorithm 2.1.

For the third step, all the remaining nodes are marked as *far* and the value of the *far* nodes is assigned by $T_{i,j} = +\infty$. These correspond to red vertices in Figure 2.14(a) and the set $\mathcal{R}$ in Algorithm 2.1. The Lines 1–10 in Algorithm 2.1 summarise the initialisation part.

From the viewpoint of the value, one may notice that each label of a node has the meaning as follows: Once a point is labelled as *known* or $\mathcal{G}$ in Algorithm 2.1, the value remains unmodified. However, the arrival time of a point tagged as *trial* or $\mathcal{B}$ in Algorithm 2.1 may be modified afterwards. The value of a point marked as *far* or $\mathcal{R}$ in Algorithm 2.1 has not been computed yet.

Marching of the Front Motion

Subsequently, the marching process of the wavefront constitutes the rest of the algorithm, which is realised by the following loop [229]:

(i) Find a point with the smallest value from the *trial* nodes, which is called "E" in Figure 2.14(b).

(ii) Change the label of the point "E" from *trial* to *known*, see Figure 2.14(c).

(iii) Modify the state of all neighbours of "E" into *trial* unless their states are *known*, see Figure 2.14(d).

(iv) Update the arrival time for all *trial* neighbours of "E" by solving (2.86).

(v) Go back to step (i) until the states of all nodes are *known*.

In contrast to the iterative approach by Rouy and Tourin [219], this loop basically provides a guidance how to visit a grid node once and update the arrival time without violating the causality. For this purpose, it is required to have a strategy to plan for the next move of the wavefront depending on the current state of each *trial* node. Since the arrival time in the *trial* class is computed by adjacent *known* points but is not fixed yet, Step (i) offers a criterion, i.e. to select the node with the minimum value, relying upon the Fermat's principle [39, 115]. The principle is sometimes called "principle of least time" which states that a ray of light takes the shortest path between two points and traverses the route in the least time. In this context, the selection process in Step (i) suggests that the wavefront leaving the *known* nodes first arrives at the node with the minimum value in the *trial* class, see Figure 2.14(b). At this moment, the state of the node with the minimum value can be changed from *trial* to *known* and its adjacent nodes belonging to the *far* class are moved to *trial* one, see Figure 2.14(c) and 2.14(d). Afterwards, the arrival time of all *trial* nodes is updated by solving (2.86) and this procedure continues until the state of all nodes

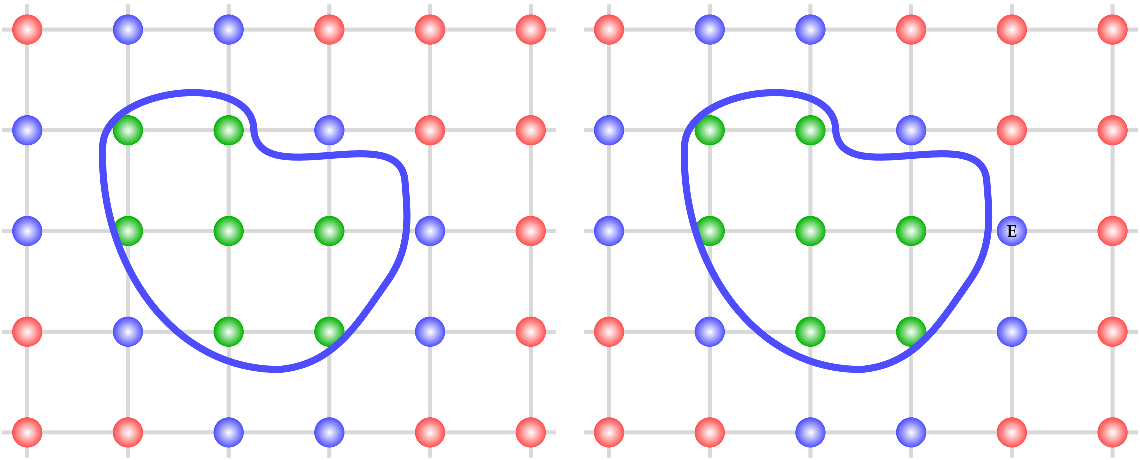

(a) Initialisation. (b) Marching step (i).

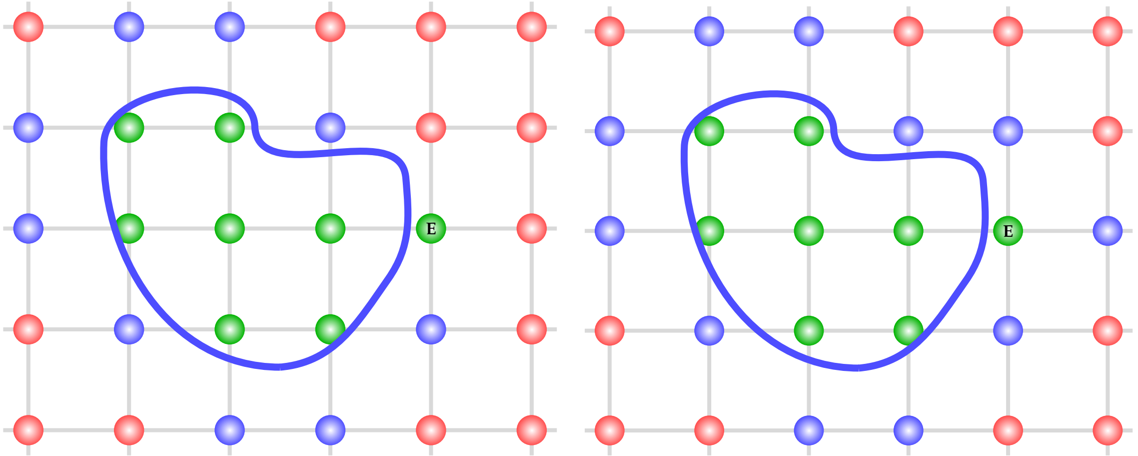

(c) Marching step (ii). (d) Marching step (iii).

Figure 2.14. The fast marching algorithm.

are *known*. The Lines 11–18 in Algorithm 2.1 summarise the marching part in the FM.

Since the upwind type scheme employed in (2.86) guarantees the causality, all updated values including the minimum in the *trial* class are greater than those in the *known* class. This implies that there is no need to revisit a node to ensure the causality. Moreover, when a min-heap data structure [225] is utilised for tracing a node with a minimum value in *trial* class the computational complexity of the algorithm amounts to be $\mathcal{O}(N \log N)$ with N being the number of nodes [229].

Algorithm 2.1. The fast marching algorithm.

```
Input: mesh points $\{x_i\}$, initial points $\{x_0\}$
Output: arrival time map $T : \overline{\Omega}_h \to \mathbb{R}$

/* initialisation */
$\mathcal{G}, \mathcal{B}, \mathcal{R} \longleftarrow \varnothing$
foreach $x_0 \in \overline{\Omega}_h$ do
    $\mathcal{G} \longleftarrow \mathcal{G} \cup \{x_0\}$                      /* $\mathcal{G}$: label known */
    $T(x_0) \longleftarrow 0$
foreach $x_0 \in \overline{\Omega}_h$ do
    if $\mathcal{N}(x_0) \notin \mathcal{G}$ then
        $\mathcal{B} \longleftarrow \mathcal{B} \cup \mathcal{N}(x_0)$             /* $\mathcal{B}$: label trial */
foreach $x_i \in \overline{\Omega}_h \setminus (\mathcal{G} \cup \mathcal{B})$ do
    $\mathcal{R} \longleftarrow \mathcal{R} \cup \{x_i\}$                       /* $\mathcal{R}$: label far */
    $T(x_i) \longleftarrow +\infty$

/* marching */
while $\mathcal{G} \neq \overline{\Omega}_h$ do
    $x_{\min} \longleftarrow \operatorname{argmin}_{x_i \in \mathcal{B}} T(x_i)$
    $\mathcal{B} \longleftarrow \mathcal{B} \setminus \{x_{\min}\}$
    $\mathcal{G} \longleftarrow \mathcal{G} \cup \{x_{\min}\}$
    if $\mathcal{N}(x_{min}) \notin \mathcal{G}$ then
        $\mathcal{B} \longleftarrow \mathcal{B} \cup \mathcal{N}(x_{\min})$
    /* update */
    foreach $x_i \in \mathcal{B}$ do
        $T^{\text{next}}(x_i) \longleftarrow T^{\text{current}}(x_i)$          /* by solving (2.88) */
```

2.4 Summary

In this chapter, we have studied the essential mathematical background for PDE-based approaches to SfS. After we have characterised important properties of HJEs, vanishing viscosity methods and the modern notion of viscosity solutions have been introduced by the example of the eikonal equation to deal with difficulties of HJEs regarding their well-posedness. Furthermore, we have seen the basic ideas behind the FM method including the underlying principles of upwind schemes and the specific grid-visiting algorithm for finding a solution of the eikonal equation in the viscosity sense and for achieving computational efficiency, respectively. In the next chapter, we have a look at PDE-based SfS models.

Chapter 3

PDE-based Shape from Shading Models

In this chapter, we investigate important PDE-based SfS models including Lambertian as well as non-Lambertian ones with respect to mathematical aspects explained in the previous chapter. Since every solution algorithm comes with its own advantages and constraints, it is inevitable in this context to gain insights of models as well as their model-specific attributes in order to apply solution algorithms to these PDE-based models appropriately.

To this end, we first review essential modelling components for modern PDE-based SfS in Section 3.1. These include a perspective camera, Lambertian and non-Lambertian surface models as well as a brightness equation with a light attenuation term. Afterwards in Section 3.2, we derive the perspective Lambertian SfS model of Prados and Faugeras [195] by combining the light attenuation term and the Lambertian reflectance with a perspective camera model. In Section 3.3 and 3.4, we then derive more advanced perspective non-Lambertian SfS models by substituting the Phong and the Oren-Nayar reflectance for the Lambertian model. This leads to the perspective Phong SfS model of Vogel *et al.* [258] and the perspective Oren-Nayar SfS model of Ahmed and Farag [6], respectively. Finally, Section 3.5 closes this chapter with a discussion of the major properties of PDE-based SfS models. Besides the type of Hamiltonian and potential ambiguities, this discussion also includes the important role of critical points.

3.1 Modelling Components

In this section, we look into indispensable modelling elements for SfS problems: a perspective camera model, Lambertian and non-Lambertian surface reflectance functions, and a brightness equation along with a light attenuation factor.

3.1.1 Camera Model

A camera model describes how to map a 3-D point onto a 2-D point on the image plane. Two models are mainly employed for SfS: the perspective and the orthographic projection. In this section, we focus on the pinhole camera model [109] that incorporates the perspective projection. The somewhat simpler orthographic projection that approximates the perspective projection for distant objects is not relevant for this thesis and hence not discussed in detail.

The Pinhole Camera Model

As illustrated in Figure 3.1, the pinhole camera model depicts a perspective projection in such a way that a point $P = (X, Y, Z)^\top$ in 3-D camera coordinates is mapped to its associated projected point $p = (x, y)^\top$ in 2-D image coordinates. The projection $\Pi : P \in \mathbb{R}^3 \mapsto p \in \mathbb{R}^2$ is performed along the straight line that passes through the optical centre C, i.e. $\overline{CP}$. Furthermore, by means of the theorem of intersecting lines, one can derive the following relationship

$$\frac{x}{X} = \frac{y}{Y} = \frac{\mathtt{f}}{Z}\,, \tag{3.1}$$

where the last equality appears because the distance between the principal point c and the optical centre C is $\mathtt{f}$. Then, the perspective projection can be expressed as

$$P := \begin{bmatrix} X \\ Y \\ Z \end{bmatrix} \mapsto p := \begin{bmatrix} x \\ y \end{bmatrix} \overset{(3.1)}{=} \begin{bmatrix} \mathtt{f}\,\dfrac{X}{Z} \\ \mathtt{f}\,\dfrac{Y}{Z} \end{bmatrix} \tag{3.2}$$

Since all the points on the extended line of $\overline{CP}$, which can be understood as the trajectory of the optical ray, are mapped to the same point p on the image plane, this is an example of a *many-to-one* mapping. Moreover, it can be noted that the projected point $p = (x, y)$ has lost the depth information originally contained in P.

Homogeneous Coordinates. Since the relationship expressed in (3.2) is a nonlinear transformation that involves divisions, it is somewhat cumbersome to deal with it. To cope with the situation, we consider *homogeneous coordinates* [213] which allow to work with the perspective geometry in terms of linear mappings.

To this end, by appending the element 1 to a given vector $\boldsymbol{x} \in \mathbb{R}^n$ we take one more coordinate element into account along with a scaling factor $w \neq 0$. Therefore, the transformation from Euclidean to homogeneous coordinates is given by

$$\begin{aligned} &H : \mathbb{R}^n \mapsto \mathbb{R}^{n+1} \\ &\boldsymbol{x} = (x_1, \ldots, x_n)^\top \mapsto \widetilde{\boldsymbol{x}} = w\;(x_1, \ldots, x_n, 1)^\top\;. \end{aligned} \tag{3.3}$$

Since the effect of the one-to-many mapping is already encoded in (3.3) by the scaling factor $w \neq 0$, this mapping forms the basis for the projective geometry, which is

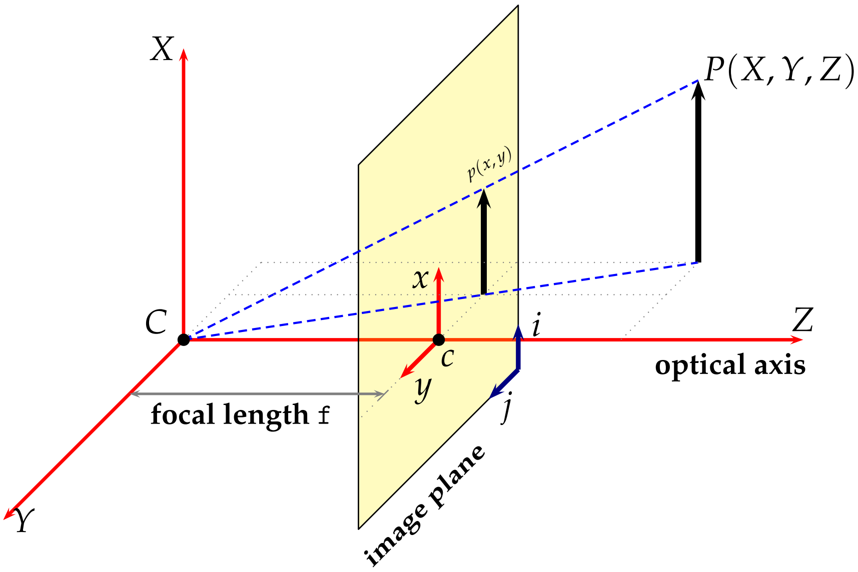

Figure 3.1. The pinhole camera model for perspective projection. C denotes the optical centre of a camera and c the principal point which is the intersection between the image plane and the optical axis. Moreover, $\mathtt{f}$ indicates the focal length of the camera which is the distance between the optical centre and the image plane.

a generalisation of the Euclidean geometry. Moreover, it is obvious that the back transformation can be obtained by the division with the last element

$$\begin{aligned} &H^{-1} : \mathbb{R}^{n+1} \mapsto \mathbb{R}^{n} \\ &\widetilde{\boldsymbol{x}} = (\widetilde{x}_1, \ldots, \widetilde{x}_n, \widetilde{x}_{n+1})^\top \mapsto \boldsymbol{x} = \left(\frac{\widetilde{x}_1}{\widetilde{x}_{n+1}}, \ldots, \frac{\widetilde{x}_n}{\widetilde{x}_{n+1}} \right)^\top . \end{aligned} \tag{3.4}$$

Please note that homogeneous coordinates containing zero as the last element, i.e. $(\widetilde{x}_1, \ldots, \widetilde{x}_n, 0)^\top$, cannot be represented in Euclidean coordinates. They refer to points at infinity.

Let us now consider how to turn the nonlinear mapping (3.2) into a linear one using homogeneous coordinates. To this end, we make use of the projected point p in (3.2) with a scaling factor $w = Z$. Then, by reformulating (3.2) in homogeneous coordinates we obtain

$$\widetilde{P} := \begin{bmatrix} X \\ Y \\ Z \\ 1 \end{bmatrix} \mapsto Z \underbrace{\begin{bmatrix} x \\ y \\ 1 \end{bmatrix}}_{=:\, \widetilde{p}} = \underbrace{\begin{bmatrix} \mathtt{f} & 0 & 0 & 0 \\ 0 & \mathtt{f} & 0 & 0 \\ 0 & 0 & 1 & 0 \end{bmatrix}}_{=:\, M} \underbrace{\begin{bmatrix} X \\ Y \\ Z \\ 1 \end{bmatrix}}_{\widetilde{P}} \quad \Leftrightarrow \quad Z\,\widetilde{p} = M\,\widetilde{P}\,, \tag{3.5}$$

where the matrix $M \in \mathbb{R}^{3\times 4}$ is called the *projection matrix*. Please note that the linear transformation (3.5) between two homogeneous coordinate points $\widetilde{p}$ and $\widetilde{P}$ holds up to a scale factor Z and only when the origin of the image coordinate coincides with that of the principal point. Therefore, we have to take the offset of the principal point into account for a general case.

Camera Calibration Matrix. In order to describe a more general case of the projection, we consider the principal point offset in terms of pixel coordinates. To this end, we assume that the origin of the pixel coordinate system is placed at the lower left corner of the image plane as shown in Figure 3.1 and the involved coordinate axes are orthogonal to each other, which makes the skew factor zero [109]. This yields the relationship

$$i = c_1 + \frac{x}{h_1} \quad \text{and} \quad j = c_2 + \frac{y}{h_2}\,, \tag{3.6}$$

where $(c_1, c_2)^\top$ stands for the position of the principal point in terms of pixel coordinates and h_1 and h_2 denote the pixel size in x- and y-direction, respectively [109]. By means of the homogeneous coordinates, the equation (3.6) can then be rewritten as

$$\begin{bmatrix} i \\ j \\ 1 \end{bmatrix} = \underbrace{\begin{bmatrix} \mathtt{f}/h_1 & 0 & c_1 \\ 0 & \mathtt{f}/h_2 & c_2 \\ 0 & 0 & 1 \end{bmatrix}}_{=:\,K} \frac{1}{\mathtt{f}} \begin{bmatrix} x \\ y \\ \mathtt{f} \end{bmatrix}, \tag{3.7}$$

where K is called the *camera calibration matrix* and it contains the information on intrinsic parameters. It allows to convert the metric 2-D image coordinates $(x, y)^\top$ into the pixel coordinates $(i, j)^\top$.

Once the camera calibration matrix K is known, the models described in image coordinates that we will see in Chapter 5 and 6 can be expressed in terms of pixel coordinates using corresponding coordinate transformations. We provide more details about this matter in Appendix A.

3.1.2 Basics on Radiometry

After we have reviewed the camera model, let us now turn to some basics on radiometry before we go into surface reflectance models. To this end, we begin with the relationship between the image brightness and the surface radiance. According to [118], the image formation process is fundamentally governed by the following relationship

$$E_i = \frac{\pi}{4}\left(\frac{d}{\mathtt{f}}\right)^2 (\cos \nu)^4\, L_s\,, \tag{3.8}$$

where E_i denotes image irradiance, L_s surface radiance, d the diameter of the lens, $\mathfrak{f}$ the focal length, and ν is the angle between the optical axis and the line of sight to a surface point of a corresponding image point.

Besides, we assume that there is a single point light source and no interreflections occur in a scene. Then, the bidirectional reflectance distribution function (BRDF) [122] that depends on the properties of an object surface determines the ratio of the surface radiance L_s to the irradiance of the surface E_s [118, 171, 193]. The radiance L_s refers to the measurement at a point of the surface in the viewing direction **V** with the surface normal **N**, see Figure 3.2. This relationship is given by

$$L_s = F\left(\theta_i, \theta_r, \phi_r\right) E_s \,, \tag{3.9}$$

where L_s denotes the radiance of the surface, F the BRDF, and E_s the irradiance of the surface. Moreover, there are three angles included in the BRDF (3.9): First, θ_i represents the angle between the direction to the light source **L** and the surface normal **N**. Second, θ_r stands for between the viewing direction **V** and the surface normal **N**. Third, ϕ_r is the azimuth angle between **L** and **V**, see Figure 3.2. Then, one can obtain the image irradiance equation in terms of the BRDF by plugging (3.9) into (3.8)

$$E_i = \frac{\pi}{4}\left(\frac{d}{\mathfrak{f}}\right)^2 (\cos\nu)^4\, F\left(\theta_i, \theta_r, \phi_r\right) E_s \,. \tag{3.10}$$

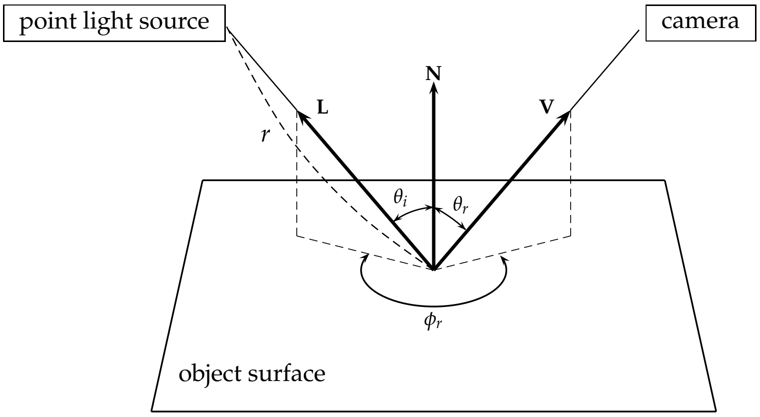

Figure 3.2. Local coordinate system on the object surface, cf. [118, 171, 193]. Here, r denotes the distance between the surface point and the light source.

3.1.3 Surface Reflectance

Based on the radiometry in the previous section, we review some surface reflectance models. The surface reflectance specifies how incoming light energy is reflected when it falls onto the surface. Evidently, it depends heavily on the material properties of the surface. Although there are many different reflection models, one can categorise them into two groups: Lambertian and non-Lambertian reflection models. While the first ones correspond to a pure diffuse reflection model, the latter ones have additional features such as specular effects. In this section, after reviewing the main properties of the Lambertian reflectance, we look into the Phong model and the Oren-Nayar reflectance as representatives for typical non-Lambertian cases.

Lambertian Reflectance

The Lambertian reflectance, which is named after Johann Heinrich Lambert, is designed to capture perfect diffuse reflection [148], i.e. it assumes an ideal matte surface without specular highlights. The main properties of the Lambertian surface are twofold: (i) When incident light falls on a small surface area, the reflected light is scattered in all directions without any preference, see Figure 3.3(a). This property makes an ideal Lambertian surface equally bright from all viewing directions. (ii) This type of surface follows Lambert's cosine law which states that the amount of reflected light intensity is directly proportional to the cosine factor of the angle θ between the surface normal and the incident light, see Figure 3.3(b). As a consequence, when an incident ray comes directly from the direction of the surface normal the reflected light attains maximum intensity, which is the case $\theta = 0$ in Figure 3.3(b).

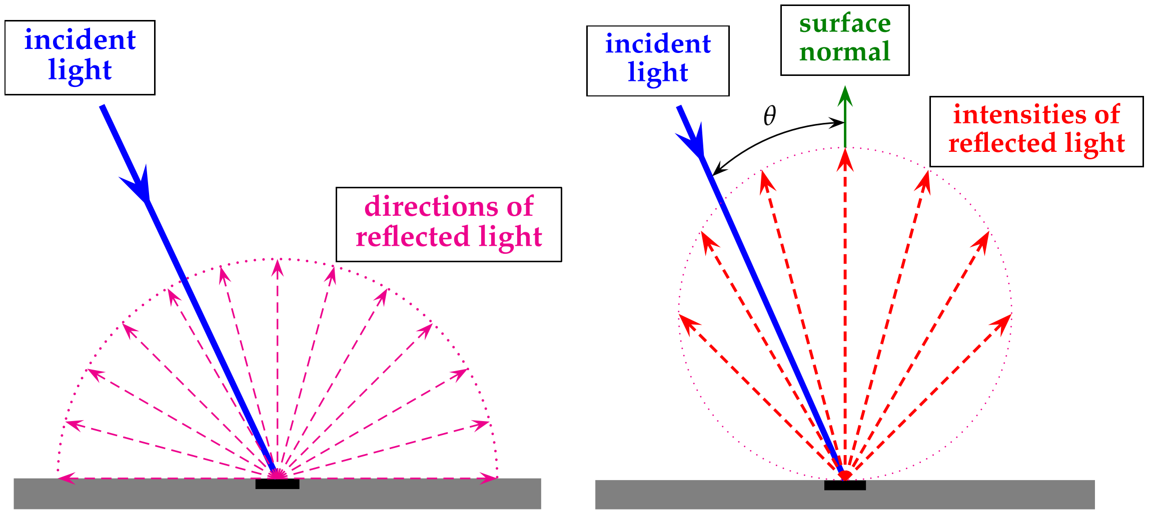

(a) Perfect diffuse reflection.

(b) Lambert's cosine law.

Figure 3.3. Properties of the Lambertian surface.

Let us now consider how to formulate the image irradiance for the Lambertian reflectance model with a distant light source. In terms of the radiometry, the main property of the Lambertian surface is the constant BRDF [118, 193]. According to

[178], it follows

$$L_s = \frac{\rho}{\pi} E_s \,, \tag{3.11}$$

where ρ denotes an albedo that is usually assumed to be uniform for the Lambertian model. This albedo has a dimensionless nature and refers to the ratio between the reflected energy by the surface and the incident light. Based on the Lambert's cosine law, we describe the irradiance E_s of the surface point as

$$E_s = I_0 \, \cos\theta_i \,, \tag{3.12}$$

where I_0 is the intensity of the light source. Then, we formulate the following image irradiance for the Lambertian reflectance model by combining (3.10), (3.11) and (3.12)

$$E_i = \underbrace{\frac{1}{4}\left(\frac{d}{\mathtt{f}}\right)^2 (\cos\nu)^4}_{=:\,\mu} I_0 \, \rho \, \cos\theta_i = \mu \, I_0 \, \rho \, \cos\theta_i \,, \tag{3.13}$$

where μ denotes a constant coefficient related to the parameters of imaging system. Since the cosine factor $\cos\theta_i$ can be encoded by $(\mathbf{N}\cdot\mathbf{L})$ and all the other parameters are assumed to be known, the image irradiance in (3.13) can be reformulated as follows [193]

$$I = \rho \, (\mathbf{N}\cdot\mathbf{L}) \,, \tag{3.14}$$

where $I := E_i/(\mu \, I_0)$ denotes the image irradiance scaled by the known parameters of the imaging system, $\mathbf{N} = \mathbf{n}/|\mathbf{n}|$ the surface normal vector, $\cdot$ the dot product between two vectors, and $\mathbf{L}$ a normalised light direction vector, respectively.

Non-Lambertian Reflectance

Among many non-Lambertian reflectance models, we focus on two particular models in the context of this thesis: the Phong model [189] that includes specular reflections and the Oren-Nayar model [178, 181] that allows to model rough surfaces.

Phong Reflectance. One of the simplest non-Lambertian reflectance model is the Phong model [189] which was applied to SfS by Vogel *et al.* [258]. The main property of a Phong-type surface is that the reflectance is modelled by three components: ambient, diffuse and specular reflections.

The *ambient* component can be understood as background light surrounding an environment of an object, which is ubiquitous in the scene. In practice, it is, therefore, often assumed to be uniform for all pixels [255]. The *diffuse* part comes from Lambertian reflections which have been previously discussed. According to [189], the *specular* reflection term is influenced by the factor $(\cos\varphi)^\alpha$, where φ denotes the angle between the viewing direction and the direction of the perfectly reflected incident light and α stands for the parameter which depends on the material of a surface, see Figure 3.4. The perfectly reflected light refers to the case when the incident angle amounts to be the same as the reflected one, e.g. in a mirror. Furthermore, a large value for α suggests that a surface has mirror-like properties. The intensity of the specular reflection decays fast as the angle of the reflection deviates from that of the perfect reflection.

Then, by putting all three components together, the image irradiance I of a scene is given by [159]

$$I = \underbrace{k_a \, I_a}_{\text{ambient}} + \sum_{l=1}^{n} \left(\underbrace{k_d \, I_l \, \cos{(\theta_i)_l}}_{\text{diffuse}} + \underbrace{k_s \, I_l \, \left(\cos \varphi_l\right)^{\alpha}}_{\text{specular}} \right), \tag{3.15}$$

where n is the number of light sources, $(\theta_i)_l$ the angle between the incident light from the l-th light source and the surface normal, and φ_l the angle between the perfectly reflected light by the l-th light source and the viewing direction. In addition, I_a stands for the intensities of the ambient component of the light sources and I_l denotes the intensities induced by the l-th light source [159], respectively. Besides, the constant coefficients k_a, k_d, and k_s determine the ratio of ambient, diffuse, and specular components, respectively. As indicated by the summation over lights in (3.15), the brightness equation (3.15) for Phong-type surfaces can also be applied to scenes with multiple light sources.

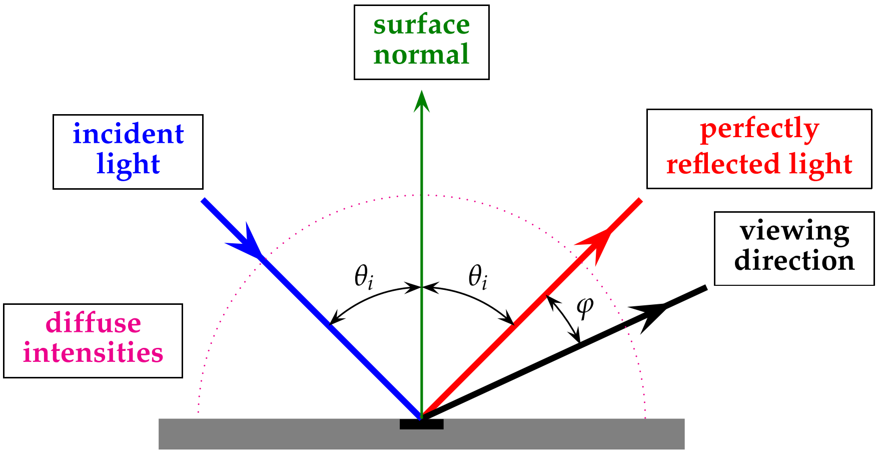

Figure 3.4. Scene geometry for Phong-type surfaces.

Oren-Nayar Reflectance. Let us now summarise the main properties of a second non-Lambertian reflectance model: the Oren-Nayar surface reflectance [178, 181] which is employed in the SfS model by Ahmed and Farag [6].

The Oren-Nayar surface reflectance is primarily designed for rough surfaces in consideration of masking, shadowing and interreflection effects [178, 179, 180, 181]. Similar to the microfacet based model of Torrance and Sparrow [245], this reflectance model assumes that a surface is a collection of long symmetric V-cavities and each V-cavity is composed of two Lambertian facets that are facing each other, see Figure 3.5. While the model of Torrance and Sparrow describes the specular reflection for rough surfaces, the Oren-Nayar model regards its facets as Lambertian. The difference between the Lambertian and the Oren-Nayar reflectance is made in that the viewing direction does have influence on the brightness of the Oren-Nayar surface because of surface roughness [178] although it does not affect the reflected intensities of the Lambertian surface, see Figure 3.3(a) and 3.7. Since a facet based V-cavity plays a significant role in the modelling of surface roughness, we have a closer look at some properties of the facet with respect to a surface geometry.

To this end, an example of a surface patch is illustrated in Figure 3.5. One can observe in this example that three V-cavities and thereby three pairs of symmetric plane facets constitute a surface patch whose area is dA. However, in practice each facet area da is supposed to be very small compared to the area dA of the surface patch, which means $da \ll dA$. Furthermore, each facet area da is assumed to be much larger than the wavelength λ of the incident light. In other words, the following holds:

$$\lambda^2 \ll da \ll dA\,. \tag{3.16}$$

Under this assumption, the principles of geometrical optics can be safely applied.

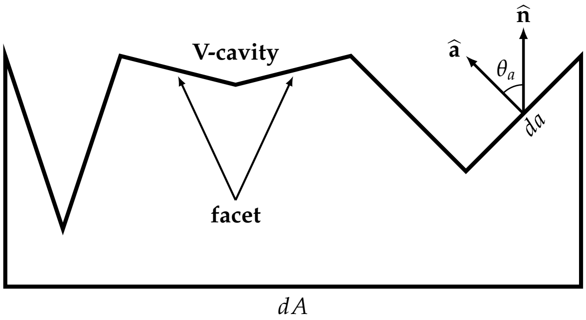

Figure 3.5. Surface model for the Oren-Nayer reflectance. dA denotes the area of a surface patch and da a facet area. The global surface normal which is perpendicular to the bottom plane is described by $\widehat{\mathbf{n}}$, a facet normal is denoted by $\widehat{\mathbf{a}}$, and θ_a stands for the angle between $\widehat{\mathbf{n}}$ and $\widehat{\mathbf{a}}$.

Then, the slope of a facet can be characterised by the angle θ_a between a facet normal $\widehat{\mathbf{a}}$ and the global surface normal $\widehat{\mathbf{n}}$ as can be seen in Figure 3.5. Evidently, a Lambertian surface is attained when all facets are aligned flat, i.e. in case $\theta_a = 0$. In addition, the orientation of the facet in a global setting can be described by an azimuth angle ϕ as in Figure 3.6.

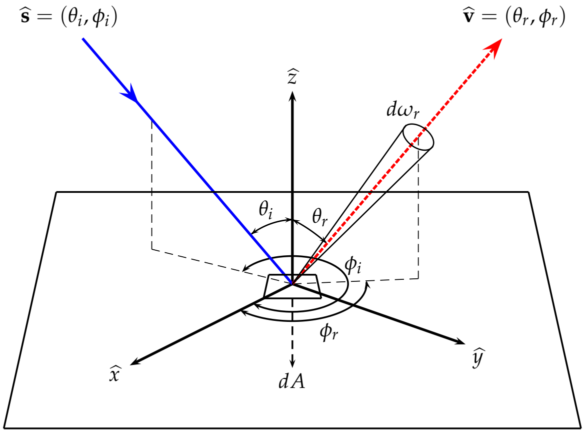

Figure 3.6. Oren-Nayar surface patch. The normalised light source direction is denoted by $\mathbf{L} = (\theta_i, \phi_i)$ depending on a polar angle θ_i and an azimuth angle ϕ_i. In a similar way, the normalised viewer direction $\mathbf{V} = (\theta_r, \phi_r)$ is defined. Besides, $d\omega_r$ stands for the solid angle subtended by a small surface patch in a reflected light direction whose unit is steradian (sr). dA denotes a patch as shown in Figure 3.5.

Since $da \ll dA$, one has to deal with a large number of facets for a surface patch. Following Torrance and Sparrow, this can be modelled with a slope area probability distribution $P(\theta_a, \phi_a)$

$$P(\theta_a, \phi_a) = N(\theta_a, \phi_a)\, da\, \cos\theta_a\,, \tag{3.17}$$

where the distribution $N(\theta_a, \phi_a)$ denotes the number of facets per unit surface area for the facet normal $\widehat{\mathbf{a}} = (\theta_a, \phi_a)$.

When all V-cavities with the same slope θ_a are uniformly distributed in the orientation of ϕ_a, the single parameter θ_a for the facet slope controls the aforementioned distribution (3.17). In this case, the facet distribution can be simplified as $N(\theta_a, \phi_a) = N(\theta_a)$ and the slope area probability distribution can also be reduced to $P(\theta_a, \phi_a) = P(\theta_a)$ with respect to the global surface normal $\widehat{\mathbf{n}}$. This type of surface is called an isotropic rough surface. If the slope area distribution follows a Gaussian with zero mean, the standard deviation σ of the normal distribution parametrises the global roughness of the surface and this is a more general case than the isotropic one [178]. Then, it can be noticed that a Oren-Nayar surface becomes a Lambertian surface when the surface is smooth, i.e. $\sigma = 0$. In this context, the Oren-Nayar case can be understood as a generalisation of the Lambertian case.

We have seen so far the modelling of rough surfaces relying on facet based V-cavities and the characterisation of roughness by the slope area distribution of the surface geometry as well as the relationship to the Lambertian reflectance. Besides these attributes, there is actually another important factor to take into account for computing the radiance of a Oran-Nayar surface as discussed in [178]: the viewing direction.

In order to see the impact of this aspect, we assume that light falls onto one single Lambertian V-cavity, see Figure 3.7(a). There are mainly two possibilities to place a camera sensor in the scene: either on the same side as the light direction, see Figure 3.7(c), or on the opposite side as shown in Figure 3.7(b). Since the light in terms of photons hits the right facet more effectively in Figure 3.7(a), a light detector aligned as in Figure 3.7(c) receives more reflected energy than the one in Figure 3.7(b). This phenomenon can be encoded as a small azimuth angle $(\phi_r - \phi_i)$ in terms of the BRDF geometry given in Figure 3.6.

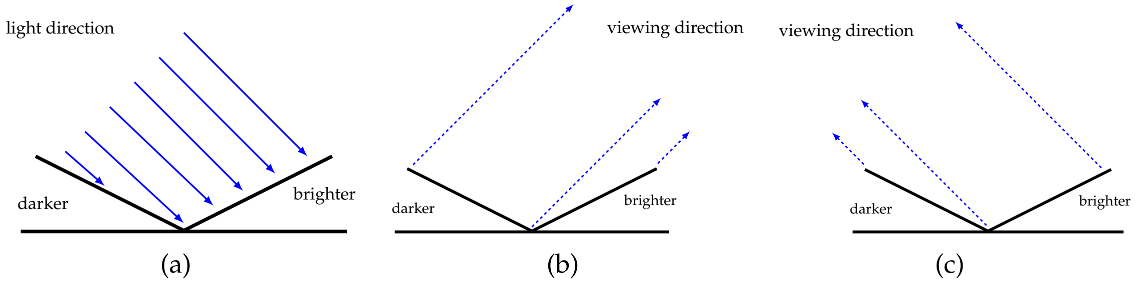

Figure 3.7. Influence of viewing directions on radiance: The radiance of the V-cavity increases when the viewer moves towards the illumination direction (solid lines for the incident light and dashed lines for the reflected light), cf. [170, 178].

Considering shadowing and masking effects with Gaussian slope area distribution, the total radiance of a surface patch can be consequently determined as an aggregate of all radiances contributed by each facet for the Oren-Nayar surface. According to [178], this reads

$$L_s\left(\theta_r, \theta_i, \phi_r - \phi_i, \sigma\right) = \frac{\rho}{\pi} I_0 \cos\theta_i \left(A + B \sin\alpha \tan\beta \max\left[0, \cos\left(\phi_r - \phi_i\right)\right]\right) , \tag{3.18}$$

where L_s denote the reflected radiance and I_0 represents the irradiance when the facet faces towards the direction of the light source, i.e. $\mathbf{L} = \widehat{\mathbf{a}}$. Moreover, A and B stand for two factors that depend on the Gaussian facet statistics that are given by

$$A = 1 - 0.5 \frac{\sigma^2}{\sigma^2 + 0.33} \quad \text{and} \quad B = 0.45 \frac{\sigma^2}{\sigma^2 + 0.09} \geqslant 0 . \tag{3.19}$$

The parameter σ denotes the standard deviation of the Gaussian distribution and it is used as a measure of the surface roughness. In this context, ρ denotes the surface albedo, θ_i represents the angle between the surface normal and light source direction, θ_r stands for the angle between the surface normal and camera direction,

ϕ_{i} is the angle between the light source and the reference direction on the surface, ϕ_{r} denotes the angle between the camera and the reference direction on the surface, and the two variables α and β defined by

$$\alpha = \max(\theta_{\mathrm{i}}, \theta_{\mathrm{r}}) \quad \text{and} \quad \beta = \min(\theta_{\mathrm{i}}, \theta_{\mathrm{r}}) \tag{3.20}$$

stand for the maximum and minimum of the angles θ_{i} and θ_{r}, respectively. An adapted scene geometry of Figure 3.6 with reference to SfS including all above mentioned angles in (3.18) is provided in Figure 3.8.

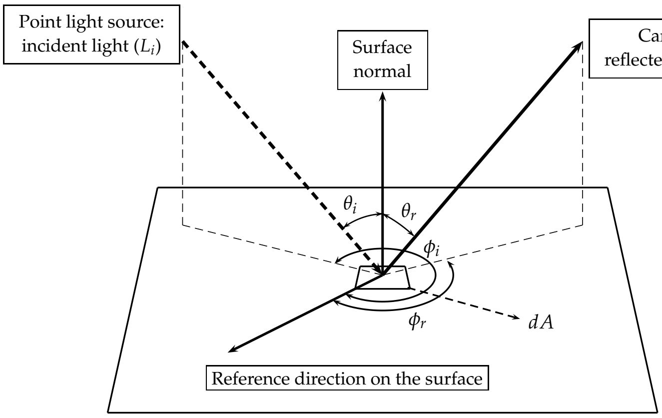

Figure 3.8. Adapted scene geometry of Oren-Nayar reflectance for SfS. dA denotes a patch shown in Figure 3.5.

3.1.4 Brightness Equation with Light Attenuation Term

In modern SfS, a physics-motivating light attenuation term plays an important role from both modelling and theoretical viewpoints [171, 195].

Since the process of taking photographs is nothing more than a physical phenomenon that a camera sensor captures (photon) energy reflected by a surface after it is radiated from the energy source, the process should obey the inverse square law of physics. This suggests that the distance r between the light source and the object surface plays an important role, see Figure 3.2. The basic principle is that when an object is far away from an energy source it receives less energy depending on the distance between the object and the energy source. An illustration is given in Figure 3.9 describing the situation: A point light source is placed at the position P and it emits the energy E outwards evenly. Moreover, S_1 and S_2 are concentric spheres sharing the centre P and their radii are given by r_1 and r_2, respectively. Then, one can observe that surface area enclosing sphere grows quadratically with increasing radius. As a consequence, the energy per constant surface area decreases quadratically with increasing radius. This gives

$$\frac{E}{4\pi r_1^2} > \frac{E}{4\pi r_2^2} \, . \tag{3.21}$$

For SfS, this light attenuation term actually helps to model a camera with a flash in a very dark space such as in endoscopy [171, 195]. Furthermore, it also helps to resolve the convex/concave ambiguity [195], which we will discuss in Section 3.5.3.

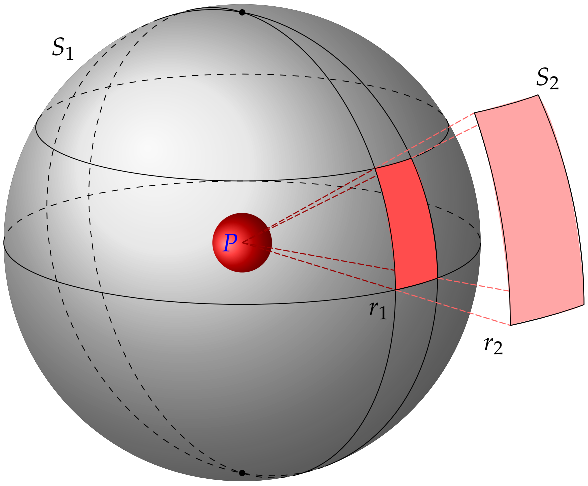

Figure 3.9. Inverse square law: S_1 and S_2 represent concentric spheres that share the centre P. Each radius of the sphere S_1 and S_2 is denoted by r_1 and r_2, respectively. A point light source is positioned at P and radiates energy E per unit time.

As a consequence, for a Lambertian surface with a uniform albedo and light attenuation term one obtains the following brightness equation (image irradiance equation)

$$I = \frac{\rho}{r^2} \left(\mathbf{N} \cdot \mathbf{L} \right) \, , \tag{3.22}$$

where r denotes the distance from the light source to the surface point, ρ the albedo, $\cdot$ the scalar product, $\mathbf{N}$ the surface normal vector, $\mathbf{L}$ the normalised light direction, and $|\cdot|$ the Euclidean norm. Please note that the only difference between (3.14) and (3.22) is the fall-off term $1/r^2$.

3.2 Perspective Lambertian SfS Model

After discussing the image irradiance equation with the light attenuation term, we are in the position to derive the perspective Lambertian PDE-based SfS model of Prados and Faugeras [195]. It is based on the following modelling assumptions [171]:

a point light source is located at the optical centre of a perspective camera and the surface reflectance is Lambertian with a uniform albedo. Furthermore, the light attenuation effect by the inverse square law that we have discussed in Section 3.1.4 is taken into account.

3.2.1 Surface Parametrisation under Perspective Projection

To parametrise a surface, we consider the scene scenario depicted in Figure 3.10. For a point $m = (x, y, -\mathtt{f})^\top$ on the image plane (image coordinate $(x, y)^\top$), the corresponding point on the surface $\mathcal{S}$ is parametrised in terms of multiples $u(\boldsymbol{x})$ of the focal length $\mathtt{f}$ in the direction of m, which yields m'. Since the two vectors m and m' share the same starting point, i.e. the optical centre, the vector m' can be expressed in terms of image coordinate $\boldsymbol{x} = (x, y)^\top$ by the ratio between the focal length $\mathtt{f}$ and the Euclidean distance from the optical centre to the point $m = (x, y, -\mathtt{f})^\top$ on the image plane. One thus obtains the relationship

$$m'(\boldsymbol{x}) = Q(\boldsymbol{x}) \underbrace{\begin{bmatrix} x \\ y \\ -\mathtt{f} \end{bmatrix}}_{=m(\boldsymbol{x})}, \tag{3.23}$$

where $Q(\boldsymbol{x})$ denotes a spatially varying factor which is given by

$$Q(\boldsymbol{x}) = \frac{\mathtt{f}}{\sqrt{|\boldsymbol{x}|^2 + \mathtt{f}^2}}. \tag{3.24}$$

As a consequence, the unknown surface $\mathcal{S} : \Omega_{\boldsymbol{x}} \to \mathbb{R}^3$, which is parameterised in terms of the radial depth u, can be described as

$$\mathcal{S}(\boldsymbol{x}, u(\boldsymbol{x})) = \left\{ Q(\boldsymbol{x})\, u(\boldsymbol{x}) \begin{bmatrix} x \\ y \\ -\mathtt{f} \end{bmatrix} \,\middle\|\, \boldsymbol{x} := (x, y)^\top \in \overline{\Omega}_{\boldsymbol{x}} \right\}, \tag{3.25}$$

where $\boldsymbol{x} = (x, y)^\top \in \Omega_{\boldsymbol{x}}$ is the position of the rectangular image domain $\Omega_{\boldsymbol{x}} \subset \mathbb{R}^2$ and $\mathtt{f}$ denotes the focal length of the camera.

3.2.2 Brightness Equation with Lambertian Reflectance

In order to express the brightness equation (3.22) under this radial surface parametrisation, we have to compute each component of the brightness equation based on the surface parametrisation (3.25).

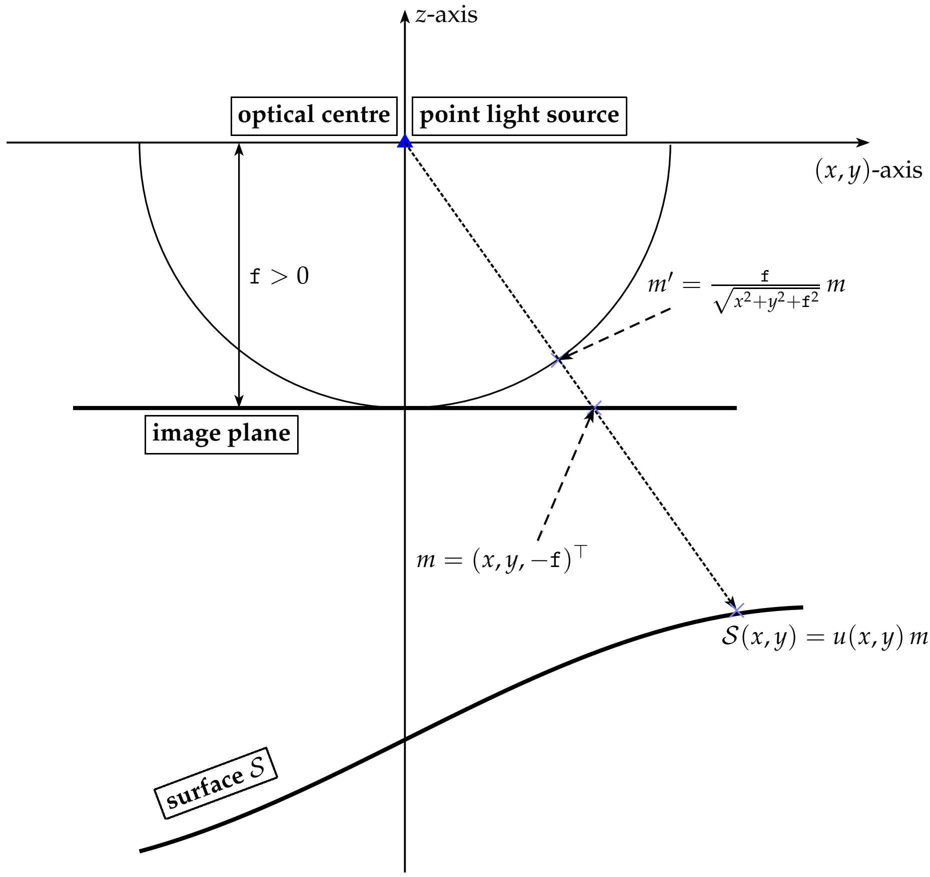

Figure 3.10. An illustration of 2-D cross-section of a 3-D scene for a surface parametrisation of the model by Prados *et al.* [195].

Surface Normal

Since the direction of the surface normal vector is perpendicular to the tangent plane of the corresponding surface point as shown in Figure 3.11, one can derive it from the surface parametrisation (3.25) by making use of vector calculus.

First, we take partial derivatives of (3.25) in x- and y-direction with respect to the image coordinates. This yields

$$\mathcal{S}_x = \begin{bmatrix} (u + x\, u_x) - \dfrac{Q^2\, x^2\, u}{\mathtt{f}^2} \\ y\, u_x - \dfrac{Q^2\, u\, y\, x}{\mathtt{f}^2} \\ -\mathtt{f}\, u_x + \dfrac{Q^2\, u\, x}{\mathtt{f}} \end{bmatrix}, \quad \mathcal{S}_y = \begin{bmatrix} u_y\, x - \dfrac{Q^2\, u\, y\, x}{\mathtt{f}^2} \\ (u_y\, y + u) - \dfrac{Q^2\, y^2\, u}{\mathtt{f}^2} \\ -\mathtt{f}\, u_y + \dfrac{Q^2\, u\, y}{\mathtt{f}} \end{bmatrix}. \tag{3.26}$$

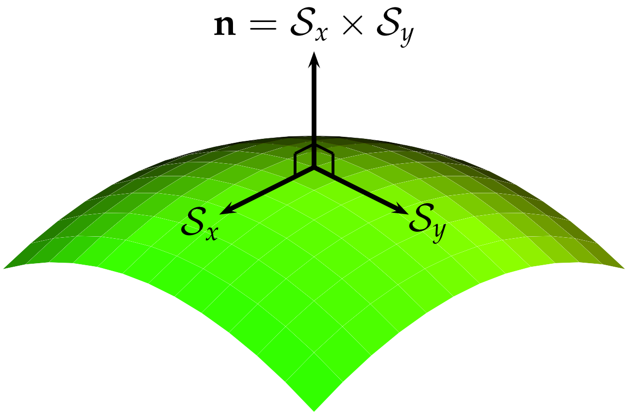

Figure 3.11. Illustration of a surface normal. $\mathcal{S}_x$ and $\mathcal{S}_y$ represent partial derivatives of the surface S in x- and y-direction, respectively. The vector $\mathbf{n}$ denotes surface normal which is orthogonal to the tangent plane spanned by $\mathcal{S}_x$ and $\mathcal{S}_y$. The normal direction is determined by the right-hand rule.

By taking the cross product of the two vectors in (3.26) we can obtain the direction of surface normal vector $\mathbf{n}(\boldsymbol{x})$ as

$$\mathbf{n}(\boldsymbol{x}) = \mathcal{S}_x \times \mathcal{S}_y = \begin{bmatrix} \mathtt{f}\, u_x \\ \mathtt{f}\, u_y \\ x\, u_x + y\, u_y \end{bmatrix} - \frac{Q^2}{\mathtt{f}} \begin{bmatrix} x\, u \\ y\, u \\ -\mathtt{f}\, u \end{bmatrix} \tag{3.27}$$

and its Euclidean norm

$$|\mathbf{n}(\boldsymbol{x})| = \sqrt{\mathtt{f}^2 \, |\nabla u(\boldsymbol{x})|^2 + (\nabla u(\boldsymbol{x}) \cdot \boldsymbol{x})^2 + u(\boldsymbol{x})^2 \, Q(\boldsymbol{x})^2}\,. \tag{3.28}$$

The corresponding surface normal vector is then given by $\mathbf{N} = \mathbf{n}(\boldsymbol{x}) \,/\, |\mathbf{n}(\boldsymbol{x})|$.

Light Direction

Since the light source is positioned at the optical centre of the camera as in Figure 3.10, the normalised light direction $\mathbf{L}$ can be expressed as

$$\mathbf{L}(\boldsymbol{x}) = \frac{Q}{\mathtt{f}} \begin{bmatrix} -x \\ -y \\ \mathtt{f} \end{bmatrix}. \tag{3.29}$$

Computation of $\mathbf{N} \cdot \mathbf{L}$

Since the surface normal vector and the light direction vector are available in (3.27) and (3.29), respectively, the computation $\mathbf{N} \cdot \mathbf{L}$ in (3.22) can be carried out in the following way

$$\begin{aligned}\mathbf{N}\cdot\mathbf{L} &\overset{(3.29)}{=} \frac{\mathbf{n}(x)}{|\mathbf{n}(x)|}\cdot\frac{Q}{\mathrm{f}}\begin{bmatrix}-x\\-y\\\mathrm{f}\end{bmatrix} \overset{(3.27)}{=} \frac{Q}{|\mathbf{n}(x)|\,\mathrm{f}}\left(\begin{bmatrix}\mathrm{f}\,u_x\\\mathrm{f}\,u_y\\x\,u_x+y\,u_y\end{bmatrix}-\frac{Q^2}{\mathrm{f}}\begin{bmatrix}x\,u\\y\,u\\-\mathrm{f}\,u\end{bmatrix}\right)\cdot\begin{bmatrix}-x\\-y\\\mathrm{f}\end{bmatrix}\\ &= \frac{Q}{|\mathbf{n}(x)|\,\mathrm{f}}\,\frac{Q^2\,u}{\mathrm{f}}\left(\underbrace{x^2+y^2}_{=|x|^2}+\mathrm{f}^2\right) = \frac{Q\,u}{|\mathbf{n}(x)|}\,. \end{aligned} \tag{3.30}$$

PDE Formulation of the Brightness Equation

In order to attain the brightness equation with the light attenuation term in (3.22), the distance r between the light source and a surface point is required. By means of the surface parametrisation (3.25), this distance r is given by

$$r = \mathrm{f}\,u\,. \tag{3.31}$$

Since all necessary elements in (3.22) are available at this moment and the albedo ρ in (3.22) is furthermore assumed to be uniform ($\rho = 1$), plugging the result (3.30) with (3.28) as well as (3.31) into (3.22) yields

$$\begin{aligned} I(x) &= \frac{1}{\mathrm{f}^2\,u(x)^2}\frac{Q(x)\;u(x)}{|\mathbf{n}(x)|} = \frac{1}{\mathrm{f}^2\,u(x)^2}\frac{Q(x)\,u(x)}{\sqrt{\mathrm{f}^2|\nabla u(x)|^2+(x\cdot\nabla u(x))^2+Q(x)^2\,u(x)^2}}\\ &= \frac{1}{\mathrm{f}^2\,u(x)^2}\frac{Q(x)}{\sqrt{\mathrm{f}^2\left|\frac{\nabla u(x)}{u(x)}\right|^2+\left(x\cdot\frac{\nabla u(x)}{u(x)}\right)^2+Q(x)^2}}\,. \end{aligned} \tag{3.32}$$

3.2.3 Hamiltonian for the Perspective Lambertian SfS

Moreover, the surface $\mathcal{S}$ is always assumed to be in front of the camera according to [193]. This makes u in (3.32) strictly positive. By using the following change of variables

$$v := \ln u \quad\Rightarrow\quad \nabla v = \frac{\nabla u}{u} \quad\Leftrightarrow\quad \nabla u = u\,\nabla v\,, \tag{3.33}$$

the brightness equation (3.32) then becomes

$$I(x) = \frac{1}{\mathrm{f}^2\,u(x)^2}\frac{Q(x)}{\sqrt{\mathrm{f}^2\,|\nabla v(x)|^2+(x\cdot\nabla v(x))^2+Q(x)^2}}\,. \tag{3.34}$$

Since

$$v := \ln u \quad \Leftrightarrow \quad e^{v} = u \quad \Leftrightarrow \quad e^{-2\,v} = u^{-2}\,, \tag{3.35}$$

one can finally obtain the following perspective Lambertian SfS model [195]

$$H_{\text{PF}}\,(\boldsymbol{x}, v(\boldsymbol{x}), \nabla v(\boldsymbol{x})) = 0\,, \tag{3.36}$$

with

$$H_{\text{PF}}\,(\boldsymbol{x}, v(\boldsymbol{x}), \nabla v(\boldsymbol{x})) := \frac{I(\boldsymbol{x})\,\mathrm{f}^2}{Q(\boldsymbol{x})}\sqrt{\mathrm{f}^2|\nabla v(\boldsymbol{x})|^2 + (\boldsymbol{x}\cdot\nabla v(\boldsymbol{x}))^2 + Q(\boldsymbol{x})^2} - e^{-2\,v(\boldsymbol{x})}\,. \tag{3.37}$$

The main properties of this model can be summarised as: (i) The PDE (3.36) is a general-type HJE based on (2.24). (ii) To solve the equation (3.36), boundary values must be provided. (iii) The solution to the HJE (3.36) should be understood in the viscosity sense [63] that we have seen in Section 2.2.3. (iv) Partial well-posedness can also be achieved in the viscosity framework [44, 67, 195]. (v) In order to solve the perspective Lambertian SfS model (3.36), proper discretisation methods such as the upwind scheme [219] must be considered that respect the hyperbolic nature of the HJEs. We discuss more details of the properties of this model in Section 3.5.

3.3 Perspective Phong SfS Model

In this section, we derive the perspective Phong SfS model according to Vogel *et al.* [258]. For most modern perspective non-Lambertian SfS models, e.g. [6, 7, 258], model assumptions for scene geometries are borrowed from the Lambertian case [195] and only the surface reflectance function is replaced with a non-Lambertian one. Therefore, the surface normal (3.27) and the light direction (3.29) that we have derived in Section 3.2 remain unchanged.

3.3.1 Brightness Equation with Phong Reflectance

To obtain the brightness equation for the perspective Phong SfS model of Vogel *et al.* [258], we employ the Phong reflectance [189] for the brightness equation with a light attenuation term. Under this condition, the brightness equation without the fall-off term (3.15), becomes

$$I = \underbrace{k_a\, I_a}_{\text{ambient}} + \sum_{l=1}^{n} \frac{1}{r_l^2}\left(\underbrace{k_d\, I_l \cos\left(\theta_i\right)_l}_{\text{diffuse}} + \underbrace{k_s\, I_l \left(\cos\varphi_l\right)^{\alpha}}_{\text{specular}}\right). \tag{3.38}$$

Since the model [258] deals with the case of a single point light source, (3.38) can be further reduced to

$$I = \kappa_a \, I_a + \frac{1}{r^2} \left(k_d \, I_0 \cos \theta_i + \kappa_s \, I_0 \left(\cos \varphi \right)^{\alpha} \right) . \tag{3.39}$$

In addition, when the point light source lies at the optical centre of the camera, we can observe in Figure 3.4 that the incident light direction coincides with the viewing direction. Then, we can obtain the relationship

$$\varphi = 2\theta_i \, . \tag{3.40}$$

This allows us to rewrite the brightness equation (3.39) with only one angle θ_i as

$$I = k_a \, I_a + \frac{1}{r^2} \left(k_d \, I_0 \cos \theta_i + k_s \, I_0 \left(\cos 2\theta_i \right)^{\alpha} \right) . \tag{3.41}$$

Since $\cos \theta$ in (3.41) can be reformulated as the scalar product between the unit surface normal vector and the normalised light direction vector, one can have

$$\cos \theta_i = \mathbf{N} \cdot \mathbf{L} \, , \tag{3.42}$$

where $\mathbf{N} = \frac{\mathbf{n}(x)}{|\mathbf{n}(x)|}$ with $\mathbf{n}$ being computed as in (3.27) and $\mathbf{L}$ is the normalised light direction vector given in (3.29). Furthermore, by relying on the trigonometric identity

$$\cos 2\theta_i = 2 \left(\cos \theta_i \right)^2 - 1 \tag{3.43}$$

with (3.42) one can attain the brightness equation for the Phong-type surfaces as

$$I = k_a \, I_a + \frac{1}{r^2} \left(k_d \, I_0 \left(\mathbf{N} \cdot \mathbf{L} \right) + k_s \, I_0 \left(2 \left(\mathbf{N} \cdot \mathbf{L} \right)^2 - 1 \right)^{\alpha} \right) , \tag{3.44}$$

which is an equivalent form of (3.41). Then, plugging corresponding expressions into this brightness equation yields

$$I(x) = k_a \, I_a + \frac{1}{\mathfrak{f}^2 u(x)^2} \left(k_d \, I_0 \frac{u(x) \, Q(x)}{|\mathbf{n}(x)|} + k_s \, I_0 \left(2 \left(\frac{u(x) \, Q(x)}{|\mathbf{n}(x)|} \right)^2 - 1 \right)^{\alpha} \right) , \tag{3.45}$$

where $|\mathbf{n}(x)|$ and $Q(x)$ are defined as previously in (3.28) and (3.24), respectively.

3.3.2 Hamiltonian for the Perspective Phong SfS

In order to obtain a more compact formulation, one may apply the technique of change of variables. To this end, we first multiply $\frac{\mathfrak{f}^2 |\mathbf{n}(x)|}{u(x) Q(x)}$ on both sides of (3.45) and move the terms on the right hand side to the left one. This gives

$$(I\,(x) - k_a\, I_a)\,\frac{\mathrm{f}^2\,|\mathbf{n}\,(x)|}{Q\,(x)\,u\,(x)} - \frac{k_d\, I_0}{u\,(x)^2} - \frac{|\mathbf{n}\,(x)|\, k_s\, I_0}{u(x)^3 Q(x)}\left(\frac{2u(x)^2 Q(x)^2}{|n(x)|^2} - 1\right)^{\alpha} = 0\,. \quad (3.46)$$

Since the surface $\mathcal{S}$ is also assumed to be in front of the camera for the model (3.46), u in (3.46) is strictly positive. We then apply the change of variables (3.33) to (3.28), which yields

$$\begin{aligned} |\mathbf{n}\,(x)| &= \sqrt{\mathrm{f}^2\,|u\,(x)\,\nabla v\,(x)|^2 + (u\,(x)\,\nabla v\,(x)\cdot x)^2 + u\,(x)^2\,Q\,(x)^2} \\ \Leftrightarrow\ \frac{|\mathbf{n}\,(x)|}{u\,(x)} &= \sqrt{\mathrm{f}^2\,|\nabla v\,(x)|^2 + (\nabla v\,(x)\cdot x)^2 + Q\,(x)^2} =: W\,(x)\ . \end{aligned} \quad (3.47)$$

By replacing corresponding parts in (3.46) with (3.47) and (3.35) we can, finally, attain the perspective SfS Phong model [258]

$$H_{\text{VBW}}(x, v(x), \nabla v(x)) = 0 \quad (3.48)$$

with

$$\begin{aligned} &H_{\text{VBW}}(x, v(x), \nabla v(x)) := \\ &\quad J(x)\,W\,(x) - k_d\,I_0\,e^{-2\,v(x)} - k_s\,I_0\,e^{-2\,v(x)}\frac{W\,(x)}{Q\,(x)}\left(\frac{2\,Q\,(x)^2}{W\,(x)^2} - 1\right)^{\alpha}\ , \end{aligned} \quad (3.49)$$

where

$$J(x) = (I\,(x) - k_a\,I_a)\,\frac{\mathrm{f}^2}{Q\,(x)}\,. \quad (3.50)$$

In the light of (2.24), it can be noted that the Hamiltonian $H_{\text{VBW}}(x, v(x), \nabla v(x))$ in (3.48) is of general-type as well. Furthermore, in the perspective Phong-type SfS [258] the cosine value in the specular term is usually substituted by zero when

$$\cos\theta = \frac{2\,Q(x)^2}{W(x)^2} - 1 < 0\,. \quad (3.51)$$

3.4 Perspective Oren-Nayar SfS Model

For the perspective Oren-Nayar SfS model of Ahmed and Farag [6], we proceed as performed in the case of Phong reflectance. We replace the Phong reflectance with the Oren-Nayar surface [178, 179]. Again, the assumptions on the scene geometry remain unchanged: A single point light source is placed at the centre of the camera.

3.4.1 Brightness Equation with Oren-Nayar Reflectance

By taking the light attenuation factor $1/r^2$ into account based on the inverse square law, the brightness equation (3.18) for Oren-Nayar surface is turned into

$$\begin{aligned} &L_s\left(\theta_r, \theta_i, \phi_r - \phi_i, \sigma\right) = \\ &\quad \frac{1}{r^2}\frac{\rho}{\pi}\, I_0\, \cos\theta_i \left(A + B\, \sin\alpha\, \tan\beta \max\left[0, \cos\left(\phi_r - \phi_i\right)\right]\right), \end{aligned} \tag{3.52}$$

where ρ denotes a uniform albedo as in (3.14). Furthermore, the two facet statistics A and B and the two angle variables α and β in (3.52) are defined as in (3.19) and (3.20), respectively.

By exploiting the assumptions on the scene geometry, one obtains the following relationship [6] from the scene geometry in Figure 3.6

$$\theta_r = \theta_i = \alpha = \beta := \theta \qquad \text{and} \qquad \phi_r - \phi_i = 0\,, \tag{3.53}$$

which suggests that the viewing direction for the camera is aligned with the direction of the light. Then, substituting (3.53) for θ_i, α, β and $\phi_r - \phi_i$ in (3.52) yields

$$L_s\left(\theta, \sigma\right) = \underbrace{\left(\frac{\rho}{\pi}\, I_0\right)}_{=:\,\eta} \frac{A\cos\theta + B\sin^2\theta}{r^2}\,, \tag{3.54}$$

where η is a constant depending on the light intensity, surface albedo as well as other parameters related to a camera as indicated in [6]. As a last step, by replacing L_s/η with I in (3.54) one can obtain the image irradiance equation for the Oren-Nayar SfS in [6]

$$I \overset{(3.54)}{:=} \frac{L_s}{\eta} = \frac{A\cos\theta + B\sin^2\theta}{r^2}\,, \tag{3.55}$$

where A and B are defined as in (3.19).

3.4.2 Hamiltonian for the Perspective Oren-Nayar SfS

As we have previously derived the HJE (3.48) for the perspective Phong SfS model [258], we turn the brightness equation (3.55) into a PDE by exploiting the computation result in (3.30) and the relationship (3.42) based on (3.53).

To this end, we first reformulate the Oren-Nayar brightness equation (3.55) with trigonometric identities and substitute $(\mathbf{N} \cdot \mathbf{L})$ for $\cos\theta$ in (3.55), which gives

$$\begin{aligned} I &= \frac{1}{r^2}\left(A\cos\theta + B\sin^2\theta\right) = \frac{1}{r^2}\left[A\cos\theta + B\left(1-\cos^2\theta\right)\right] \\ &\overset{(3.42)}{=} \frac{1}{r^2}\left[A\left(\mathbf{N}\cdot\mathbf{L}\right) + B\left(1-\left(\mathbf{N}\cdot\mathbf{L}\right)^2\right)\right] . \end{aligned} \tag{3.56}$$

Then, replacing $(\mathbf{N} \cdot \mathbf{L})$ in (3.56) with (3.30) yields

$$I(x) \overset{(3.30)}{=} \frac{1}{r^2}\left[A\left(\frac{Q(x)\;u(x)}{|\mathbf{n}(x)|}\right) + B\left(1-\left(\frac{Q(x)\;u(x)}{|\mathbf{n}(x)|}\right)^2\right)\right] . \tag{3.57}$$

Before we further develop the expression (3.57), we take care of necessary computations beforehand. For the first part in (3.57), with the result of (3.28) one can derive that

$$\frac{Q(x)\;u(x)}{|\mathbf{n}(x)|} \overset{(3.28)}{=} \frac{Q(x)\;u(x)}{\sqrt{\mathrm{f}^2\,|\nabla u(x)|^2 + (\nabla u(x)\cdot x)^2 + u(x)^2\,Q(x)^2}} . \tag{3.58}$$

By dividing the right hand side of (3.58) with $Q(x)$, we obtain

$$\frac{Q(x)\;u(x)}{|\mathbf{n}(x)|} = \frac{u(x)}{\sqrt{\left[\mathrm{f}^2\,|\nabla u(x)|^2 + (\nabla u(x)\cdot x)^2\right]\,Q^{-2}(x) + u(x)^2}} . \tag{3.59}$$

Then, the result (3.59) can be more compactly formulated as

$$\frac{Q(x)\;u(x)}{|\mathbf{n}(x)|\sqrt{|x|^2+\mathrm{f}^2}} = \frac{u(x)}{\sqrt{P(x,\nabla u(x)) + u(x)^2}} \tag{3.60}$$

with

$$P(x,\nabla u(x)) := \left[\mathrm{f}^2\,|\nabla u(x)|^2 + (\nabla u(x)\cdot x)^2\right]\,Q^{-2}(x) . \tag{3.61}$$

For the second part in (3.57), one can derive the following with simple algebraic manipulations

$$\begin{aligned} 1-\left(\frac{Q(x)\;u(x)}{|\mathbf{n}(x)|}\right)^2 &\overset{(3.60)}{=} 1-\left(\frac{u(x)}{\sqrt{P(x,\nabla u(x)) + u(x)^2}}\right)^2 \\ &= \frac{P(x,\nabla u(x)) + u(x)^2 - u(x)^2}{P(x,\nabla u(x)) + u(x)^2} = \frac{P(x,\nabla u(x))}{P(x,\nabla u(x)) + u(x)^2} . \end{aligned} \tag{3.62}$$

Plugging (3.31), (3.60), and (3.62) into (3.57) yields

$$\begin{aligned} I(x) &= \frac{1}{\mathrm{f}^2\, u(x)^2} \left(A \frac{u(x)}{\sqrt{P(x, \nabla u(x)) + u(x)^2}} + B \frac{P(x, \nabla u(x))}{P(x, \nabla u(x)) + u(x)^2} \right) \\ &= \frac{1}{\mathrm{f}^2\, u(x)^2} \left(A \frac{u(x) \sqrt{P(x, \nabla u(x)) + u(x)^2}}{P(x, \nabla u(x)) + u(x)^2} + B \frac{P(x, \nabla u(x))}{P(x, \nabla u(x)) + u(x)^2} \right) . \end{aligned} \tag{3.63}$$

By rearranging (3.63) one can finally attain the HJE for the perspective Oren-Nayar SfS [6]

$$H_{\mathrm{AF}}(x, u(x), \nabla u(x)) = 0 \,, \tag{3.64}$$

where

$$\begin{aligned} H_{\mathrm{AF}}(x, u(x), \nabla u(x)) := {} & \mathrm{f}^2\, u(x)^2\, I(x) \left(P(x, \nabla u(x)) + u(x)^2 \right) \\ & - A\, u(x) \sqrt{P(x, \nabla u(x)) + u(x)^2} - B\, P(x, \nabla u(x)) \end{aligned} \tag{3.65}$$

with the same facet statistics being defined in (3.19). One can note that the Hamiltonian H_{AF} in (3.64) is of general-type (3.64) according to (2.24).

As for the case of Phong SfS, we apply the variable transformations in (3.33) to (3.61) in order to obtain a more compact formulation by supposing that $\mathcal{S}$ is placed in front of the camera. Then, we have

$$\begin{aligned} P(x, \nabla u(x)) &= \left[\mathrm{f}^2 \left| \nabla u(x) \right|^2 + \left(\nabla u(x) \cdot x \right)^2 \right] Q^{-2}(x) \\ &\overset{(3.33)}{=} \left[\mathrm{f}^2 \left| u(x) \nabla v(x) \right|^2 + \left(u(x) \nabla v(x) \cdot x \right)^2 \right] Q^{-2}(x) \,. \end{aligned} \tag{3.66}$$

Since we have assumed $u > 0$, (3.66) can be rewritten as

$$\frac{P(x, \nabla u(x))}{u(x)^2} = \left[\mathrm{f}^2 \left| \nabla v(x) \right|^2 + \left(\nabla v(x) \cdot x \right)^2 \right] Q^{-2}(x) =: M(x, \nabla v(x)) \,. \tag{3.67}$$

At this point, we can reformulate the HJE (3.64) in a way that we exploit the result of (3.67)

$$\begin{aligned} & \mathrm{f}^2\, u^2\, I(x) \left(P(x, \nabla u) + u^2 \right) - A\, u \sqrt{P(x, \nabla u) + u^2} - B\, P(x, \nabla u) = 0 \\ \Leftrightarrow {} & \mathrm{f}^2\, u^2\, I(x)\, u^2 \left(\frac{P(x, \nabla u)}{u^2} + 1 \right) - A\, u^2 \sqrt{\frac{P(x, \nabla u)}{u^2} + 1} - B\, \frac{P(x, \nabla u)}{u^2} u^2 = 0 \,. \end{aligned} \tag{3.68}$$

By means of the result in (3.67), this becomes

$$
\begin{aligned}
(3.68) \overset{(3.67)}{\underset{u^2>0}{\iff}}\; & \mathfrak{f}^2\, u^2\, I(\boldsymbol{x})\,(M(\boldsymbol{x},\nabla v)+1) - A\,\sqrt{M(\boldsymbol{x},\nabla v)+1} - B\,M(\boldsymbol{x},\nabla v) = 0 \\
\overset{(3.35)}{\iff}\; & \mathfrak{f}^2\, e^{2\,v}\, I(\boldsymbol{x})\,(M(\boldsymbol{x},\nabla v)+1) - A\,\sqrt{M(\boldsymbol{x},\nabla v)+1} - B\,M(\boldsymbol{x},\nabla v) = 0 \\
\iff\; & \mathfrak{f}^2\, e^{2\,v}\, I(\boldsymbol{x})\,(M(\boldsymbol{x},\nabla v)+1) - \Big(A\,\sqrt{M(\boldsymbol{x},\nabla v)+1} + B\,M(\boldsymbol{x},\nabla v)\Big) = 0 \\
\iff\; & \mathfrak{f}^2\, e^{2\,v}\, I(\boldsymbol{x})\,\frac{M(\boldsymbol{x},\nabla v)+1}{A\,\sqrt{M(\boldsymbol{x},\nabla v)+1} + B\,M(\boldsymbol{x},\nabla v)} - 1 = 0 \qquad (3.69)
\end{aligned}
$$

Then, one attains the perspective Oren-Nayar SfS model [6]

$$
H_{\mathrm{AF}}(\boldsymbol{x}, v(\boldsymbol{x}), \nabla v(\boldsymbol{x})) = 0 \tag{3.70}
$$

with

$$
\begin{aligned}
& H_{\mathrm{AF}}(\boldsymbol{x}, v(\boldsymbol{x}), \nabla v(\boldsymbol{x})) := \\
& \qquad \mathfrak{f}^2\, I(\boldsymbol{x})\,\frac{M(\boldsymbol{x},\nabla v(\boldsymbol{x}))+1}{A\,\sqrt{M(\boldsymbol{x},\nabla v(\boldsymbol{x}))+1} + B\,M(\boldsymbol{x},\nabla v(\boldsymbol{x}))} - e^{-2\,v(\boldsymbol{x})}\,.
\end{aligned} \tag{3.71}
$$

We have, so far, derived the perspective Lambertian SfS model by Prados and Faugeras [195] and the perspective non-Lambertian models associated with the Oren-Nayar and the Phong reflectance by Ahmed and Farag [6] and Vogel *et al.* [258], respectively.

3.5 Properties of PDE-based SfS Models

In this section, we discuss important properties of the previously introduced PDE-based SfS models such as the type and the convexity of underlying Hamiltonians as well as appropriate algorithms for solving them, especially the FM method. As we will see, these properties are closely related with each other. Moreover, we investigate possible ambiguities and discuss appropriate boundary conditions.

3.5.1 Types of Hamiltonians

When it comes to PDE-based SfS models, there are mainly two categories for classification: In view of (2.23) and (2.24) a model may have either an *eikonal-type* Hamiltonian or one of *general-type*. An overview of the most prominent PDE-based models of the last years can be found in Table 3.1 and Table 3.2 respectively.

In general, relative early PDE-based models with simple assumptions on the scene geometry such as an orthographic camera projection with a distant light source usually have an eikonal-type Hamiltonian, see "RT92 [219]" and "PFR02 [197]" in

Table 3.1. Employing a perspective camera projection instead of an orthographic one does not affect the type of the Hamiltonian – as can be seen in “CCDG04 [60]” and “TSY04 [237]” listed in Table 3.1 as well as from the unification model [196] combining both orthographic and perspective projections with different light source positions.

Table 3.1. Comparison of PDE-based Shape from Shading models *without* the light attenuation term.

	RT92 [219]	PFR02 [197]	CCDG04 [60]	TSY04 [237]
camera projection	orthographic	orthographic	perspective	perspective
light source	infinity	infinity	infinity	infinity
surface	Lambertian	Lambertian	Lambertian	Lambertian
Hamiltonian	eikonal-type	eikonal-type	eikonal-type	eikonal-type
light attenuation	–	–	–	–
convexity	convex	convex	convex	convex

By comparing the list of models in Table 3.2 with the ones in Table 3.1, one can note that the position of the light source is moved from infinity to the optical centre. To handle the scenario, the models in Table 3.2 have employed the light attenuation term. This term actually makes a difference in the type of the Hamiltonian. As can be observed in (3.36), this is because the unknown v, i.e. the log transformation of u from (3.31), eventually appears in the resulting Hamiltonian which is associated with the brightness equation via the light fall-off term.

In order to solve SfS problems described by HJEs, depending on the type of Hamiltonian a set of appropriate algorithms with necessary information, e.g. initial conditions or boundary conditions, can be derived.

3.5.2 Fast Marching Methods for PDE-based SfS Models

In this section, we provide an exposition on numerical methods to solve the HJEs representing PDE-based SfS models that we have seen so far depending on the type as well as the convexity of the Hamiltonians. As primary algorithmic strategy, we focus on the fast marching method along with an initialisation and its applicability to the models. However, we also mention other methods as well as model-specific variants including related work in the field.

Table 3.2. Comparison of PDE-based perspective Shape from Shading models *with* the light attenuation term.

	PF05 [195]	AF06 [6]	VBW08 [258]
camera projection	perspective	perspective	perspective
light source	optical centre	optical centre	optical centre
surface type	Lambertian	Oren-Nayar	Phong
Hamiltonian	general-type	general-type	general-type
light attenuation	✓	✓	✓
convexity	convex	non-convex [1]	convex [2]

[1] assumed to be non-convex [6]
[2] convexity depends on the value of the specular exponent [42]

Fast Marching Methods for Eikonal-type Hamiltonians

Convexity for FM Method. Let us discuss the convexity of the Hamiltonian which is a requirement for applying the FM method. As we have seen in Section 2.3.3, the FM method computes a solution by tracking the movement of the initial wavefront. This suggests that the FM method is designed to assign larger values to grid points as time elapses since the wavefront moves in one direction, e.g. outwards. This principle is encoded in terms of convexity of Hamiltonians with respect to the second argument in (2.23), i.e. the gradient of unknown. This property can be understood in a way that the model must allow to compute the depth in one direction in order to use the FM method, e.g. from closer points to farther ones. As long as the convexity of the Hamiltonian is satisfied, the FM method can be applied not only to the ones listed in Table 3.1 but also to the ones with the form of eikonal-type HJEs in (2.23), e.g. [79, 281].

Initialisation with Critical Points. Apart from the convexity of Hamiltonian, there is one difficulty for applying the FM method to eikonal-type HJEs: Information on starting points must additionally be provided. Moreover, it is essentially associated with local extrema, i.e. critical points or singular points, where, in general, as shown in Section 2.2.3 viscosity solutions are not defined. In this context, the initialisation procedure for the FM method can be interpreted as providing adequate information at critical points. Then, the FM method makes use of the initial depth as source of information and makes it spread to the remaining computational domain by means of the upwind scheme.

However, concerning eikonal-type SfS models with the FM method, not all approaches reveal explicitly how critical points are identified and initial depth values are assigned accordingly, e.g. [262]. In this context, especially for real-world images one follows the strategy in [237] for an initialisation: a human viewer identifies brightest points in the input image and assigns them arbitrarily the same depth value. This procedure, however, may suffer from convex/concave ambiguities even in the viscosity framework, since the same brightest grey value may represent different starting points as well as surface profiles and thereby lead to different reconstructions as can be observed in Figure 3.12. We will discuss more about this matter in more detail in Section 3.5.3.

Direct Computation. Regarding the properties of the FM method, one should note that the FM method allows to compute the surface depth directly for eikonal-type Hamiltonians if the information on singular points is available. Hence, one needs no further steps or restrictions to reconstruct the surface such as the integration of gradient fields or integrability constraints [89]. In fact, this makes the FM approach different from the propagation method with characteristic strips from early days [116, 173, 174, 177]. For such a method with characteristic strips, another time variable is necessary to derive the Hamiltonian system in addition to auxiliary variables for a depth gradient. Once a solution for systems of the differential equations is obtained, the resulting gradient field must be integrated along the characteristic curves which provides the information on the surface profiles [116, 174, 177].

Comparison with Iterative Methods. For eikonal-type Hamiltonians, an iterative method with the upwind discretisation [219] may be an alternative to the FM method, if proper boundary conditions are given. Although both the FM method by Sethian [228] and the iterative method by Rouy and Tourin [219] strive for a solution in the viscosity sense, the FM method is much faster than the iterative method. Aside from the computational efficiency, the starting point of the computation is different as well, i.e. the location where the initial information is given. In the example (2.25), the iterative scheme by Rouy and Tourin [219] starts at the boundary points, $(-1, 0)^\top$ and $(1, 0)^\top$, whereas the local extremum $(0, 1)^\top$ is the initial point for the FM method by Sethian [228, 229].

FM in Optimal Control Based Approaches. The FM method can also be applied to optimal control based propagation approaches [75, 76, 175, 176]. To that end, one has to derive a cost function associated with the original eikonal-type HJEs and find a minimal cost, e.g. by relying on the dynamic programming principle [31]. This can be understood in the context of HJBEs [16], where recent development of semi-Lagrangian [59] based FM methods can be utilised [67, 68, 83, 246].

Fast Marching Methods for General-type Hamiltonians

In general, the FM method can also be applied to general-type HJEs as long as the associated Hamiltonians are convex. Since it is, however, not so trivial to verify the convexity of Hamiltonians, the employed algorithms are usually model specific: Assuming that the scene geometry stays unchanged (a point light source being placed at the optical centre of a perspective camera), the convexity of Hamiltonians is influenced by the properties of the incorporated surface reflectance model. Let us have a look how the FM method is applied to different models with respect to the convexity of Hamiltonians.

Perspective Lambertian SfS. For the perspective Lambertian SfS model (3.36), the FM method is not directly applied to the model described by the HJE but to the associated HJBE based on that the Hamiltonian of the model is convex [193, 195]. Therefore, this approach utilises an optimal control based formulation relying on the dynamic programming principle [31, 249].

Perspective Phong SfS. Regarding the perspective Phong SfS model (3.48), an iterative method with the upwind scheme [219] is employed in [258], since the model convexity had not been investigated by the time. Afterwards, the FM method had been used for the same model in [259] but without any theoretical justifications until we have investigated the model with respect to critical points and convexity in [42]. Based on [42], it turns out that the model (3.48) is conditionally convex depending on the value of the specular exponent α. However, as long as the Hamiltonian is convex for the employed value of the specular exponent, the FM method is an appropriate choice for the model (3.48), e.g. [259]. One can also note that the regula falsi method is used as a root finding strategy to update radial depth values at "trial" points in [259]. To apply the FM method to general-type HJEs, this type of strategy is necessary because it is difficult to solve analytically the corresponding nonlinear equations for the update procedure.

Perspective Oren-Nayar SfS. Concerning the perspective Oren-Nayar SfS model in (3.70), a Lax-Friedrichs sweeping scheme [133], i.e. a stabilised scheme for hyperbolic PDEs, is employed in [6]. This method is suitable for both convex and non-convex Hamiltonians. However, one can also find a work in the literature which makes use of the FM method for the model without investigating the model convexity, e.g. [256]. To clear up the situation, we provide an in-depth analysis of the model in [129] with respect to *Osher's criterion* [182, 200, 248]. This criterion gives a theoretical justification whether the FM method can be applied to the model without directly investigating the convexity. Our findings in [129] show that the applicability of the FM method can be determined by the range of the roughness parameter σ and the value used in [256] is actually within the safe range which is based on Osher's criterion.

Initialisation with Critical Points. As indicated in the eikonal-type case, the information on critical points plays a key role for the FM method but such information is, in general, not available in practice. One way to approximate the radial depth at such points is to plug $\nabla v = 0$ into the model (3.36) at the brightest points [193]. This corresponds to

$$\frac{I(x)\,\mathrm{f}^2}{Q(x)}\sqrt{Q(x)^2} = e^{-2\,v(x)} \Leftrightarrow I(x)\,\mathrm{f}^2 = e^{-2\,v(x)} \Leftrightarrow v(x) = -\frac{1}{2}\,\ln\big(I(x)\,\mathrm{f}^2\big)\,. \tag{3.72}$$

Since the light attenuation term (3.31) is integrated in (3.36), the brightest pixels are supposed to be closest points from the light source. The approximation in (3.72), therefore, accounts for finding *critical points*, i.e. closest points from the light source, in terms of the radial depth v in the scene. The same strategy can also be used to initialise other general-type Hamiltonians [93, 130, 259].

Boundary Conditions

When dealing with PDE-based methods, one necessarily needs to consider some kind of boundary conditions for finding a solution [79]. From different types of boundary conditions, the selection depends primarily on the available information of a problem at hand. Let us discuss three main boundary conditions for SfS that can usually be encountered in literature: Dirichlet boundary conditions, Neumann boundary conditions (NBCs), and "state constraint" boundary conditions.

Dirichlet Boundary Conditions. Dirichlet boundary conditions refer to the case when specific values are prescribed at boundary points. Obviously, this type of BCs can be applied if the surface depth at boundaries is known a priori (or at least presumed to be known). Otherwise, there requires another way to impose this condition. Especially when it comes to PDE-based SfS models described by general-type HJEs, e.g. [6, 195], one way to realise this BC in practice is to make use of the depth information at singular points (or critical points) [193, 255]. As can be seen in (3.72), one can obtain an analytical expression (at least by means of an approximation) for the depth at those points. This suggests that the depth at singular points is already included in the model and is consequently encoded as DBCs. In other words, singular points can be understood as boundary points and their depth information corresponds to DBCs. Hence, in this case BCs do not necessarily indicate actual image boundaries, i.e. upper, lower, left or right.

Neumann Boundary Conditions. While DBCs assign certain values along boundaries, Neumann boundary conditions only specify the derivative of outward normal. Thus, this type of BCs can be used when the level set of the surface are perpendicular to the boundary (or at least assumed as such) [79]. One can also note that imposing NBCs may lead to different reconstructions in comparison to the case with DBCs since the derivative is translation invariant w.r.t. the depth.

State Constraint Boundary Conditions. Aside from DBCs and NBCs, "state constraint" boundary conditions are used as well in SfS, see e.g. [193, 195, 199]. This type of BCs can be realised by means of DBCs, i.e. by assigning $+\infty$ (or very large values in practice) on the boundary [193, 195, 255]. Interestingly, the state constraint boundary conditions have actually the same effect as that of NBCs if the upwind schemes in (2.89) and (2.90) are employed [255]. To verify the statement, we consider the right boundary of a domain. By the state boundary condition, the upwind scheme in (2.89) becomes

$$\widehat{T}_x = \max\left(\frac{T_{i,j} - T_{i-1,j}}{h_1}, -\frac{+\infty - T_{i,j}}{h_1}, 0\right), \tag{3.73}$$

which makes the second argument never being selected. When applying NBCs to (2.89), one obtains

$$\widehat{T}_x = \max\left(\frac{T_{i,j} - T_{i-1,j}}{h_1}, -\frac{T_{i,j} - T_{i,j}}{h_1}, 0\right), \tag{3.74}$$

which makes the second argument zero. Therefore, both (3.73) and (3.74) have the same effect within this type of discretisations. The large value on the boundary serves as a barrier which guarantees that no outside information flows into the interior of a computational domain.

Since the state constraint BCs do not require specific values or normal derivatives, they are sometimes referred to the method "without image boundary data" as in [193, 195, 199]. However, this interpretation is somewhat misleading because they have exploited the depth information at singular points. Based on our discussion in DBCs, which states that singular points are, in fact, boundary points and their depth values are DBCs, they have actually used DBCs even though the terms are not explicitly mentioned.

3.5.3 Ambiguities

It is well-known from early days that SfS problems suffer from several types of ambiguities and thereby solutions for the problem are, in general, not unique. This, in other words, indicates that there are more than one surface profiles ending up with the same grey values as those of the input image. In this context, serious efforts were made to analyse difficulties, to somehow circumvent this ill-posed property, or to strive for achieving uniqueness results at least partially [29, 30, 46, 67, 143, 144, 145, 173, 174, 177, 187, 196].

Bas-relief Ambiguity

One ambiguity is the *bas-relief*[1] *ambiguity* described by Belhumeur *et al.* [29, 30]. This ambiguity is concerned with interrelationship between collimated parallel light beams by a distant light source and a rather flat surface such as coins or carving work in sculpture under the orthographic camera projection.

In [29, 30], it is mathematically shown that there is an equivalence class of Lambertian surfaces with which only one image can be obtained under the orthographic projection with a distance light source. Furthermore, these different surface profiles in the same class are connected with one another through the generalised bas-relief (GBR) transformation [29, 30] belonging to the class of affine transformations.

This ambiguity, further, implicates that the information on the light direction of a scene and the albedo of a surface is crucial for reconstructing a surface unambiguously. In particular, when it comes to SfS, these difficulties account for the assumptions in [195], which states that all parameters of the light source and the camera as well as the albedo of a surface are assumed to be available.

Convex/Concave Ambiguity

Besides the bas-relief ambiguity, among others the *convex/concave ambiguity* is one of the most notorious ambiguities not only for computer vision [242] but also psychology as well as cognitive science [141, 206, 207]. Let us have a look how this phenomenon occurs. To this end, we assume that a light source is positioned at a distant location (ideally at infinity), only collimated light, i.e. parallel beams, falls onto an object having matte surface with a uniform albedo, and an orthographic camera projection is carried out for the scene geometry. Then, as we have already seen in (3.22), the light intensity depends only upon the normalised surface normal vector **N** and the light direction **L**. As a consequence, one cannot distinguish between the two different surfaces in Figure 3.12, since both surface profiles have the same grey values owing to the same angle θ. Furthermore, a model that cannot tell a surface as in Figure 3.12 apart, cannot distinguish between the surface profiles in Figure 3.13.

To understand the situation from the viewpoint of the model, we consider the following brightness equation by Rouy and Tourin [219]

$$|\nabla u(x)| = \sqrt{\frac{1}{I(x)^2} - 1}\,. \tag{3.75}$$

---

[1] also called low-relief or shallow-relief

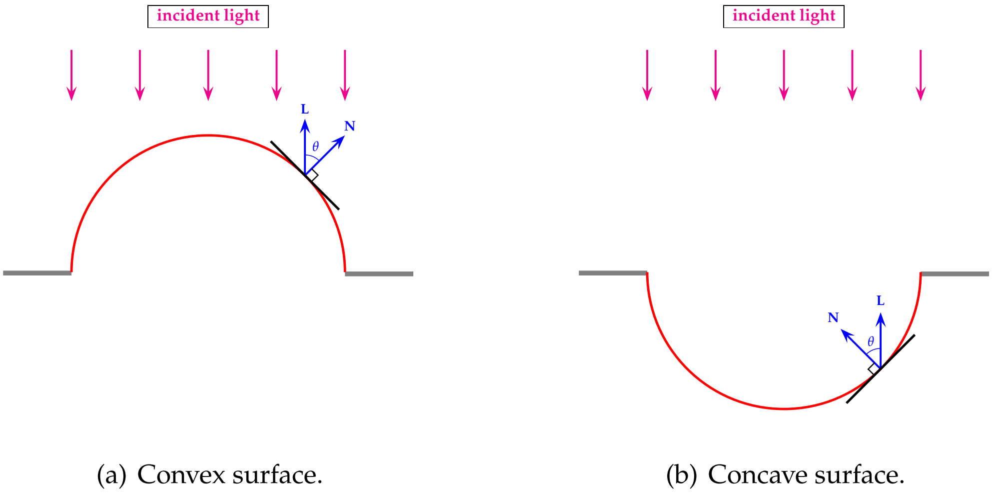

(a) Convex surface. (b) Concave surface.

Figure 3.12. Convex/concave ambiguities.

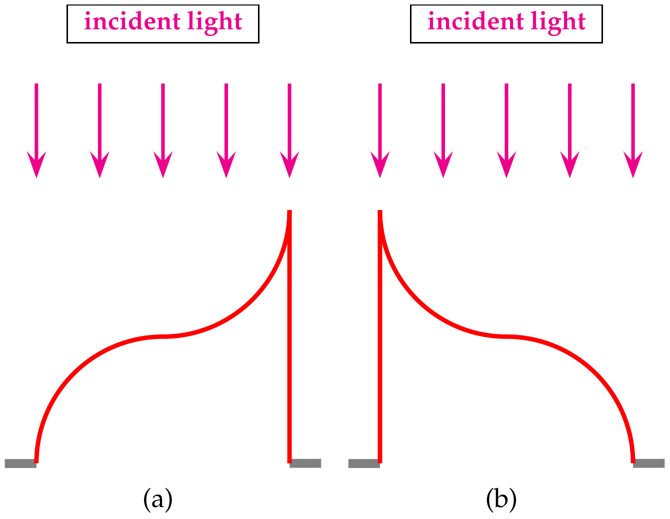

Figure 3.13. Different surface profiles generating same grey values.

From (3.75), it can be observed that being u a solution to (3.75) makes $u + c$ with $c \in \mathbb{R}$ another solution due to the gradient operator. Moreover, $-u$ must necessarily be a solution as well because of the Euclidean norm, which manifests itself as the convex/concave ambiguity.

Singular Points

Eikonal-type Hamiltonians. Another source of the ambiguity comes from singular points [78, 172, 193, 219]. Singular points refer to the ones with maximal intensity, i.e. $I(x) = 1$, and by (3.14) one can notice that this phenomenon occurs when the surface normal is parallel to the light direction. If such points exist, from (3.75) one attains

$$|\nabla u(x)| = 0\,. \tag{3.76}$$

Since there are several surface profiles that meet this condition, e.g. extrema or an inflection point, an additional condition is necessary to determine a meaningful solution. In this respect, one may consider a pointwise maximum solution in the viscosity sense, see Figure 2.8 for instance. This explains that the uniqueness result obtained in [219] is valid except singular points. However, to obtain a complete surface profile additional information on the shape at singular points must be available as suggested in [78, 172, 174, 177]. This means that the type of singular points has to be classified into the following classes: convex, concave or saddle [78, 172, 173, 174, 177].

General-type Hamiltonians. In contrast to the case of eikonal-type Hamiltonians, general-type model is helpful for resolving convex/concave ambiguities to some degree [193, 195]. This is because the general-type Hamiltonians in [6, 195, 258] contain the physics motivated light attenuation term formulated by the radial distance and this term makes a farther object from a light source receive less energy. Hence, the models containing the light fall-off term cannot have a concave surface as in Figure 3.12(b) at singular points by construction. However, this "change of type" for Hamiltonians does not ensure that all difficulties are resolved completely. Regarding the uniqueness, there are the following constraints especially for singular points according to [44]: (i) A solution at singular points must be determined. (ii) The solution at singular points must be smooth. (iii) If the value of the solution increases when moving away from such singular points, then the solution can be determined uniquely. In the light of (i) and (ii) the initialisation performed in (3.72), therefore, can be interpreted as finding an approximate smooth solution at singular points. Moreover, in view of (iii) one can note that the FM-based algorithm such as [259] is a proper strategy to solve a problem based on the properties of the FM method as discussed in Section 2.3.

3.6 Summary

In this chapter, we have investigated important PDE-based SfS models with respect to several aspects. After reviewing necessary modelling ingredients for SfS, by employing the perspective camera projection, Lambertian surface reflectance, and a brightness equation with the light attenuation term we have derived the perspective Lambertian SfS model [195] which forms the basis for other advanced models in the field. Subsequently, by incorporating Phong and Oren-Nayar reflectance we have derived two non-Lambertian models: One is the perspective Phong SfS model

[258] the other is the perspective Oren-Nayar SfS model [6], respectively. Finally, we have looked into important model properties such as the type of Hamiltonians that is related to the possible choice of numerical algorithms, e.g. the FM method. In addition, we have also discussed the convexity of Hamiltonians as well as ambiguity issues including the significant role of singular points.

CHAPTER 4

GENERALISED PERSPECTIVE SHAPE FROM SHADING MODELS

In the previous chapter, we have extensively studied various aspects of modern PDE-based SfS models: Starting with the essential modelling components we have derived the standard perspective SfS models [6, 195, 258] with Lambertian reflectance [195] as well as the corresponding non-Lambertian models based on the Phong [189] and the Oren-Nayar reflectance [6]. Moreover, we have discussed the properties of these models along with suitable FM methods – with special emphasis on critical points. However, as shown in Table 3.2 these standard models have a serious limitation when it comes to the position of the light source: The light source is assumed to be placed at the optical centre of the camera, which is often not the case by construction, e.g. in the case of a flash device in photography.

In this chapter, we relax this unrealistic assumption and extend the standard perspective SfS models from Chapter 3 in such a way that the resulting model can handle a flexible scene geometry with respect to the position of the light source. Moreover, we show by the example of the Oren-Nayar reflectance that such models can also be derived from non-Lambertian surfaces. In order to handle critical points effectively in such general scenarios, we formulate the resulting generalised brightness equations as HJEs in terms of spherical coordinates instead of Cartesian ones. Therefore, solutions to these models still can be understood in the viscosity sense that we have covered in Section 2.2.3. Furthermore, we also develop a highly efficient numerical algorithm to deal with the resulting set of highly nonlinear complex HJEs in spherical systems. This FM-based algorithm is specifically customised: On the one hand, it takes full advantage of the efficient grid traversing scheme from the FM method [227]. On the other hand, it is able to take care of general-type Hamiltonians by adding a correction step to the iterative regula falsi framework and thereby to attain solutions in the viscosity sense.

To this end, we first parameterise a surface for flexible light positions in terms of spherical coordinates in Section 4.1. Afterwards, with the spherical parametrisation we derive generalised brightness equations by incorporating the Lambertian surface and the Oren-Nayar reflectance in Section 4.2 and 4.3, respectively. In Section 4.4, we then provide an exposition on the adapted FM scheme. Subsequently, we present experimental results by making use of synthetic and real-world images in Section

4.5. The models described in this chapter are based on the papers [93, 130] that were presented at SSVM and BMVC.

4.1 Surface Parametrisation for Arbitrary Light Source Positions

As can be noticed in Table 3.1 and 3.2 as well as [79, 200], PDE-based perspective SfS models typically have a *fixed* position of the light source: it is either located at infinity or at the optical centre of the camera. However, when it comes to application dealing with realistic scenarios, this scene geometry is considerably restricted because the assumption is quite limited and thereby often violated, which may lead to suboptimal results. Therefore, we now take a more flexible scene geometry into account that is depicted in Figure 4.1. As one can see, the position of the light source can be anywhere in the scene.

In order to deal with this case, we have to select a proper measurement system with respect to critical points, i.e. the brightest points which have minimal distance to a light source. The important principle is that brightest points must be identified as closest points to the light source. This suggests that the depth parametrisation must contain the information of the distance with respect to the light source. If a light source is located at the optical centre of the camera, this parametrisation can be performed by placing the origin at the position of the light source in Cartesian coordinates, see Figure 4.2. The same rule applies to the case of a flexible scene geometry: By assigning the origin to the position of the light source and parametrising the distance from the light source, one can achieve the goal, see Figure 4.3. However, since the realisation of this procedure in the Cartesian system leads to complex formulations, we consider this parametrisation in *spherical* coordinate system.

In order to gain full benefits of the spherical coordinate system, one needs to parametrise the entire SfS model in these coordinates. As we will see later on, we also have to adapt the FM method such that it works in spherical coordinates. In the following, we show how to parametrise all components of the brightness equation with Lambertian reflectance model as well as the Oren-Nayar reflectance. To this end, we assume a uniform albedo, i.e. $\rho = 1$.

4.1.1 Surface Representation in Spherical Coordinates

In this section, we express a vector representing a surface point and its gradient in terms of a spherical coordinate system. To this end, we follow the conventions in Figure 4.4, where the vector **r** is represented in both coordinates.

First, let us derive a relationship between the Cartesian and the spherical systems for a point. By supposing that the vector **r** points to the surface point $S = (X, Y, Z)^\top$

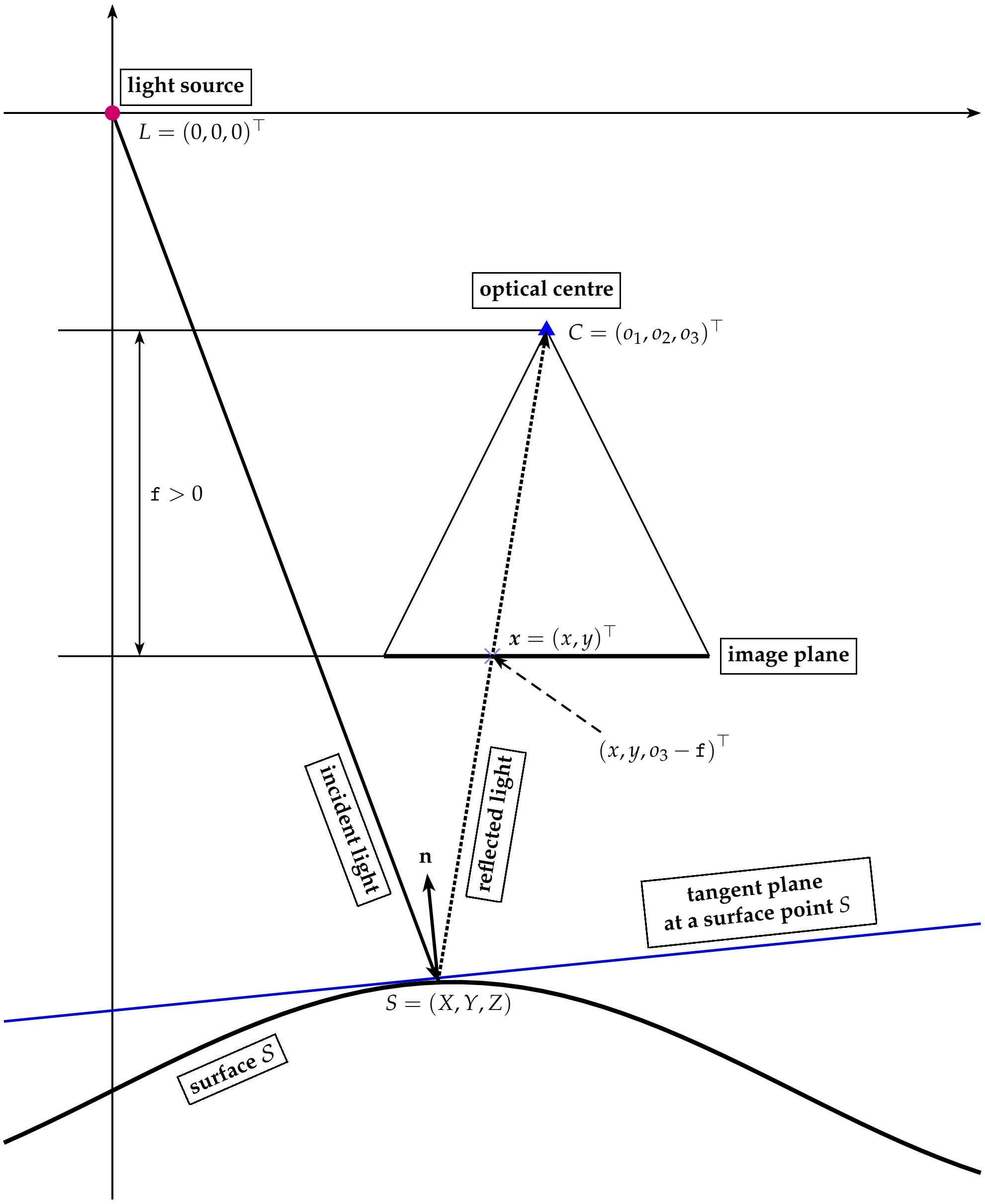

Figure 4.1. Cross section of a 3-D model for perspective SfS with arbitrary position of the light source. The distance between the light source L and the point S on the surface is denoted by r given in (3.22).

in Figure 4.1, we obtain

$$\mathcal{S} := \overrightarrow{LS} = [X, Y, Z]^\top =: \mathbf{r} := r\,\mathbf{e}_r \qquad \text{with} \qquad r = \sqrt{X^2 + Y^2 + Z^2}\,, \tag{4.1}$$

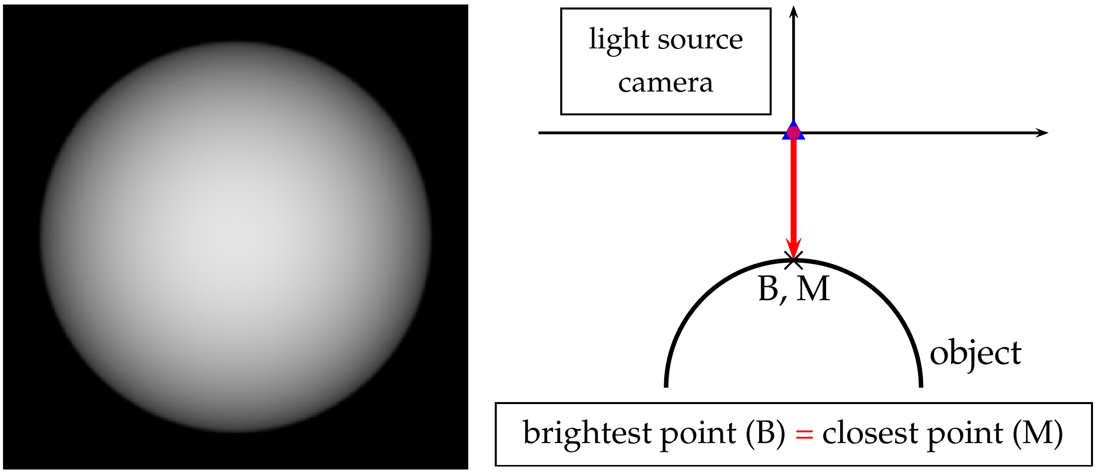

(a) Light source being at optical centre. (b) Depth parametrisation from the light source.

Figure 4.2. When the light source is placed at the optical centre of the camera.

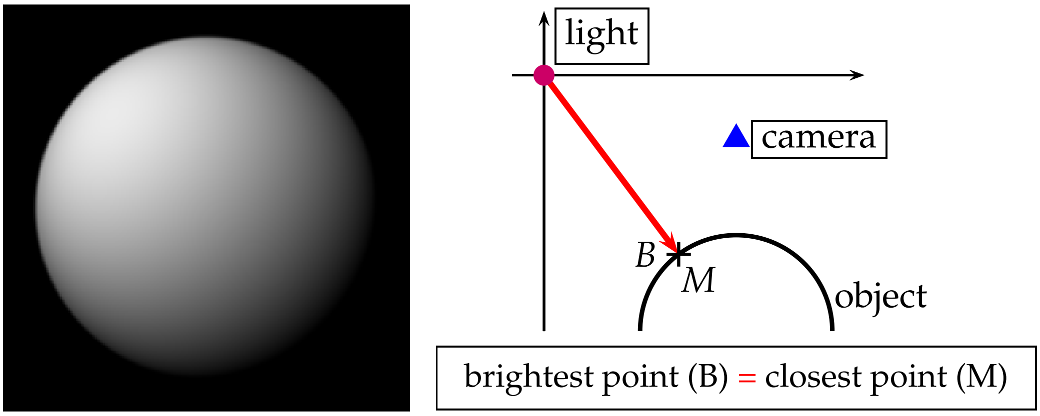

(a) Light source *not* being at optical centre. (b) Depth parametrisation from the light source.

Figure 4.3. When the light source is *not* placed at the optical centre of the camera.

where $\mathbf{e}_r$ represents the basis vector in the direction from the position of the light source to the surface point. Hence, it has the form

$$\mathbf{e}_r = \frac{1}{\sqrt{X^2 + Y^2 + Z^2}} (X, Y, Z)^\top \overset{(4.1)}{=} \frac{1}{r} (X, Y, Z)^\top \tag{4.2}$$

and will be derived in spherical coordinates. Applying trigonometric identities to (4.1) further leads to

$$\mathcal{S} \overset{(4.1)}{=} \mathbf{r} = \begin{bmatrix} X \\ Y \\ Z \end{bmatrix} = \begin{bmatrix} r\,\cos\left(\frac{\pi}{2} - \theta\right)\,\cos\phi \\ r\,\cos\left(\frac{\pi}{2} - \theta\right)\,\sin\phi \\ r\,\sin\left(\frac{\pi}{2} - \theta\right) \end{bmatrix} = \begin{bmatrix} r\,\sin\theta\,\cos\phi \\ r\,\sin\theta\,\sin\phi \\ r\,\cos\theta \end{bmatrix}, \tag{4.3}$$

where

$$(\theta, \phi)^\top = \left(\arccos\frac{Z}{\sqrt{X^2 + Y^2 + Z^2}}, \arctan\frac{Y}{X}\right)^\top. \tag{4.4}$$

It can be noted that the surface point in (4.3) is described in terms of world coordinates in comparison to Chapter 3, cf. (3.25). The relationship between image and world coordinates can be obtained based on Figure 4.1. This is given by

$$\frac{x - o_1}{X - o_1} = \frac{y - o_2}{Y - o_2} = \frac{-\mathrm{f}}{Z - o_3}. \tag{4.5}$$

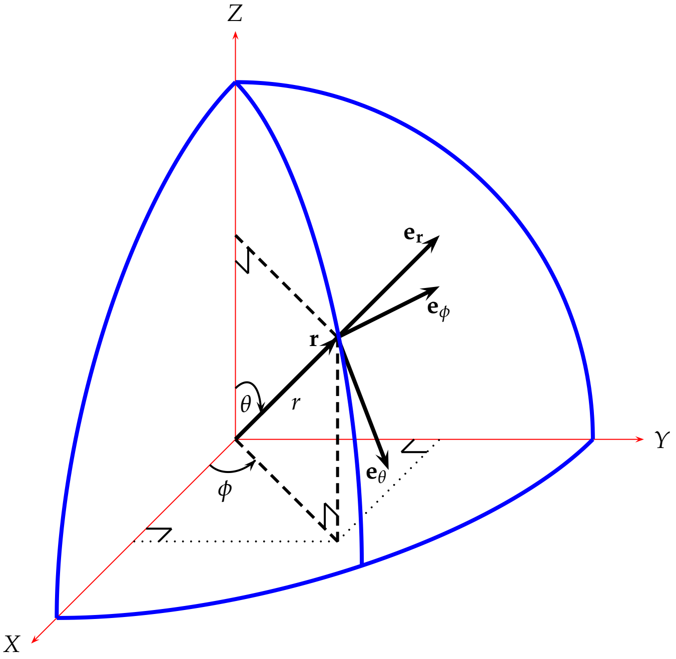

Figure 4.4. Spherical coordinate system: $\mathbf{e}_r$, $\mathbf{e}_\varphi$ and $\mathbf{e}_\theta$ stand for orthonormal basis vectors with respect to each direction in the spherical system. The distance between the light source L and the point S on the surface in Figure 4.1 corresponds to r.

Gradient and Basis Vectors in Spherical Coordinates

Let us now proceed to establish a relationship with respect to the gradient between spherical and Cartesian coordinates. To this end, we express the gradient in the spherical coordinates as an operator form using the chain rule. This yields

$$\frac{\partial}{\partial r} = \frac{\partial X}{\partial r}\frac{\partial}{\partial X} + \frac{\partial Y}{\partial r}\frac{\partial}{\partial Y} + \frac{\partial Z}{\partial r}\frac{\partial}{\partial Z}, \tag{4.6}$$

$$\frac{\partial}{\partial \theta} = \frac{\partial X}{\partial \theta}\frac{\partial}{\partial X} + \frac{\partial Y}{\partial \theta}\frac{\partial}{\partial Y} + \frac{\partial Z}{\partial \theta}\frac{\partial}{\partial Z}, \tag{4.7}$$

and

$$\frac{\partial}{\partial \phi} = \frac{\partial X}{\partial \phi}\frac{\partial}{\partial X} + \frac{\partial Y}{\partial \phi}\frac{\partial}{\partial Y} + \frac{\partial Z}{\partial \phi}\frac{\partial}{\partial Z}. \tag{4.8}$$

Moreover, by plugging all the computations of partial derivatives based on (4.3) we reformulate these expressions as a compact form. This is given by

$$\begin{aligned}
\begin{bmatrix} \frac{\partial}{\partial r} \\ \frac{\partial}{\partial \theta} \\ \frac{\partial}{\partial \phi} \end{bmatrix}
&= \begin{bmatrix} \frac{\partial X}{\partial r} & \frac{\partial Y}{\partial r} & \frac{\partial Z}{\partial r} \\ \frac{\partial X}{\partial \theta} & \frac{\partial Y}{\partial \theta} & \frac{\partial Z}{\partial \theta} \\ \frac{\partial X}{\partial \phi} & \frac{\partial Y}{\partial \phi} & \frac{\partial Z}{\partial \phi} \end{bmatrix}
\begin{bmatrix} \frac{\partial}{\partial X} \\ \frac{\partial}{\partial Y} \\ \frac{\partial}{\partial Z} \end{bmatrix} \\
&\overset{(4.3)}{=} \underbrace{\begin{bmatrix} \sin\theta\,\cos\phi & \sin\theta\,\sin\phi & \cos\theta \\ r\,\cos\theta\,\cos\phi & r\,\cos\theta\,\sin\phi & -r\,\sin\theta \\ -r\,\sin\theta\,\sin\phi & -r\,\sin\theta\,\cos\phi & 0 \end{bmatrix}}_{=:\,B}
\begin{bmatrix} \frac{\partial}{\partial X} \\ \frac{\partial}{\partial Y} \\ \frac{\partial}{\partial Z} \end{bmatrix}.
\end{aligned} \tag{4.9}$$

Therefore, we can reformulate the Cartesian gradient in (4.9) in terms of spherical coordinates as

$$\begin{aligned}
\begin{bmatrix} \frac{\partial}{\partial X} \\ \frac{\partial}{\partial Y} \\ \frac{\partial}{\partial Z} \end{bmatrix}
&= \overbrace{\begin{bmatrix} \sin\theta\,\cos\phi & \frac{1}{r}\,\cos\theta\,\cos\phi & \frac{1}{r\,\sin\theta}\,(-\sin\phi) \\ \sin\theta\,\sin\phi & \frac{1}{r}\,\cos\theta\,\sin\phi & \frac{1}{r\,\sin\theta}\,\cos\phi \\ \cos\theta & \frac{1}{r}\,(-\sin\theta) & 0 \end{bmatrix}}^{=:\,B^{-1}}
\begin{bmatrix} \frac{\partial}{\partial r} \\ \frac{\partial}{\partial \theta} \\ \frac{\partial}{\partial \phi} \end{bmatrix} \\
&= \mathbf{e}_r \left(\frac{\partial}{\partial r}\right) + \mathbf{e}_\theta \frac{1}{r}\left(\frac{\partial}{\partial \theta}\right) + \mathbf{e}_\phi \frac{1}{r\sin\theta}\left(\frac{\partial}{\partial \phi}\right),
\end{aligned} \tag{4.10}$$

where each column vector of B^{-1} serves as a basis vector

$$\mathbf{e}_r = \begin{bmatrix} \sin\theta\,\cos\phi \\ \sin\theta\,\sin\phi \\ \cos\theta \end{bmatrix}, \quad \mathbf{e}_\theta = \begin{bmatrix} \cos\theta\,\cos\phi \\ \cos\theta\,\sin\phi \\ -\sin\theta \end{bmatrix}, \quad \mathbf{e}_\phi = \begin{bmatrix} -\sin\phi \\ \cos\phi \\ 0 \end{bmatrix}. \tag{4.11}$$

These basis vectors can also be obtained by using rotation matrices as follows: We first rotate the vector $(0,0,r)^\top$ by an angle θ about Y-axis. Subsequently, we further rotate the previously rotated vector by an angle ϕ about Z-axis. These series of actions can be expressed by applying two rotational matrices to the vector $(0,0,r)^\top$ sequentially, i.e. first $R_Y(\theta)$ and then $R_Z(\phi)$. This reads

$$\mathbf{r} = R_Z(\phi)\,R_Y(\theta)\begin{bmatrix} 0 \\ 0 \\ r \end{bmatrix} = \begin{bmatrix} \cos\phi\,\cos\theta & -\sin\phi & \cos\phi\,\sin\theta \\ \sin\phi\,\cos\theta & \cos\phi & \sin\phi\,\sin\theta \\ -\sin\theta & 0 & \cos\theta \end{bmatrix}\begin{bmatrix} 0 \\ 0 \\ r \end{bmatrix}, \tag{4.12}$$

where the two matrices

$$R_Z(\phi) = \begin{bmatrix} \cos\phi & -\sin\phi & 0 \\ \sin\phi & \cos\phi & 0 \\ 0 & 0 & 1 \end{bmatrix}, \quad R_Y(\theta) = \begin{bmatrix} \cos\theta & 0 & \sin\theta \\ 0 & 1 & 0 \\ -\sin\theta & 0 & \cos\theta \end{bmatrix} \tag{4.13}$$

represent rotations around the Z- and Y-axis by an angle ϕ and an angle θ, respectively.

Since the properties of rotation matrices are still preserved after series of matrix multiplications [13], one can validate the orthonormal properties of these basis vectors:

$$\mathbf{e}_\theta\cdot\mathbf{e}_\phi = \mathbf{e}_\theta\cdot\mathbf{e}_r = \mathbf{e}_\phi\cdot\mathbf{e}_r = 0 \quad\text{and}\quad |\mathbf{e}_\theta| = |\mathbf{e}_\phi| = |\mathbf{e}_r| = 1\,. \tag{4.14}$$

Moreover, these basis vectors have the following properties with respect to derivatives

$$\frac{\partial\,\mathbf{e}_r}{\partial\theta} = \begin{bmatrix} \cos\theta\,\cos\phi \\ \cos\theta\,\sin\phi \\ -\sin\theta \end{bmatrix} \overset{(4.11)}{=} \mathbf{e}_\theta\,, \quad \frac{\partial\,\mathbf{e}_r}{\partial\phi} = \begin{bmatrix} -\sin\theta\,\sin\phi \\ \sin\theta\,\cos\phi \\ 0 \end{bmatrix} \overset{(4.11)}{=} \sin\theta\,\mathbf{e}_\phi \tag{4.15}$$

as well as the properties of the right-handed coordinate system $(\mathbf{e}_r, \mathbf{e}_\theta, \mathbf{e}_\phi)$

$$\mathbf{e}_\theta\times\mathbf{e}_\phi = \mathbf{e}_r\,,\quad \mathbf{e}_\phi\times\mathbf{e}_r = \mathbf{e}_\theta\,,\quad \mathbf{e}_r\times\mathbf{e}_\theta = \mathbf{e}_\phi\,. \tag{4.16}$$

These properties are used for computing the direction of surface normal in the next section.

4.2 Lambertian SfS Model in Spherical Coordinates

In order to obtain a brightness equation in terms of the spherical coordinate system, we perform computations on each element of the brightness equation by means of basis vectors (4.11) as well as the radial vector (4.1). To this end, we first deal with the direction of surface normal **n** in (3.22). For the computations of a surface normal vector in a spherical system, we adopt the same strategy as we have performed for the Cartesian case in Section 3.2.2. Since the surface parametrisation vector **r** in (4.1) is orthogonal to both θ- and ϕ-direction as shown in (4.14), the direction of surface normal can be determined by taking a cross product between the partial derivatives of **r** with respect to θ and ϕ. In this case, one can note that a tangent plane is spanned by $\mathbf{r}_\phi$ and $\mathbf{r}_\theta$ instead of $\mathcal{S}_x$ and $\mathcal{S}_y$, cf. Figure 3.11. Then, using the spherical surface representation we obtain the direction of surface normal as

$$\begin{aligned}
\mathbf{n} &= \frac{\partial \mathcal{S}}{\partial \phi} \times \frac{\partial \mathcal{S}}{\partial \theta} \overset{(4.3)}{=} \frac{\partial \mathbf{r}}{\partial \phi} \times \frac{\partial \mathbf{r}}{\partial \theta} \overset{(4.1)}{=} \frac{\partial (r\,\mathbf{e}_r)}{\partial \phi} \times \frac{\partial (r\,\mathbf{e}_r)}{\partial \theta} \\
&= \left(\frac{\partial r}{\partial \phi}\,\mathbf{e}_r + r \frac{\partial \mathbf{e}_r}{\partial \phi} \right) \times \left(\frac{\partial r}{\partial \theta}\,\mathbf{e}_r + r \frac{\partial \mathbf{e}_r}{\partial \theta} \right) \\
&= \left(\frac{\partial r}{\partial \phi}\mathbf{e}_r \times \frac{\partial r}{\partial \theta}\mathbf{e}_r \right) + \left(\frac{\partial r}{\partial \phi}\mathbf{e}_r \times r \frac{\partial \mathbf{e}_r}{\partial \theta} \right) + \left(r \frac{\partial \mathbf{e}_r}{\partial \phi} \times \frac{\partial r}{\partial \theta}\mathbf{e}_r \right) + \left(r\, \frac{\partial \mathbf{e}_r}{\partial \phi} \times r\, \frac{\partial \mathbf{e}_r}{\partial \theta} \right) \\
&= \frac{\partial r}{\partial \phi}\, \frac{\partial r}{\partial \theta}\, \underbrace{(\mathbf{e}_r \times \mathbf{e}_r)}_{=0} + r\, \frac{\partial r}{\partial \phi} \left(\mathbf{e}_r \times \frac{\partial \mathbf{e}_r}{\partial \theta} \right) + r\, \frac{\partial r}{\partial \theta} \left(\frac{\partial \mathbf{e}_r}{\partial \phi} \times \mathbf{e}_r \right) + r^2 \left(\frac{\partial \mathbf{e}_r}{\partial \phi} \times \frac{\partial \mathbf{e}_r}{\partial \theta} \right) \\
&= r\, \frac{\partial r}{\partial \phi} \left(\mathbf{e}_r \times \frac{\partial \mathbf{e}_r}{\partial \theta} \right) + r\, \frac{\partial r}{\partial \theta} \left(\frac{\partial \mathbf{e}_r}{\partial \phi} \times \mathbf{e}_r \right) + r^2 \left(\frac{\partial \mathbf{e}_r}{\partial \phi} \times \frac{\partial \mathbf{e}_r}{\partial \theta} \right) \\
&\overset{(4.15)}{=} r\, \frac{\partial r}{\partial \phi} \left(\mathbf{e}_r \times \mathbf{e}_\theta \right) + r\, \frac{\partial r}{\partial \theta} \left(\sin\theta\, \mathbf{e}_\phi \times \mathbf{e}_r \right) + r^2 \left(\sin\theta\, \mathbf{e}_\phi \times \mathbf{e}_\theta \right) \\
&\overset{(4.16)}{=} r\, \frac{\partial r}{\partial \phi}\, \mathbf{e}_\phi + r\, \sin\theta\, \frac{\partial r}{\partial \theta}\, \mathbf{e}_\theta - r^2\, \sin\theta\, \mathbf{e}_r \,. \qquad (4.17)
\end{aligned}$$

Once we have the surface normal direction, by exploiting orthonormal properties it is not difficult to express its Euclidean norm as

$$\begin{aligned}
|\mathbf{n}|^2 = \mathbf{n} \cdot \mathbf{n} &= r^2 \left[\left(\frac{\partial r}{\partial \phi} \right)^2 + \sin^2\theta \left(\frac{\partial r}{\partial \theta} \right)^2 + r^2 \sin^2\theta \right] \\
\Leftrightarrow \quad |\mathbf{n}| &= r \sqrt{ \left(\frac{\partial r}{\partial \phi} \right)^2 + \sin^2\theta \left(\frac{\partial r}{\partial \theta} \right)^2 + r^2 \sin^2\theta } \,. \qquad (4.18)
\end{aligned}$$

Now, we are in the position to evaluate the expression $\mathbf{n} \cdot \mathbf{L}$ which will be used to derive the generalised brightness equation in the next section. Based on Figure 4.1, the light direction **L** is given by

$$\mathbf{L} = -\,\mathbf{e}_r\,. \tag{4.19}$$

Hence, using the surface normal vector (4.17) and the light direction (4.19) we obtain

$$\mathbf{n}\cdot\mathbf{L} = \left(r\,\frac{\partial r}{\partial\phi}\,\mathbf{e}_\phi + r\,\sin\theta\,\frac{\partial r}{\partial\theta}\,\mathbf{e}_\theta - r^2\,\sin\theta\,\mathbf{e}_r \right)\cdot(-\,\mathbf{e}_r) = r^2\,\sin\theta\,. \tag{4.20}$$

This computation result will be used in the next section for deriving the generalised Lambertian brightness equation.

4.2.1 Generalised Lambertian Brightness Equation

At this point, we have all the necessary components at hand for computing the brightness equation in spherical coordinates. Plugging all computed expressions into the brightness equation yields

$$\begin{aligned}
& I = \frac{1}{r^2}\left(\frac{\mathbf{n}}{|\mathbf{n}|}\cdot\mathbf{L}\right) \\
\iff\quad & r^2\,I\,|\mathbf{n}| - \mathbf{n}\cdot\mathbf{L} = 0 \\
\underset{(4.20)}{\overset{(4.18)}{\iff}}\quad & r^3\,I\sqrt{\left(\frac{\partial r}{\partial\phi}\right)^2 + \sin^2\theta\left(\frac{\partial r}{\partial\theta}\right)^2 + r^2\,\sin^2\theta} - r^2\,\sin\theta = 0 \\
\iff\quad & r^4\,\sin\theta\,I\sqrt{\frac{1}{r^2\,\sin^2\theta}\left(\frac{\partial r}{\partial\phi}\right)^2 + \frac{1}{r^2}\left(\frac{\partial r}{\partial\theta}\right)^2 + 1} - r^2\,\sin\theta = 0 \\
\iff\quad & I\sqrt{\frac{1}{r^2\,\sin^2\theta}\left(\frac{\partial r}{\partial\phi}\right)^2 + \frac{1}{r^2}\left(\frac{\partial r}{\partial\theta}\right)^2 + 1} - \frac{1}{r^2} = 0\,.
\end{aligned} \tag{4.21}$$

Since the term inside the square root of (4.21) corresponds to the gradient with respect to φ and θ in the spherical system, we finally attain the following compact *generalised Lambertian brightness equation* [93]

$$H_{\text{GBE-L}}\,(\boldsymbol{\theta},\nabla r, r) = 0\,, \tag{4.22}$$

where the Hamiltonian H is defined by

$$H_{\text{GBE-L}}\,(\boldsymbol{\theta},\nabla r, r) = I\,\sqrt{|\nabla r|^2 + 1} - \frac{1}{r^2}\,. \tag{4.23}$$

The gradient ∇ in (4.23) must be understood in terms of spherical systems [49] based on the relationship (4.10). This means that

$$\nabla r := \nabla_{\boldsymbol{\theta}}\, r = \nabla_{(\theta,\phi)}\, r = \frac{1}{r}\left(\frac{\partial r}{\partial \theta}\right)\mathbf{e}_\theta + \frac{1}{r\sin\theta}\left(\frac{\partial r}{\partial \phi}\right)\mathbf{e}_\phi\,. \tag{4.24}$$

As in the Cartesian case, the model (4.22) also takes the form of general-type Hamiltonian. In this context, solutions to the HJE (4.22) can also be understood in the viscosity sense [63].

4.3 Oren-Nayar SfS in Spherical Coordinates

After we have derived the general brightness equation in spherical coordinates for the Lambertian case, let us now discuss how this idea can be extended to non-Lambertian surface models. In this context, we consider the surface models of Oren-Nayar as an example. To this end, based on (3.52) and (3.55) we define the image intensity I as the ratio between the reflected light radiance and the irradiance of the light source with the uniform albedo ρ. This yields

$$I := \frac{L_s}{\left(\dfrac{\rho}{\pi}\, I_0\right)} = \frac{\pi}{\rho}\frac{L_s}{I_0}\,. \tag{4.25}$$

By combining the result (4.25) and (3.52), we obtain the following brightness equation [6] with the Oren-Nayar surface reflectance

$$I = \frac{1}{r^2}\cos\theta_i\;\big(A + B\sin\alpha\;\tan\beta\;\max\big(0, \cos(\phi_r - \phi_i)\big)\big)\,, \tag{4.26}$$

where A and B depend on the Gaussian facet statistics via the roughness parameter (standard deviation) σ. Besides, two angle variables α and β are defined as in (3.19) and (3.20), respectively.

For general scene geometry, it can be noted that the brightness equation (4.26) depends on several angles instead of one, as in the case of the limited scene geometry (3.55). As already observed in Figure 3.7, this is due to the fact that the viewing direction plays actually a prominent role for the image irradiance when dealing with Oren-Nayar reflectance, cf. Figure 3.3(a).

In this context, to establish a relationship between the scene geometry illustrated in Figure 4.1 and the Oren-Nayar BRDF geometry including several angles depicted in Figure 3.6 and 3.8, we adhere to the following conventions on the angles in the Oren-Nayar brightness equation (4.26): θ_i represents the angle between the surface normal vector $\mathbf{N}$ and the light source direction $\mathbf{L}$, θ_r stands for the angle between the surface normal vector $\mathbf{N}$ and the camera direction $\mathbf{V}$, ϕ_i is the angle between the projection of the light source direction **L** and the x-axis onto the (x, y)-plane, ϕ_r denotes the angle between the projection of the viewing direction **V** and the x-axis onto the (x, y)-plane, and the two variables α and β select the maximum and minimum between the angles θ_i and θ_r, respectively.

4.3.1 Generalised Oren-Nayar Brightness Equation

To derive a generalised Oren-Nayar brightness equation, all the terms in the brightness equation (4.26) should be formulated in terms of spherical coordinates as we have conducted for the Lambertian case in Section 4.2. However, since the difference between the Lambertian surface and the Oren-Nayar one is made only in the reflectance not in the scene geometry, most expressions from Section 4.2 can be readily used for the Oren-Nayar case. Hence, what remains to be computed is the viewing direction **v** of the camera and the trigonometric terms.

Viewing Direction

From Figure 4.1, the viewing direction corresponds to

$$\mathbf{v} \;=\; \overrightarrow{SC} \;=\; \overrightarrow{LC} - \overrightarrow{LS}\,. \tag{4.27}$$

By means of the spherical basis vectors, we reformulate the viewing direction vector as

$$\mathbf{v} \overset{(4.1)}{=} \left(v_1\,\mathbf{e}_r + v_2\,\mathbf{e}_\theta + v_3\,\mathbf{e}_\phi\right) - r\,\mathbf{e}_r = (v_1 - r)\;\mathbf{e}_r + v_2\,\mathbf{e}_\theta + v_3\,\mathbf{e}_\phi \tag{4.28}$$

where

$$v_1 = \sqrt{o_1^2 + o_2^2 + o_3^2}\,, \quad v_2 = \arctan\left(\frac{o_2}{o_1}\right)\,, \quad v_3 = \arccos\left(\frac{o_3}{\sqrt{o_1^2 + o_2^2 + o_3^2}}\right). \tag{4.29}$$

Hence, the normalised viewing vector **V** of (4.28) is given by

$$\mathbf{V} = \frac{\mathbf{v}}{|\mathbf{v}|} \overset{(4.28)}{=} \frac{(v_1 - r)\;\mathbf{e}_r + v_2\,\mathbf{e}_\theta + v_3\,\mathbf{e}_\phi}{\sqrt{(v_1 - r)^2 + v_2^2 + v_3^2}}\,. \tag{4.30}$$

Trigonometric Terms

Now we are in the position to express all the trigonometric terms in the Oren-Nayar brightness equation (4.26) with reference to the spherical system because we know at this point all necessary elements: the surface normal vector **N**, the light direction **L**, as well as the viewing direction **V**.

Term $\cos\theta_i$**.** Since θ_i represents the angle between the surface normal (4.17) and light source direction (4.19) based on Figure 3.8, its cosine can be described as

$$\begin{aligned}
\cos\,\theta_i = \mathbf{N}\cdot\mathbf{L} = \frac{\mathbf{n}}{|\mathbf{n}|}\cdot\mathbf{L} &\overset{(4.17)}{\underset{(4.19)}{=}} \frac{\left(r\,\dfrac{\partial r}{\partial\phi}\,\mathbf{e}_\phi + r\,\sin\theta\,\dfrac{\partial r}{\partial\theta}\,\mathbf{e}_\theta - r^2\,\sin\theta\,\mathbf{e}_r\right)\cdot(-\mathbf{e}_r)}{|\mathbf{n}|} \\
&\overset{(4.18)}{=} \frac{r^2\,\sin\theta}{r\sqrt{\left(\dfrac{\partial r}{\partial\phi}\right)^2 + \sin^2\theta\left(\dfrac{\partial r}{\partial\theta}\right)^2 + r^2\,\sin^2\theta}} \\
&= \frac{r^2\,\sin\theta}{r^2\,\sin\theta\sqrt{\dfrac{1}{r^2\,\sin^2\theta}\left(\dfrac{\partial r}{\partial\phi}\right)^2 + \dfrac{1}{r^2}\left(\dfrac{\partial r}{\partial\theta}\right)^2 + 1}} \overset{(4.24)}{=} \frac{1}{\sqrt{|\nabla r|^2+1}}\,. \qquad (4.31)
\end{aligned}$$

Term $\cos\theta_r$**.** This term can be handled in an analogous manner to the case of $\cos\theta_i$. Since θ_r stands for the angle between the surface normal and camera direction based on Figure 3.8, we can formulate the term $\cos\theta_r$ as

$$\begin{aligned}
&\cos\theta_r = \mathbf{N}\cdot\mathbf{V} = \frac{\mathbf{n}}{|\mathbf{n}|}\cdot\frac{\mathbf{v}}{|\mathbf{v}|} \\
&\overset{(4.17)}{\underset{(4.30)}{=}} \frac{\left(r\left(\dfrac{\partial r}{\partial\phi}\right)\mathbf{e}_\phi + r\,\sin\theta\left(\dfrac{\partial r}{\partial\theta}\right)\mathbf{e}_\theta - r^2\,\sin\theta\,\mathbf{e}_r\right)\cdot\big((v_1-r)\,\mathbf{e}_r + v_2\,\mathbf{e}_\theta + v_3\,\mathbf{e}_\phi\big)}{|\mathbf{n}|\,|\mathbf{v}|} \\
&\overset{(4.18)}{=} \frac{r\left(\dfrac{\partial r}{\partial\phi}\right)v_3 + r\,\sin\theta\left(\dfrac{\partial r}{\partial\theta}\right)v_2 - r^2\,(v_1-r)\,\sin\theta}{r\,|\mathbf{v}|\sqrt{\left(\dfrac{\partial r}{\partial\phi}\right)^2 + \sin^2\theta\left(\dfrac{\partial r}{\partial\theta}\right)^2 + r^2\,\sin^2\theta}} \\
&= \frac{r^2\,\sin\theta\left(\dfrac{v_3}{r\,\sin\theta}\left(\dfrac{\partial r}{\partial\phi}\right) + \dfrac{v_2}{r}\left(\dfrac{\partial r}{\partial\theta}\right) - (v_1-r)\right)}{r^2\,\sin\theta\,|\mathbf{v}|\sqrt{\dfrac{1}{r^2\,\sin^2\theta}\left(\dfrac{\partial r}{\partial\phi}\right)^2 + \dfrac{1}{r^2}\left(\dfrac{\partial r}{\partial\theta}\right)^2 + 1}} \\
&\overset{(4.24)}{=} \frac{1}{|\mathbf{v}|\sqrt{|\nabla r|^2+1}}\underbrace{\left(\frac{v_3}{r\,\sin\theta}\left(\frac{\partial r}{\partial\phi}\right) + \frac{v_2}{r}\left(\frac{\partial r}{\partial\theta}\right) - (v_1-r)\right)}_{=:\,W_{\cos\theta_r}} = \frac{W_{\cos\theta_r}}{|\mathbf{v}|\sqrt{|\nabla r|^2+1}}\,. \qquad (4.32)
\end{aligned}$$

Term $\sin\theta_i$ **and Term** $\sin\theta_r$**.** Once we have the cosine terms determined by the angle θ_i as well as the angle θ_r, respectively, the corresponding sine terms can be obtained with the help of trigonometric identities. This is given by

$$\sin\theta_i = \sqrt{1-\cos^2\theta_i} \overset{(4.31)}{=} \sqrt{1-\left(\frac{1}{\sqrt{|\nabla r|^2+1}}\right)^2} = \frac{|\nabla r|}{\sqrt{|\nabla r|^2+1}} \tag{4.33}$$

and

$$\begin{aligned}\sin\theta_r &= \sqrt{1-\cos^2\theta_r} \overset{(4.32)}{=} \sqrt{1-\left(\frac{W_{\cos\theta_r}}{|\mathbf{v}|\sqrt{|\nabla r|^2+1}}\right)^2} \\ &= \sqrt{\frac{|\mathbf{v}|^2\left(|\nabla r|^2+1\right)-W^2_{\cos\theta_r}}{|\mathbf{v}|^2\left(|\nabla r|^2+1\right)}} = \frac{\sqrt{|\mathbf{v}|^2\left(|\nabla r|^2+1\right)-W^2_{\cos\theta_r}}}{|\mathbf{v}|\sqrt{|\nabla r|^2+1}}\,.\end{aligned} \tag{4.34}$$

Term $\sin\alpha$ **and Term** $\tan\beta$**.** In addition to the cosine terms from the incident and viewing angles, we also need the terms $\sin\alpha$ and $\tan\beta$ in the Oren-Nayar brightness equation (4.26). According to (3.20), these are defined as

$$\sin\alpha \overset{(3.20)}{=} \sin\left(\max\left(\theta_{\mathrm{i}},\theta_{\mathrm{r}}\right)\right) \quad \text{and} \quad \tan\beta \overset{(3.20)}{=} \tan\left(\min\left(\theta_{\mathrm{i}},\theta_{\mathrm{r}}\right)\right)\,. \tag{4.35}$$

Since we have already derived the sine and the cosine expressions with respect to each angle θ_i and θ_r, the tangent function in (4.35) can be obtained by the properties of trigonometric functions.

Term $\cos(\phi_r-\phi_i)$**.** At this point, what finally remains to be computed is the expression $\cos\left(\phi_r-\phi_i\right)$ in the Oren-Nayar brightness equation (4.26). As shown in Figure 3.6 and 3.8, the angle $\left(\phi_r-\phi_i\right)$ in the expression represents the difference of two azimuth angles that are projected onto the (x,y)-plane by the light direction $\mathbf{L}$ and the viewing direction $\mathbf{V}$. To distinguish the projected vectors from the original one, we define the projected vectors of $\mathbf{L}$ and $\mathbf{V}$ as $\widehat{\mathbf{L}}$ and $\widehat{\mathbf{V}}$, respectively. Then, the computation $\cos\left(\phi_r-\phi_i\right)$ can be realised by substituting $\frac{\pi}{2}$ for θ in the orthonormal basis vectors (4.11). This means that we use only the (x,y)-plane related elements in (4.1) and (4.29), respectively. As a result, from the light direction we obtain the projected light vector $\widehat{\mathbf{L}}$ as

$$\widehat{\mathbf{L}} \overset{(4.19)}{=} -\hat{\mathbf{e}}_r \underset{\left(\theta=\frac{\pi}{2}\right)}{\overset{(4.11)}{=}} -\begin{bmatrix}\cos\phi\\ \sin\phi\\ 0\end{bmatrix}. \tag{4.36}$$

In a similar way, from the viewing direction (4.28) we obtain the projected viewing vector $\widehat{\mathbf{v}}$ as

$$\hat{\mathbf{v}} \overset{(4.28)}{=} (\hat{v}_1 - \hat{r})\ \hat{\mathbf{e}}_r + \hat{v}_2\,\hat{\mathbf{e}}_\theta + \hat{v}_3\,\hat{\mathbf{e}}_\phi \underset{(\theta = \frac{\pi}{2})}{\overset{(4.11)}{=}} (\hat{v}_1 - \hat{r}) \begin{bmatrix} \cos\phi \\ \sin\phi \\ 0 \end{bmatrix} + \hat{v}_2 \begin{bmatrix} 0 \\ 0 \\ -1 \end{bmatrix} + \hat{v}_3 \begin{bmatrix} -\sin\phi \\ \cos\phi \\ 0 \end{bmatrix}$$

$$= \begin{bmatrix} (\hat{v}_1 - \hat{r})\ \cos\phi - \hat{v}_3\ \sin\phi \\ (\hat{v}_1 - \hat{r})\ \sin\phi + \hat{v}_3\ \cos\phi \\ -\hat{v}_2 \end{bmatrix} \qquad \text{with} \qquad |\hat{\mathbf{v}}| = \sqrt{(\hat{v}_1 - \hat{r})^2 + \hat{v}_2^2 + \hat{v}_3^2}\,, \tag{4.37}$$

where $\hat{r}$ and $\hat{v}_1, \hat{v}_2, \hat{v}_3$ denote the projected version onto (x, y)-plane of r (4.1) and v (4.29), respectively. These correspond to

$$\hat{r} \overset{(4.1)}{=} \sqrt{X^2 + Y^2} \overset{(4.3)}{=} \sqrt{r^2\ \sin^2\theta\ \left(\cos^2\phi + \sin^2\phi\right)} = r\ \sin\theta \tag{4.38}$$

and

$$\hat{v}_1 \overset{(4.29)}{=} \sqrt{o_1^2 + o_2^2}\,, \quad \hat{v}_2 \overset{(4.29)}{=} \arccos\left(\frac{0}{\sqrt{o_1^2 + o_2^2}}\right) = \frac{\pi}{2}\,, \quad \hat{v}_3 \overset{(4.29)}{=} \arctan\left(\frac{o_2}{o_1}\right). \tag{4.39}$$

Therefore, taking a dot product between the projected light vector and the projected viewing vector yields

$$\widehat{\mathbf{L}} \cdot \widehat{\mathbf{V}} = \widehat{\mathbf{L}} \cdot \frac{\hat{\mathbf{v}}}{|\hat{\mathbf{v}}|} = \cos\left(\phi_r - \phi_i\right) = \frac{\hat{r} - \hat{v}_1}{|\hat{\mathbf{v}}|}\,. \tag{4.40}$$

Derivation of Hamilton-Jacobi Equations with Oren-Nayar Reflectance

At this point, all necessary computations for deriving the Oren-Nayar brightness equation (4.26) are available in terms of spherical coordinates. This leaves the last step to obtain the generalised brightness equation: case distinctions. In contrast to the brightness equation with Lambertian surface, this step is necessary because the brightness equation of the Oren-Nayar surface (4.26) is described by several trigonometric terms of polar and azimuth angles as well as *min* and *max* operators.

Case I. First, we deal with the case $(\theta_i \geqslant \theta_r)$ and $(\phi_r - \phi_i) \in [0, \frac{\pi}{2}) \cup (\frac{3}{2}\pi, 2\pi]$. If the angles are in the given range, by the properties of the trigonometric functions the following implication holds

$$\max\left(0, \cos\left(\phi_r - \phi_i\right)\right) = \cos\left(\phi_r - \phi_i\right) \tag{4.41}$$

and

$$\sin\alpha \overset{(4.35)}{=} \sin\left(\max\left(\theta_{\mathrm{i}},\theta_{\mathrm{r}}\right)\right) = \sin\theta_i\,, \qquad \tan\beta \overset{(4.35)}{=} \tan\left(\min\left(\theta_{\mathrm{i}},\theta_{\mathrm{r}}\right)\right) = \tan\theta_r\,. \tag{4.42}$$

Then, by plugging (4.41) and (4.42) into the brightness equation (4.26) we obtain

$$\begin{aligned} I &= \frac{1}{r^2}\,\cos\theta_i\left(A + B\cos\left(\phi_r - \phi_i\right)\,\sin\theta_i\,\frac{\sin\theta_r}{\cos\theta_r}\right) \\ \Leftrightarrow \quad r^2\,I &= A\cos\theta_i + B\cos\left(\phi_r-\phi_i\right)\,\cos\theta_i\,\sin\theta_i\,\frac{\sin\theta_r}{\cos\theta_r}\,. \end{aligned} \tag{4.43}$$

Moreover, replacing the trigonometric terms in (4.43) with corresponding formulations given in (4.31), (4.33), (4.34), and (4.40) further leads to the following HJE

$$\begin{aligned} (4.43) \Leftrightarrow\; & A\,(\mathbf{N}\cdot\mathbf{L}) + B\,\left(\widehat{\mathbf{L}}\cdot\widehat{\mathbf{V}}\right)\,(\mathbf{N}\cdot\mathbf{L})\,\sqrt{1-(\mathbf{N}\cdot\mathbf{L})^2}\,\frac{\sqrt{1-(\mathbf{N}\cdot\mathbf{V})^2}}{(\mathbf{N}\cdot\mathbf{V})} - r^2\,I = 0 \\ \Leftrightarrow\; & \frac{A}{\sqrt{|\nabla r|^2+1}} + \frac{B\,\left(\widehat{\mathbf{L}}\cdot\widehat{\mathbf{V}}\right)}{\sqrt{|\nabla r|^2+1}}\,\frac{|\nabla r|}{\sqrt{|\nabla r|^2+1}}\,\frac{\dfrac{\sqrt{|\mathbf{v}|^2\,\left(|\nabla r|^2+1\right) - W_{\cos\theta_r}^2}}{|\mathbf{v}|\,\sqrt{|\nabla r|^2+1}}}{\dfrac{W_{\cos\theta_r}}{|\mathbf{v}|\,\sqrt{|\nabla r|^2+1}}} - r^2\,I = 0 \\ \Leftrightarrow\; & \frac{A}{\sqrt{|\nabla r|^2+1}} + \frac{B\,(\widehat{\mathbf{L}}\cdot\widehat{\mathbf{V}})\,|\nabla r|}{|\nabla r|^2+1}\,\frac{\sqrt{|\mathbf{v}|^2\,\left(|\nabla r|^2+1\right) - W_{\cos\theta_r}^2}}{W_{\cos\theta_r}} - r^2\,I = 0\,. \end{aligned} \tag{4.44}$$

Special Case of Case I. Before we turn to the second case, we describe the standard setting, i.e. the light source being located at the optical centre of the camera for the perspective Oren-Nayar SfS [6]. We have seen the Cartesian formulations of this model in Section 3.4. This situation describes if $\theta_i = \theta_r$ and $\phi_i = \phi_r$ and is actually a special case of **Case I**. Hence, in view of (3.53) and (4.42) we obtain the following relationship

$$\sin\alpha \underset{(4.42)}{\overset{(3.53)}{=}} \sin\theta\,, \qquad \tan\beta \underset{(4.42)}{\overset{(3.53)}{=}} \tan\theta\,. \tag{4.45}$$

In addition, the same azimuth angle implies

$$\max\left(0,\cos\left(\phi_r-\phi_i\right)\right) = \max\left(0,\cos 0\right) = 1\,. \tag{4.46}$$

The expressions (4.45) and (4.46) allows us to reformulate the brightness equation (4.26) as

$$I = \frac{1}{r^2}\,\left(A\,\cos\theta + B\,\sin^2\theta\right)\,. \tag{4.47}$$

Consequently, by applying (4.31) and (4.33) to (4.47) we attain the following HJE

$$
\begin{aligned}
(4.47) \Leftrightarrow\ & A \cos\theta + B \sin^2\theta - r^2 I = 0 \\
\Leftrightarrow\ & \frac{A}{\sqrt{|\nabla r|^2+1}} + B\left(\frac{|\nabla r|}{\sqrt{|\nabla r|^2+1}}\right)^2 - r^2 I = 0 \\
\Leftrightarrow\ & \frac{A}{\sqrt{|\nabla r|^2+1}} + \frac{B\,|\nabla r|^2}{|\nabla r|^2+1} - r^2 I = 0\,.
\end{aligned}
\tag{4.48}
$$

Case II. For the second case, we consider when $\theta_i < \theta_r$ and $(\phi_r - \phi_i) \in [0, \frac{\pi}{2}) \cup (\frac{3}{2}\pi, 2\pi]$. Since the only difference for the second case is for the inequality of normal angles, i.e. instead of $\theta_i \geqslant \theta_r$ we assume $\theta_i < \theta_r$, the implication for the first case (4.41) still remains valid:

$$
\max\left(0, \cos\left(\phi_r - \phi_i\right)\right) = \cos\left(\phi_r - \phi_i\right)\,. \tag{4.49}
$$

However, the expression (4.42) has different result for this case

$$
\sin\alpha \overset{(4.35)}{=} \sin\left(\max\left(\theta_\mathrm{i}, \theta_\mathrm{r}\right)\right) = \sin\theta_r\,, \qquad \tan\beta \overset{(4.35)}{=} \tan\left(\min\left(\theta_\mathrm{i}, \theta_\mathrm{r}\right)\right) = \tan\theta_i\,. \tag{4.50}
$$

As a result, the brightness equation becomes

$$
\begin{aligned}
& I = \frac{1}{r^2} \cos\theta_i \left(A + B\cos\left(\phi_r - \phi_i\right)\, \sin\theta_r\, \frac{\sin\theta_i}{\cos\theta_i}\right) \\
\Leftrightarrow\quad & r^2 I = A\cos\theta_i + B\cos\left(\phi_r - \phi_i\right)\, \sin\theta_r\, \sin\theta_i\,.
\end{aligned}
\tag{4.51}
$$

As carried out for the first case, plugging the corresponding expressions into the brightness equation (4.51) gives the HJE

$$
\begin{aligned}
(4.51) \Leftrightarrow\ & A\ (\mathbf{N}\cdot\mathbf{L}) + B\left(\widehat{\mathbf{L}}\cdot\widehat{\mathbf{V}}\right)\sqrt{1-(\mathbf{N}\cdot\mathbf{V})^2}\sqrt{1-(\mathbf{N}\cdot\mathbf{L})^2} - r^2 I = 0 \\
\Leftrightarrow\ & \frac{A}{\sqrt{|\nabla r|^2+1}} + B\left(\widehat{\mathbf{L}}\cdot\widehat{\mathbf{V}}\right)\frac{|\nabla r|}{\sqrt{|\nabla r|^2+1}}\,\frac{\sqrt{|\mathbf{v}|^2\left(|\nabla r|^2+1\right) - W^2_{\cos\theta_r}}}{|\mathbf{v}|\ \sqrt{|\nabla r|^2+1}} - r^2 I = 0 \\
\Leftrightarrow\ & \frac{A}{\sqrt{|\nabla r|^2+1}} + \frac{B\,(\widehat{\mathbf{L}}\cdot\widehat{\mathbf{V}})\,|\nabla r|}{|\mathbf{v}|\ (|\nabla r|^2+1)}\sqrt{|\mathbf{v}|^2\left(|\nabla r|^2+1\right) - W^2_{\cos\theta_r}} - r^2 I = 0\,.
\end{aligned}
\tag{4.52}
$$

Case III. The rest case covers the range of the azimuth angle $(\phi_r - \phi_i) \in [\frac{\pi}{2}, \frac{3}{2}\pi]$. This suggests that the value of the cosine function is negative. Therefore, we obtain

$$
\max\left(0, \cos\left(\phi_r - \phi_i\right)\right) = 0\,. \tag{4.53}
$$

This turns the brightness equation into

$$I = \frac{1}{r^2} \, A \, \cos\theta_i \, . \tag{4.54}$$

Hence, from (4.54) we attain the following HJE using the computation result in (4.31)

$$\begin{aligned}
(4.54) \Leftrightarrow {} & r^2 I - A \, (\mathbf{N} \cdot \mathbf{L}) = 0 \\
\Leftrightarrow {} & r^2 I - \frac{A}{\sqrt{|\nabla r|^2 + 1}} = 0 \\
\Leftrightarrow {} & r^2 I \sqrt{|\nabla r|^2 + 1} - A = 0 \\
\Leftrightarrow {} & I \sqrt{|\nabla r|^2 + 1} - \frac{A}{r^2} = 0 \, .
\end{aligned} \tag{4.55}$$

One should note that this HJE becomes the generalised brightness equation with the Lambertian reflectance if the roughness parameter is $\sigma = 0$, cf. (4.23).

We have made case distinctions so far depending on the values of the involved trigonometric functions in the Oren-Nayar brightness equation (4.26). In what follows, we summarise the result of these case distinctions for an overview. This includes the implications of the trigonometric terms after applying the *min* and *max* operators within the specified range of the indicated angles. Moreover, we also state the corresponding generalised brightness equation according to the case dependent trigonometric terms as well as the associated Hamilton-Jacobi equation with a Hamiltonian.

Case I: $(\theta_i \geqslant \theta_r)$ and $(\phi_r - \phi_i) \in \left[0, \frac{\pi}{2}\right) \cup \left(\frac{3}{2}\pi, 2\pi\right]$

1. Azimuth angle implication: $\max\left(0, \cos\left(\phi_r - \phi_i\right)\right) = \cos\left(\phi_r - \phi_i\right)$
2. Polar angle implication: $\sin\alpha = \sin\theta_i$, $\tan\beta = \tan\theta_r$
3. Brightness equation: $I = \frac{1}{r^2} \cos\theta_i \left(A + B \cos\left(\phi_r - \phi_i\right) \, \sin\theta_i \, \frac{\sin\theta_r}{\cos\theta_r} \right)$
4. Hamilton-Jacobi equation: $H_{\text{GBE-ON}}\left(\boldsymbol{\theta}, \nabla r, r\right) = 0$ with Hamiltonian

$$H_{\text{GBE-ON}}\left(\boldsymbol{\theta}, \nabla r, r\right) = \frac{A}{\sqrt{|\nabla r|^2 + 1}} + \frac{B \, (\widehat{\mathbf{L}} \cdot \widehat{\mathbf{V}}) \, |\nabla r|}{|\nabla r|^2 + 1} \, \frac{\sqrt{|\mathbf{v}|^2 \, \left(|\nabla r|^2 + 1\right) - W_{\cos\theta_r}^2}}{W_{\cos\theta_r}} - r^2 I$$

Special Case of Case I: $(\theta_i = \theta_r)$ and $(\phi_r = \phi_i)$

1. Azimuth angle implication: $\max\left(0, \cos\left(\phi_r - \phi_i\right)\right) = 1$
2. Polar angle implication: $\sin\alpha = \sin\theta\,, \tan\beta = \tan\theta \; \left(\theta := \theta_i = \theta_r = \alpha = \beta\right)$
3. Brightness equation: $I = \frac{1}{r^2}\left(A\ \cos\theta + B\ \sin^2\theta\right)$
4. Hamilton-Jacobi equation: $H_{\text{GBE-ON}}\left(\boldsymbol{\theta}, \nabla r, r\right) = 0$ with Hamiltonian

$$H_{\text{GBE-ON}}\left(\boldsymbol{\theta}, \nabla r, r\right) = \frac{A}{\sqrt{|\nabla r|^2+1}} + \frac{B\,|\nabla r|^2}{|\nabla r|^2+1} - r^2\,I$$

Case II: $(\theta_i < \theta_r)$ and $\left(\phi_r - \phi_i\right) \in \left[0, \frac{\pi}{2}\right) \cup \left(\frac{3}{2}\pi, 2\pi\right]$

1. Azimuth angle implication: $\max\left(0, \cos\left(\phi_r - \phi_i\right)\right) = \cos\left(\phi_r - \phi_i\right)$
2. Polar angle implication: $\sin\alpha = \sin\theta_r\,, \tan\beta = \tan\theta_i$
3. Brightness equation: $I = \frac{1}{r^2}\cos\theta_i\left(A + B\cos\left(\phi_r - \phi_i\right)\ \sin\theta_i\ \frac{\sin\theta_r}{\cos\theta_r}\right)$
4. Hamilton-Jacobi equation: $H_{\text{GBE-ON}}\left(\boldsymbol{\theta}, \nabla r, r\right) = 0$ with Hamiltonian

$$H_{\text{GBE-ON}}\left(\boldsymbol{\theta}, \nabla r, r\right) = \frac{A}{\sqrt{|\nabla r|^2+1}} + \frac{B\,(\widehat{\mathbf{L}}\cdot\widehat{\mathbf{V}})\,|\nabla r|}{|\mathbf{v}|\,\left(|\nabla r|^2+1\right)}\sqrt{|\mathbf{v}|^2\,\left(|\nabla r|^2+1\right) - W^2_{\cos\theta_r}} - r^2\,I$$

Case III: For any θ_i, θ_r and $\left(\phi_r - \phi_i\right) \in \left[\frac{\pi}{2}, \frac{3}{2}\pi\right]$

1. Azimuth angle implication: $\max\left(0, \cos\left(\phi_r - \phi_i\right)\right) = 0$
2. Polar angle implication: No influence
3. Brightness equation: $I = \frac{1}{r^2}A\ \cos\theta_i$
4. Hamilton-Jacobi equation: $H_{\text{GBE-ON}}\left(\boldsymbol{\theta}, \nabla r, r\right) = 0$ with Hamiltonian

$$H_{\text{GBE-ON}}\left(\boldsymbol{\theta}, \nabla r, r\right) = I\,\sqrt{|\nabla r|^2+1} - \frac{A}{r^2}$$

So far, we have derived and lined up the brightness equations as well as the corresponding HJEs for each case. As can be observed, the HJEs for the general scene geometry with Oren-Nayar surface, i.e. (4.44), (4.48), (4.52), and (4.55), are much more complex than that of the Lambertian surface (3.70) and actually contain the Lambertian one as a special case as previously indicated. From the listed HJEs, it can be noticed that they all belong to the general-type of Hamiltonian by taking (2.24) into account, where the notion of viscosity solutions is required. In the next section, we present a FM-based algorithm for solving these HJEs.

4.4 Adapted Fast Marching Scheme for Spherical Coordinates

In this section, we derive an efficient numerical scheme for solving the general-type of HJEs that we have obtained in Section 4.2.1 for the Lambertian reflection model and in Section 4.3.1 for the Oren-Nayar reflection model with a flexible position of the light source.

In order to gain computational efficiency of the modern viscosity framework [63], we count on the FM method [229] that we have reviewed in Section 2.3. Given the fact that the FM method has been recognised as one of the most efficient solution algorithms for this kind of PDEs, we extend the adapted FM method [259], which is described in Cartesian coordinates. Therefore, the resulting scheme becomes a specifically tailored variant of the FM method that can handle general-type of Hamiltonians in a spherical system for a Cartesian input image. However, the fundamental principles of the adapted FM method remain unchanged even in a spherical system.

4.4.1 Initialisation

Based on the discussions in Section 3.5.2, the information of starting points must be provided for FM-based methods. Therefore, as a first step we determine critical points on the surface by identifying brightest pixels in the input image and use these pixels as seed points. As pointed out in Section 4.1, it should be noted that these brightest points are actually the closest points in a spherical coordinate system with the origin at the light source. While this would be possible with the same parametrisation and Cartesian coordinates, the resulting equations would be much more complex.

Consequently, the approximate solutions r at those locations can be computed by applying the first-order optimality condition $\nabla r = 0$ to the given HJEs without taking the information of neighbouring pixels into account. The same procedure has previously been applied for the Cartesian case in (3.72). Moreover, it can also be noted that this initialisation procedure is useful not only for finding critical points on the surface but also for partial well-posedness [44, 67, 195] with respect to the discussions on ambiguities of models in Section 3.5.3.

4.4.2 Update Process in Fast Marching Scheme

Once critical points are identified, we can let the radial depth information at critical points propagate to neighbouring grid points by updating depth values there relying on the update process of the FM method. This update process continues successively until all grid nodes have been visited and have a green label "known" as shown in Figure 2.14. Besides, this process is carried out with respect to the spherical grid (θ, ϕ) instead of the Cartesian one (X, Y). On that account, the decision how the depth values of "trial" nodes can be updated should be made first, i.e. neighbouring nodes in terms of FM terminology as in Section 2.3.3.

In order to update the radial depth, the corresponding HJEs must be solved at adjacent nodes. Since these HJEs are of general-type, we cannot directly find a solution like the eikonal equation that we have seen in Section 2.3. For this reason, we apply the regula falsi method as a root-finding algorithm and solve the nonlinear equation iteratively. For discretising the HJEs, the standard upwind scheme [219], i.e. (2.89) and (2.90), can be employed respecting the hyperbolic properties of the HJEs. This approach was previously realised with the Phong reflectance [259] and with the Oren-Nayar reflectance [256] for the restricted scene geometry in the Cartesian coordinate system, respectively.

During the iteration by the regula falsi method, it is inevitable to estimate the grey values of the input image at subpixel locations and to update accordingly based on the fact that the input image $I(X(\theta, \phi, r), Y(\theta, \phi, r))$ is first given in terms of Cartesian coordinates. The computation of the radial depth r is influenced by $(X, Y)^\top$ via the relationship (4.4) and (4.1). To take care of the situation, we evaluate the image brightness at subpixel positions by means of bilinear interpolation and update this image intensity at each iteration as a correction step within the iterative regula falsi framework. The iterations come to an end if the residual of successive results drops below a certain threshold.

4.4.3 Benefits of Adapted Fast Marching Method

Let us briefly summarise two major advantages of our adaptive FM-based approach.

Direct Computation of Radial Depth

On the one hand, one can compute the radial depth r directly in the viscosity sense with this method. Once the update process is over for all grid nodes, the result that we have attained corresponds to the one that we desired for. No further steps or constraints for surface reconstruction are required such as integration of gradient fields along with integrability constraints [89], which are often necessary in early work, e.g. [116]. One can also note that the direct computation is possible because of the combination between the general-type Hamiltonians from the modelling side and the construction of the iterative regula falsi framework that can actually handle the general-type HJEs from the numerical side.

Efficiency

On the other hand, one can gain the full efficiency that is directly inherited from the FM algorithm [229] with this approach. As we have seen in Section 2.3.3, this specific grid traversing strategy which starts from critical points and complies with Fermat's principle allows to compute a solution on each node by visiting it only once. During the computation, the only extra cost comes from the update process of the FM method because we have to solve complex nonlinear equations on each node with respect to the spherical system and this involves the iterative correction of the input grey values given by the typical Cartesian coordinates as we have pointed out. Thus, one can achieve high efficiency with the adapted FM method when it comes to PDE-based SfS models for the general scene geometry described by HJEs. The statement is valid not only for the model with the basic Lambertian surface but also for the model with the sophisticated Oren-Nayar one as well as potential models with other realistic reflectance functions.

4.5 Experimental Evaluation

In this section, we evaluate the perspective SfS method for the general scene geometry, first with a Lambertian surface, then with a Oren-Nayar type one. To this end, we consider both synthetic and real-world images.

4.5.1 Lambertian Surface

For the Lambertian surface, we first reconstruct the surface of a vase by applying the adapted FM method to our generalised brightness equation for Lambertian reflectance (4.22), which is equivalent to the Eq. (4.55) with $\sigma = 0$. The vase input image and the ground truth surface are displayed in Figure 4.5(a) and 4.5(b), respectively. From the shading patterns in Figure 4.5(a), one can infer that the light comes from the upper left corner on the scene. For the grid size in ϕ- and θ-direction, we have used the same value in both directions, i.e. $h_\phi = h_\theta =: \Delta_{\phi\theta} = 0.002$ (max of $\Delta_{\phi\theta} = 0.755$).

The computation result using our generalised model is shown in Figure 4.5(c). As can be clearly observed, the attained shape reconstruction is very close to that of the ground truth in Figure 4.5(b). However, when we make use of the standard SfS model (3.36) with grid spacing $h_1 = h_2 =: \Delta_{h_1 h_2} = 0.001465$ (max of $\Delta_{h_1 h_2} = 1.5$), i.e. the one with the light source being at the optical centre, by means of the same brightest points in the Cartesian system, the reconstruction quality seems to be rather poor as presented in Figure 4.5(d). This evidently demonstrates that the general brightness equation (4.22) has the capability of handling the flexible scene geometry and plays a crucial role in practice especially when the location of the light source is not close enough to the optical centre. This also follows our discussions in Section 4.1.

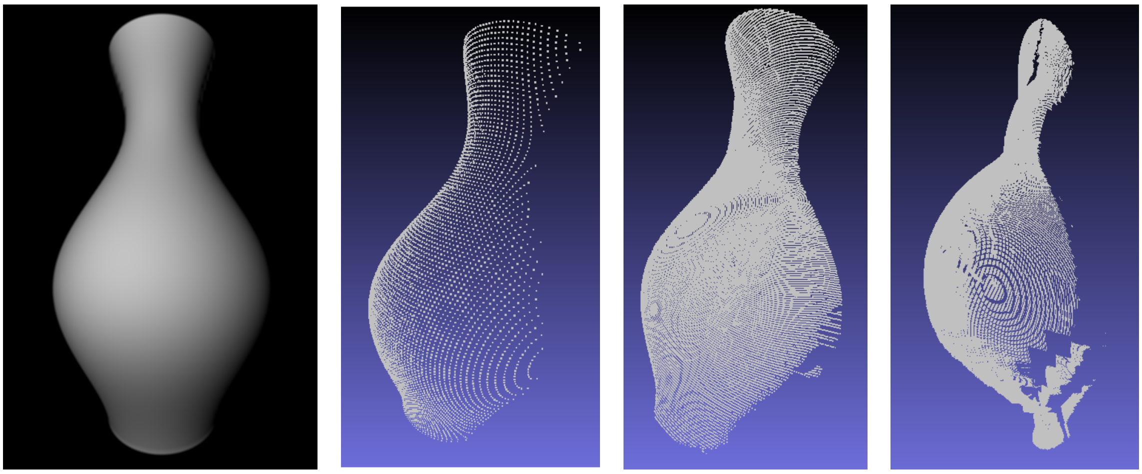
(a) Vase input image. (b) Ground truth. (c) Generalised Model. (d) Standard Model.

Figure 4.5. Reconstruction of the Vase with our generalised model for Lambertian surface. The employed grid sizes are $\Delta_{\phi\theta} = 0.002$ for the generalised model and $\Delta_{h_1 h_2} = 0.001465$ for the standard one, respectively.

Subsequently, we carry out a second experiment on a real-world image. The input image in Figure 4.6(a) is taken from a sculpture showing the head of a frog and there is a slight tilt of the light direction towards the right centre on the scene. The reconstructions are presented in Figure 4.6(b) and 4.6(c). Since our generalised model reconstructs a surface from the viewpoint of the light source, our computation results are reasonable. In fact, this implies that there exist certain limitations in practice on the difference of locations between a light source and the optical centre of a camera, although our general model is flexible enough to handle various scenarios with respect to the light positions.

Concerning the efficiency of our adapted FM method, the runtime amounts to approximately 40 seconds for a high resolution grid size 1024 × 1024. As indicated in Section 4.4.3, most overhead in this runtime does not come from the size of the input image but from the iterative correction step of the radial depth in the regula falsi framework.

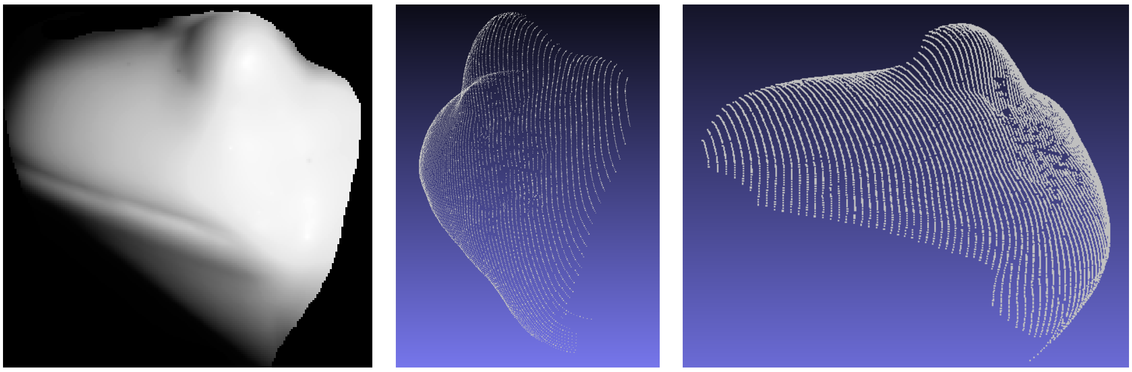

(a) Frog input image. (b) Generalised Model. (c) Generalised Model, rotated view.

Figure 4.6. Reconstruction of the Frog with our generalised model for Lambertian surface. The employed grid spacing is $\Delta_{\phi\theta} = 0.002$.

4.5.2 Oren-Nayar Surface

For evaluating the quality and robustness of our advanced model, we have applied the set of HJEs in Section 4.3.1 to endoscopic images provided by [94]. However, experiments with such real-world images are highly challenging [204, 238] since typically not all model parameters are available. Although the information on the position of the optical centre of the camera with reference to the light source is absolutely essential to our advanced model and moreover our model can actually handle flexible scenarios regarding light positions, typical data sets do not provide this important parameter, since it is, in general, not necessary for standard SfS models based on the restricted geometry [6, 171, 195, 258]. This, therefore, makes us estimate the relative position of the camera to the light source roughly by relying on the visual inspection of the images. In this context, we have chosen the position of the camera in a way that it is close by but *not negligibly adjacent* to the origin. Since in Section 4.5.1 we have demonstrated with the Lambertian surface that our generalised model which is capable of handling flexible scene geometry can gain significant advantages over a standard approach [93], let us focus on in this section the other two important aspects of our approach: the visual quality of the reconstruction as well as its robustness with respect to parameter variations.

In our first experiment, we investigate how grid resolutions in spherical coordinates influence on the quality of the reconstruction. To this end, we have applied our specifically tailored variant of FM method in Section 4.4 to the image of gastric antrum shown in Figure 4.7(a) by changing resolutions in spherical coordinate systems. During the computation, the roughness parameter $\sigma = \frac{\pi}{6}$ is used for the Oren-Nayar surface and the distance between two grid points in both ϕ- and θ-direction is the same constant value as in the Lambertian case, i.e. $h_\phi = h_\theta =: \Delta_{\phi\theta}$.

Figure 4.7 shows the different reconstruction qualities from lower to higher resolutions. While it is obvious that the reconstruction with a higher resolution demonstrates the considerable enhancement on the visual quality compared with that of lower ones, it should also be noted that the actual quality of the reconstruction has an upper bound, i.e. the resolution of the input image. During the update process within our FM framework, the input image is iteratively reevaluated at subpixel locations even though one makes use of finer meshes by refining the grid. Since we have placed the light source at the origin in our coordinate system as indicated previously, the computation is performed with reference to the light source. This makes the reconstruction have a slightly different inclined viewpoint comparing to that of the input image.

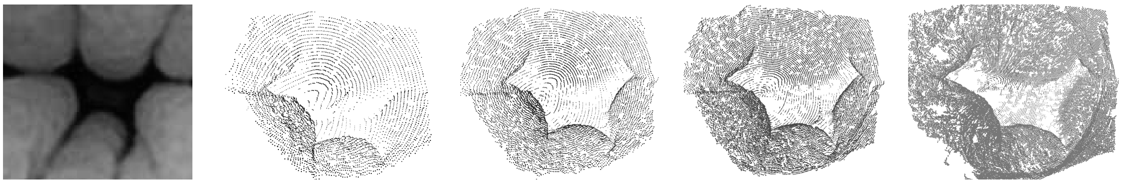

(a) Input image (115×106). (b) $\Delta_{\phi\theta} = 0.025$. (c) $\Delta_{\phi\theta} = 0.0175$. (d) $\Delta_{\phi\theta} = 0.0125$. (e) $\Delta_{\phi\theta} = 0.0075$.

Figure 4.7. Impact of grid resolutions on the quality of reconstructions. Reconstruction of gastric antrum with our generalised model for Oren-Nayar surface. The employed roughness parameter is $\sigma = \frac{\pi}{6}$.

In a second experiment, we look into how robust and stable our approach is subject to the selection of the roughness parameter σ for the Oren-Nayar reflectance model. Therefore, we have computed the reconstructions by applying our method to four different endoscopic images with different values of σ. The input images are displayed in Figure 4.8(a), 4.9(a), 4.10(a), and 4.11(a), each of which is denoted by the duodenum, the oesophagus, the papilla of Vater, and the stomach of lining, respectively. The corresponding reconstructions with different values of the roughness parameter σ are placed side by side according to each input image.

From the reconstructions, one can observe that the model yields reasonable results by showing important structures in the scene such as creases on the bottom in Figure 4.8, extruded region in Figure 4.9, a branched ridge in Figure 4.10 as well as the curved shape of the object and several valleys in Figure 4.11. Apart from the visual quality, the model behaves in a well-posed way with respect to the model parameter σ in the sense that the reconstructions are stable and continuously depend on it. This feature is particularly useful for SfS when it comes to real-world data sets without the information on parameter values, since one still has to estimate and specify the unknown values as well as adjust them accordingly.

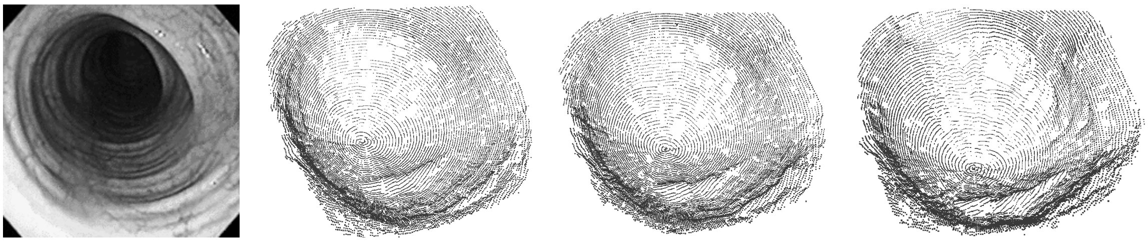

(a) Input image(211×208). (b) $\sigma = \frac{\pi}{6}$. (c) $\sigma = \frac{\pi}{4}$. (d) $\sigma = \frac{\pi}{2}$.

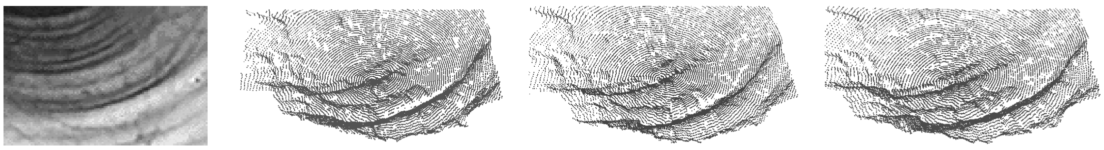

(e) Input image (cropped, 106 × 78). (f) $\sigma = \frac{\pi}{6}$. (g) $\sigma = \frac{\pi}{4}$. (h) $\sigma = \frac{\pi}{2}$.

Figure 4.8. Reconstruction of the duodenum with a mesh width $\Delta_{\phi\theta} = 0.0125$ and a grid size 504 × 504.

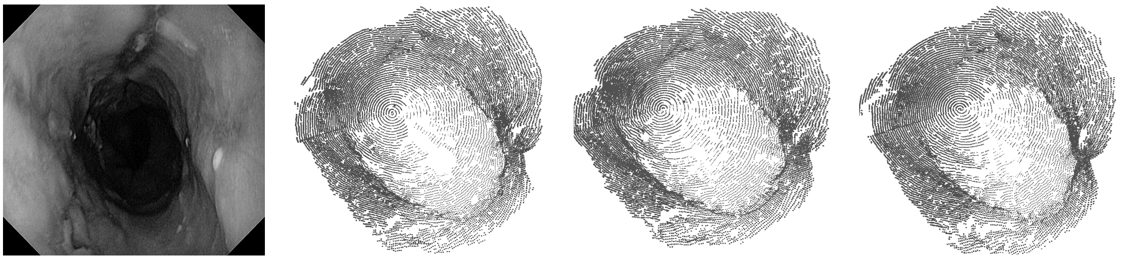

(a) Input image (586 × 502). (b) $\sigma = \frac{\pi}{6}$. (c) $\sigma = \frac{\pi}{4}$. (d) $\sigma = \frac{\pi}{2}$.

Figure 4.9. Reconstruction of the oesophagus with a mesh width $\Delta_{\phi\theta} = 0.0125$ and a grid size 504 × 504.

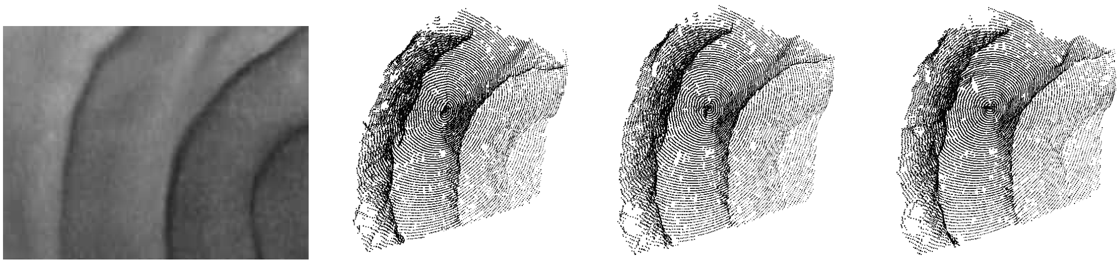

(a) Input image (210 × 160). (b) $\sigma = \frac{\pi}{6}$. (c) $\sigma = \frac{\pi}{4}$. (d) $\sigma = \frac{\pi}{2}$.

Figure 4.10. Reconstruction of the papilla of Vater with a mesh width $\Delta_{\phi\theta} = 0.0125$ and a grid size 504 × 504.

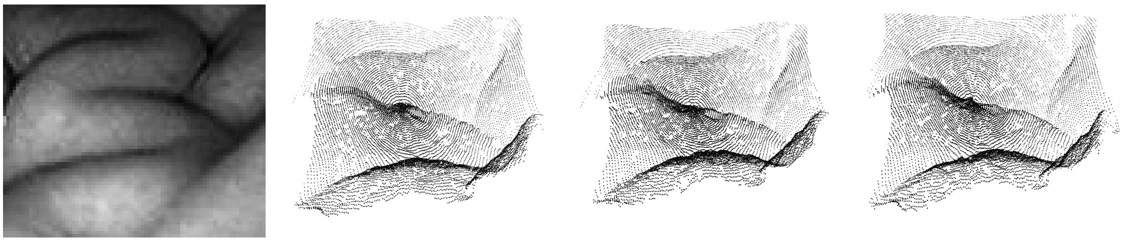

(a) Input image (80 × 71). (b) $\sigma = \frac{\pi}{6}$. (c) $\sigma = \frac{\pi}{4}$. (d) $\sigma = \frac{\pi}{2}$.

Figure 4.11. Reconstruction of the stomach lining with a mesh width $\Delta_{\phi\theta} = 0.0125$ and a grid size 504×504.

4.6 Summary

In this chapter, we have addressed two important issues for PDE-based perspective SfS approaches: One is on the position of the light source for flexible scene settings and the other is on the combination between the general scene geometry and the advanced non-Lambertian reflectance model. By introducing a spherical parametrisation in spherical coordinates for exploiting critical points, we have achieved the goals and thereby described the whole model in the form of HJEs. Moreover, we have designed an adapted FM method specifically for the general model to gain full efficiency as well as functionality and it allows to reconstruct even a high resolution image with a reasonable runtime. Finally, we have confirmed that the derived model is able to cope with general scenarios by demonstrating experimental results.

Part II

Variational Methods

Chapter 5

Variational Perspective Shape from Shading

In the first part, we have focussed on PDE-based methods for perspective shape from shading within the modern framework of viscosity solutions [63] that we have seen in Section 2.2.3. Although these approaches can enjoy the benefit of partial well-posedness [44, 67, 195] as pointed out in Chapter 3, an issue on the robustness with the methods still may arise from various scenarios especially when it comes to noise [162] or missing information. To address this issue, variational approaches can be an attractive option, since they can provide the desired property by relying on smoothness terms which have been demonstrated to be highly effective in a wide range of image processing and computer vision problems, e.g. image segmentation [52, 168], optical flow [48, 121], denoising [220].

In this chapter, we therefore turn our attention to variational methods. To this end, we investigate the major limitations of existing variational models: Most models are either based on the simple orthographic projection or they select surface normals as unknowns [119], which necessarily requires auxiliary variables as well as an integrability constraint [89] and thereby leads to the two-step reconstruction strategy instead of a direct estimation. While there are some models incorporating the perspective projection in variational methods [270, 278], these models have used the orthographic surface normal for the perspective case. In this case, the resulting models are only valid for weak perspective effects and some brightness equation become unnecessarily complex. Other perspective models still need an additional term for the integrability constraint [1]. A final important aspect is the preservation of surface edge during the reconstruction. This aspect, however, has not been addressed at all in the literature so far.

Being aware of all these shortcomings, we construct a direct variational method for perspective SfS by means of a discontinuity-preserving second-order smoothness term. This method offers a substantially higher degree of robustness compared to existing PDE-based approaches.

This chapter is based on the paper [131] that was presented at SSVM and is organised as follows: Section 5.1 provides fundamentals on variational methods including the calculus of variations as well as the corresponding Euler-Lagrange equations. In Section 5.2, we then derive a variational model with Lambertian surface reflectance under the perspective camera projection in consideration of the aforementioned shortcomings. Section 5.3 deals with a suitable minimisation strategy along with discretisations for the established model. Finally, we present experimental results in Section 5.4, which demonstrate the effectiveness of the presented variational method especially when it comes to scenarios with noise or partially missing information.

5.1 Mathematical Background on Variational Methods

The main idea of variational methods is to compute the solution of a problem as minimiser of a suitable energy functional. This energy functional penalises deviations from previously made assumptions such that the minimiser is the solution that fits the assumptions best. In our case, the energy takes the following general form

$$\mathcal{E}(u) = \int_{\Omega} \mathcal{L}\left(x, u\left(x\right), Du\left(x\right), D^2 u\left(x\right)\right) dx\,. \tag{5.1}$$

Here, $u : \Omega \to \mathbb{R}$ stands for the sought scalar function, $\mathcal{L}$ is the *Lagrangian* which contains the assumptions $\Omega \subset \mathbb{R}^n$ denotes an n-dimensional bounded open subset of $\mathbb{R}^n$, and Du and D^2u represent the gradient vector and the Hessian as defined in (2.10) and (2.11), respectively. The order of derivatives of the Lagrangian $\mathcal{L}$ in (5.1) may vary according to the requirements of the problem. In order to construct a Lagrangian $\mathcal{L}$ for the perspective SfS problem, we consider a 2-D model with derivatives up to second order.

Before we move on to variational SfS models, we first discuss how the energy functional $\mathcal{E}$ in (5.1) can be minimised. This inevitably entails the *calculus of variations* [58, 95] which we discuss in the next section.

5.1.1 Calculus of Variations

Calculus of variations is a branch of mathematics concerned with the problem of optimising functionals. This mathematical framework offers a necessary condition called *Euler-Lagrange (EL) equations* [1] which must be satisfied by such minimiser of a given functional. However, the condition is not sufficient in that all local extrema as well as inflection points meet the requirements, too. If the given energy functional is strictly convex, a unique minimiser may be found. The role of this criterion is similar to that of the first-order necessary condition for optimality in standard differential calculus, i.e. the first derivatives with respect to variables of a given function must vanish at extrema. In order to understand the idea how the EL equations are derived,

---

[1] This optimality condition is named after two influential mathematicians in honour of their contributions to the field: Leonhard Euler (1707–1783) and Joseph-Louis Lagrange (1736–1813).

we first look into the simplest case: a 1-D first-order functional. Then, we consider the second-order case in 2-D – the case we are actually interested in.

Euler-Lagrange Equation for 1-D First-order Lagrangians

The requirement to be a minimiser states that for a given functional

$$E\left(u\right) = \int_{x_a}^{x_b} L\left(x, u\left(x\right), u'\left(x\right)\right)\, dx\,, \tag{5.2}$$

a smooth function $u : [x_a, x_b] \to \mathbb{R}$ must fulfil the EL equation

$$\frac{\partial L}{\partial u} - \frac{d}{dx}\left(\frac{\partial L}{\partial u'}\right) = 0 \tag{5.3}$$

with *natural boundary conditions*

$$\frac{\partial L}{\partial u'} = 0 \tag{5.4}$$

at x_a and x_b. Here, u' denotes $\frac{\partial u}{\partial x}$.

To verify the statement, we suppose that $\underline{u}$ is a differentiable minimiser for the functional E in (5.2). Furthermore, to characterise the minimiser with respect to other functions we embed the minimiser $\underline{u}$ into a family of general functions $u(x, \varepsilon)$ by constructing

$$u\left(x, \varepsilon\right) := \underline{u}\left(x\right) + \varepsilon\, \eta\left(x\right) =: \underline{u}\left(x\right) + \delta\underline{u}\left(x\right)\,, \tag{5.5}$$

where $\varepsilon \in \mathbb{R}$ denotes a constant parameter, $\eta : [x_a, x_b] \to \mathbb{R}$ stands for a differentiable perturbation function. Here, the second term $\delta\underline{u}$ is called a *variation* of the minimiser $\underline{u}$ [58] from which the name of "calculus of variations" originates. The perturbation function η is assumed to be arbitrary in the interval (x_a, x_b).

Based on the construction (5.5), one can observe that the minimiser $\underline{u}$ of (5.2) is attained when $\varepsilon = 0$ for an arbitrary perturbation function η. Thus, the energy functional E in (5.2) can be regarded as a scalar valued function Φ depending on the parameter ε. This yields

$$\Phi\left(\varepsilon\right) := E\left(u\left(x, \varepsilon\right)\right) \overset{(5.5)}{=} E\left(\underline{u} + \varepsilon\, \eta\right)\,, \tag{5.6}$$

Besides, since Φ has a minimum when $\varepsilon = 0$, we know that

$$0 = \Phi'\left(0\right) = \left.\frac{d\Phi\left(\varepsilon\right)}{d\varepsilon}\right|_{\varepsilon=0} \overset{(5.6)}{=} \left.\frac{d}{d\varepsilon} E\left(\underline{u} + \varepsilon\, \eta\right)\right|_{\varepsilon=0}\,. \tag{5.7}$$

By means of (5.2) with (5.5), we can rewrite (5.7) as

$$0 \overset{(5.2)}{\underset{(5.5)}{=}} \frac{d}{d\varepsilon} \int_{x_a}^{x_b} L\left(x, \underline{u} + \varepsilon\, \eta, \underline{u}' + \varepsilon\, \eta'\right) dx \bigg|_{\varepsilon=0} . \tag{5.8}$$

Given the fact that only the integrand L is under the influence of the differential operator $\frac{d}{d\varepsilon}$ and ε is independent of x in (5.8), the Leibniz rule allows to take the differential operator inside the integral sign and apply directly to the Lagrangian function L. This leads to

$$0 = \int_{x_a}^{x_b} \frac{d}{d\varepsilon} L\left(x, \underline{u} + \varepsilon\, \eta, \underline{u}' + \varepsilon\, \eta'\right) dx \bigg|_{\varepsilon=0} . \tag{5.9}$$

Since only the second and the third argument in (5.9) depend on ε by virtue of (5.6), i.e. $u\,(\cdot, \varepsilon)$ and $u'\,(\cdot, \varepsilon)$, respectively, applying the chain rule to (5.9) further yields

$$\begin{aligned} 0 &= \int_{x_a}^{x_b} \left(\frac{\partial L\,(x, u, u')}{\partial u} \frac{\partial u}{\partial \varepsilon} + \frac{\partial L\,(x, u, u')}{\partial u'} \frac{\partial u'}{\partial \varepsilon} \right) dx \bigg|_{\varepsilon=0} \\ &\overset{(5.5)}{=} \int_{x_a}^{x_b} \left(\frac{\partial L\,(x, u, u')}{\partial u}\, \eta + \frac{\partial L\,(x, u, u')}{\partial u'}\, \eta' \right) dx \bigg|_{\varepsilon=0} \\ &= \int_{x_a}^{x_b} \left(\frac{\partial L\left(x, \underline{u}, \underline{u}'\right)}{\partial u}\, \eta + \frac{\partial L\left(x, \underline{u}, \underline{u}'\right)}{\partial u'}\, \eta' \right) dx \, . \end{aligned} \tag{5.10}$$

In addition, integrating the second term in (5.10) by parts gives

$$\int_{x_a}^{x_b} \frac{\partial L}{\partial u'}\, \eta'\, dx = \left[\frac{\partial L}{\partial u'}\, \eta \right]_{x_a}^{x_b} - \int_{x_a}^{x_b} \frac{d}{dx} \left(\frac{\partial L}{\partial u'} \right) \eta\, dx \, . \tag{5.11}$$

By substituting (5.11) for the second term in (5.10), it follows that

$$0 = \int_{x_a}^{x_b} \left(\frac{\partial L}{\partial u} - \frac{d}{dx} \left(\frac{\partial L}{\partial u'} \right) \right) \eta\, dx + \left[\frac{\partial L}{\partial u'}\, \eta \right]_{x_a}^{x_b} . \tag{5.12}$$

Hence, for (5.12) to be valid with all perturbation functions η, each term must vanish irrespective of η according to the fundamental lemma of calculus of variations [58]. This corresponds to the EL equation (5.3) for the first term and the natural boundary conditions (5.4) for the second term, which follows the assertions. One can further note that the EL equation (5.3) is a second-order ordinary differential equation (ODE).

Shortest Path Example. In order to see how calculus of variations with EL equations can be applied, we consider a simple problem for finding the shortest path between two points on a plane. The answer to this problem is already known as the straight line between the two points which we call A and B, see Figure 5.1.

To this end, we first establish an energy functional for this problem. By means of the Pythagorean theorem, one may describe an arc length between two points as [50, 95]

$$\int_{x_a}^{x_b} \sqrt{1 + u_x^2}\, dx\,, \tag{5.13}$$

where $u_x = \frac{\partial u}{\partial x}$.

From the perspective of calculus of variations, the shortest path between the two points on a plane is equivalent to the minimiser of the functional (5.13). As previously indicated, the minimiser has to satisfy the EL equation (5.3). Hence, we compute the associated one. Since the Lagrangian for (5.13) does not depend on u, the EL equation amounts to be

$$\frac{d}{dx}\left(\frac{\partial E}{\partial u_x}\right) = 0 \quad \Leftrightarrow \quad \frac{d}{dx}\left(u_x\,\left(1 + u_x^2\right)^{-\frac{1}{2}}\right) = 0\,. \tag{5.14}$$

Applying the chain rule to the right hand side of (5.14) yields

$$\begin{aligned} \frac{d}{dx}\left(u_x\,\left(1 + u_x^2\right)^{-\frac{1}{2}}\right) &= u_{xx}\,\left(1 + u_x^2\right)^{-\frac{1}{2}} + u_x\,\left(-\frac{1}{2}\left(1 + u_x^2\right)^{-\frac{3}{2}}\right)\left(2\,u_x\right)\,u_{xx} \\ &= \frac{u_{xx}}{\left(1 + u_x^2\right)\sqrt{1 + u_x^2}} \overset{!}{=} 0\,. \end{aligned} \tag{5.15}$$

Then, from (5.15) one can notice that the numerator u_{xx} must be 0 based on the positiveness of the denominator. This suggests that a first-order polynomial fulfils the condition (5.15) and the slope and the intercept may be determined when the coordinates of two points are given as in Figure 5.1. As a consequence, calculus of variations confirms that a straight line is the geodesic path between two points on a plane.

When we interpret the situation geometrically, the minimal path $\underline{u}$ between the two points on a plane is clearly a straight line as shown in Figure 5.1(a). However, if a path is not geodesic, the route necessarily bends, which leads to curved lines such as u_1 and u_2 in Figure 5.1(a). One may note that the family of functions (5.5) contains these curves with different values of the $\varepsilon \neq 0$ as well as the geodesic path $\underline{u}$ with $\varepsilon = 0$. Then, the role of the EL equation is preventing even slight deviations from the straight line, i.e. to keep the variations from arising with respect to the minimiser in (5.5) such as δu_1 and δu_2 in Figure 5.1(a). This makes the quantity $\delta \underline{u}$ always disappearing and thereby the path stays on the optimal track.

This shows that there is a different focus on the change of rate between calculus of variations and differential calculus: By changing the parameter ε close to 0, calculus of variations concerns variations of a family of functions with respect to a fixed function for a given perturbation function at a fixed point. The fixed function and the fixed point correspond to $\underline{u}$ and x_0 in Figure 5.1(a). Since the function family has been constructed by the assumed minimiser $\underline{u}$ as in (5.5), the EL equations provide a condition to avoid function variations as previously indicated.

However, differential calculus concerns the change rate of a given function with respect to a change of a given point in x-direction for 1-D. In Figure 5.1(b), the change rate of functions $\underline{u}$, u_1 and u_2 is illustrated by $\Delta\underline{u}$, Δu_1, Δu_2 as the value of x changes from x_0 to $x_0 + \Delta x$. This suggests that differential calculus is capable of considering only a single function at a time instead of a family of functions.

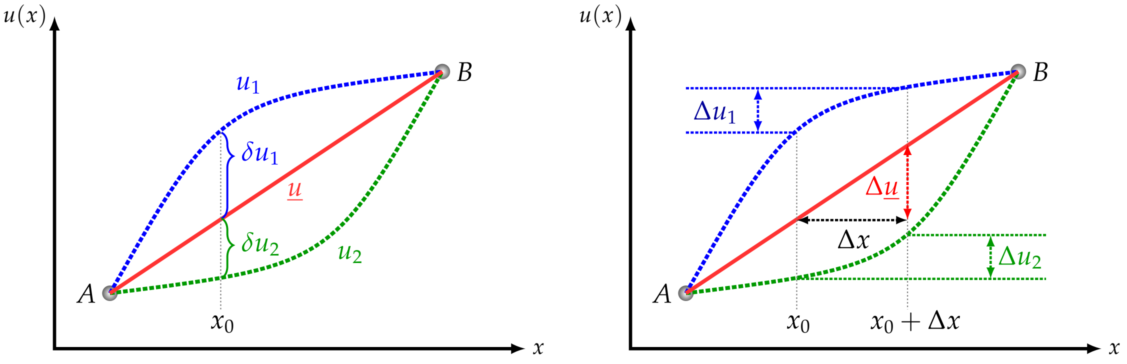

(a) Calculus of variations.

(b) Differential calculus.

Figure 5.1. Comparisons by geometrical interpretations between calculus of variations and differential calculus.

Extension to 2-D Second-order Lagrangians

Let us now turn to 2-D second-order Lagrangians. Since the variational SfS models that we are dealing with in this chapter as well as in the next one are of this type, we are especially interested in this case.

For 2-D second order Lagrangians, EL equations with corresponding natural boundary conditions can be derived by repeated integration by parts and the Gauss's theorem [58] along with the fundamental lemma of calculus of variations. Hence, for an energy functional of the form

$$E(u) = \int_{\Omega} L\left(x, y, u, u_x, u_y, u_{xx}, u_{xy}, u_{yx}, u_{yy}\right)\, dx\, dy\,, \tag{5.16}$$

the variation of the functional (5.16) can be attained as

$$\begin{aligned}
0 = \int_{\Omega} \Bigg(& L_u - \frac{\partial}{\partial x} L_{u_x} - \frac{\partial}{\partial y} L_{u_y} \\
& + \frac{\partial^2}{\partial x^2} L_{u_{xx}} + \frac{\partial^2}{\partial x \partial y} L_{u_{xy}} + \frac{\partial^2}{\partial y \partial x} L_{u_{yx}} + \frac{\partial^2}{\partial y^2} L_{u_{yy}} \Bigg) \, \eta \, dx \, dy \\
& + \int_{\partial\Omega} n_1 \left(L_{u_x} - \frac{\partial}{\partial x} L_{u_{xx}} - \frac{\partial}{\partial y} L_{u_{xy}} \right) \eta \, dx \, dy \\
& + \int_{\partial\Omega} n_2 \left(L_{u_y} - \frac{\partial}{\partial x} L_{u_{yx}} - \frac{\partial}{\partial y} L_{u_{yy}} \right) \eta \, dx \, dy \\
& + \int_{\partial\Omega} \left(L_{u_{xx}} n_1 + L_{u_{xy}} n_2 \right) \eta_x \, dx \, dy \\
& + \int_{\partial\Omega} \left(L_{u_{yx}} n_1 + L_{u_{yy}} n_2 \right) \eta_y \, dx \, dy \, .
\end{aligned} \tag{5.17}$$

Therefore, the EL equation can be described by the following fourth-order PDE

$$0 = L_u - \frac{\partial}{\partial x} L_{u_x} - \frac{\partial}{\partial y} L_{u_y} + \frac{\partial^2}{\partial x^2} L_{u_{xx}} + \frac{\partial^2}{\partial x \partial y} L_{u_{xy}} + \frac{\partial^2}{\partial y \partial x} L_{u_{yx}} + \frac{\partial^2}{\partial y^2} L_{u_{yy}} \tag{5.18}$$

with the natural boundary conditions on $\partial\Omega$

$$0 = \boldsymbol{n}^\top \begin{bmatrix} L_{u_x} - \frac{\partial}{\partial x} L_{u_{xx}} - \frac{\partial}{\partial y} L_{u_{xy}} \\ L_{u_y} - \frac{\partial}{\partial x} L_{u_{yx}} - \frac{\partial}{\partial y} L_{u_{yy}} \end{bmatrix} , \tag{5.19}$$

where $\boldsymbol{n}$ stands for an outer normal vector $(n_1, n_2)^\top$. This even holds for an arbitrary η at the boundary, i.e. for the case of $\eta \neq 0$ on $\partial\Omega$. To ensure that the equality in (5.17) holds, by supposing $\nabla\eta \neq \mathbf{0}$ one must further impose the conditions

$$\boldsymbol{n}^\top \begin{bmatrix} L_{u_{xx}} \\ L_{u_{xy}} \end{bmatrix} = 0 \, , \quad \boldsymbol{n}^\top \begin{bmatrix} L_{u_{yx}} \\ L_{u_{yy}} \end{bmatrix} = 0 \tag{5.20}$$

with the outer normal vector $\boldsymbol{n} = (n_1, n_2)^\top$.

5.1.2 Regularisation by Smoothness Terms

So far we have reviewed how to compute EL equations depending on different types of Lagrangians. In this section, we consider the role of the regularisation to form an energy functional for SfS problems in a way that the variational framework we have seen in Section 5.1.1 can be utilised.

Since the nature of SfS problems is inherently ill-posed as other problems in computer vision [32, 192], e.g. optical flow [48, 121], image segmentation [52, 168], multi-view reconstructions [4], the construction of energy functionals for SfS typically follows the structure of Tikhonov regularisation [243, 244]. The cornerstone of the regularisation theory lies in that the aforementioned ill-posed problems may be reformulated in such a way that an appropriate solution to the problem can be found, which approximates the given data best in an admissible solution set depending on the requirements for the problems at hand. Moreover, the reformulation may be realised by imposing some meaningful constraints such as smoothness (regularities) on the given problems [32, 158, 192]. Then, the desired solution can be attained by minimising the formulated energy functional with the help of calculus of variations.

In this context, energy functionals for SfS are usually composed of two parts: the *data term* and the *smoothness term* as can be observed e.g. from [131, 132, 160, 257, 270]. Therefore, one may represent the general form of energy functionals for SfS as

$$\mathcal{E}(u) = \int_{\Omega} \Big(\underbrace{\mathcal{E}_D\left(\cdot, D^n u(\boldsymbol{x}), \cdot\right)}_{\text{data term}} + \alpha \underbrace{\mathcal{E}_S\left(\cdot, D^{n+1} u(\boldsymbol{x}), \cdot\right)}_{\text{smoothness term}} \Big)\, d\boldsymbol{x}\,, \tag{5.21}$$

where $\Omega \subset \mathbb{R}^2$ denotes a 2-D rectangular image domain, $\boldsymbol{x} = (x, y)^\top \in \Omega$ describes a data point in 2-D, D^n represents an n-th order differential operator such as (2.10) and (2.11), α is a regularisation parameter, and $\mathcal{E}_D$ and $\mathcal{E}_S$ stand for a data term and a smoothness term, respectively.

In the energy functional (5.21), the role of the data term is to ensure that a solution is as close to the given data as possible in the sense of a predefined measure, e.g. a norm. For SfS problems, a brightness equation usually takes the place of the data term, which is called the "brightness constraint" according to [233, 281]. Therefore, the main properties of the energy functional for the problem are characterised by this data term, e.g. whether the perspective projection is considered or the light attenuation term is taken into account, etc.

For the smoothness term, it can be noted that the order of the differential operator is often selected at least one order higher than that of the data term. This is based on the fact that using the same derivative order as in the data term would directly lead to competing assumptions. Moreover, as shown in [131, 132, 160] the robust behaviour of variational methods is actually attributed to the smoothness term that is capable of exerting the filling-in effect guided by information of neighbouring data points. One can note that this feature is particularly useful especially when it comes to missing information and noise in the given data. In this context, the regularisation parameter $\alpha \in \mathbb{R}^+$ thereby permits to control the degree of smoothness for solutions.

5.2 Variational Shape from Shading Models

Before we turn to our novel variational approach, let us first look into the shortcomings of existing models in Section 5.2.1. Afterwards, by taking the limitations from existing models into account we construct our variational perspective SfS model [131] in Section 5.2.2.

5.2.1 Shortcomings of Existing Models for Variational SfS

In order to establish a model for variational SfS, there are three main components involved [79]: (i) the selection of parametrisations, (ii) a functional that has to be minimised, (iii) minimisation methods. Let us first discuss the parametrisation in terms of the surface normal. Its drawbacks will motivate the direct depth as a better choice for the parametrisation.

Selection of Parametrisations and Functionals for Variational SfS

Since reconstructions are obtained as a minimiser of the energy functional in variational methods, the selection of the parametrisation for the data term plays a key role on the formation of functionals. However, the intuitive choice of the parametrisation, i.e. the depth itself, has hardly been used in the literature except for [149, 257]. Instead, many variational models usually take two auxiliary variables p and q as the parametrisation [69, 70, 89, 119, 233, 278], which are defined by

$$p := \frac{\partial u}{\partial x} \quad \text{and} \quad q := \frac{\partial u}{\partial y} \tag{5.22}$$

with the unknown depth u. These variables typically represent surface normal vectors in the orthographic projection, since for a surface parametrisation $\mathcal{S} = \left(x, y, u\left(x, y\right)\right)^\top$ its normal vector can be computed by

$$\mathcal{S}_x \times \mathcal{S}_y = \frac{\partial}{\partial x}\begin{bmatrix} x \\ y \\ u \end{bmatrix} \times \frac{\partial}{\partial y}\begin{bmatrix} x \\ y \\ u \end{bmatrix} \overset{(5.22)}{=} \begin{bmatrix} 1 \\ 0 \\ p \end{bmatrix} \times \begin{bmatrix} 0 \\ 1 \\ q \end{bmatrix} = \begin{bmatrix} -p \\ -q \\ 1 \end{bmatrix}. \tag{5.23}$$

This particular selection of the parametrisation is attributed to the brightness equation described by the reflectance map [122] that formulates the scene radiance as a function of surface orientations instead of the depth itself.

One should note that the surface normals given in (5.23) are only valid for an orthographic projection and not for a perspective one. The main difference comes from whether the cross derivatives $\frac{\partial y}{\partial x}$ and $\frac{\partial x}{\partial y}$ disappear or not. Contrary to the orthographic case, these cross derivatives, in general, do not vanish in the perspective projection. This is because the line from the optical centre to the surface point through the corresponding mapping point on the image plane is *not parallel* to the z-axis, see Figure 3.10. This suggests that the strategy of deriving surface normals by simply substituting the orthographic normals for perspective ones as in [270, 278] turns out to be *not completely correct*. In this context, it is not surprising if such methods yield poor results under the strong influence of perspective distortions.

The selection of the parametrisation is also related to the form of functionals. If the surface normals are the parametrisation, the computed normals must be integrated for reconstruction. To this end, the integrability constraint must be enforced [89] in a way that the constraints are directly combined as an additional term in the energy functional [69, 119, 233, 278]. Then, the energy functional takes the form of

$$\begin{aligned}\mathcal{E}(p,q) = \int_\Omega \underbrace{\mathcal{E}_D\left(\mathbf{x}, p(\mathbf{x}), q(\mathbf{x})\right)}_{\text{data term}} d\mathbf{x} + \alpha_s \int_\Omega \underbrace{\mathcal{E}_S\left(\nabla p(\mathbf{x}), \nabla q(\mathbf{x})\right)}_{\text{smoothness term}} d\mathbf{x} \\ + \alpha_i \int_\Omega \underbrace{\mathcal{E}_I\left(\frac{\partial p(\mathbf{x})}{\partial y}, \frac{\partial q(\mathbf{x})}{\partial x}\right)}_{\text{integrability constraint}} d\mathbf{x}\,, \end{aligned} \tag{5.24}$$

where $\mathcal{E}_D$, $\mathcal{E}_S$, and $\mathcal{E}_I$ represent the data term, the smoothness term, and the integrability constraint term, respectively, α_s denotes the regularisation parameter and α_i is called integrability factor [79].

Apart from the additional term of the integrability constraint, the energy functional (5.24) also contains the smoothness term affecting the gradient of auxiliary variables, which is difficult to interpret. In addition, dedicated integration algorithms of normal fields must be utilised for reconstruction, e.g. [5, 80, 92, 202]. As a consequence, a direct parametrisation is desirable. It contains no auxiliary variables, requires no additional term of integrability constraint and no extra steps for reconstruction.

5.2.2 Variational Perspective SfS Model

Being aware of the aforementioned shortcomings, let us now consider our novel variational approach for perspective SfS [131] by embedding a PDE-based perspective SfS model into the variational framework. To this end, we make use of the brightness equation based on the PDE-based perspective SfS model of Prados and Faugeras [195] for the data term and incorporate the second-order smoothness term which was proposed in the context of orthographic SfS by Vogel *et al.* [257]. By rearranging the brightness equation, we can obtain the following new model for *variational perspective*

SfS [131]

$$E\left(v\left(\boldsymbol{x}\right)\right)=\int_{\Omega}\underbrace{\left\{E_{D}\left(\boldsymbol{x},v\left(\boldsymbol{x}\right),\nabla v\left(\boldsymbol{x}\right)\right)\right\}^{2}}_{\text{data term}}+\alpha\;\underbrace{E_{S}\left(D^{2}\,v\left(\boldsymbol{x}\right)\right)}_{\text{smoothness term}}\,d\boldsymbol{x}\,,\tag{5.25}$$

where v denotes the unknown radial depth, E_D stands for the data term defined by

$$E_{D}\left(\boldsymbol{x},v\left(\boldsymbol{x}\right),\nabla v\left(\boldsymbol{x}\right)\right)=\text{f}^{2}\,I\left(\boldsymbol{x}\right)\;W\left(\boldsymbol{x}\right)-Q\left(\boldsymbol{x}\right)\;e^{-2\,v(\boldsymbol{x})}\tag{5.26}$$

with

$$W\left(\boldsymbol{x}\right)=\sqrt{\text{f}^{2}\left|\nabla v\left(\boldsymbol{x}\right)\right|^{2}+\left(\boldsymbol{x}\cdot\nabla v\left(\boldsymbol{x}\right)\right)^{2}+Q\left(\boldsymbol{x}\right)^{2}}\tag{5.27}$$

and $Q(\boldsymbol{x})$ being defined as in (3.24). In addition, E_S represents the smoothness term defined by

$$E_{S}\left(\cdot\right)=\left\|\cdot\right\|_{F}^{2}\;,\tag{5.28}$$

where $\|\cdot\|_F$ denotes the Frobenius norm. Then, based on that $\boldsymbol{x}=\left(x,y\right)^{\top}\in\Omega\subset\mathbb{R}^{2}$ is a 2-D position vector in the rectangular image plane, one can obtain the following expression for the smoothness term in (5.25)

$$E_{S}\left(D^{2}\,v\left(\boldsymbol{x}\right)\right)\overset{(5.28)}{=}\left\|D^{2}\,v\left(\boldsymbol{x}\right)\right\|_{F}^{2}\overset{(2.11)}{=}\left\|\begin{bmatrix}v_{xx}&v_{xy}\\v_{xy}&v_{yy}\end{bmatrix}\right\|_{F}^{2}=\left(v_{xx}\right)^{2}+2\,\left(v_{xy}\right)^{2}+\left(v_{yy}\right)^{2}\;,\tag{5.29}$$

where the integrability constraint $v_{xy}=v_{yx}$ is considered. Since the data term E_D contains already the first order term ∇v, a second-order smoothness term is used based on the discussion in Section 5.1.2. Besides, $\alpha\in\mathbb{R}^{+}$ in (5.25) is a regularisation parameter that determines the amount of smoothness for solutions as described in Section 5.1.2. The variational model (5.25) has the following notable features:

(i) The model takes the full perspective camera projection along with correct surface normals into consideration, since the data term is derived from the PDE-based perspective SfS model [195].

(ii) One can estimate the unknown radial depth v *directly* by minimising the energy functional with respect to v, because the parametrisation has been selected accordingly in contrast to other (orthographic) approaches, for instance [45, 89, 119, 125]. These aforementioned approaches adopt the two-step strategies for reconstruction based on that the data terms in the models rely on the brightness equation described by the reflectance map [122] and thereby surface normals denoted by auxiliary variables had been selected as the parametrisation. Hence, after finding the surface normals as the minimiser in the associated variational model, the integration step of the computed normal fields, e.g. depth from gradient field [119] or similar methods such as [5, 80, 92], is inevitable, as pointed out in Section 5.2.1.

(iii) The solution of the model satisfies the *integrability constraint* per construction in that the smoothness term (5.29) has encoded the condition into the model compactly by means of $v_{xy} = v_{yx}$ and the minimiser is found in terms of v. Therefore, no extra form of constraints are required in the model contrary to the case of (5.24).

Model Extensions

Aside from the listed attributes, we consider extensions of the basis model (5.25) in two possible ways within the variational framework.

Confidence Function. On the one hand, we extend the model in such a way that it has the capability of decomposing the computational domain into two parts once the locations of corrupted regions have been recognised *a priori* e.g. by a noise or texture detector or by a background segmentation algorithm. To this end, we introduce a binary confidence function $c : \boldsymbol{x} \in \Omega \subset \mathbb{R}^2 \to \{0, 1\}$ into the basis model. Then, the extended model takes the form

$$E(v) = \int_{\Omega} c(\boldsymbol{x}) \, \{E_D(\boldsymbol{x}, v, \nabla v)\}^2 + \alpha \, (1 - c(\boldsymbol{x})) \, E_S\left(D^2 v\right) \, d\boldsymbol{x} \,, \tag{5.30}$$

where the confidence function $c(\boldsymbol{x})$ is given by

$$c(\boldsymbol{x}) = \begin{cases} 1\,, & \boldsymbol{x} \in (\Omega \setminus \Gamma)\,, \\ 0\,, & \boldsymbol{x} \in \Gamma\,. \end{cases} \tag{5.31}$$

It can be noted that the confidence function makes the decision whether the data term or the smoothness term is in operation. Therefore, as long as the information is reliable, i.e. $c(\boldsymbol{x}) = 1$ with $\boldsymbol{x} \in (\Omega \setminus \Gamma)$, the reconstruction is carried out only by the data term since the smoothness term is switched off in Γ. If this is not the case, i.e. $c(\boldsymbol{x}) = 0$ with $\boldsymbol{x} \in \Gamma$, the smoothness term fills in information in the unreliable domain Γ under the guidance of adjacent regions. This attribute is highly beneficial especially when it comes to real-world data [61, 131].

Edge-preserving Smoothness Term. On the other hand, we extend the basis model by incorporating an edge-preserving smoothness term, since a quadratic regulariser such as (5.29) usually leads to oversmoothed solutions [54, 173, 174, 191, 283].

To overcome the problem, one needs a regulariser that enables to smooth the region selectively depending on the structures [15, 252]: Strong diffusion may be applied within planar regions, where relatively small variations occur. However, the diffusion effect must be as minimal as possible at the boundaries of these regions that correspond to edge structures with high curvatures [157].

Since subquadratic regularisation turns out to be an appropriate choice for this situation [15, 53, 54, 96, 97, 239, 252], by means of such smoothness terms the basis model can be extended to the edge-preserving one [131]

$$E(v) = \int_\Omega \{E_D(\boldsymbol{x}, v, \nabla v)\}^2 + \alpha\, E_S\left(D^2 v\right) d\boldsymbol{x}\,, \tag{5.32}$$

where the smoothness term E_S is given by the Charbonnier regulariser Ψ [54]

$$E_S\left(D^2 v\right) := \Psi\left(\left\|D^2 z\right\|_F^2\right) \overset{(5.29)}{=} \Psi\left(v_{xx}^2 + 2\, v_{xy}^2 + v_{yy}^2\right) =: \Psi\left(s^2\right) = 2\,\lambda^2 \sqrt{1 + \frac{s^2}{\lambda^2}} \tag{5.33}$$

with $s = \left\|D^2 v\right\|_F$ and the contrast parameter λ.

One should note that the Frobenius norm of the Hessian of the radial depth corresponds to a curvature measure. The subquadratic regulariser is designed such that the associated diffusivity decreases and thereby preserves edge structures as the curvature measure increases. The contrast parameter λ plays a role in a way that a small amount of the parameter strongly influences on retaining edges but becomes less effective as the value of λ increases. This type of edge-preserving regulariser has been widely adopted not only in SfS [257] but also in various contexts, e.g. image denoising [156, 215], optical lithography [81] as well as motion estimation [72].

5.3 Minimisation

In Section 5.2.2, we have constructed a mathematical model for perspective SfS in the variational framework. Once a model is established, the formulated energy functional must be minimised in order to reconstruct a surface as indicated in Section 5.1. In this section, we devote ourselves to the minimisation of the energy functionals from the previous section.

5.3.1 The Base Case

First, we turn to the basis model (5.25). Since the unknown radial depth $v(\boldsymbol{x})$ corresponds to the minimiser of the given energy functional, the solution must satisfy the associated Euler-Lagrange equation according to "calculus of variations."

Since the basis model belongs to the class of 2-D second-order Lagrangian, the EL equation can be computed with corresponding natural boundary conditions. This yields the following EL equation in Ω

$$\begin{aligned} 0 \;=\; & \left[E_D^2+\alpha\,E_S\right]_v - \frac{\partial}{\partial x}\left[E_D^2+\alpha\,E_S\right]_{v_x} - \frac{\partial}{\partial y}\left[E_D^2+\alpha\,E_S\right]_{v_y} \\ & + \frac{\partial^2}{\partial x^2}\left[E_D^2+\alpha\,E_S\right]_{v_{xx}} + 2\,\frac{\partial^2}{\partial x\partial y}\left[E_D^2+\alpha\,E_S\right]_{v_{xy}} + \frac{\partial^2}{\partial y^2}\left[E_D^2+\alpha\,E_S\right]_{v_{yy}}\,. \end{aligned} \tag{5.34}$$

with the boundary conditions on $\partial\Omega$

$$0 = \boldsymbol{n}^\top \begin{bmatrix} \left[E_D^2+\alpha\,E_S\right]_{v_x} - \frac{\partial}{\partial x}\left[E_D^2+\alpha\,E_S\right]_{v_{xx}} - \frac{\partial}{\partial y}\left[E_D^2+\alpha\,E_S\right]_{v_{xy}} \\ \left[E_D^2+\alpha\,E_S\right]_{v_y} - \frac{\partial}{\partial x}\left[E_D^2+\alpha\,E_S\right]_{v_{xy}} - \frac{\partial}{\partial y}\left[E_D^2+\alpha\,E_S\right]_{v_{yy}} \end{bmatrix}, \tag{5.35}$$

as well as

$$\boldsymbol{n}^\top \begin{bmatrix} \left[E_D^2+\alpha\,E_S\right]_{v_{xx}} \\ \left[E_D^2+\alpha\,E_S\right]_{v_{xy}} \end{bmatrix} = 0 = \boldsymbol{n}^\top \begin{bmatrix} \left[E_D^2+\alpha\,E_S\right]_{v_{xy}} \\ \left[E_D^2+\alpha\,E_S\right]_{v_{yy}} \end{bmatrix}, \tag{5.36}$$

where $\boldsymbol{n} = (n_1, n_2)^\top$ denotes the outer normal vector.

Euler-Lagrange Equation

When dealing with the EL equation (5.34), one can attain the following formulation by rearranging the terms on the right hand side with respect to the contributions of the data term and the smoothness term

$$\begin{aligned} 0 = \; & \left[E_D^2\right]_v - \frac{\partial}{\partial x}\left[E_D^2\right]_{v_x} - \frac{\partial}{\partial y}\left[E_D^2\right]_{v_y} \\ & + \overbrace{\frac{\partial^2}{\partial x^2}\left[E_D^2\right]_{v_{xx}}}^{=0} + 2\,\overbrace{\frac{\partial^2}{\partial x\partial y}\left[E_D^2\right]_{v_{xy}}}^{=0} + \overbrace{\frac{\partial^2}{\partial y^2}\left[E_D^2\right]_{v_{yy}}}^{=0} \\ & + \underbrace{\left[\alpha\,E_S\right]_v}_{=0} - \underbrace{\frac{\partial}{\partial x}\left[\alpha\,E_S\right]_{v_x}}_{=0} - \underbrace{\frac{\partial}{\partial y}\left[\alpha\,E_S\right]_{v_y}}_{=0} \\ & + \frac{\partial^2}{\partial x^2}\left[\alpha\,E_S\right]_{v_{xx}} + 2\,\frac{\partial^2}{\partial x\partial y}\left[\alpha\,E_S\right]_{v_{xy}} + \frac{\partial^2}{\partial y^2}\left[\alpha\,E_S\right]_{v_{yy}} \end{aligned} \tag{5.37}$$

by means of

$$\frac{\partial^2}{\partial x\partial y}\left[E_D^2+\alpha\,E_S\right]_{v_{xy}} = \frac{\partial^2}{\partial y\partial x}\left[E_D^2+\alpha\,E_S\right]_{v_{xy}}\,. \tag{5.38}$$

Dropping the zero contribution terms gives the equivalent form of the EL equation

$$\begin{aligned} 0 = \quad & \left[E_D^2\right]_v - \frac{\partial}{\partial x}\left[E_D^2\right]_{v_x} - \frac{\partial}{\partial y}\left[E_D^2\right]_{v_y} \\ & + \frac{\partial^2}{\partial x^2}\left[\alpha\, E_S\right]_{v_{xx}} + 2\frac{\partial^2}{\partial x \partial y}\left[\alpha\, E_S\right]_{v_{xy}} + \frac{\partial^2}{\partial y^2}\left[\alpha\, E_S\right]_{v_{yy}} \,. \end{aligned} \tag{5.39}$$

One can note that the terms $\frac{\partial}{\partial x}\left[E_D^2\right]_{v_x}$ and $\frac{\partial}{\partial y}\left[E_D^2\right]_{v_y}$ do not disappear, because the data term depends on both v and ∇v. This is significantly different from other models in computer vision, e.g. optical flow estimation [48, 72].

The computation results from the data terms in (5.39) correspond to

$$\left[E_D^2\right]_v = 2\, E_D\, \left[E_D\right]_v \overset{(5.26)}{=} 4\, Q\, e^{-2\,v}\, E_D \,, \tag{5.40}$$

$$\frac{\partial}{\partial x}\left[E_D^2\right]_{v_x} = 2\,\mathfrak{f}^2\left(I_x\,\zeta_1\,\frac{E_D}{W} + I\left[\zeta_1\right]_x\frac{E_D}{W} + I\,\zeta_1\,\left[\frac{E_D}{W}\right]_x\right) , \tag{5.41}$$

$$\frac{\partial}{\partial y}\left[E_D^2\right]_{v_y} = 2\,\mathfrak{f}^2\left(I_y\,\zeta_2\,\frac{E_D}{W} + I\left[\zeta_2\right]_y\frac{E_D}{W} + I\,\zeta_2\,\left[\frac{E_D}{W}\right]_y\right) , \tag{5.42}$$

with

$$\zeta_1 := \mathfrak{f}^2\, v_x + (\nabla v \cdot \boldsymbol{x})\; x \qquad \text{and} \qquad \zeta_2 := \mathfrak{f}^2\, v_y + (\nabla v \cdot \boldsymbol{x})\; y \,. \tag{5.43}$$

Besides, the contributions from the smoothness term yield the biharmonic operator

$$\Delta^2 v = \nabla^4 v = v_{xxxx} + 2\, v_{xxyy} + v_{yyyy} \,. \tag{5.44}$$

Then, this leads to the compact form of the EL equation

$$\underbrace{\left[E_D^2\right]_v - \frac{\partial}{\partial x}\left[E_D^2\right]_{v_x} - \frac{\partial}{\partial y}\left[E_D^2\right]_{v_y}}_{\text{data term (reaction)}} + \alpha \underbrace{\left(2\,\Delta^2\, v\right)}_{\text{smoothness term (diffusion)}} = 0 \,, \tag{5.45}$$

where the fourth-order diffusion process results from the second-order smoothness term.

Boundary Conditions

As conducted for the EL equation, we handle the boundary conditions, i.e. (5.35) and (5.36). Since the computation results of the second condition can be used for the first one, we proceed in reverse order.

To compute the second condition, we make use of

$$\left[E_D^2 + \alpha\, E_S\right]_{v_{xx}} = 2\,\alpha\, v_{xx}\,,\ \left[E_D^2 + \alpha\, E_S\right]_{v_{xy}} = 2\,\alpha\, v_{xy}\,,\ \left[E_D^2 + \alpha\, E_S\right]_{v_{yy}} = 2\,\alpha\, v_{yy}\,. \tag{5.46}$$

Moreover, by means of the positive α we obtain

$$\boldsymbol{n}^\top \begin{bmatrix} v_{xx} \\ v_{xy} \end{bmatrix} = 0\,, \quad \boldsymbol{n}^\top \begin{bmatrix} v_{xy} \\ v_{yy} \end{bmatrix} = 0 \tag{5.47}$$

with an outer normal vector $\boldsymbol{n} = (n_1, n_2)^\top$.

To deal with the first condition (5.35), we develop the term row by row and use the result of the second condition. This leads to

$$\begin{aligned} 0 &= \boldsymbol{n}^\top \begin{bmatrix} \left[E_D^2\right]_{v_x} - \dfrac{\partial}{\partial x}\left[\alpha\, E_S\right]_{v_{xx}} - \dfrac{\partial}{\partial y}\left[\alpha\, E_S\right]_{v_{xy}} \\ \left[E_D^2\right]_{v_y} - \dfrac{\partial}{\partial x}\left[\alpha\, E_S\right]_{v_{xy}} - \dfrac{\partial}{\partial y}\left[\alpha\, E_S\right]_{v_{yy}} \end{bmatrix} \\ &= \boldsymbol{n}^\top \begin{bmatrix} \left[E_D^2\right]_{v_x} - 2\,\alpha\,\left(v_{xxx} + v_{xyy}\right) \\ \left[E_D^2\right]_{v_y} - 2\,\alpha\,\left(v_{xyx} + v_{yyy}\right) \end{bmatrix} \end{aligned} \tag{5.48}$$

with an outer normal vector $\boldsymbol{n} = (n_1, n_2)^\top$.

5.3.2 The Extension Cases

Based on the previous section, we derive EL equations along with boundary conditions for the extended models.

Model with Confidence Function

Euler-Lagrange Equation. When it comes to the model with the confidence function (5.30), we integrate the confidence function c into the EL equation of the basis model based on the assumption that the confidence on each pixel is already available at the preprocessing step. This gives

$$\left(\left[c\, E_D^2\right]_v - \frac{\partial}{\partial x}\left[c\, E_D^2\right]_{v_x} - \frac{\partial}{\partial y}\left[c\, E_D^2\right]_{v_y}\right) + 2\,\alpha\,(1-c)\,\left(\Delta^2 v\right) = 0\,. \tag{5.49}$$

As previously indicated, this EL equation suggests that the fourth-order diffusion process by the biharmonic operator is active for reconstruction in the unreliable regions, i.e. when $c = 0$. This effect allows to fill in the information from the neighbourhood and thereby further leads to dense reconstructions even if no data is available at some locations.

Boundary Conditions. Aside from the EL equation, the boundary conditions can be adapted accordingly. Since the confidence function acts as a scaling factor in the integrated EL equation, the second condition (5.47) is not affected. The other condition (5.48) is changed by the factor $(1 - c)$, which reads

$$0 = \boldsymbol{n}^\top \begin{bmatrix} \left[c\, E_D^2\right]_{v_x} - 2\,\alpha\,(1-c)\,\left(v_{xxx} + v_{xyy}\right) \\ \left[c\, E_D^2\right]_{v_y} - 2\,\alpha\,(1-c)\,\left(v_{xyx} + v_{yyy}\right) \end{bmatrix} . \tag{5.50}$$

Model with Edge-preserving Smoothness Term

Euler-Lagrange equation. To derive the associated EL equation with the edge-preserving model extension (5.32), we need to compute the derivatives for the smoothness term accordingly. Since the smoothness term involves the subquadratic penaliser, applying the chain rule to $\Psi(s^2)$ yields

$$\left[\Psi\left(s^2\right)\right]_{v_{xx}} = \frac{\partial \Psi\left(s^2\right)}{\partial s^2}\,\frac{\partial s^2}{\partial v_{xx}} \overset{(5.29)}{=} 2\,\Psi'\left(s^2\right)\,v_{xx}\,, \tag{5.51}$$

$$\left[\Psi\left(s^2\right)\right]_{v_{xy}} = \frac{\partial \Psi\left(s^2\right)}{\partial s^2}\,\frac{\partial s^2}{\partial v_{xy}} \overset{(5.29)}{=} 2\,\Psi'\left(s^2\right)\,v_{xy}\,, \tag{5.52}$$

$$\left[\Psi\left(s^2\right)\right]_{v_{yy}} = \frac{\partial \Psi\left(s^2\right)}{\partial s^2}\,\frac{\partial s^2}{\partial v_{yy}} \overset{(5.29)}{=} 2\,\Psi'\left(s^2\right)\,v_{yy}\,, \tag{5.53}$$

where $s := \|D^2 v\|_F$ is defined as in (5.29) and the derivative of the penaliser function $\Psi'(s^2)$ denotes

$$\Psi'\left(s^2\right) = \frac{\partial}{\partial s^2}\Psi(s^2) = \frac{1}{\sqrt{1+\frac{s^2}{\lambda^2}}} . \tag{5.54}$$

Hence, by plugging the derivative result of the smoothness term into the EL equation for the base case one can obtain the corresponding EL equation

$$\begin{aligned} &\left[E_D^2\right]_v - \frac{\partial}{\partial x}\left[E_D^2\right]_{v_x} - \frac{\partial}{\partial y}\left[E_D^2\right]_{v_y} \\ &+ 2\,\alpha\left(\frac{\partial^2}{\partial x^2}\left[\Psi'\left(s^2\right)\,v_{xx}\right] + 2\,\frac{\partial^2}{\partial x \partial y}\left[\Psi'\left(s^2\right)\,v_{xy}\right] + \frac{\partial^2}{\partial y^2}\left[\Psi'\left(s^2\right)\,v_{yy}\right]\right) = 0\,. \end{aligned} \tag{5.55}$$

It can be noted that the Charbonnier diffusivity $\Psi'(s^2)$, i.e. the amount of smoothing, decreases as the value of s^2 increases. This suggests that the desired edge-preserving effect can be achieved, since the smoothing effect is reduced when an edge structure is recognised by high curvature, i.e. locations with high values of s^2. Furthermore, the EL equation for the edge-preserving case (5.55) can be reduced to the one for the base case (5.45), when the subquadratic penaliser becomes the quadratic one $\Psi(s^2) = s^2$ with $\Psi'(s^2) = 1$.

Boundary Conditions. Concerning the boundary conditions, the second condition remains the same because it is only influenced by the smoothness term and all elements have the same positive common factor $\Psi'(s^2)$. Moreover, the other condition can also be adapted for the smoothness term. This leads to

$$0 = \boldsymbol{n}^\top \begin{bmatrix} \left[E_D^2\right]_{v_x} - 2\,\alpha \dfrac{\partial}{\partial x}\left[\Psi'\left(s^2\right)\, v_{xx}\right] - 2\,\alpha \dfrac{\partial}{\partial y}\left[\Psi'\left(s^2\right)\, v_{xy}\right] \\ \left[E_D^2\right]_{v_y} - 2\,\alpha \dfrac{\partial}{\partial x}\left[\Psi'\left(s^2\right)\, v_{xy}\right] - 2\,\alpha \dfrac{\partial}{\partial y}\left[\Psi'\left(s^2\right)\, v_{yy}\right] \end{bmatrix} \tag{5.56}$$

with an outer normal vector $\boldsymbol{n} = (n_1, n_2)^\top$.

5.3.3 Discretisation

For minimising an energy functional, there are mainly two categories of approaches: One method is to discretise the associated EL equations to the original energy functional. Since this approach requires to compute EL equations explicitly as a necessary condition to the minimiser and thereby does not deal with the energy functional directly, it is called *first optimise then discretise approach* or *indirect method* [33, 111, 261]. The other one is to minimise the energy functional directly by finding the optimal condition for the corresponding discrete energy instead of using EL equations. Therefore, this type of optimisation method is called *first discretise then optimise approach* or *direct method* [33, 111, 261]. Both methods are different from each other in that they deal with EL equations explicitly or not but they rely on the same principle for a minimiser whose first variations or gradient vector should vanish.

To deal with the variational models for perspective SfS, we follow a hybrid approach: we apply the indirect method for the data term and the direct method for the smoothness term. This strategy offers a considerable advantage in that we do not need to deal with the boundary conditions explicitly, which are quite difficult to discretise: Since the data term has a hyperbolic nature and the information propagates from the critical points that are actually inside the computational domain, the differentiation of the discrete energy of the smoothness term with respect to all pixels allows to provide a proper discretisation including the correct handling of the boundary conditions. The direct approach fulfils the natural boundary conditions implicitly without requiring boundary conditions explicitly [77, 201, 202].

Data Term. When discretising the first order derivative ∇v from the contributions of the data term in the derived EL equations, we respect the hyperbolic nature of the HJE and employ an upwind discretisation [219]. Moreover, when a second-order or mixed derivative terms arise during the computation, we follow the discretisation strategy as subsequently specified.

Smoothness Term. For discretising the contributions from the smoothness term, we make use of a central difference scheme based on the nature of the regulariser. Moreover, we only deal with the edge-preserving case, since this case covers the basic case as well. Hence, we consider the smoothness term

$$\int_\Omega \Psi\left(v_{xx}^2 + 2\,v_{xy}^2 + v_{yy}^2\right)\,d\boldsymbol{x}\,. \tag{5.57}$$

To discretise (5.57), we use the following approximations

$$(v_{xx})_{i,j} \approx \frac{1}{h_1^2}\left(v_{i+1,j} - 2\,v_{i,j} + v_{i-1,j}\right) =: (\hat{v}_{xx})_{i,j} \tag{5.58}$$

and

$$\left(v_{yy}\right)_{i,j} \approx \frac{1}{h_2^2}\left(v_{i,j+1} - 2\,v_{i,j} + v_{i,j-1}\right) =: \left(\hat{v}_{yy}\right)_{i,j} \tag{5.59}$$

for the second-order derivatives v_{xx} and v_{yy}, respectively. Regarding the mixed derivative term v_{xy}, utilising the central difference approximation for both x- and y-direction yields

$$v_{xy} \approx \frac{1}{4\,h_1\,h_2}\left(v_{i+1,j+1} - v_{i-1,j+1} - v_{i+1,j-1} + v_{i-1,j-1}\right) =: \left(\hat{v}_{xy}\right)_{i,j}\,. \tag{5.60}$$

Then, we can state the discrete version of the continuous smoothness term as

$$\left(\widehat{E}_S\right)_{i,j} = \sum_{j=by}^{by+ny-1}\ \sum_{i=bx}^{bx+nx-1} \Psi\left((v_{**})_{i,j}^2\right)\,, \tag{5.61}$$

where $(v_{**})_{i,j}^2$ stands for

$$(v_{**})_{i,j}^2 := (\hat{v}_{xx})_{i,j}^2 + 2\,\left(\hat{v}_{xy}\right)_{i,j}^2 + \left(\hat{v}_{yy}\right)_{i,j}^2\,. \tag{5.62}$$

Furthermore, as illustrated in Figure 5.2, bx stands for the number of left and right boundary pixels in x-direction, by denotes the number of upper and lower boundary pixels in y-direction, and nx and ny the number of pixels of the input image in x- and y-direction, respectively.

Differentiation of the Discrete Energy for Smoothness Term

For obtaining a minimiser of the discrete energy, its differentiation at each point must vanish. This means

$$\frac{\partial \left(\widehat{E}_S\right)_{k,l}}{\partial v_{k,l}} \overset{!}{=} 0\,, \quad \forall\, k,l \in \Omega\,, \tag{5.63}$$

where $k \in [bx, bx + nx - 1]$ and $l \in [by, by + ny - 1]$.

One should note that this expression usually takes a different form depending on the grid position due to the implicit boundary conditions. Hence, we make use of the characteristic function as well as running indices $(k,l)^\top \in \mathbb{N}^2$ to formulate this optimality condition in a compact way. In particular, this approach allows to describe not only the influence of neighbouring grid positions but also the suitable range when the running indices $(k,l)^\top$ correspond to each subscript of the argument in the discrete energy. Since the discrete energy of the smoothness term contains ten arguments, there are ten cases to consider. To this end, we define the following expression

$$\Psi'_{k,l} := \Psi'\left((v_{**})^2_{k,l}\right)\,. \tag{5.64}$$

Case 1: $(k,l)^\top = (i+1, j)^\top$. In this case, the three terms from the approximation of the second-order derivative in x-direction are involved. This yields the form

$$2\,\chi_{[bx+2,bx+nx-1][by,by+ny-1]}\;\Psi'_{k-1,l}\,\frac{v_{k,l} - 2\,v_{k-1,l} + v_{k-2,l}}{h_1^4} =: C_1\,, \tag{5.65}$$

where χ denotes the characteristic function. Moreover, the ranges of k and l can be obtained by

$$\left\{\begin{array}{l} (bx \leqslant k-2) \wedge (k \leqslant bx + nx - 1)\,, \\ by \leqslant l \leqslant by + ny - 1 \end{array}\right. \quad\Leftrightarrow\quad \left\{\begin{array}{l} bx + 2 \leqslant k \leqslant bx + nx - 1\,, \\ by \leqslant l \leqslant by + ny - 1\,, \end{array}\right. \tag{5.66}$$

since the leftmost node $(k-2,l)^\top$ and the rightmost one $(k,l)^\top$ must be inside the computational domain Ω, see Figure 5.2.

Case 2: $(k,l)^\top = (i,j)^\top$. In the same way as the first case, we obtain

$$-\,4\,\chi_{[bx+1,bx+nx-2][by,by+ny-1]}\;\Psi'_{k,l}\,\frac{v_{k+1,l} - 2\,v_{k,l} + v_{k-1,l}}{h_1^4} =: C_2\,. \tag{5.67}$$

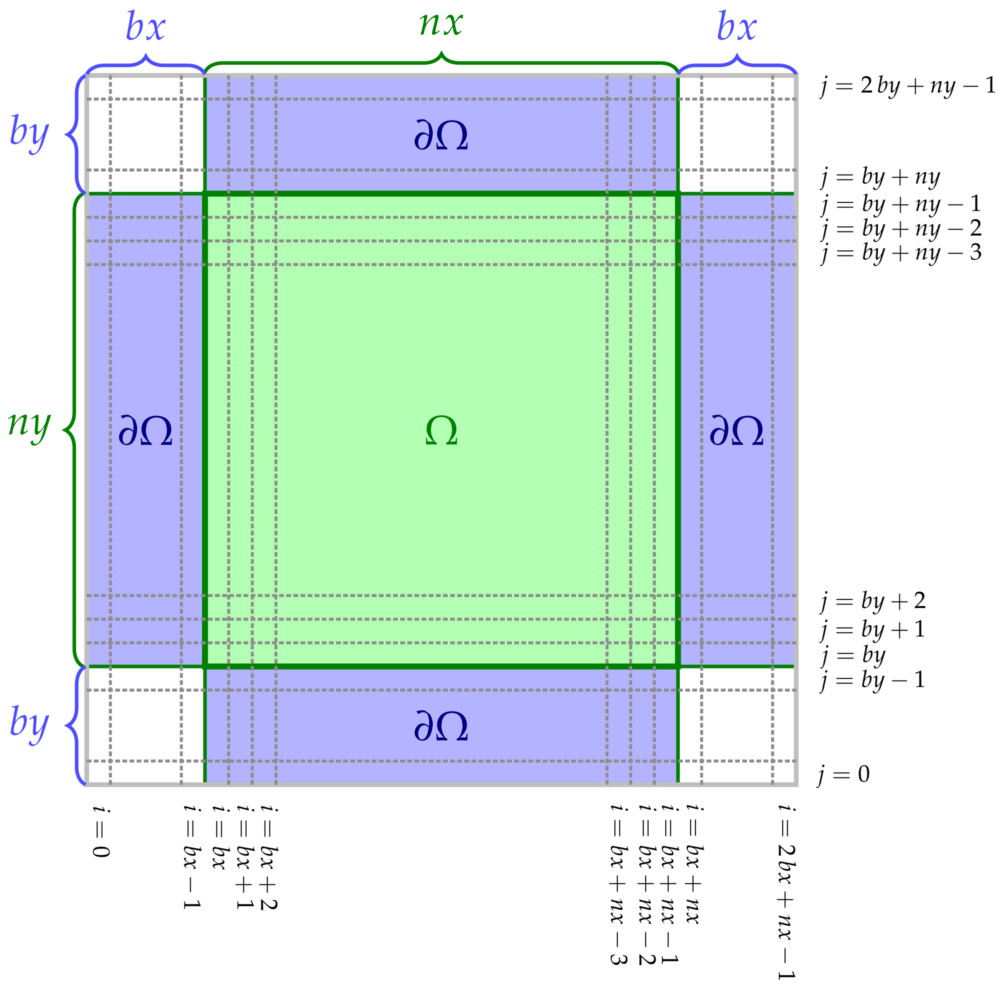

Figure 5.2. The grid structure of the domain Ω and the boundaries $\partial\Omega$.

The proper scope of k and l is given by

$$\begin{cases} (bx \leqslant k-1) \wedge (k+1 \leqslant bx+nx-1)\,, \\ by \leqslant l \leqslant by+ny-1 \end{cases} \Leftrightarrow \begin{cases} bx+1 \leqslant k \leqslant bx+nx-2\,, \\ by \leqslant l \leqslant by+ny-1\,, \end{cases} \tag{5.68}$$

based on the fact that the leftmost node and the rightmost one correspond to $(k-1,l)^\top$ and $(k+1,l)^\top$, respectively.

Case 3: $(k,l)^\top = (i-1,j)^\top$**.** This case is not any different from the first two ones except the relative positions of the arguments. Therefore, we obtain

$$2\,\chi_{[bx,bx+nx-3][by,by+ny-1]}\,\Psi'_{k+1,l}\,\frac{v_{k+2,l}-2\,v_{k+1,l}+v_{k,l}}{h_1^4} =: C_3\,. \tag{5.69}$$

Apart from no constraints for l as in the first two cases, the leftmost node $(k,l)^\top$ and the rightmost one $(k+2,l)^\top$ must stay inside the domain Ω. This yields the condition for k and l

$$\begin{cases} (bx \leqslant k) \wedge (k+2 \leqslant bx+nx-1)\,, \\ by \leqslant l \leqslant by+ny-1 \end{cases} \Leftrightarrow \begin{cases} bx \leqslant k \leqslant bx+nx-3\,, \\ by \leqslant l \leqslant by+ny-1\,. \end{cases} \tag{5.70}$$

Case 4: $(k,l)^\top = (i+1,j+1)^\top$. This case incorporates the four terms approximating the first-order derivative. This leads to

$$\chi_{[bx+2,bx+nx-1][by+2,by+ny-1]}\,\Psi'_{k-1,l-1}\,\frac{v_{k,l}-v_{k-2,l}-v_{k,l-2}+v_{k-2,l-2}}{4\,h_1^2\,h_2^2} =: C_4\,. \tag{5.71}$$

In this case, the range of variables for k and l are bounded by the lowest leftmost node $(k-2,l-2)^\top$ and the right uppermost one $(k,l)^\top$:

$$\begin{cases} (bx-2 \leqslant k) \wedge (k \leqslant bx+nx-1)\,, \\ \big(by-2 \leqslant l\big) \wedge \big(l \leqslant by+ny-1\big) \end{cases} \Leftrightarrow \begin{cases} bx+2 \leqslant k \leqslant bx+nx-1\,, \\ by+2 \leqslant l \leqslant by+ny-1\,. \end{cases} \tag{5.72}$$

Case 5: $(k,l)^\top = (i-1,j+1)^\top$. As in the previous case, we can attain the following form for this case

$$-\,\chi_{[bx,bx+nx-3][by+2,by+ny-1]}\,\Psi'_{k+1,l-1}\,\frac{v_{k+2,l}-v_{k,l}-v_{k+2,l-2}+v_{k,l-2}}{4\,h_1^2\,h_2^2} =: C_5\,. \tag{5.73}$$

It can be observed that the left and right bounds are determined by k and $k+2$. When it comes to the y-direction, $l-2$ and l decide the lower and upper bounds. In view of bounds on both directions, the suitable ranges for k and l are given by

$$\begin{cases} (bx \leqslant k) \wedge (k+2 \leqslant bx+nx-1)\,, \\ \big(by-2 \leqslant l\big) \wedge \big(l \leqslant by+ny-1\big) \end{cases} \Leftrightarrow \begin{cases} bx \leqslant k \leqslant bx+nx-3\,, \\ by+2 \leqslant l \leqslant by+ny-1\,. \end{cases} \tag{5.74}$$

Case 6: $(k,l)^\top = (i+1,j-1)^\top$. In the same way as the previous one, we can derive the following form for this case

$$-\,\chi_{[bx+2,bx+nx-1][by,by+ny-3]}\,\Psi'_{k-1,l+1}\,\frac{v_{k,l+2}-v_{k-2,l+2}-v_{k,l}+v_{k-2,l}}{4\,h_1^2\,h_2^2} =: C_6\,. \tag{5.75}$$

The appropriate ranges of k and l are determined by

$$\begin{cases} (bx \leqslant k-2) \wedge (k \leqslant bx+nx-1)\,, \\ \big(by \leqslant l\big) \wedge \big(l+2 \leqslant by+ny-1\big) \end{cases} \Leftrightarrow \begin{cases} bx+2 \leqslant k \leqslant bx+nx-1\,, \\ by \leqslant l \leqslant by+ny-3\,. \end{cases} \tag{5.76}$$

Case 7: $(k,l)^\top = (i-1, j-1)^\top$**.** When compared with the "Case 6," this case is only different in k for which we have already obtained in "Case 5." This gives

$$\chi_{[bx,bx+nx-3][by,by+ny-3]}\,\Psi'_{k+1,l+1}\,\frac{v_{k+2,l+2} - v_{k,l+2} - v_{k+2,l} + v_{k,l}}{4\,h_1^2\,h_2^2} =: C_7\,. \tag{5.77}$$

The constraints on the ranges of k and l are imposed by

$$\begin{cases} (bx \leqslant k) \wedge (k+2 \leqslant bx+nx-1)\,, \\ (by \leqslant l) \wedge \big(l+2 \leqslant by+ny-1\big) \end{cases} \Leftrightarrow \quad \begin{cases} bx \leqslant k \leqslant bx+nx-3\,, \\ by \leqslant l \leqslant by+ny-3\,. \end{cases} \tag{5.78}$$

Case 8: $(k,l)^\top = (i, j+1)^\top$**.** This case concerns the approximation of the second-order derivative in y-direction which has the same structure as the "Case 1" except the direction. This gives

$$2\,\chi_{[bx,bx+nx-1][by+2,by+ny-1]}\,\Psi'_{k,l-1}\,\frac{v_{k,l} - 2\,v_{k,l-1} + v_{k,l-2}}{h_2^4} =: C_8\,. \tag{5.79}$$

Moreover, we can obtain the ranges of k and l by exploiting the symmetric structures.

Case 9: $(k,l)^\top = (i, j)^\top$**.** The structure of this case is the same as the second one and only the role of indices is changed. As a result, we have

$$-\,4\,\chi_{[bx,bx+nx-1][by+1,by+ny-2]}\,\Psi'_{k,l}\,\frac{v_{k,l+1} - 2\,v_{k,l} + v_{k,l-1}}{h_2^4} =: C_9\,. \tag{5.80}$$

As indicated in the previous case, the ranges of k and l can be attained by exchanging the intervals of k and l in "Case 2."

Case 10: $(k,l)^\top = (i, j-1)^\top$**.** When it comes to the last case, the third case is the counterpart of this one. Therefore, we have

$$2\,\chi_{[bx,bx+nx-1][by,by+ny-3]}\,\Psi'_{k,l+1}\,\frac{v_{k,l+2} - 2\,v_{k,l+1} + v_{k,l}}{h_2^4} =: C_{10}\,. \tag{5.81}$$

The ranges of k and l can be attained by switching the roles of both indices in the third case based on the symmetric structures.

As a consequence, by putting all the cases together we can reformulate the optimality condition as

$$0 = \frac{\partial \left(\widehat{E}_S\right)_{k,l}}{\partial v_{k,l}} = \sum_{p=1}^{10} C_p\,, \quad \forall\,(k,l)^\top \in \Omega\,. \tag{5.82}$$

Moreover, we also obtain the stencil notation given in Table 5.1 by rearranging the whole terms from all cases and grouping coefficients with respect to the relative positions.

Table 5.1. The 5×5 stencil diagram with the Charbonnier diffusivity (5.54). The circled numbers refer to the case where the terms come from and thereby they share the same colour.

	$i-2$	$i-1$	i	$i+1$	$i+2$
$j+2$	$\frac{\Psi'_{k-1,l+1}\textcircled{6}}{4\,h_1^2\,h_2^2}$	0	$-\frac{\Psi'_{k-1,l+1}\textcircled{6}}{4\,h_1^2\,h_2^2}-\frac{\Psi'_{k+1,l+1}\textcircled{7}}{4\,h_1^2\,h_2^2}+\frac{2\,\Psi'_{k,l+1}\textcircled{10}}{h_2^4}$	0	$\frac{\Psi'_{k+1,l+1}\textcircled{7}}{4\,h_1^2\,h_2^2}$
$j+1$	0	0	$-\frac{4\,\Psi'_{k,l}\textcircled{9}}{h_2^4}-\frac{4\,\Psi'_{k,l+1}\textcircled{10}}{h_2^4}$	0	0
j	$\frac{2\,\Psi'_{k-1,l}\textcircled{1}}{h_1^4}$ $-\frac{\Psi'_{k-1,l-1}\textcircled{4}}{4\,h_1^2\,h_2^2}$ $-\frac{\Psi'_{k-1,l+1}\textcircled{6}}{4\,h_1^2\,h_2^2}$	$-\frac{4\,\Psi'_{k-1,l}\textcircled{1}}{h_1^4}$ $-\frac{4\,\Psi'_{k,l}\textcircled{2}}{h_1^4}$	$\frac{2\,\Psi'_{k-1,l}\textcircled{1}}{h_1^4}+\frac{8\,\Psi'_{k,l}\textcircled{2}}{h_1^4}+\frac{2\,\Psi'_{k+1,l}\textcircled{3}}{h_1^4}$ $+\frac{\Psi'_{k-1,l-1}\textcircled{4}}{4\,h_1^2\,h_2^2}+\frac{\Psi'_{k+1,l-1}\textcircled{5}}{4\,h_1^2\,h_2^2}$ $+\frac{\Psi'_{k-1,l+1}\textcircled{6}}{4\,h_1^2\,h_2^2}+\frac{\Psi'_{k+1,l+1}\textcircled{7}}{4\,h_1^2\,h_2^2}$ $+\frac{2\,\Psi'_{k,l-1}\textcircled{8}}{h_2^4}+\frac{8\,\Psi'_{k,l}\textcircled{9}}{h_2^4}+\frac{2\,\Psi'_{k,l+1}\textcircled{10}}{h_2^4}$	$-\frac{4\,\Psi'_{k,l}\textcircled{2}}{h_1^4}$ $-\frac{4\,\Psi'_{k+1,l}\textcircled{3}}{h_1^4}$	$\frac{2\,\Psi'_{k+1,l}\textcircled{3}}{h_1^4}$ $-\frac{\Psi'_{k+1,l-1}\textcircled{5}}{4\,h_1^2\,h_2^2}$ $-\frac{\Psi'_{k+1,l+1}\textcircled{7}}{4\,h_1^2\,h_2^2}$
$j-1$	0	0	$-\frac{4\,\Psi'_{k,l-1}\textcircled{8}}{h_2^4}-\frac{4\,\Psi'_{k,l}\textcircled{9}}{h_2^4}$	0	0
$j-2$	$\frac{\Psi'_{k-1,l-1}\textcircled{4}}{4\,h_1^2\,h_2^2}$	0	$-\frac{\Psi'_{k-1,l-1}\textcircled{4}}{4\,h_1^2\,h_2^2}-\frac{\Psi'_{k+1,l-1}\textcircled{5}}{4\,h_1^2\,h_2^2}+\frac{2\,\Psi'_{k,l-1}\textcircled{8}}{h_2^4}$	0	$\frac{\Psi'_{k+1,l-1}\textcircled{5}}{4\,h_1^2\,h_2^2}$

5.3.4 Numerical Solution

Once discretisations from both the data and the smoothness term are obtained, the solution of the EL equations can be reformulated as the steady state of the corresponding evolution equation in artificial time. To this end, we apply the Euler forward time discretisation method

$$v_t \approx \frac{v^{n+1} - v^n}{\tau}\,, \tag{5.83}$$

where τ denotes the time step size. Then, we obtain the following explicit scheme

$$\frac{v^{n+1} - v^n}{\tau} = -\left(\mathrm{EL}_D^n + \alpha\, \mathrm{EL}_S^n\right) \qquad \Leftrightarrow \qquad v^{n+1} = v^n - \tau\, \left(\mathrm{EL}_D^n + \alpha\, \mathrm{EL}_S^n\right)\,, \tag{5.84}$$

where EL_D^n and EL_S^n denotes the corresponding discretisations by means of the indirect method for the data term and the direct method for the smoothness term, respectively. These discretisations can be applied to the derived Euler-Lagrange equations which are evaluated at time step n.

Concerning the stability of the explicit scheme, the highly intricate nonlinear contributions from the data term cause difficulties in procuring a stability constraint for the whole terms, although the eigenvalues of the biharmonic operator are available and thereby can provide the information on the time step size τ to secure the numerical stability for the smoothness term. On this account, for numerical experiments the time step size τ has been selected in such a way that the total energy is decreasing and the reconstruction look visually appealing.

5.4 Experimental Results

In this section, we present our experimental results by investigating various aspects on the variational perspective SfS model in Section 5.2.2.

5.4.1 Influence of Regularisations

The first experiment concerns the influence of the homogeneous and edge-preserving smoothness terms on the reconstruction. In order to demonstrate the impact of the smoothness term, we first perform the reconstruction *without* the smoothness term, which is equivalent to $\alpha = 0$ according to (5.25). To this end, we have used the classical vase input image shown in Figure 5.3(a) that has been rendered with a perspective camera model. For the explicit scheme (5.84), we apply the time step size $\tau = 10^{-1}$ with 2000 iterations by employing the initialisation method as explained in (3.72).

The corresponding reconstruction is given in Figure 5.3(b), where the legend indicates colour-coded Cartesian depth values. It clearly shows that the object surface is separated from the background owing to the substantial difference of the grey value between them. This suggests that, despite the methodological difference from PDE-based approaches, variational methods are capable of giving similar results, if the smoothness term is turned off.

(a) Input image (128 × 128).

(b) Reconstruction with $\alpha = 0$.

Figure 5.3. Reconstruction without the smoothness term.

Homogeneous versus Edge-preserving Regularisation

Let us now compare the results between the homogeneous and the edge-preserving regularisation. To this end, we turn on the smoothness term (5.29) and increase the regularisation parameter α in (5.25) from 10^{-4} to 10^{-1}. The corresponding results are exhibited in Figure 5.4(a) – 5.4(d). It can be observed that the reconstruction of the object becomes stronger connected to the background plane as the smoothness parameter α increases. As previously mentioned in Section 5.2.2, this is because the employed regulariser (5.29) is everywhere homogeneous and non-adaptive and thereby causes the oversmoothing effect at the border between an object and the background.

To cope with the situation, we can apply the edge-preserving smoothness term (5.32). By comparing the results with the results of homogeneous regulariser in Figure 5.4(d), one can notice that the reconstruction with the Charbonnier regulariser in Figure 5.5(b) can retain the discontinuity at the object boundary – for the same value of the regularisation parameter $\alpha = 0.1$. This effect has been achieved by reducing the diffusivity at high curvature regions based on the discussions in Section 5.2.2. For the experiment, the runtime amounts to be approximately 20 seconds.

5.4.2 Influence of Confidence Function

The next experiment demonstrates the impact of the confidence function that is employed in the model (5.30). To this end, we have taken Figure 5.6(a) as an input image containing the corrupt region that is marked black inside the object. Since this degraded region corresponds to Γ in (5.31), we can make use of the binary confidence function (5.31) shown in Figure 5.6(b) for reconstruction. Moreover, by comparing the black region in Figure 5.6(a) with that of the confidence function in Figure 5.6(b) it can be noted that the black area in the confidence function has been extended by means of a morphological erosion filter such that no spoiled data is included and

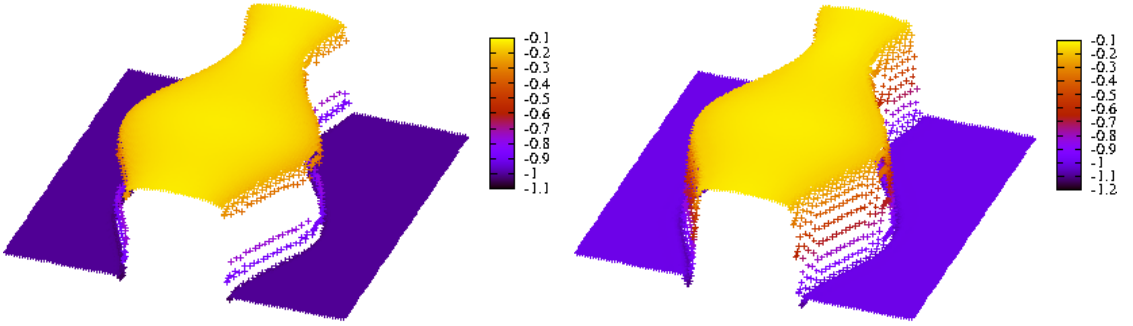

(a) Homogeneous smoothness with $\alpha = 10^{-4}$. (b) Homogeneous smoothness with $\alpha = 10^{-3}$.

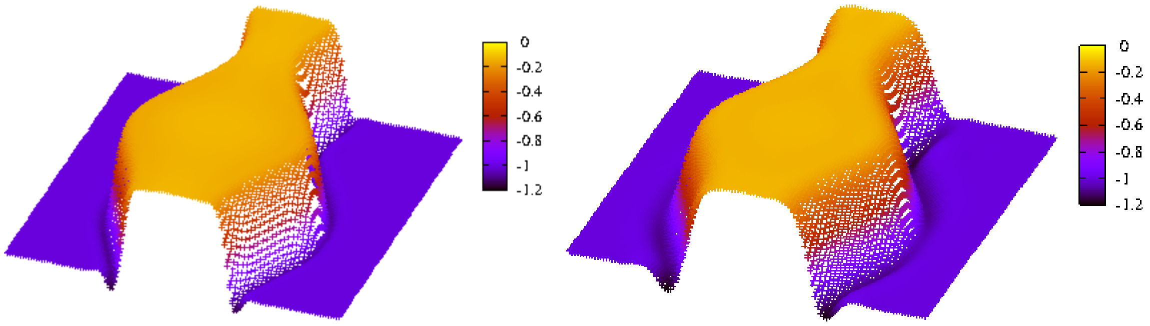

(c) Homogeneous smoothness with $\alpha = 10^{-2}$. (d) Homogeneous smoothness with $\alpha = 10^{-1}$.

Figure 5.4. Influence of the homogeneous regulariser for reconstruction.

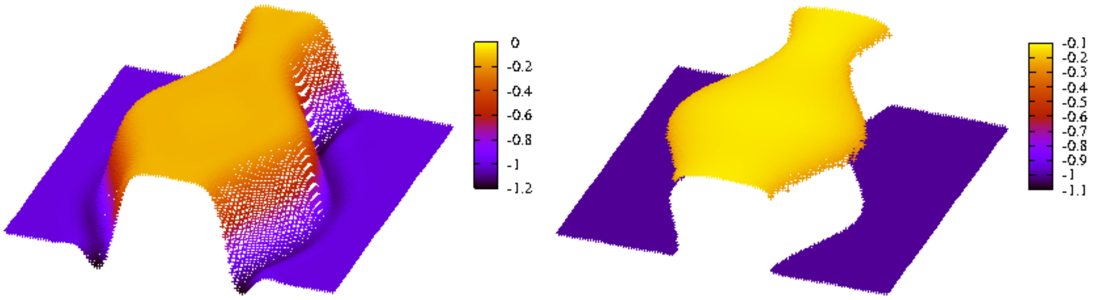

(a) No edge preservation ($\alpha = 0.1$). (b) Edge preservation ($\alpha = 0.1, \lambda = 10^{-5}$).

Figure 5.5. Influence of the edge-preserving regulariser.

potential difficulties with derivatives at the boundaries between $\Omega \setminus \Gamma$ and Γ are be avoided.

Figure 5.6(c) and 5.6(d) demonstrate the reconstruction without and with the smoothness term, respectively. As can be noticed in Figure 5.6(c), the reconstruction without the smoothness term cannot achieve an appropriate result in the region Γ. In contrast to that, as shown in Figure 5.6(d), one obtains a reasonable and smoothly inpainted object surface in the region Γ, when utilising the smoothness term equipped with the confidence function (5.31). As pointed out in Section 5.2.2, this accounts for the filling-in effect of the smoothness term in the region Γ by propagating information from neighbouring pixels. For the region $\Omega \setminus \Gamma$, however, the data term still plays the dominant role in the reconstruction.

(a) Input image (690×590).

(b) Confidence function.

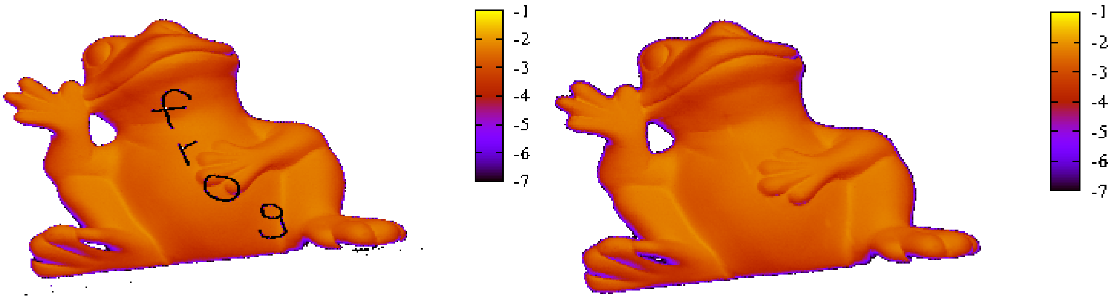

(c) Reconstruction with $\alpha = 0$.

(d) Reconstruction with $\alpha = 0.2$.

Figure 5.6. Impact of confidence function: Inpainting a reconstruction. Employed parameters are: Time step size $\tau = 10^{-1}$, 2500 iterations. The runtime is 890 seconds.

Moreover, we further investigate the inpainting capability of the model with respect to more challenging images containing difficult structures such as kinks and ridges as shown in Figure 5.7(a). The inpainted reconstructions through the homogeneous regulariser with the confidence function depending on the regions are displayed in Figure 5.7(d), 5.7(f) and 5.7(h), respectively. Given the fact that particularly important and meaningful features have been removed from the input data, the interpolated surface still demonstrates compelling results when compared with the one without the confidence function, cf. Figure 5.7(c), 5.7(e), and 5.7(g).

5.4.3 Robustness with Respect to Noise

In this section, we look into the robustness of our variational approaches with respect to noise. To this end, we make the unspoiled original image in Figure 5.8(a) deteriorated by adding 5 % salt and pepper noise and Gaussian noise with standard deviation $\sigma = 20$ as shown in Figure 5.8(b) and 5.9(b), respectively.

The reconstruction results without and with the confidence function in the presence of salt and pepper noise are exhibited in Figure 5.8(d) and 5.8(e), respectively. While the computed solution without confidence function in Figure 5.8(d) clearly demonstrates that the surface seems to be bumpy with many holes and fluctuations according to the noise pattern, the one with confidence function produces a significantly better outcome by harnessing the smoothness term. This is realised in a way that the confidence function excludes the noisy pixels that have been previously identified by their brightness and the smoothness term fills in missing information.

Regarding Gaussian noise, the estimated surfaces are placed side by side as displayed in Figure 5.9, i.e. the one in the absence of the smoothness term and the one with the regulariser. It can be clearly observed that the estimations with the smoothness term, show a denoising effect and provides robust results w.r.t. the reconstruction, see Figure 5.9(d), 5.9(f), and 5.9(h). However, as shown in Figure 5.9(c), 5.9(e), 5.9(g), the reconstruction without the regulariser suffers from irregular oscillations since the noisy pixels cannot be properly handled. This suggests that variational approaches offer a clear advantage over PDE-based ones, especially when it comes to the noise. The reason for this is the smoothness term that is not available in PDE-based methods.

5.5 Summary

In this chapter, we have developed a first variational approach for perspective shape from shading by combining the Hamilton-Jacobi equation of the recent PDE-based approach described in Chapter 3 as the data term with a homogeneous second-order smoothness term. Furthermore, we have extended the basis model by introducing a spatially varing confidence function and an edge-preserving smoothness term in order to eliminate unreliable information and to retain edge structures, respectively. Afterwards, we have presented experimental results, which show the advantages of the smoothness term for perspective SfS: Not only does it deliver a substantially better performance in various noisy situations, but it also opens up the possibility to inpaint the information for missing or corrupted data.

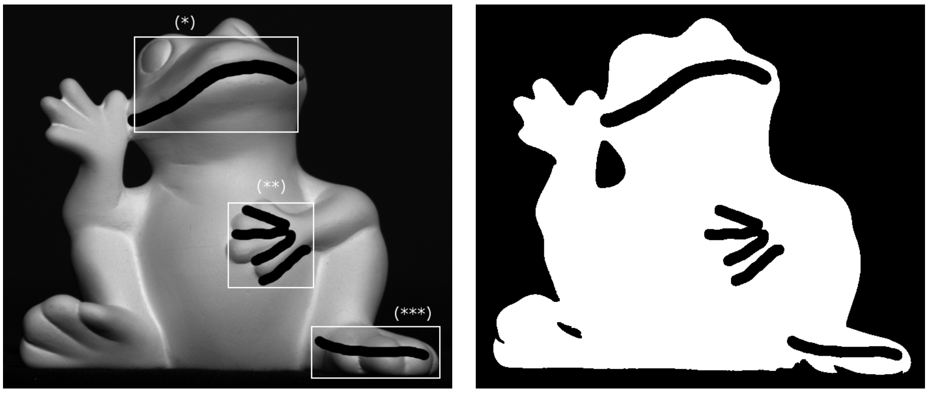

(a) Input image (690 × 590). (b) Confidence function.

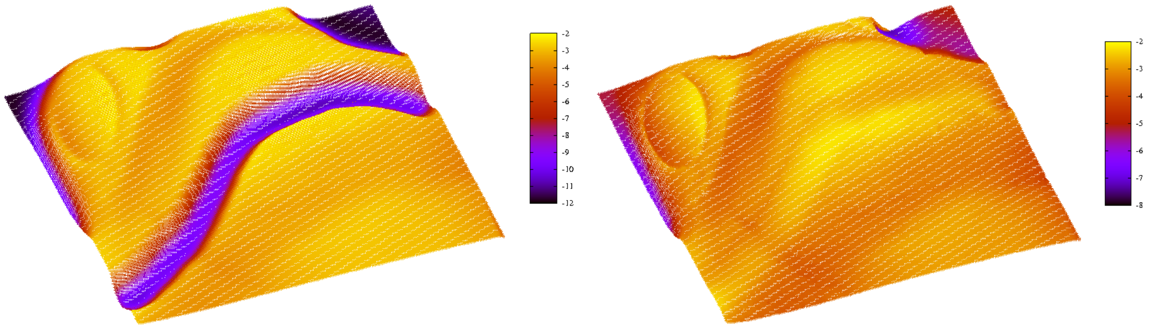

(c) Without confidence function for (∗). (d) With confidence function for (∗).

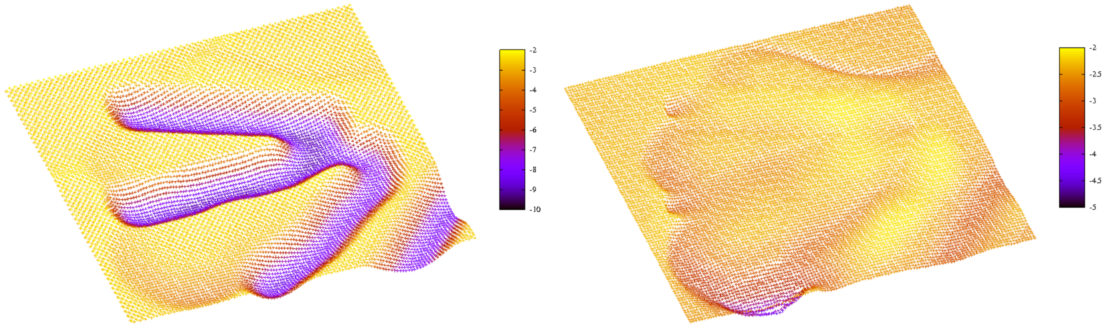

(e) $\alpha = 0.3$. (f) Reconstruction at region (∗∗).

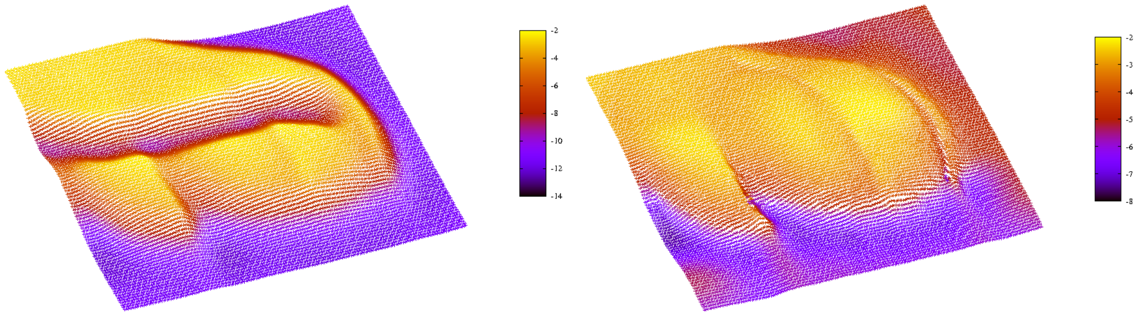

(g) $\alpha = 0.3$. (h) Reconstruction at region (∗ ∗ ∗).

Figure 5.7. Interpolation with the confidence function and the smoothness term. Employed parameters are: Time step size $\tau = 10^{-1}$, 25000 iterations, $\alpha = 0.3$. The runtime is 9200 seconds.

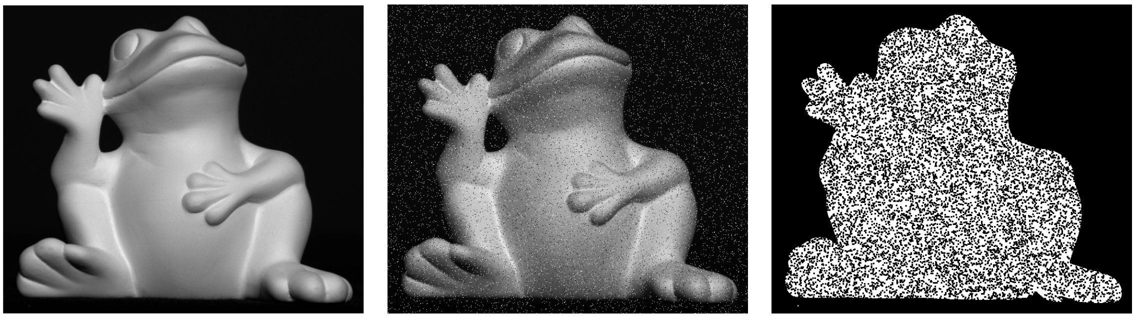

(a) Original image (690 × 590). (b) 5 % salt and pepper noise. (c) Confidence function.

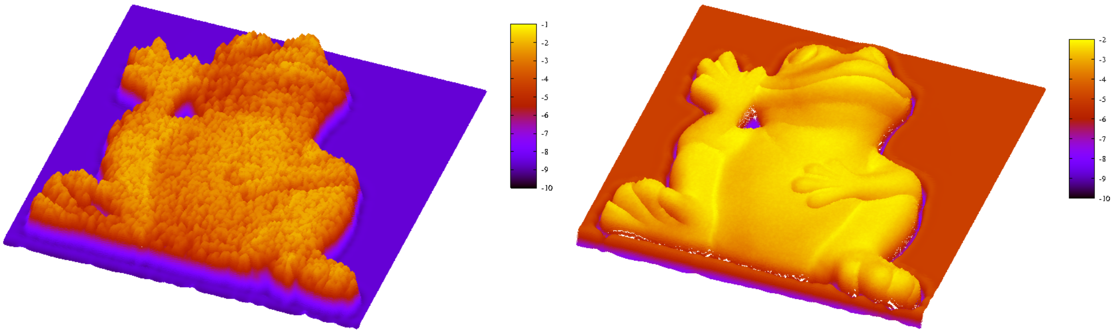

(d) $\alpha = 0.3$ without confidence function. (e) $\alpha = 0.3$ with confidence function.

Figure 5.8. Reconstruction under salt and pepper noise. Employed parameters are: Time step size $\tau = 10^{-1}$, 5000 iterations. Runtime: 1720 seconds.

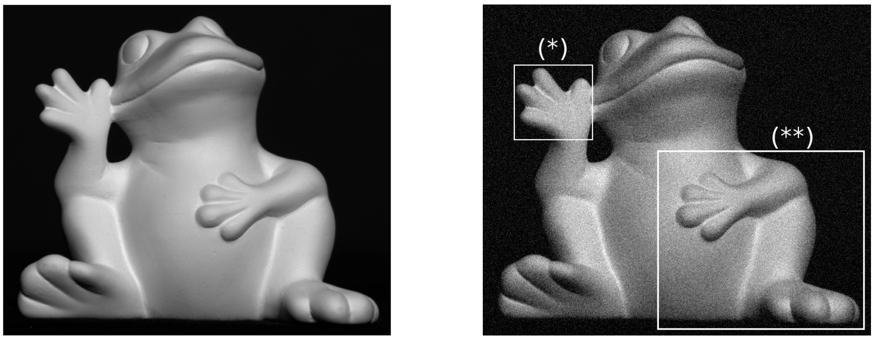

(a) Original image (690 × 590). (b) Gaussian noise with $\sigma = 20$.

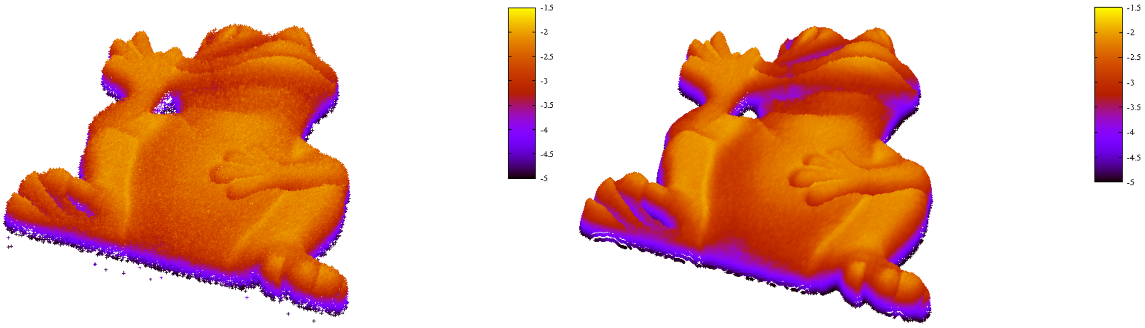

(c) $\alpha = 0$. (d) $\alpha = 0.3$.

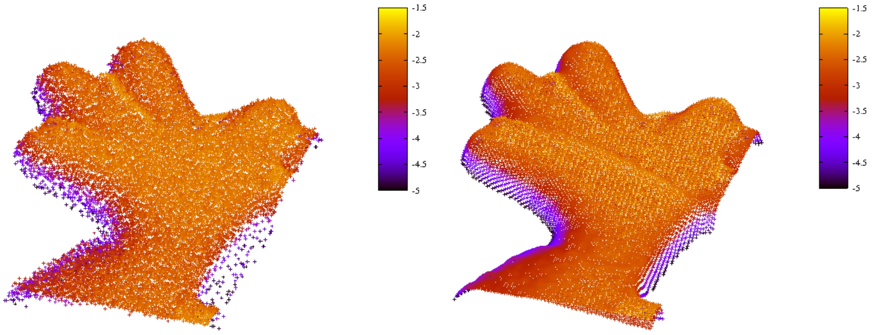

(e) Close-up view of (*) with $\alpha = 0$. (f) Close-up view of (*) with $\alpha = 0.3$.

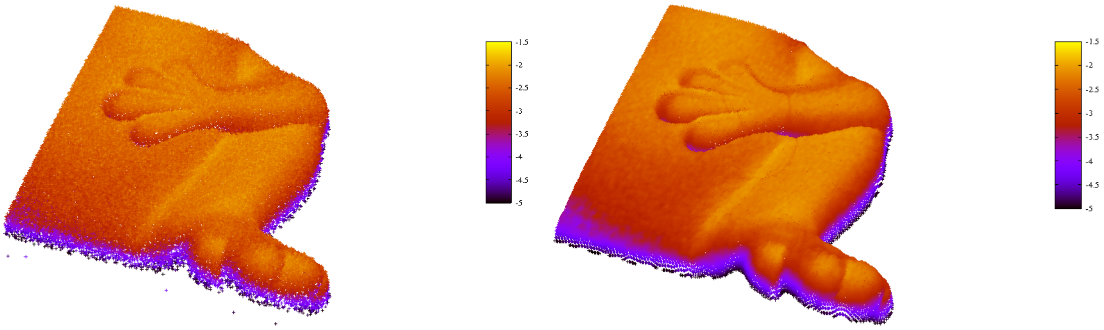

(g) Close-up view of (**) with $\alpha = 0$. (h) Close-up view of (**) with $\alpha = 0.3$.

Figure 5.9. Reconstruction under Gaussian noise. Employed parameters are: Time step size $\tau = 10^{-1}$, 5000 iterations. The runtime is 1830 seconds.

Chapter 6

Variational Perspective SfS with Cartesian Depth Parametrisation

In the previous chapter, we have constructed a first variational model for perspective shape from shading whose parametrisation is based on the radial depth by making use of the PDE-based model from Section 3.2. Although this approach offers the robustness of a variational method with respect to noise and missing information, the model introduced in Chapter 5 has two main shortcomings: On the one hand, the data term of the model is not formulated in a way that the reprojection error can be evaluated from a photometric viewpoint. On the other hand, the employed surface parametrisation makes the interpretation of the employed regularisation difficult from a geometric viewpoint. Aside from the modelling side, the optimisation process still depends on the information on the critical points for initialisation.

In this chapter, we establish a variational model for perspective shape from shading as well as design a corresponding optimisation strategy in consideration of the aforementioned issues: (i) First, we build a direct variational model by deriving a brightness equation for the data term in terms of the Cartesian depth and by utilising a subquadratic edge-preserving regulariser for the smoothness term. The change of the surface parametrisation from the radial depth to the Cartesian one gains considerable advantages in that it allows to regularise the Cartesian depth in the smoothness term directly. At the same time, since deviations for the brightness equation are penalised directly, the interpretation of the model becomes more intuitive and meaningful from a photometric and geometrical standpoint when compared with the case of the radial depth parametrisation. Moreover, the Cartesian depth parametrisation can also be beneficial for combining with other reconstruction methods, e.g. multi-view stereopsis [271, 273], because such models usually formulate the depth in axis-aligned coordinates. (ii) Apart from the model, we also develop a hierarchical graduated minimisation method by embedding an alternating explicit scheme into a coarse-to-fine framework to find a suitable minimiser of the originally non-convex energy. The proposed algorithm demonstrates not only the robustness with respect to various initialisation strategies but it also dramatically accelerates the convergence speed without considerably sacrificing the reconstruction quality when compared with the traditional explicit scheme.

This chapter is based on work that has been published as a book chapter [132]. Its outline is as follows: Based on the derivation of a PDE-based SfS model by means of the Cartesian depth parametrisation in Section 6.1, we formulate a corresponding variational model by embedding the PDE-based model into the data term and complementing an edge-preserving regulariser for the smoothness term in Section 6.2. Afterwards, we provide details on the coarse-to-fine minimisation framework including the approximation strategy as well as the alternating explicit scheme in Section 6.3. Finally, an extensive evaluation of our approach in various scenarios is carried out in Section 6.4.

6.1 PDE-based Model with Cartesian Depth Parametrisation

In this section, we derive a novel PDE-based SfS model for perspective SfS which is parametrised with respect to the *Cartesian* depth. To this end, we make standard assumptions on the SfS model as in [195]: A point light source is placed at the optical centre of a camera under perspective projection and the surface reflectance is Lambertian with uniform albedo. In the following section, this model is then embedded into a variational framework.

6.1.1 Cartesian Depth Parametrisation of the Surface

To derive the desired Cartesian depth parametrisation of the surface, we establish a relationship between the Cartesian depth and the radial one that we have used in Section 3.2.1. Since the negative Cartesian depth z is equivalent to the third element of the radial depth parametrisation in (3.25). It can be described by

$$z\,(\boldsymbol{x}) \overset{(3.25)}{=} \frac{\mathrm{f}}{\sqrt{|\boldsymbol{x}|^2 + \mathrm{f}^2}}\, u(\boldsymbol{x})\, \mathrm{f} \overset{(3.24)}{=} Q(\boldsymbol{x})\, u(\boldsymbol{x})\, \mathrm{f}\,, \tag{6.1}$$

where the spatially varying factor Q is defined as in (3.24).

Hence, the radial depth factor u can be described in terms of z. This in turn allows us to turn the radial depth parametrisation of the surface $\mathcal{S}$ in (3.25) into the Cartesian one as follows

$$\mathcal{S}\,(\boldsymbol{x}, z(\boldsymbol{x})) \overset{(3.25)}{=} Q(\boldsymbol{x})\, u\,(\boldsymbol{x}) \begin{bmatrix} x \\ y \\ -\mathrm{f} \end{bmatrix} \overset{(6.1)}{=} Q(\boldsymbol{x}) \left(\frac{z(\boldsymbol{x})}{\mathrm{f}\, Q(\boldsymbol{x})} \right) \begin{bmatrix} x \\ y \\ -\mathrm{f} \end{bmatrix} = \begin{bmatrix} \dfrac{z(\boldsymbol{x})\, x}{\mathrm{f}} \\ \dfrac{z(\boldsymbol{x})\, y}{\mathrm{f}} \\ -z\,(\boldsymbol{x}) \end{bmatrix}. \tag{6.2}$$

In the surface parametrisation (6.2), the unknown is now directly expressed as $z(\boldsymbol{x})$, which measures the actual Euclidean distance along Z-axis between the surface point $\mathcal{S}$ and its projected counterpart $\mathcal{S}'$ onto the $X-Y$ plane, see Figure 6.1.

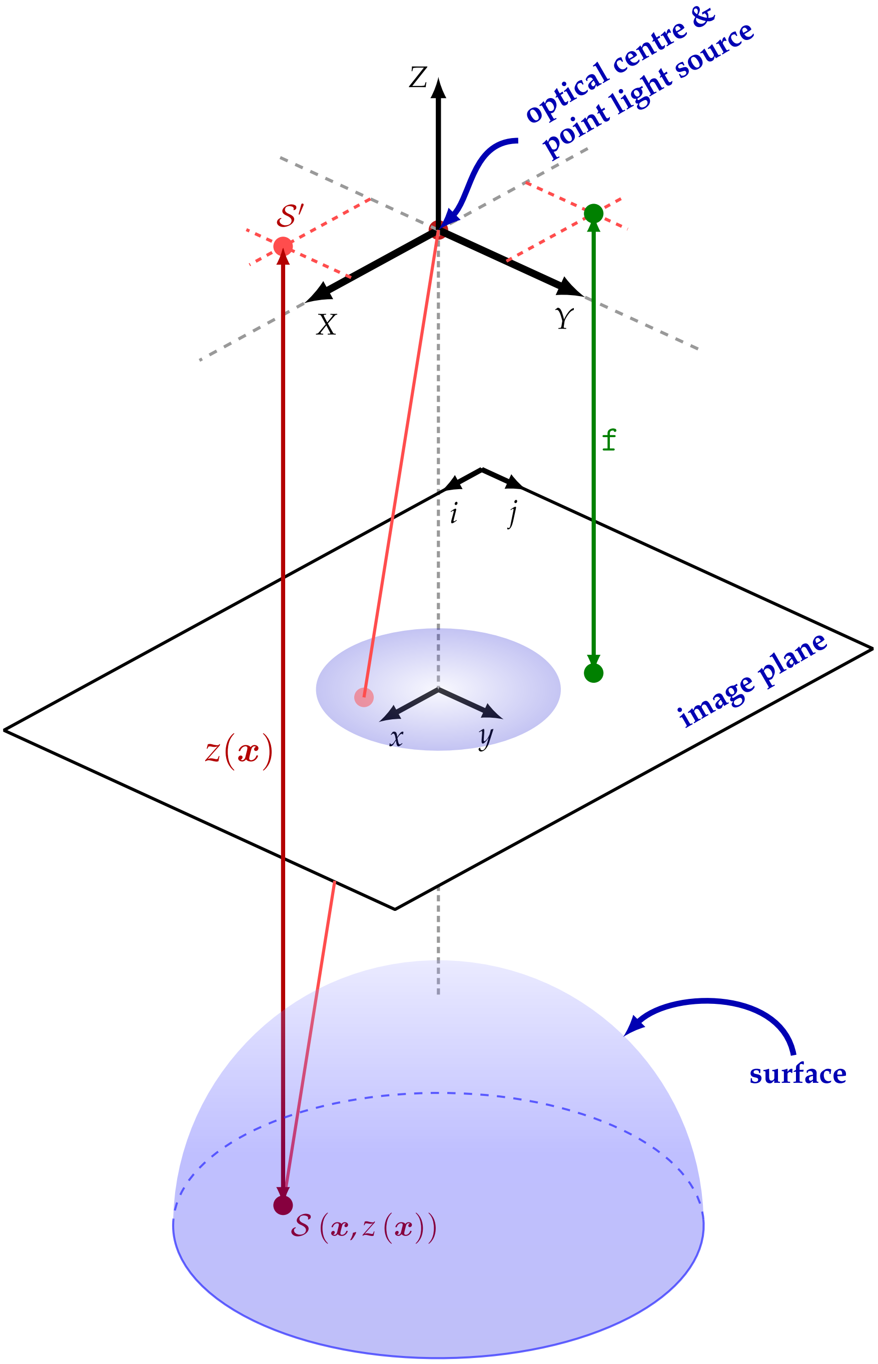

Figure 6.1. Perspective view of the Cartesian depth parametrisation.

This is contrary to the standard SfS case [195], where the unknown is expressed in terms of the radial depth r given in (3.31) or multiples thereof as we have seen in Section 3.2.1. The connection between the Cartesian depth z and the radial one r in (3.31) is depicted in Figure 6.2.

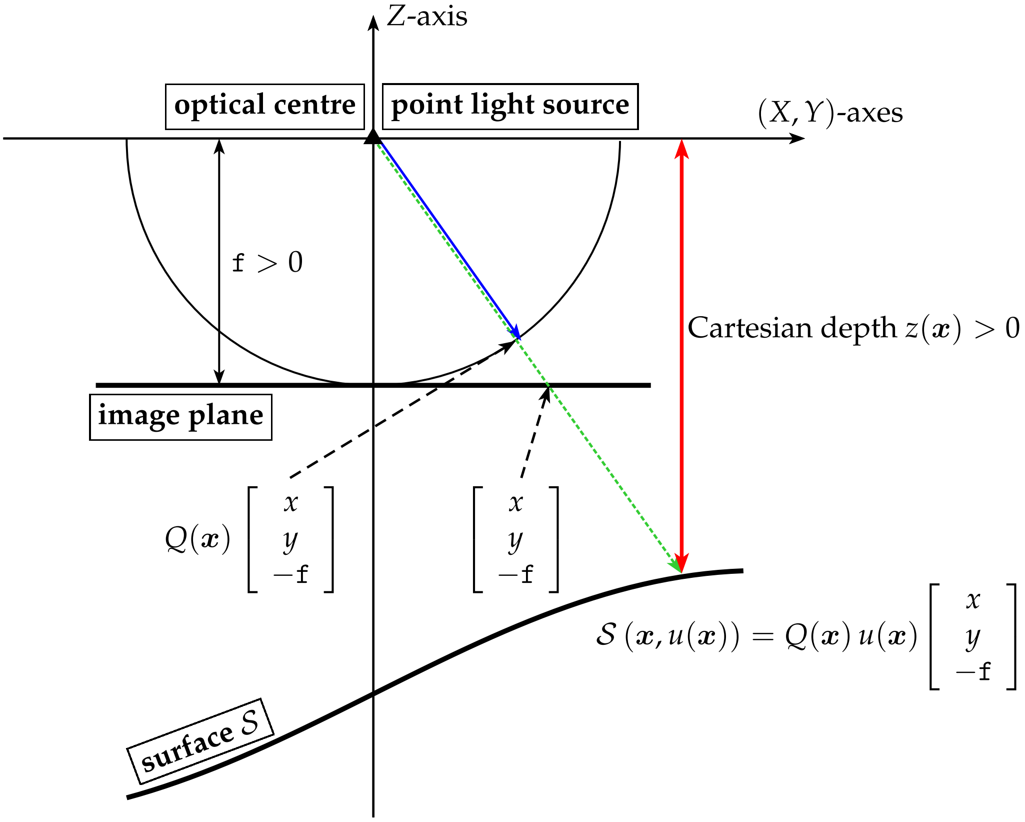

Figure 6.2. Relation between the radial depth factor $u(\boldsymbol{x})$ (quotient between green and blue distance) that denotes the depth in multiples of the focal length $\mathtt{f}$ and the Cartesian depth $z(\boldsymbol{x})$ (red distance).

6.1.2 Brightness Equation with Cartesian Depth Parametrisation

Once we have derived the parametrisation of the surface, we can reformulate each component of the brightness equation with the light attenuation term (3.22) in terms of the Cartesian depth.

Surface Normal

To derive the brightness equation in terms of the Cartesian depth, we first compute the surface normal vector with the parametrisation (6.2). As shown in Section 3.2.2, this can be achieved by taking the cross product between the two partial derivatives of the parametric surface (6.2) in x- and y-direction based on the vector calculus. Since the corresponding derivatives are given by

$$\mathcal{S}_x(\boldsymbol{x}, z, \nabla z) = \begin{bmatrix} \dfrac{z_x\, x + z}{\mathrm{f}} \\ \dfrac{z_x\, y}{\mathrm{f}} \\ -z_x \end{bmatrix}, \quad \mathcal{S}_y(\boldsymbol{x}, z, \nabla z) = \begin{bmatrix} \dfrac{z_y\, x}{\mathrm{f}} \\ \dfrac{z_y\, y + z}{\mathrm{f}} \\ -z_y \end{bmatrix}, \tag{6.3}$$

the surface normal can be obtained as

$$\mathbf{n}\,(\boldsymbol{x}, z, \nabla z) = \mathcal{S}_x(\boldsymbol{x}, z, \nabla z) \times \mathcal{S}_y(\boldsymbol{x}, z, \nabla z) = \begin{bmatrix} \dfrac{z_x\, z}{\mathrm{f}} \\ \dfrac{z_y\, z}{\mathrm{f}} \\ \dfrac{z\ [(\nabla z \cdot \boldsymbol{x}) + z]}{\mathrm{f}^2} \end{bmatrix}. \tag{6.4}$$

It can be noted that the surface normal in (6.4) has been attained in terms of the 2-D image coordinate x and y, see Figure 6.1. Alternatively, one can also compute the normal vector by relating the surface (6.2) with the 3-D coordinates $(X, Y, Z(X, Y))$ as shown in Figure 6.1. This leads to the form

$$\mathcal{S}\,(X(\boldsymbol{x}, z), Y(\boldsymbol{x}, z), Z(X(\boldsymbol{x}, z), Y(\boldsymbol{x}, z))) = \begin{bmatrix} X(\boldsymbol{x}, z) \\ Y(\boldsymbol{x}, z) \\ Z(X(\boldsymbol{x}, z), Y(\boldsymbol{x}, z)) \end{bmatrix} := \begin{bmatrix} \dfrac{z\, x}{\mathrm{f}} \\ \dfrac{z\, y}{\mathrm{f}} \\ -z \end{bmatrix}. \tag{6.5}$$

Then, by means of the chain rule

$$\frac{\partial X}{\partial Y} = \frac{\partial X}{\partial x}\frac{\partial x}{\partial Y}, \qquad \frac{\partial Y}{\partial X} = \frac{\partial Y}{\partial y}\frac{\partial y}{\partial X} \tag{6.6}$$

the tangent vectors to the surface can be attained as

$$\mathcal{S}_X(\boldsymbol{x}, z, \nabla z) = \begin{bmatrix} 1 \\ \dfrac{z_x y}{z + z_x\, x} \\ -\dfrac{z_x\, \mathrm{f}}{z + z_x\, x} \end{bmatrix}, \quad \mathcal{S}_Y(\boldsymbol{x}, z, \nabla z) = \begin{bmatrix} \dfrac{z_y\, x}{z + z_y\, y} \\ 1 \\ -\dfrac{z_y\, \mathrm{f}}{z + z_y\, y} \end{bmatrix}. \tag{6.7}$$

Taking the cross product between these two tangent vectors yields the normal vector $\widehat{\mathbf{n}}$ with the following relation

$$\widehat{\mathbf{n}}(\boldsymbol{x}, z, \nabla z) = \mathcal{S}_X(\boldsymbol{x}, z, \nabla z) \times \mathcal{S}_Y(\boldsymbol{x}, z, \nabla z) = \frac{\mathrm{f}^2}{(z + z_x\, x)(z + z_y\, y)}\, \mathbf{n}(\boldsymbol{x}, z, \nabla z)\,. \tag{6.8}$$

Since X- and Y-direction are parallel to x- and y-direction on the image plane, respectively, the result given in (6.8) corresponds to what we have anticipated: the direction of the new derived normal $\widehat{\mathbf{n}}$ is not different from that of $\mathbf{n}$ and the only difference has been made up to scale, see Figure 6.1. Moreover, this actually makes their normalised vectors $\frac{\mathbf{n}}{|\mathbf{n}|}$ and $\frac{\widehat{\mathbf{n}}}{|\widehat{\mathbf{n}}|}$ equivalent. However, one should note that the cross derivatives in (6.6) still do not vanish for the perspective projection, as discussed for the case of 2-D image coordinate x and y in Section 5.2.1. Therefore, the strategy adopted by [270, 278] is *not* on the right track for proper derivation, which is merely substituting the entries of the surface normal from the orthographic model such as [120] for the perspective case instead of recomputing the surface normal.

Light Direction

Concerning the normalised light direction $\mathbf{L}$ in (3.22), the formulation in (3.29) can still be applied because the light position still remains at the origin, which is also the optical centre at the same time, and the surface parametrisation does not influence its direction.

PDE-based Model with Cartesian Depth Parametrisation

At this point, we have all components at hand for deriving the new PDE-based model. By inserting the surface normal (6.4) and the light direction (3.29) in the brightness equation (3.22) with uniform albedo $\rho = 1$, we can acquire the perspective SfS model in terms of the Cartesian depth parametrisation [132]

$$I - \frac{Q^3}{z\sqrt{\mathrm{f}^2\ |\nabla z|^2 + [(\nabla z \cdot \boldsymbol{x}) + z]^2}} = 0\,. \tag{6.9}$$

Since the model (6.9) can still be classified as a general-type HJE, the PDE (6.9) shares the essential properties with the model (3.36). In other words, the listed five properties of (3.36) in Section 3.2.2 are also be valid for (6.9) with the Cartesian depth z instead of the radial one. Please note that the proposed model resembles the PDE-based approach in [279] that also makes use of the Cartesian depth. However, in contrast to the approach in [279], the proposed approach incorporates the light attenuation term based on the inverse square law.

6.2 Variational Model with Cartesian Depth Parametrisation

So far we have acquired a PDE-based model for perspective SfS with Cartesian depth parametrisation. Let us now construct a variational model by embedding the PDE-based model into a variational approach.

6.2.1 Variational Model

To establish a corresponding variational model, we make use of the PDE (6.9) for the quadratic data term and the same subquadratic regulariser as in (5.33) for the smoothness term. Then, the energy functional to be minimised for computing the Cartesian depth z has the form of

$$E\,(z) = \int_{\Omega_x} c(\boldsymbol{x}) \; \underbrace{\{E_D\,(\boldsymbol{x}, z, \nabla z)\}^2}_{\text{data term}} + \; \alpha \; \underbrace{E_S(D^2\,z)}_{\text{smoothness term}} \; d\boldsymbol{x}\ , \tag{6.10}$$

where E_D and E_S denote the data term and the smoothness term, respectively.

The role of the quadratic data term E_D in (6.10) is to make sure that the computed Cartesian depth z satisfies the photometric constraints, i.e. the brightness equation, in the squared sense. Hence, it is given by

$$E_D\,(\boldsymbol{x}, z, \nabla z) = I\,(\boldsymbol{x}) - \frac{Q(\boldsymbol{x})^3}{z\,W\,(\boldsymbol{x}, z, \nabla z)} \tag{6.11}$$

with

$$W\,(\boldsymbol{x}, z, \nabla z) = \sqrt{\mathfrak{f}^2\;|\nabla z|^2 + [(\nabla z \cdot \boldsymbol{x}) + z]^2}\ . \tag{6.12}$$

Moreover, the smoothness term E_S has the form

$$E_S\,(D^2\,z) = \Psi\left(\|D^2\,z\|_F^2\right) \overset{(5.29)}{=} \Psi\left(z_{xx}^2 + 2\,z_{xy}^2 + z_{yy}^2\right) =: \Psi\left(s^2\right)\ . \tag{6.13}$$

Aside from the change of parametrisation from the radial depth to the Cartesian one, the basic principles for the smoothness term and the confidence function remain unchanged as in the previous chapter.

6.2.2 Model Properties

In this section, we discuss the distinctive features of the variational model (6.10) which is directly parametrised in terms of the Cartesian depth. The first feature (i) comes from the fact that we use the brightness equation directly. Moreover, the listed features in (ii)–(iv) are attributed to the parametrisation using the Cartesian depth instead of the radial one and the properties from (v) to (viii) are basically inherited from the use of the variational framework in [131] that we have seen in Section 5.2.2.

(i) The variational model (6.10) takes already the perspective camera projection into account as in the case of (5.25), because the data term in (6.10) is based on the HJE (6.9). However, unlike (5.26) the data term (6.11) is expressed with respect to the photometric reprojection error measured by deviations between the grey values of the input image and the computed intensity with the estimated Cartesian depth based on the reflection and the camera model. Therefore, the penalisation addresses directly brightness inconsistencies, which makes the deviations interpretable from a *photometric* viewpoint.

(ii) The change of parametrisation from the radial depth to the Cartesian one has influence not only on the data term but also on the regularisation of the smoothness term. In particular, an object of constant depth describes a plane instead of a sphere as in the model based on the radial depth. Hence, the model allows a *geometrically* more meaningful interpretation of the smoothness induced by the regulariser.

(iii) The Cartesian parametrisation can have real benefits when it comes to a *combination* with different cue modules, e.g. stereo [216], or scene flow [24, 25]. Based on the fact that the same parametrisation has usually been applied to such approaches, the variational model (6.10) can share the Cartesian depth as a common unknown with such models and thereby easily form a joint framework to exploit the full strength of SfS, e.g. shading based depth refinement [271, 272, 273].

(iv) Apart from the benefits of integrating other depth cues, the new parametrisation can also offer a considerable advantage when *multi-view* scenarios are considered, e.g. [25, 271, 273]. Evidently, the model (6.10) can easily be extended to such situations because view conversions among different cameras are simpler to deal with than the case with the radial depth which is derived from the projected parametrisation on the half-sphere [162, 195].

(v) The *confidence function* in the data term of (6.10) gives the feasibility to set aside unreliable regions where the smoothness term steps in and takes the essential role in the reconstruction process by propagating information from the vicinity, which is particularly useful when it comes to texture, noise, or missing data. This is an exclusive feature that only variational methods can provide, since PDE-based approaches are solely based on the given data, e.g. [7, 8, 49, 195, 237], and hence do not offer any means to handle such situations effectively.

One can note from (6.10) that contrary to our previous model in (5.30) a fixed quantity of regularisation is assured during the reconstruction even if a pixel does not belong to the corrupt area. This is based on the observation that in the presence of noise the regularisation has an overall positive influence on the quality of the reconstruction as we show in Section 6.4.

(vi) As indicated previously, the employed subquadratic regulariser does have the capability of *preserving edges* in spite of the smoothing effect caused by regularisers, whereas most existing approaches for variational SfS do not offer this feature, e.g. [1, 89, 119, 125, 257, 270, 278].

(vii) Since the depth z has been selected as the parametrisation for the energy functional (6.10), finding a minimiser of the energy makes the *direct estimation* possible. Please note that most variational methods except [257] follow two-step strategies as in [45, 89, 125]: (i) As a first step, the surface normals should be obtained since the variational models have chosen them as unknowns, which typically introduce auxiliary variables. (ii) Once the normals are computed, as a second step they should be integrated to determine the depth map by means of, for instance, [5, 80, 92].

(viii) The aforementioned two-step reconstruction procedure via surface normal integration requires an *integrability constraint*, because the normals may not be integrable. Since the energy (6.10) is minimised with respect to z by exploiting $z_{xy} = z_{yx}$ as in the smoothness term (5.33), the acquired solution by our model satisfies the constraint per construction. If the integrability condition is not integrated as in our model, other necessary means must be devised to enforce integrability of solutions, either through an extra integrability term [1] or through a dedicated energy functional [89].

The listed notable features and the differences between the model (6.10) and other perspective variational approaches are compared in Table 6.1. It also shows how models have advanced recently. It can be noted that our variational model (6.10) overcomes existing limitations in the literature from a modelling viewpoint.

6.3 Minimisation

In this section, we proceed with the minimisation strategy for the energy functional (6.10). To this end, we derive the associated Euler-Lagrange equation as well as the corresponding boundary conditions. Subsequently, we approximate the spatial derivatives for the data term using the upwind type method and formulate the associated EL equation based on the approximate energy. Finally, we discuss its discretisation.

Table 6.1. Comparison of variational models for perspective Shape from Shading.

	Zhang *et al.* [278]	Wu *et al.* [270]	Abdelrahim *et al.* [1]	this work [131]	this work [132]
assumptions					
camera projection	perspective	perspective	perspective	perspective	perspective
surface type	Lambertian	Lambertian	Lambertian	Lambertian	Lambertian
light source position	distant	close to optical centre	distant	optical centre	optical centre
features					
selection of unknowns	Cartesian depth	Cartesian depth	Cartesian depth	radial depth	Cartesian depth
parametrisation	Cartesian depth	Cartesian depth	Cartesian depth	radial depth	Cartesian depth
reprojection error as data term	✓	✓	✓	–	✓
regularisation	Cartesian depth	Cartesian depth	Cartesian surface normal	radial depth	Cartesian depth
light attenuation factor	–	✓	✓ [3]	✓	✓
correct surface normal	–	–	✓ [4]	✓	✓
no auxiliary variables	–	–	✓	✓	✓
no integrability term	–	– [2]	–	✓	✓
direct estimation [1]	–	–	✓	✓	✓
edge preservation	–	–	–	✓	✓

[1] depth is computed without using extra variables for surface normals
[2] integrability constraint realised through repeated integration of surface normals
[3] factor not explicitly formulated in terms of the Cartesian depth
[4] based on the derivation in [2]

6.3.1 Euler-Lagrange Equations

Following the calculus of variations [58], a minimiser of the energy functional in (6.10) has to fulfil the corresponding Euler-Lagrange equation along with the boundary conditions, cf. Section 5.1.1. Exploiting the structural similarities between the radial depth based model in Section 5.3, and the Cartesian model (6.10), we obtain the following EL equation in Ω

$$\begin{aligned} 0 \;=\; & \left[c\,E_D^2 + \alpha\,E_S\right]_z - \frac{\partial}{\partial x}\left[c\,E_D^2 + \alpha\,E_S\right]_{z_x} - \frac{\partial}{\partial y}\left[c\,E_D^2 + \alpha\,E_S\right]_{z_y} \\ & + \frac{\partial^2}{\partial x^2}\left[c\,E_D^2 + \alpha\,E_S\right]_{z_{xx}} + 2\,\frac{\partial^2}{\partial x \partial y}\left[c\,E_D^2 + \alpha\,E_S\right]_{z_{xy}} + \frac{\partial^2}{\partial y^2}\left[c\,E_D^2 + \alpha\,E_S\right]_{z_{yy}} \end{aligned} \tag{6.14}$$

with the boundary conditions on $\partial\Omega$ given by

$$0 = \boldsymbol{n}^\top \begin{bmatrix} \left[c\,E_D^2 + \alpha\,E_S\right]_{z_x} - \dfrac{\partial}{\partial x}\left[c\,E_D^2 + \alpha\,E_S\right]_{z_{xx}} - \dfrac{\partial}{\partial y}\left[c\,E_D^2 + \alpha\,E_S\right]_{z_{xy}} \\ \left[c\,E_D^2 + \alpha\,E_S\right]_{z_y} - \dfrac{\partial}{\partial x}\left[c\,E_D^2 + \alpha\,E_S\right]_{z_{xy}} - \dfrac{\partial}{\partial y}\left[c\,E_D^2 + \alpha\,E_S\right]_{z_{yy}} \end{bmatrix}, \tag{6.15}$$

as well as

$$\boldsymbol{n}^\top \begin{bmatrix} \left[c\,E_D^2 + \alpha\,E_S\right]_{z_{xx}} \\ \left[c\,E_D^2 + \alpha\,E_S\right]_{z_{xy}} \end{bmatrix} = 0\,, \quad \boldsymbol{n}^\top \begin{bmatrix} \left[c\,E_D^2 + \alpha\,E_S\right]_{z_{xy}} \\ \left[c\,E_D^2 + \alpha\,E_S\right]_{z_{yy}} \end{bmatrix} = 0\,. \tag{6.16}$$

Simplifications

Euler-Lagrange Equation. As carried out in Section 5.3.1, we further simplify the EL equation (6.14) by rearranging the terms with respect to the data term and the smoothness term in consideration of the zero contributions. Hence, from (6.14) we obtain

$$\begin{aligned} 0 &= \left[c\,E_D^2\right]_z - \frac{\partial}{\partial x}\left[c\,E_D^2\right]_{z_x} - \frac{\partial}{\partial y}\left[c\,E_D^2\right]_{z_y} + \overbrace{\frac{\partial^2}{\partial x^2}\left[c\,E_D^2\right]_{z_{xx}}}^{\equiv 0} + \overbrace{2\,\frac{\partial^2}{\partial x \partial y}\left[c\,E_D^2\right]_{z_{xy}}}^{\equiv 0} \\ &\quad + \underbrace{\frac{\partial^2}{\partial y^2}\left[c\,E_D^2\right]_{z_{yy}}}_{\equiv 0} + \underbrace{\left[\alpha\,E_S\right]_z}_{\equiv 0} - \underbrace{\frac{\partial}{\partial x}\left[\alpha\,E_S\right]_{z_x}}_{\equiv 0} - \underbrace{\frac{\partial}{\partial y}\left[\alpha\,E_S\right]_{z_y}}_{\equiv 0} \\ &\quad + \frac{\partial^2}{\partial x^2}\left[\alpha\,E_S\right]_{z_{xx}} + 2\,\frac{\partial^2}{\partial x \partial y}\left[\alpha\,E_S\right]_{z_{xy}} + \frac{\partial^2}{\partial y^2}\left[\alpha\,E_S\right]_{z_{yy}} \\ &= \left(\left[c\,E_D^2\right]_z - \frac{\partial}{\partial x}\left[c\,E_D^2\right]_{z_x} - \frac{\partial}{\partial y}\left[c\,E_D^2\right]_{z_y}\right) \\ &\quad + \frac{\partial^2}{\partial x^2}\left[\alpha\,E_S\right]_{z_{xx}} + 2\,\frac{\partial^2}{\partial x \partial y}\left[\alpha\,E_S\right]_{z_{xy}} + \frac{\partial^2}{\partial y^2}\left[\alpha\,E_S\right]_{z_{yy}}\,, \end{aligned} \tag{6.17}$$

where we exploited that

$$\frac{\partial^2}{\partial x\,\partial y}\left[c\,E_D^2 + \alpha\,E_S\right]_{z_{xy}} = \frac{\partial^2}{\partial y\,\partial x}\left[c\,E_D^2 + \alpha\,E_S\right]_{z_{xy}}\,. \tag{6.18}$$

Since the information on the confidence function c is assumed to be accessible at the preprocessing stage, it may be directly integrated into the EL equation (6.17) as indicated in Section 5.3.2. The first three terms in (6.17) including $\frac{\partial}{\partial x}\left[E_D^2\right]_{z_x}$ and $\frac{\partial}{\partial y}\left[E_D^2\right]_{z_y}$ comprise the contributions for the data term. This is because the data term (6.11) encoding the brightness constraint depends not only on the Cartesian depth z but also on its gradient ∇z, cf. (5.34). Please note that the latter two terms do not appear when auxiliary variables, i.e. $p := z_x$ and $q := z_y$, are used for surface normals as in [270, 278].

Let us now give details on the contributions of the data term. They can be computed as

$$\begin{aligned}\left[E_D^2\right]_z &= 2\,E_D\;[E_D]_z \overset{(6.11)}{=} 2\left(I-\frac{Q^3}{z\,W}\right)\left(\frac{Q^3}{z^2\,W}+\frac{Q^3}{z\,W^2}\,[W]_z\right)\\ &= 2\left(I-\frac{Q^3}{z\,W}\right)\frac{Q^3}{z\,W}\left(\frac{1}{z}+\frac{\nabla z\cdot \boldsymbol{x}+z}{W^2}\right),\end{aligned} \tag{6.19}$$

$$\begin{aligned}\frac{\partial}{\partial x}\left[E_D^2\right]_{z_x} &= \left[2\,E_D\;[E_D]_{z_x}\right]_x \overset{(6.11)}{=} \left[2\left(I-\frac{Q^3}{z\,W}\right)\frac{Q^3}{z\,W^2}\;[W]_{z_x}\right]_x\\ &= 2\left[\left(I-\frac{Q^3}{z\,W}\right)\frac{Q^3}{z\,W^3}\left(\mathrm{f}^2\,z_x+[\nabla z\cdot\boldsymbol{x}+z]\;x\right)\right]_x,\end{aligned} \tag{6.20}$$

and

$$\begin{aligned}\frac{\partial}{\partial y}\left[E_D^2\right]_{z_y} &= \left[2\,E_D\;[E_D]_{z_y}\right]_y \overset{(6.11)}{=} \left[2\left(I-\frac{Q^3}{z\,W}\right)\frac{Q^3}{z\,W^2}\;[W]_{z_y}\right]_y\\ &= 2\left[\left(I-\frac{Q^3}{z\,W}\right)\frac{Q^3}{z\,W^3}\left(\mathrm{f}^2\,z_y+[\nabla z\cdot\boldsymbol{x}+z]\;y\right)\right]_y.\end{aligned} \tag{6.21}$$

Concerning the contribution from the smoothness term, due to the same structure, one can utilise (5.51), (5.52), and (5.53) by substituting the Cartesian depth z for the radial one v. This yields

$$\frac{\partial^2}{\partial x^2}\,[E_S]_{z_{xx}} = 2\,\frac{\partial^2}{\partial x^2}\left[\Psi'\left(s^2\right)\;z_{xx}\right], \tag{6.22}$$

$$2\frac{\partial^2}{\partial x\,\partial y}\,[E_S]_{z_{xy}} = 4\,\frac{\partial^2}{\partial x\,\partial y}\left[\Psi'\left(s^2\right)\;z_{xy}\right], \tag{6.23}$$

$$\frac{\partial^2}{\partial y^2}\,[E_S]_{z_{yy}} = 2\,\frac{\partial^2}{\partial y^2}\left[\Psi'\left(s^2\right)\;z_{yy}\right], \tag{6.24}$$

where the Charbonnier diffusivity $\Psi'(s^2) = 1/\sqrt{1+s^2/\lambda^2}$ is defined as in (5.54) with $s = \left\|D^2 z\right\|_F$. Hence, the final EL equation (6.17) is obtained by plugging (6.22), (6.23), and (6.24) into (6.17), which reads

$$\begin{aligned}0 = &\left(\left[c\,E_D^2\right]_z - \frac{\partial}{\partial x}\left[c\,E_D^2\right]_{z_x} - \frac{\partial}{\partial y}\left[c\,E_D^2\right]_{z_y}\right)\\ &+ 2\,\alpha\left(\frac{\partial^2}{\partial x^2}\left[\Psi'\left(s^2\right)\,z_{xx}\right] + 2\,\frac{\partial^2}{\partial x \partial y}\left[\Psi'\left(s^2\right)\,z_{xy}\right] + \frac{\partial^2}{\partial y^2}\left[\Psi'\left(s^2\right)\,z_{yy}\right]\right)\,.\end{aligned} \tag{6.25}$$

Boundary Conditions. Regarding the boundary conditions given in (6.15) and (6.16), we may proceed as conducted in Section 5.3.2. As a result, the compact form of (6.15) is given by

$$0 = \boldsymbol{n}^\top \begin{bmatrix} \left[c\,E_D^2\right]_{z_x} - \alpha\,\frac{\partial}{\partial x}\left[\Psi'\left(s^2\right)\,z_{xx}\right] - \alpha\,\frac{\partial}{\partial y}\left[\Psi'\left(s^2\right)\,z_{xy}\right] \\ \left[c\,E_D^2\right]_{z_y} - \alpha\,\frac{\partial}{\partial x}\left[\Psi'\left(s^2\right)\,z_{xy}\right] - \alpha\,\frac{\partial}{\partial y}\left[\Psi'\left(s^2\right)\,z_{yy}\right] \end{bmatrix} \tag{6.26}$$

with an outer normal vector $\boldsymbol{n} = (n_1, n_2)^\top$.

Since the condition (6.16) is only influenced by the smoothness term and shares the positive common factor $\Psi'(s^2)$, it can be simplified to

$$\boldsymbol{n}^\top \begin{bmatrix} z_{xx} \\ z_{xy} \end{bmatrix} = 0\,, \quad \boldsymbol{n}^\top \begin{bmatrix} z_{xy} \\ z_{yy} \end{bmatrix} = 0\,. \tag{6.27}$$

6.3.2 Approximation of Spatial Derivative for Data Term

To find a minimiser of the energy functional (6.10), we follow the "first approximate then optimise" scheme [33, 111, 261]. Since we have already applied this strategy to the smoothness term for the radial depth case, we focus on the data term. For approximating the spatial derivatives z_x and z_y in the data term (6.11), we employ the upwind type scheme based on (2.89) in view of the underlying hyperbolic nature but with similar formulations as in [247]. This reads

$$\widetilde{z}_x = \max\left(\mathcal{D}^{-x}\,z, -\mathcal{D}^{+x}\,z, 0\right)\,, \tag{6.28}$$

where the backward and forward difference approximations are given by

$$\mathcal{D}^{-x}\,z = \frac{z\left(x,y\right) - z\left(x-h_1,y\right)}{h_1}\,, \tag{6.29}$$

and

$$\mathcal{D}^{+x}\,z = \frac{z\left(x+h_1,y\right) - z\left(x,y\right)}{h_1} \tag{6.30}$$

with grid sizes h_1 and h_2 in x- and y direction, respectively. By comparing (6.29) and (6.30) with (2.91) and (2.92), it can be noted that the representations of neighbouring positions of $z(x,y)$ corresponding to $z_{i,j}$ in backward and forward difference schemes are replaced with $z(x-h_1,y)$ and $z(x+h_1,y)$. The same procedure can be applied to the y-direction in a straightforward way. This leads to

$$\widetilde{z}_y = \max\left(\mathcal{D}^{-y} z, -\mathcal{D}^{+y} z, 0\right) , \tag{6.31}$$

where the backward and forward difference approximations are given by

$$\mathcal{D}^{-y} z = \frac{z(x,y) - z(x,y-h_2)}{h_2} , \tag{6.32}$$

and

$$\mathcal{D}^{+y} z = \frac{z(x,y+h_2) - z(x,y)}{h_2} . \tag{6.33}$$

This corresponds to the y-direction counterparts of (2.90), cf. (2.93) and (2.94). Moreover, as in (2.98) and (2.99) the actual sign of the forward difference must be restored when the second argument is selected in (6.28) and (6.31) [44, 132]:

$$z_x \approx \begin{cases} -\widetilde{z}_x & \text{if } \widetilde{z}_x = -\mathcal{D}^{+x} z , \\ \widetilde{z}_x & \text{otherwise} , \end{cases} \qquad z_y \approx \begin{cases} -\widetilde{z}_y & \text{if } \widetilde{z}_y = -\mathcal{D}^{+y} z , \\ \widetilde{z}_y & \text{otherwise} . \end{cases} \tag{6.34}$$

By plugging the approximations of the spatial derivatives, i.e. (6.28) and (6.31), into the data term (6.11), we obtain the following formulation for the approximate data term

$$E_D\left(\boldsymbol{x}, z(\boldsymbol{x}), \nabla z(\boldsymbol{x})\right) \approx E_D\left(\boldsymbol{x}, \{z(\boldsymbol{x}+\boldsymbol{h})\}\right) \tag{6.35}$$

where

$$\boldsymbol{h} := \{-\boldsymbol{h}_2, -\boldsymbol{h}_1, \boldsymbol{0}, \boldsymbol{h}_1, \boldsymbol{h}_2\} \tag{6.36}$$

with

$$\boldsymbol{0} = (0,0)^\top \ , \ \boldsymbol{h}_1 = (h_1, 0)^\top \ , \ \boldsymbol{h}_2 = (0, h_2)^\top \ . \tag{6.37}$$

In contrast to the original data term (6.11), the approximate version (6.35) depends only upon z instead of the gradient ∇z by incorporating values of neighbouring positions due to the gradient approximations in (6.28) and (6.31).

6.3.3 Euler-Lagrange Equation with Approximate Energy

Based on the approximation of the data term (6.35), we derive Euler-Lagrange equation. To this end, we consider contributions from the data term and the smoothness term, respectively. Moreover, this investigation forms a basis not only for the discretisation in the next section but also for our linearisation approach in Chapter 7.

Data Term

Since the approximation of the data term (6.35) contains five arguments with z, its EL equation corresponds to

$$\begin{aligned} \mathrm{EL}_D \; = \; & \left[c\left(\boldsymbol{x}\right)\, E_D^2\left(\boldsymbol{x}, \left\{z\left(\boldsymbol{x}\right)\right\}\right)\right]_{z(\boldsymbol{x})} \\ & + \left[c\left(\boldsymbol{x}+\boldsymbol{h}_1\right)\, E_D^2\left(\boldsymbol{x}+\boldsymbol{h}_1, \left\{z\left(\boldsymbol{x}+\boldsymbol{h}_1\right)\right\}\right)\right]_{z(\boldsymbol{x})} \\ & + \left[c\left(\boldsymbol{x}-\boldsymbol{h}_1\right)\, E_D^2\left(\boldsymbol{x}-\boldsymbol{h}_1, \left\{z\left(\boldsymbol{x}-\boldsymbol{h}_1\right)\right\}\right)\right]_{z(\boldsymbol{x})} \\ & + \left[c\left(\boldsymbol{x}+\boldsymbol{h}_2\right)\, E_D^2\left(\boldsymbol{x}+\boldsymbol{h}_2, \left\{z\left(\boldsymbol{x}+\boldsymbol{h}_2\right)\right\}\right)\right]_{z(\boldsymbol{x})} \\ & + \left[c\left(\boldsymbol{x}-\boldsymbol{h}_2\right)\, E_D^2\left(\boldsymbol{x}-\boldsymbol{h}_2, \left\{z\left(\boldsymbol{x}-\boldsymbol{h}_2\right)\right\}\right)\right]_{z(\boldsymbol{x})} \, . \end{aligned} \tag{6.38}$$

Concerning the structure of this EL equation, it can be noted that the contributions from the gradient related terms $\frac{\partial}{\partial x}\left[\cdot\right]$ and $\frac{\partial}{\partial y}\left[\cdot\right]$ in (6.14) are substituted by those of the corresponding four terms, i.e. $\left[\cdot\left(\boldsymbol{x}+\boldsymbol{h}_1\right)\right]_{z(\boldsymbol{x})}$, $\left[\cdot\left(\boldsymbol{x}-\boldsymbol{h}_1\right)\right]_{z(\boldsymbol{x})}$, $\left[\cdot\left(\boldsymbol{x}+\boldsymbol{h}_2\right)\right]_{z(\boldsymbol{x})}$, $\left[\cdot\left(\boldsymbol{x}-\boldsymbol{h}_2\right)\right]_{z(\boldsymbol{x})}$. This is because the first order derivatives are not present in the approximated version of the data term (6.35). Instead, it may contain the four adjacent positions due to the upwind approximation for the hyperbolic nature. In what follows, we look into contributions of each term to the derivative with respect to $z(\boldsymbol{x})$ depending on the selected difference.

First Term. For the first term of the EL equation (6.38), we have

$$\left[c\left(\boldsymbol{x}\right)\, E_D^2\left(\boldsymbol{x}\right)\right]_{z(\boldsymbol{x})} = c\left(\boldsymbol{x}\right)\, \left[E_D^2\left(\boldsymbol{x}\right)\right]_{z(\boldsymbol{x})} \overset{(6.35)}{=} 2\, c^{xy}\, E_D^{xy}\, \left[E_D^{xy}\right]_{z^{xy}} \, , \tag{6.39}$$

where the notations in (6.39) are defined by

$$c^{xy} = c\left(x, y\right) = c\left(\boldsymbol{x}\right) \, , \qquad z^{xy} = z\left(x, y\right) = z\left(\boldsymbol{x}\right) \, , \tag{6.40}$$

and

$$\begin{aligned} E_D^{xy} & = E_D\left(x, y, z\left(x, y\right), z\left(x-h_1, y\right), z\left(x+h_1, y\right), z\left(x, y-h_2\right), z\left(x, y+h_2\right)\right) \\ & \underset{(6.37)}{\overset{(6.36)}{=}} E_D\left(\boldsymbol{x}, \left\{z\left(\boldsymbol{x}+\boldsymbol{h}\right)\right\}\right) \, . \end{aligned} \tag{6.41}$$

For compact notations, we denote the superscript to be the central point of the approximation which is highlighted as light green in Figure 6.3. Besides, the corresponding adjacent positions of the central point in x- and y-direction are marked as light purple and light red, respectively. In this case, one should note that both selections of the forward and the backward difference in each x- and y-direction have influences on the derivatives with respect to $z(\boldsymbol{x})$.

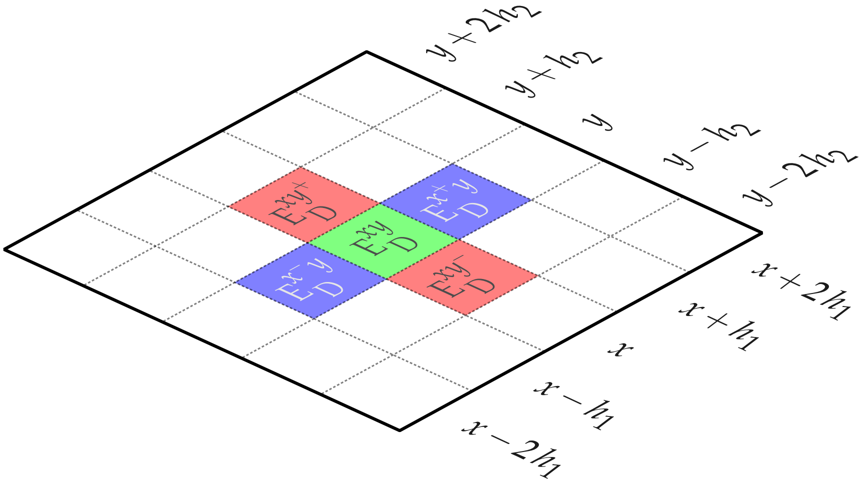

Figure 6.3. Points of interest for the approximation of E_D^{xy}. The central point of concern is denoted as light green and corresponding neighbouring points in x- and y-direction are coloured in light purple and light red, respectively. In this case, both selections of the forward and the backward difference in both x- and y-direction have influences on the derivative with respect to $z(\boldsymbol{x})$.

Second Term. Turning to the second term in (6.38), the central point for approximation becomes $(x+h_1, y)^\top$ which can be expressed as $E_D^{x^+y}$ by following the notations in (6.39), see Figure 6.4. This gives

$$\begin{aligned}\left[c\left(\boldsymbol{x}+\boldsymbol{h}_1\right) E_D^2\left(\boldsymbol{x}+\boldsymbol{h}_1\right)\right]_{z(\boldsymbol{x})} &= c\left(\boldsymbol{x}+\boldsymbol{h}_1\right)\left[E_D^2\left(\boldsymbol{x}+\boldsymbol{h}_1\right)\right]_{z(\boldsymbol{x})} \\ &= 2\, c^{x^+y}\, E_D^{x^+y}\left[E_D^{x^+y}\right]_{z^{xy}}\,, \end{aligned} \tag{6.42}$$

where the notations in (6.42) are defined by

$$c^{x^+y} = c\left(x+h_1, y\right) = c\left(\boldsymbol{x}+\boldsymbol{h}_1\right)\,, \qquad z^{x^+y} = z\left(x+h_1, y\right) = z\left(\boldsymbol{x}+\boldsymbol{h}_1\right)\,, \tag{6.43}$$

and

$$\begin{aligned} E_D^{x^+y} &= E_D\left(x+h_1, y, z\left(x+h_1, y\right), z\left(x, y\right), z\left(x+2h_1, y\right),\right. \\ &\qquad\qquad \left. z\left(x+h_1, y-h_2\right), z\left(x+h_1, y+h_2\right)\right) \\ &\underset{(6.37)}{\overset{(6.36)}{=}} E_D\left(\boldsymbol{x}+\boldsymbol{h}_1, \left\{z\left(\boldsymbol{x}+\boldsymbol{h}_1+\boldsymbol{h}\right)\right\}\right)\,. \end{aligned} \tag{6.44}$$

As can be observed in Figure 6.4, $z(\boldsymbol{x})$ appears if the backward difference in x-direction is selected. This makes the backward difference in x-direction influence on the derivative with respect to $z(\boldsymbol{x})$.

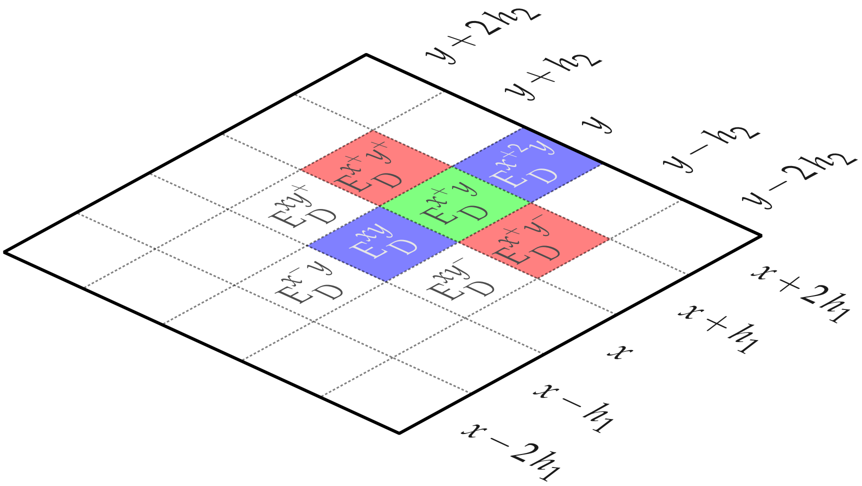

Figure 6.4. Points of interest for the approximation of $E_D^{x^+y}$. The same colour scheme is applied as in Figure 6.3: Light green for the central point of interest, light purple and light red for corresponding neighbouring points in x- and y-direction, respectively. In this case, only the selection of the backward difference in x-direction has influence on the derivative with respect to $z(\boldsymbol{x})$.

Third Term. In an analogous way, we proceed to the third term where the central point for the approximation corresponds to $E_D^{x^-y}$, see Figure 6.5. This yields

$$\begin{aligned}\left[c\left(\boldsymbol{x}-\boldsymbol{h}_1\right) E_D^2\left(\boldsymbol{x}-\boldsymbol{h}_1\right)\right]_{z(\boldsymbol{x})} &= c\left(\boldsymbol{x}-\boldsymbol{h}_1\right)\left[E_D^2\left(\boldsymbol{x}-\boldsymbol{h}_1\right)\right]_{z(\boldsymbol{x})} \\ &= 2\, c^{x^-y}\, E_D^{x^-y}\left[E_D^{x^-y}\right]_{z^{xy}} , \end{aligned} \tag{6.45}$$

where the notations in (6.45) are defined by

$$c^{x^-y} = c\left(x-h_1, y\right) = c\left(\boldsymbol{x}-\boldsymbol{h}_1\right) , \qquad z^{x^-y} = z\left(x-h_1, y\right) = z\left(\boldsymbol{x}-\boldsymbol{h}_1\right) , \tag{6.46}$$

and

$$\begin{aligned} E_D^{x^-y} &= E_D\left(x-h_1, y, z\left(x-h_1, y\right), z\left(x-2\,h_1, y\right), z\left(x, y\right),\right. \\ &\qquad\qquad \left. z\left(x-h_1, y-h_2\right), z\left(x-h_1, y+h_2\right)\right) \\ &\underset{(6.37)}{\overset{(6.36)}{=}} E_D\left(\boldsymbol{x}-\boldsymbol{h}_1, \left\{z\left(\boldsymbol{x}-\boldsymbol{h}_1+\boldsymbol{h}\right)\right\}\right) . \end{aligned} \tag{6.47}$$

In this case, $z(\boldsymbol{x})$ appears if the forward difference in x-direction is selected as can be observed in Figure 6.4. Hence, the backward difference in x-direction has influence on the derivative with respect to $z(\boldsymbol{x})$. So far we have taken care of x-direction. The extension to y-direction is straightforward.

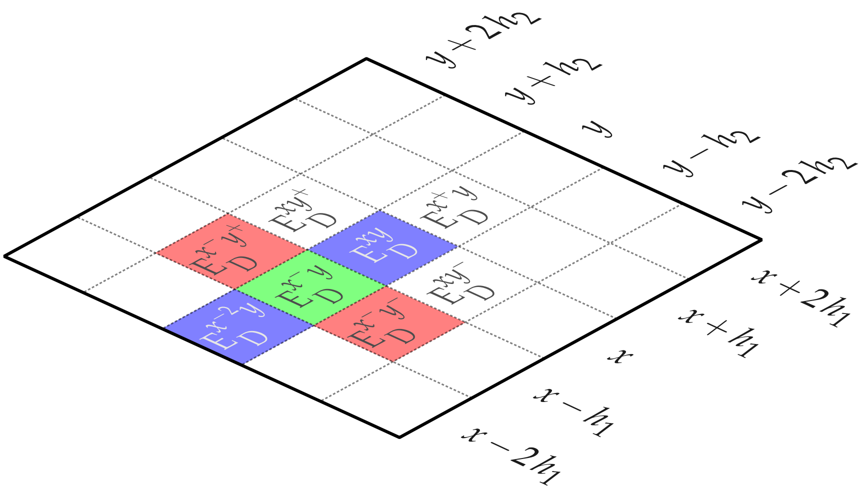

Figure 6.5. Points of interest for the approximation of $E_D^{x^-y}$. The same colour scheme is applied as in Figure 6.3: Light green for the central point of interest, light purple and light red for corresponding neighbouring points in x- and y-direction, respectively. In this case, only the selection of the forward difference in x-direction has influence on the derivative with respect to $z(\boldsymbol{x})$.

Fourth Term. For the fourth term in (6.38), the central point for approximation is $E_D^{xy^+}$ as shown in Figure 6.6. This leads to

$$\begin{aligned} \left[c\left(\boldsymbol{x}+\boldsymbol{h}_2\right) E_D^2\left(\boldsymbol{x}+\boldsymbol{h}_2\right)\right]_{z(\boldsymbol{x})} &= c\left(\boldsymbol{x}+\boldsymbol{h}_2\right)\left[E_D^2\left(\boldsymbol{x}+\boldsymbol{h}_2\right)\right]_{z(\boldsymbol{x})} \\ &= 2\, c^{xy^+} E_D^{xy^+} \left[E_D^{xy^+}\right]_{z^{xy}} , \end{aligned} \tag{6.48}$$

where the notations in (6.48) are given by

$$c^{xy^+} = c\left(x, y+h_2\right) = c\left(\boldsymbol{x}+\boldsymbol{h}_2\right), \qquad z^{xy^+} = z\left(x, y+h_2\right) = z\left(\boldsymbol{x}+\boldsymbol{h}_2\right), \tag{6.49}$$

and

$$\begin{aligned} E_D^{xy^+} &= E_D\left(x, y+h_2, z\left(x, y+h_2\right), z\left(x-h_1, y+h_2\right), z\left(x+h_1, y+h_2\right),\right. \\ &\qquad \left. z\left(x, y\right), z\left(x, y+2\,h_2\right)\right) \\ &\underset{(6.37)}{\overset{(6.36)}{=}} E_D\left(\boldsymbol{x}+\boldsymbol{h}_2, \left\{z\left(\boldsymbol{x}+\boldsymbol{h}_2+\boldsymbol{h}\right)\right\}\right) . \end{aligned} \tag{6.50}$$

One can note that this case actually corresponds to the counterpart in y-direction for the second term. Hence, the selection of the backward difference in y-direction affects the differentiation with respect to $z(\boldsymbol{x})$, see Figure 6.6.

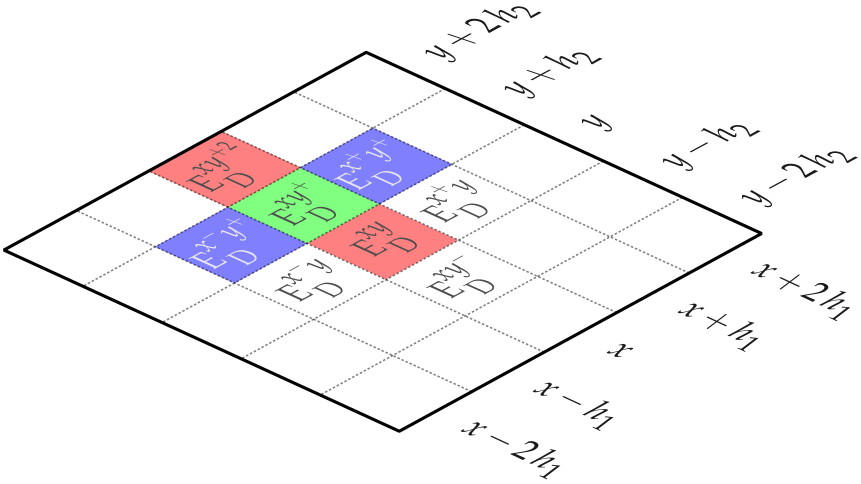

Figure 6.6. Points of interest for the approximation of $E_D^{xy^+}$. The same colour scheme is applied as in Figure 6.3: Light green for the central point of interest, light purple and light red for corresponding neighbouring points in x- and y-direction, respectively. In this case, only the selection of the backward difference in y-direction has influence on the derivative with respect to $z(\boldsymbol{x})$.

Fifth Term. In a similar way, one can obtain the following formulation for $E_D^{xy^-}$

$$\begin{aligned} \left[c\left(\boldsymbol{x}-\boldsymbol{h}_2\right) E_D^2\left(\boldsymbol{x}-\boldsymbol{h}_2\right)\right]_{z(\boldsymbol{x})} &= c\left(\boldsymbol{x}-\boldsymbol{h}_2\right) \left[E_D^2\left(\boldsymbol{x}-\boldsymbol{h}_2\right)\right]_{z(\boldsymbol{x})} \\ &= 2\, c^{xy^-} E_D^{xy^-} \left[E_D^{xy^-}\right]_{z^{xy}} , \end{aligned} \tag{6.51}$$

where the notations in (6.51) are defined by

$$c^{xy^-} = c\left(x, y-h_2\right) = c\left(\boldsymbol{x}-\boldsymbol{h}_2\right) , \qquad z^{xy^-} = z\left(x, y-h_2\right) = z\left(\boldsymbol{x}-\boldsymbol{h}_2\right) , \tag{6.52}$$

and

$$\begin{aligned} E_D^{xy^-} &= E_D\left(x, y-h_2, z\left(x, y-h_2\right), z\left(x-h_1, y-h_2\right), z\left(x+h_1, y-h_2\right),\right. \\ &\qquad\qquad \left. z\left(x, y-2\,h_2\right), z\left(x, y\right)\right) \\ &\underset{(6.37)}{\overset{(6.36)}{=}} E_D\left(\boldsymbol{x}-\boldsymbol{h}_2, \left\{z\left(\boldsymbol{x}-\boldsymbol{h}_2-\boldsymbol{h}\right)\right\}\right) . \end{aligned} \tag{6.53}$$

Based on the case of the third term, the selection of the forward difference in y-direction makes contributions to the derivative with respect to $z(\boldsymbol{x})$, see Figure 6.7.

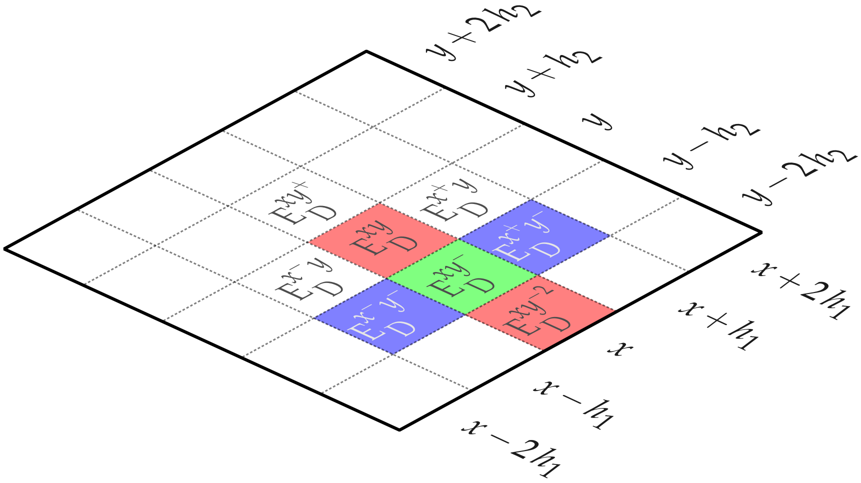

Figure 6.7. Points of interest for the approximation of $E_D^{xy^-}$. The same colour scheme is applied as in Figure 6.3: Light green for the central point of interest, light purple and light red for corresponding neighbouring points in x- and y-direction, respectively. In this case, only the selection of the forward difference in y-direction has influence on the derivative with respect to $z(\boldsymbol{x})$.

Smoothness Term. So far we have considered the contributions from the data term. Let us now focus on the ones from the smoothness term. Regarding the smoothness term, the structure in Section 5.3.3 stays basically unchanged since we follow "the first approximate then optimise" scheme based on the standard central difference type approximation. This leads to

$$\begin{aligned}\mathrm{EL}_S &= \left[\Psi\left((s^{xy})^2\right)\right]_{z^{xy}} = \Psi'\left((s^{xy})^2\right)\left[(s^{xy})^2\right]_{z^{xy}} \\ &= 2\,\Psi'_{h_1^2}\left((s^{xy})^2\right)\left(z_{xx}\right)^{xy} + 4\,\Psi'_{h_1 h_2}\left((s^{xy})^2\right)\left(z_{xy}\right)^{xy} + 2\,\Psi'_{h_2^2}\left((s^{xy})^2\right)\left(z_{yy}\right)^{xy}\end{aligned} \tag{6.54}$$

where

$$\Psi'_{h_1^2}\left((s^{xy})^2\right) = \frac{\Psi'\left((s^{xy})^2\right)}{h_1^2}\,, \tag{6.55}$$

$$\Psi'_{h_1 h_2}\left((s^{xy})^2\right) = \frac{\Psi'\left((s^{xy})^2\right)}{16\,h_1\,h_2}\,, \tag{6.56}$$

$$\Psi'_{h_2^2}\left((s^{xy})^2\right) = \frac{\Psi'\left((s^{xy})^2\right)}{h_2^2}\,, \tag{6.57}$$

and

$$(z_{xx})^{xy} = \frac{z^{x^+y} - 2\,z^{xy} + z^{x^-y}}{h_1^2}\,, \tag{6.58}$$

$$\left(z_{xy}\right)^{xy} = \frac{z^{x^+y^+} - z^{x^-y^+} - z^{x^+y^-} + z^{x^-y^-}}{4\,h_1\,h_2}\,, \tag{6.59}$$

$$\left(z_{yy}\right)^{xy} = \frac{z^{xy^+} - 2\,z^{xy} + z^{xy^-}}{h_2^2}\,. \tag{6.60}$$

As in the data term, the superscript denotes the central point for the approximation and the subscript stands for the derivatives. The Charbonnier diffusivity Ψ' is defined as in (5.64). Therefore, we have

$$\Psi'\left((s^{xy})^2\right) = \frac{1}{\sqrt{1 + \dfrac{(s^{xy})^2}{\lambda^2}}} \tag{6.61}$$

with the following curvature measure

$$(s^{xy})^2 \overset{(6.13)}{:=} \left((z_{xx})^{xy}\right)^2 + 2\,\left(\left(z_{xy}\right)^{xy}\right)^2 + \left(\left(z_{yy}\right)^{xy}\right)^2\,. \tag{6.62}$$

Moreover, one can note that the constant factors in (6.55) – (6.57) come from the term $[(s^{xy})^2]_{z^{xy}}$ in (6.54), cf. Section 5.3.3.

As a consequence, by putting all contributions together from the data term and the smoothness term and taking out the common factor 2 we finally obtain the following expression for the EL equation

$$\begin{aligned}
0 =\;& \mathrm{EL}_D + \mathrm{EL}_S \\
=\;& c^{xy}\,E_D^{xy}\,\left[E_D^{xy}\right]_{z^{xy}} + c^{x^+y}\,E_D^{x^+y}\left[E_D^{x^+y}\right]_{z^{xy}} + c^{x^-y}\,E_D^{x^-y}\left[E_D^{x^-y}\right]_{z^{xy}} \\
& \qquad + c^{xy^+}\,E_D^{xy^+}\left[E_D^{xy^+}\right]_{z^{xy}} + c^{xy^-}\,E_D^{xy^-}\left[E_D^{xy^-}\right]_{z^{xy}} \\
& + \;\alpha\left(\Psi'_{h_1^2}\left((s^{xy})^2\right)(z_{xx})^{xy} + 2\,\Psi'_{h_1h_2}\left((s^{xy})^2\right)\left(z_{xy}\right)^{xy} + \Psi'_{h_2^2}\left((s^{xy})^2\right)\left(z_{yy}\right)^{xy}\right).
\end{aligned} \tag{6.63}$$

6.3.4 Discretisation

Based on the approximation in the previous section, let us now discuss how to minimise the discrete energy. Since being a minimiser means that the first derivative of the discrete energy with respect to $z_{i,j}$ must vanish at each point $(i,j)^\top$, this condition is formulated as

$$0 \overset{!}{=} \frac{\partial E_{i,j}}{\partial z_{i,j}} \quad \forall i,j \in \Omega\,, \tag{6.64}$$

where $E_{i,j}$ denotes a discrete version of the energy given in (6.10).

To obtain the discrete energy, we discretise the data term by applying the upwind scheme from (2.89) and (2.90) in view of the underlying hyperbolic nature. For the smoothness term, a central difference approximation can be utilised. Then, taking derivatives of the acquired discrete energy with respect to $z_{i,j}$ for all i, j in the computational domain Ω leads to a proper discretisation for the optimality condition (6.64). In principle, this corresponds to the EL equation (6.63). Moreover, it can be noted that the computations for the smoothness term in Section 5.3.3 can be directly used here owing to the same structure by substituting the Cartesian depth z for the radial one v. As a consequence, what remains to be handled is only the contributions from the data term for which the discrete energy takes the form

$$\widehat{E}_D = \sum_{j=by}^{by+ny-1} \sum_{i=bx}^{bx+nx-1} \left(I_{i,j} - \frac{Q_{i,j}^3}{z_{i,j}\, W_{i,j}} \right)^2 =: \sum_{j=by}^{by+ny-1} \sum_{i=bx}^{bx+nx-1} \left\{ (E_D)_{i,j} \right\}^2 , \tag{6.65}$$

where $Q_{i,j}$ and $W_{i,j}$ describe the discrete version of (3.24) and (6.12), respectively. They are given by

$$Q_{i,j} = \frac{\mathfrak{f}}{\sqrt{|\boldsymbol{x}_{i,j}|^2 + \mathfrak{f}^2}} \tag{6.66}$$

and

$$W_{i,j} = \sqrt{\mathfrak{f}^2 \left| \boldsymbol{D}_{i,j}^{\boldsymbol{x}}\, z \right|^2 + \left[\left(\boldsymbol{D}_{i,j}^{\boldsymbol{x}}\, z \right) \cdot \boldsymbol{x}_{i,j} + z_{i,j} \right]^2} , \tag{6.67}$$

where

$$\boldsymbol{D}_{i,j}^{\boldsymbol{x}}\, z = \left(D_{i,j}^{x}\, z, D_{i,j}^{y}\, z \right)^\top \tag{6.68}$$

with

$$D_{i,j}^{x}\, z := \chi_{i,j}^{+x} \left(D_{i,j}^{+x}\, z \right) + \chi_{i,j}^{-x} \left(D_{i,j}^{-x}\, z \right) \tag{6.69}$$

and

$$D_{i,j}^{y}\, z := \chi_{i,j}^{+y} \left(D_{i,j}^{+y}\, z \right) + \chi_{i,j}^{-y} \left(D_{i,j}^{-y}\, z \right) . \tag{6.70}$$

The characteristic function $\chi_{i,j}^{+x}$ in (6.69) denotes that the forward difference is selected at a point $(i, j)^\top$ in x-direction. In an analogous way, $\chi_{i,j}^{-x}$ denotes the backward difference is selected at a point $(i, j)^\top$ in x-direction. This convention can be extended to y-direction in a straightforward way: $\chi_{i,j}^{+y}$ is for the selection of the forward difference and $\chi_{i,j}^{-y}$ is for the selection of the backward difference, respectively. One should note that this selection process is described by the *max* operator in the upwind scheme, cf. (2.89) and (2.90). Moreover, the case for no contributions in both directions corresponding to the gradient being zero is also covered by both characteristic functions being zero. The discussion of this case will be given in next Section.

Differentiation of the Discrete Energy for Data Term

When differentiating the discrete energy (6.65) with respect to $z_{i,j}$, due to the upwind properties there are five ways to make contributions:

1. If the discrete energy (6.65) is evaluated at (i, j), then both selections of the forward and the backward difference make contributions.

2. If the discrete energy (6.65) is evaluated at $(i+1, j)$, then the backward difference in x-direction makes contributions.

3. If the discrete energy (6.65) is evaluated at $(i-1, j)$, then the forward difference in x-direction makes contributions.

4. If the discrete energy (6.65) is evaluated at $(i, j+1)$, then the backward difference in y-direction makes contributions.

5. If the discrete energy (6.65) is evaluated at $(i, j-1)$, then the forward difference in y-direction makes contributions.

One can note that these cases, in fact, refer to the five terms in (6.38) that we have derived for the approximate energy in the previous section. Hence, the derivative of the discrete energy (6.65) with respect to $z_{i,j}$ at each point $(i, j)^\top \in \Omega$ can be described as

$$\begin{aligned}\left[\left\{(E_D)_{i,j}\right\}^2\right]_{z_{i,j}} &= 2\,(E_D)_{i,j}\left[-\frac{Q^3_{i,j}}{z_{i,j}\,W_{i,j}}\right]_{z_{i,j}} \\ &\quad + 2\,(E_D)_{i+1,j}\left[-\frac{Q^3_{i+1,j}}{z_{i+1,j}\,W^{-x}_{i+1,j}}\right]_{z_{i,j}} + 2\,(E_D)_{i-1,j}\left[-\frac{Q^3_{i-1,j}}{z_{i-1,j}\,W^{+x}_{i-1,j}}\right]_{z_{i,j}} \\ &\quad + 2\,(E_D)_{i,j+1}\left[-\frac{Q^3_{i+1,j}}{z_{i,j+1}\,W^{-y}_{i,j+1}}\right]_{z_{i,j}} + 2\,(E_D)_{i,j-1}\left[-\frac{Q^3_{i-1,l}}{z_{i,j-1}\,W^{+y}_{i,j-1}}\right]_{z_{i,j}}\,,\end{aligned} \tag{6.71}$$

where the subscript denotes an evaluation point, $\pm x$ and $\pm y$ in the superscript refer to the forward and the backward difference in x- and y-direction, respectively.

Let us now take a closer look at each term in (6.71) regarding on the selection in each direction and what implications they have.

First Term. Concerning the first term of (6.71), we investigate which cases are covered with respect to the selection in each direction. If the backward difference in x-direction is chosen, all three cases are possible in y-direction, i.e. forward, backward and no contributions. We formulate these cases as

$$W_{i,j}^{-x} = \left\{ W_{i,j}^{-x,+y}, W_{i,j}^{-x,-y}, W_{i,j}^{-x,y_0} \right\}, \tag{6.72}$$

where $W_{i,j}^{-x}$ denotes the selection of the backward difference in x-direction with no specification in y-direction and $W_{i,j}^{-x,\pm y}$ indicates the selection of the backward difference in x-direction combined with the forward and backward difference in y-direction, respectively. In addition, $W_{i,j}^{-x,y_0}$ represents the case of the selection of the backward difference in x-direction and no contribution in y-direction. Each of these cases is illustrated in Figure 6.8. One should note that no contributions in y-direction means that a wavefront arrives locally concurrently at points $(i-1, j-1)^\top$, $(i-1, j)^\top$, $(i-1, j+1)^\top$ and thereby the information propagates purely in x-direction, see Figure 6.8(b). Moreover, this result can be extended in a straightforward way when the forward difference in x-direction is chosen. This yields

$$W_{i,j}^{+x} = \left\{ W_{i,j}^{+x,+y}, W_{i,j}^{+x,-y}, W_{i,j}^{+x,y_0} \right\}. \tag{6.73}$$

If no contribution is made in x-direction, there are two ways to propagate the information purely in y-direction, i.e. by means of either forward or backward difference. This gives

$$W_{i,j}^{x_0} = \left\{ W_{i,j}^{x_0,+y}, W_{i,j}^{x_0,-y} \right\}. \tag{6.74}$$

Therefore, by putting all these together, $W_{i,j}$ in the first term of (6.71) can have one of the aforementioned choices. This is described by

$$\begin{aligned} W_{i,j} &= W_{i,j}^{-x} \cup W_{i,j}^{+x} \cup W_{i,j}^{x_0} \\ &= \left\{ W_{i,j}^{-x,+y}, W_{i,j}^{-x,-y}, W_{i,j}^{-x,y_0} \right\} \cup \left\{ W_{i,j}^{+x,+y}, W_{i,j}^{+x,-y}, W_{i,j}^{+x,y_0} \right\} \\ &\qquad \cup \left\{ W_{i,j}^{x_0,+y}, W_{i,j}^{x_0,-y} \right\}. \end{aligned} \tag{6.75}$$

Please note that the case of no contributions in both directions $W_{i,j}^{x_0,y_0}$ is not listed in (6.75). This is because the case of $W_{i,j}^{x_0,y_0}$ corresponds to critical points, i.e. when $\nabla z = 0$, and thereby the information at those points must be obtained from the model not from neighbouring points.

Second Term. Since the second term is evaluated at a point $(i+1, j)^\top$, only the backward difference in x-direction makes contributions when differentiating the

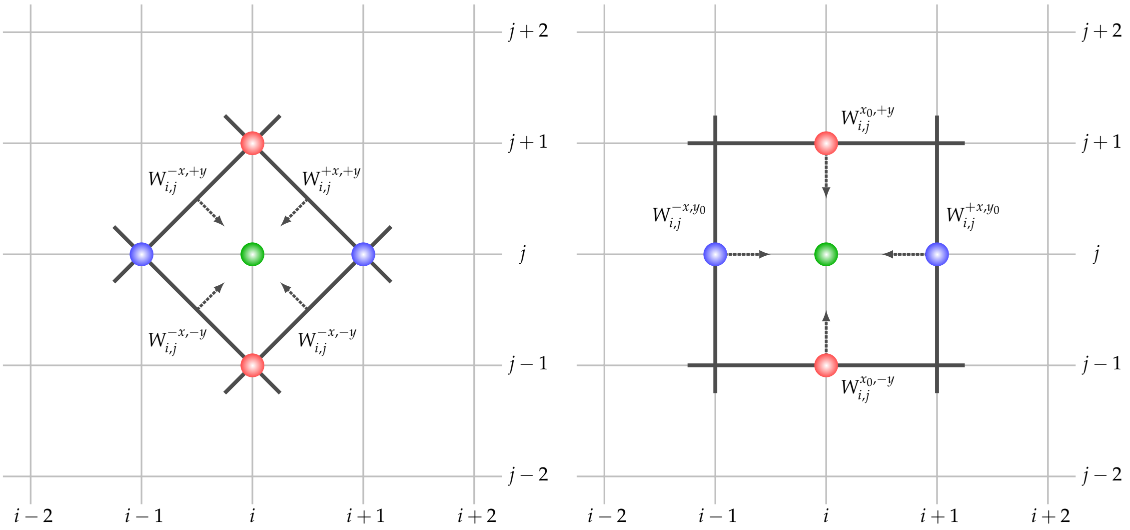

(a) Contributions from both x- and y-direction. (b) Contributions from one direction.

Figure 6.8. Illustration of information propagation depending on the selection of upwind directions at a grid point $(i, j)^\top$. The same colour scheme is used as in Figure 6.3: The central point of concern is denoted as light green and corresponding neighbouring points in x- and y-direction are coloured in light purple and light red, respectively. The arrow indicates the propagation direction of information (or wavefront) in each case.

discrete energy with respect to $z_{i,j}$. This gives

$$W_{i+1,j}^{-x} = \left\{ W_{i+1,j}^{-x,+y}, W_{i+1,j}^{-x,-y}, W_{i+1,j}^{-x,y_0} \right\} . \tag{6.76}$$

As in the first term, case distinctions are made in y-direction: forward, backward and no contributions, see Figure 6.9.

Third Term. In an analogous way to the second term, the backward difference has influence on the derivative with respect to $z_{i,j}$ when the discrete energy is evaluated at a point $(i-1, j)^\top$. This gives the following cases

$$W_{i-1,j}^{-x} = \left\{ W_{i-1,j}^{+x,+y}, W_{i-1,j}^{+x,-y}, W_{i-1,j}^{+x,y_0} \right\} . \tag{6.77}$$

As in the second term, each case of (6.77) is depicted in Figure 6.10.

Fourth Term. Based on that the fourth term corresponds to the second term in y-direction, only the backward difference in y-direction makes contributions to the derivative with respect to $z_{i,j}$ when the discrete energy is evaluated at $(i, j+1)^\top$, see

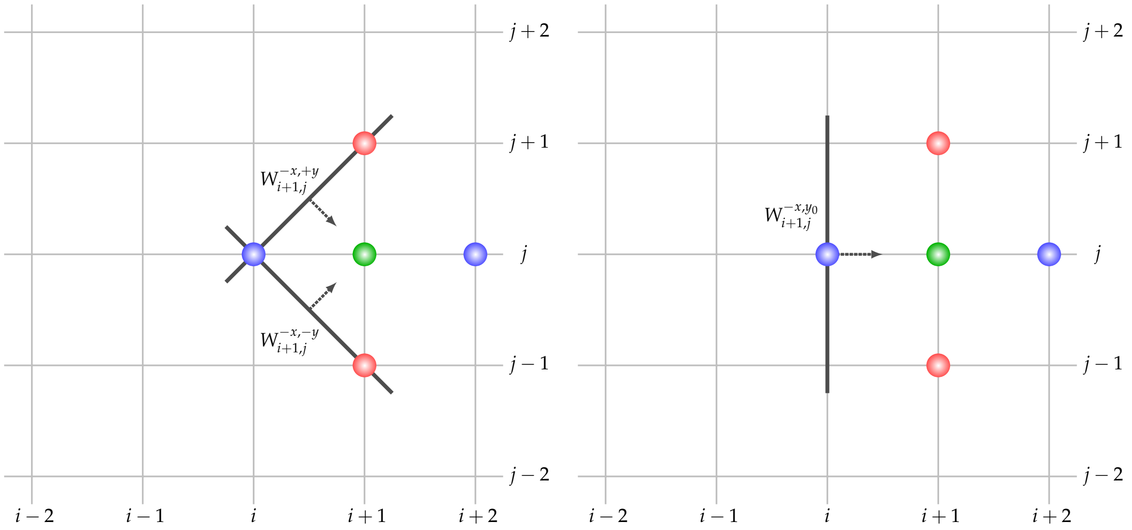

(a) Contributions from both x- and y-direction. (b) No contribution in y-direction.

Figure 6.9. Illustration of information propagation depending on the selection of upwind directions at a grid point $(i+1, j)^\top$. In this case, only the backward difference in x-direction makes contributions.

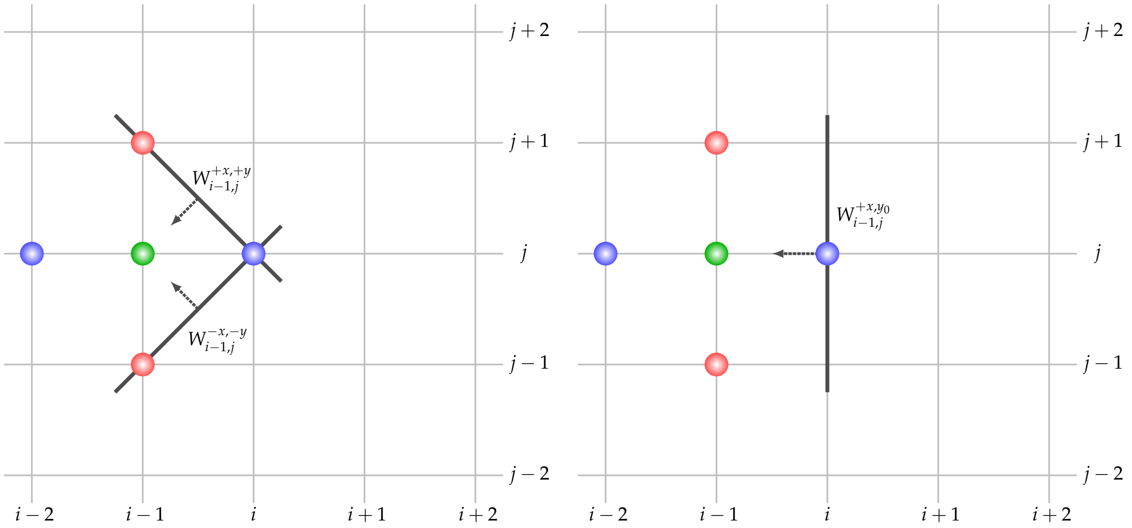

(a) Contributions from both x- and y-direction. (b) No contribution in y-direction.

Figure 6.10. Illustration of information propagation depending on the selection of upwind directions at a grid point $(i-1, j)^\top$. In this case, only the forward difference in x-direction makes contributions.

Figure 6.11. Therefore, we obtain

$$W^{-y}_{i,j+1} = \left\{ W^{-x,-y}_{i,j+1}, W^{+x,-y}_{i,j+1}, W^{x_0,-y}_{i,j+1} \right\} . \tag{6.78}$$

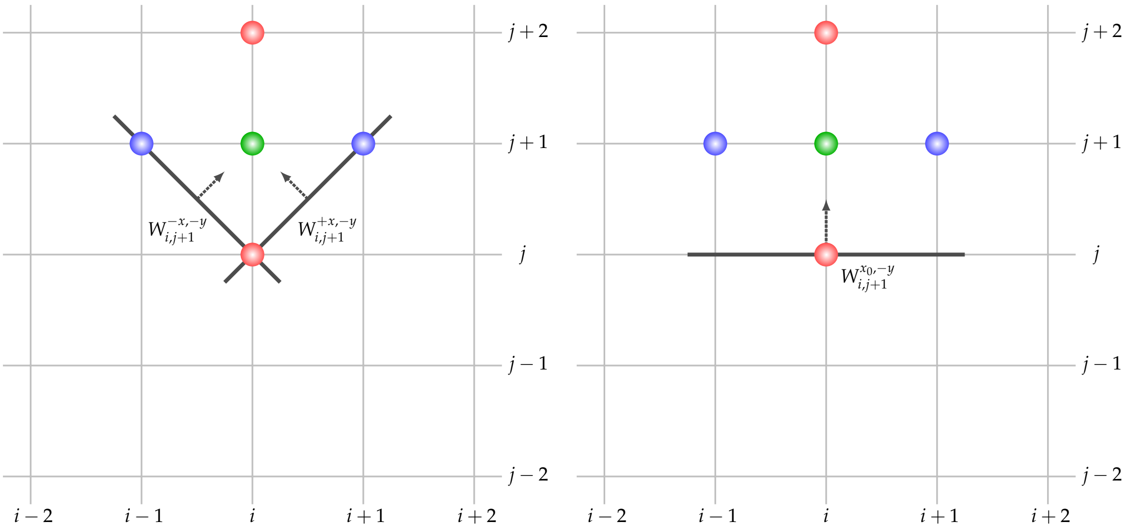

(a) Contributions from both x- and y-direction. (b) No contribution in x-direction.

Figure 6.11. Illustration of information propagation depending on the selection of upwind directions at a grid point $(i, j+1)^\top$. In this case, only the backward difference in y-direction makes contributions.

Fifth Term. Since this case is the counterpart of the third term in y-direction, only the forward difference in y-direction makes contributions to the differentiation of the discrete energy evaluated at $(i, j-1)^\top$ see Figure 6.12. This yields

$$W^{+y}_{i,j-1} = \left\{ W^{-x,+y}_{i,j-1}, W^{+x,+y}_{i,j-1}, W^{x_0,+y}_{i,j-1} \right\} . \tag{6.79}$$

Explicit Scheme

After the discretisation is performed, the solution of the EL equation (6.63) can be expressed as the steady state evolution equation in artificial time by means of the Euler forward time discretisation method

$$z_t \approx \frac{z^{n+1} - z^n}{\tau} \tag{6.80}$$

with τ being a time step size. Therefore, we can obtain the explicit scheme

$$\frac{z^{n+1} - z^n}{\tau} = -\left(\mathrm{EL}^n_D + \alpha\, \mathrm{EL}^n_S\right) \quad \Leftrightarrow \quad z^{n+1} = z^n - \tau\, \left(\mathrm{EL}^n_D + \alpha\, \mathrm{EL}^n_S\right) , \tag{6.81}$$

where EL^n_D and EL^n_S denote the discretisation of the data term and the smoothness term in the optimality condition (6.64) evaluated at time n, respectively.

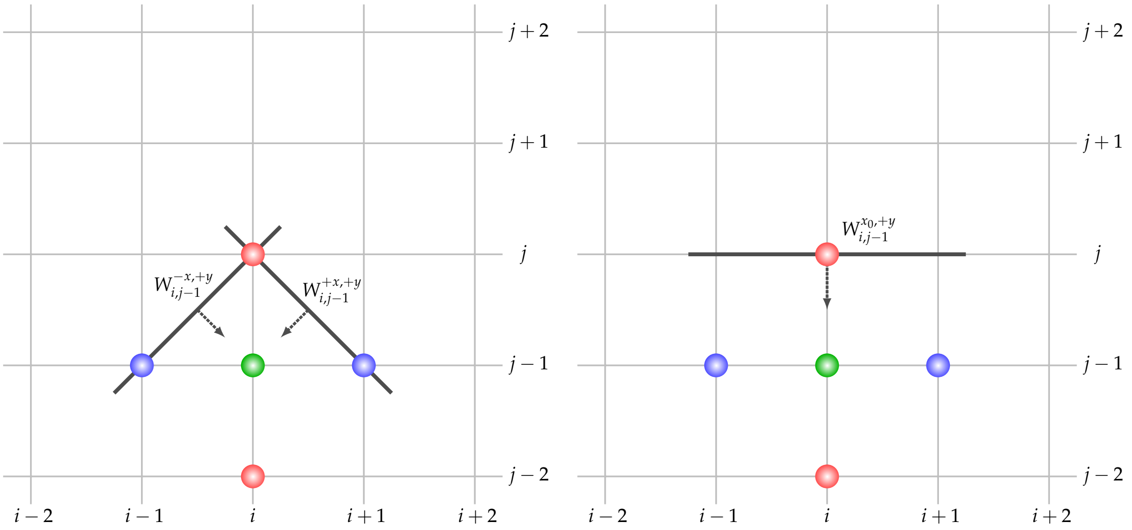

(a) Contributions from both x- and y-direction. (b) No contribution in x-direction.

Figure 6.12. Illustration of information propagation depending on the selection of upwind directions at a grid point $(i, j-1)^\top$. In this case, only the forward difference in y-direction makes contributions.

It can be noted that the discretisation in (6.81) adapts itself during the iterations depending on the selection of the direction guided by the employed upwind scheme as shown in (6.75). In this context, this can be understood as a *lagged* discretisation approach.

Coarse-to-fine Approach

The underlying structure of the energy functional (6.10) is more challenging to handle than that of the radial depth based model (5.32), since the unknown z and the term W in (6.12) which contains its gradient ∇z occur in the denominator of the data term (6.11), cf. (5.26) and (6.11). This makes the optimisation problem highly non-convex and thereby it may happen that the explicit scheme (6.81) gets trapped in one of multiple local minima, e.g. the point $\tilde{e}^{\,\ell-1}$ in Figure 6.13(a).

To deal with the difficult situation, we make use of a coarse-to-fine approach that is based on the *homotopy continuation* method [9, 10, 211]. The basic idea of this approach is as follows: By prescribing a parameter, we may reformulate the original optimisation problem into a family of multiscale representations, which allows to describe the original non-convex energy as different degrees of energy families depending on the resolution level. Since the simplified problem with the corresponding energy has a specific form in a way that it progressively deforms to the original one as the grid is refined, solutions from the previous coarser level serve as an initialisation for more difficult optimisation problems at the next finer

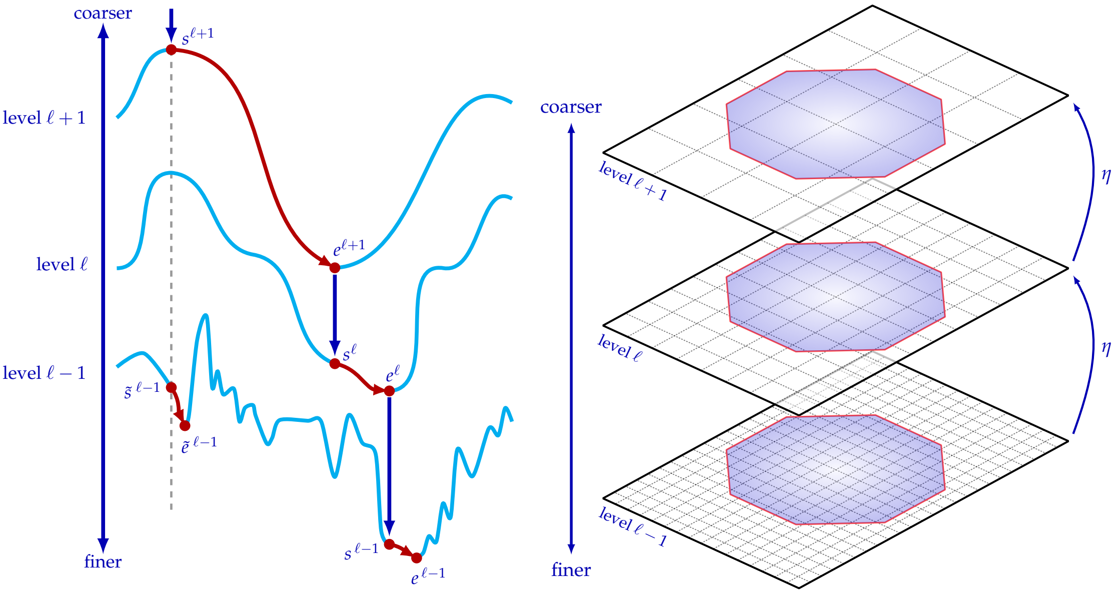

(a) Energy.

(b) Image pyramid.

Figure 6.13. Coarse-to-fine approach: Multi-resolution representations of the problem.

scales by tracking all the solutions along the way. On this account, solving the family of problems sequentially from the lowest resolution allows one to obtain a global solution (or at least the one that is very close to a desired endpoint solution), see Figure 6.13(a). This strategy is helpful to escape from poor local minima because the local high frequency details are usually smoothed out at coarser resolutions and thereby the optimisation process at that level is more manageable than at finer ones. Besides, this type of hierarchical graduated optimisation method lays down the fundamental principle of some global non-convex optimisation algorithms such as *graduated non-convexity* (GNC) [36] , which is actually the discrete counterpart of the continuation method, and *mean field annealing* (MFA) [34], which corresponds to a deterministic approximation of simulated annealing [140], and has been employed successfully in various domains of applications [164, 165, 166], e.g. blur kernel computation [166], optical flow estimation [47, 48, 72, 232, 274] as well as shape estimation [19, 20, 21, 43, 240, 241].

This type of coarse-to-fine scheme not only seeks to overcome the difficulties of non-convexity but it also offers another advantage regarding the initialisation for variational SfS. As indicated in [270], the quality of reconstruction for most variational SfS algorithms depends largely upon a good initialisation which has usually been selected to be very close to a true solution and may be derived from either PDE-based approaches [1, 278] or surface integration methods [270]. However, as we will demonstrate in Section 6.4 the coarse-to-fine optimisation framework that we have incorporated belongs to a global method [211] and thereby makes the reconstruction result hardly susceptible to the selection of the initial depth map as long as sufficiently many resolution layers are used. This evidently becomes another benefit of our approach, since our approach does not require any *a priori* information on initialisation for reconstruction in contrast to other variational methods. Nevertheless, to *only* accelerate the convergence of the algorithm we may initialise the depth as we have carried out in (3.72). This can be realised by plugging $\nabla z = 0$ into the data term (6.11) and solving the resulting equation with respect to z

$$E_D\,(\boldsymbol{x}, z, 0) = 0 \quad \Rightarrow \quad z = \sqrt{\frac{Q(\boldsymbol{x})^3}{I(\boldsymbol{x})}} \overset{(3.24)}{\leqslant} \frac{1}{\sqrt{I(\boldsymbol{x})}}\,. \tag{6.82}$$

Since the attained initial depth in (6.82) has not taken the surface orientation into consideration, it is only affected by the inverse square law in view of (3.22) and thereby serves as a local upper bound in the sense that the surface depth value grows from the initial value to the negative z-direction.

In order to apply the coarse-to-fine scheme, we define the subsampling factor η between two adjacent layers of resolution for generating image pyramids as illustrated in Figure 6.13(b). The downsampling factor η has been selected in the range $\eta \in (0.5, 1)$. As an immediate effect of the subsampling, it can be observed that the grid size in each direction increases as multiple downsampling operations are preformed. This is based on that the number of pixels has been reduced and yet the size of the original image plane remains unchanged during the process, see Figure 6.13(b). Therefore, the grid size h_1^ℓ and h_2^ℓ in each direction at level ℓ can be expressed as

$$h_1^\ell = h_1 \cdot \eta^{-\ell} \qquad \text{and} \qquad h_2^\ell = h_2 \cdot \eta^{-\ell} \tag{6.83}$$

with the original gird size h_1 and h_2 in x- and y-direction, respectively. The case $\ell = 0$ and $\ell = \ell_{\max}$ in (6.83) correspond to the original and the lowest resolution layer, respectively.

The growth of the grid size by the subsampling process makes also a considerable impact on the regularisation and the key observation is that the fourth-order derivatives given in (6.22), (6.23), and (6.24), make the amount of the contribution by the smoothness term behave asymptotically according to $1/h^4$. By means of the Landau symbol, this may be formulated as

$$\alpha\ [E_S\,(h)]_{(\ell=0)} = \alpha\, \mathcal{O}(h^{-4})\,, \tag{6.84}$$

where $[E_S\,(h)]_{(\ell=0)}$ stands for the contributions of the smoothness term in the case of the original resolution at level $\ell = 0$ and $\mathcal{O}$ denotes the big-O notation as in [56].

Moreover, from (6.83) it can be noticed that

$$h^{\ell} \overset{(6.83)}{=} h \cdot \eta^{-\ell} \Rightarrow h^{-4\ell} = h^{-4} \cdot \eta^{4\ell} \tag{6.85}$$

$$\Rightarrow \quad \mathcal{O}\left(h^{-4\ell}\right) \overset{(6.85)}{=} \mathcal{O}\left(h^{-4} \cdot \eta^{4\ell}\right) = \mathcal{O}\left(h^{-4}\right) \mathcal{O}\left(\eta^{4\ell}\right) . \tag{6.86}$$

Then, the amount of the contributions from the smoothness term at coarser levels, i.e. for the case of $\ell \neq 0$, corresponds to

$$\alpha \left[E_S\left(h^{\ell}\right)\right]_{(\ell>0)} = \alpha\, \mathcal{O}\left(h^{-4\ell}\right) \overset{(6.86)}{=} \alpha\, \mathcal{O}\left(h^{-4}\right) \mathcal{O}\left(\eta^{4\ell}\right) . \tag{6.87}$$

By comparing the result (6.87) with (6.84), it can be realised that the regularisation at lower resolution layers is less influential than that of the original scales by the factor $\mathcal{O}\left(\eta^{4\ell}\right)$. To neutralise the undesired effect, we adjust the regularisation weight at each level ℓ as

$$\alpha^{\ell} = \eta^{-4\ell} \cdot \alpha , \tag{6.88}$$

which ensures the same amount of regularisation for all layers.

Aside from the adaptation of the regularisation parameter, the effect of the subsampling process also requires to adjust the camera calibration matrix K in (3.7) depending on the level ℓ, since the principal point offset in terms of the pixel coordinates is influenced as well. Hence, in consideration of (6.83) at level ℓ the camera calibration matrix K_{η}^{ℓ} can be described by

$$K_{\eta}^{\ell} = \underbrace{\begin{bmatrix} \eta^{\ell} & 0 & 0 \\ 0 & \eta^{\ell} & 0 \\ 0 & 0 & 1 \end{bmatrix}}_{=\,\mathrm{diag}(\eta^{\ell},\eta^{\ell},1)} \underbrace{\begin{bmatrix} \mathtt{f}/h_1 & 0 & c_1 \\ 0 & \mathtt{f}/h_2 & c_2 \\ 0 & 0 & 1 \end{bmatrix}}_{\overset{(3.7)}{=} K} = \begin{bmatrix} \eta^{\ell}\,(\mathtt{f}/h_1) & 0 & \eta^{\ell}\, c_1 \\ 0 & \eta^{\ell}\,(\mathtt{f}/h_2) & \eta^{\ell}\, c_2 \\ 0 & 0 & 1 \end{bmatrix} . \tag{6.89}$$

Alternating Explicit Scheme for Data Term

Based on our experiments, it turned out that the additional contributions of the data term given in (6.20) and (6.21) which are induced by the depth gradient ∇z from (6.12) are the source of a bottleneck for the minimisation and forbids us to select a large time step size τ for fast convergence of the explicit scheme (6.81). As a result, this inevitably entails several thousands or even millions of iterations for the minimisation process. However, in contrast to the case of the smoothness term there is, in fact, no control mechanism to make a trade-off between the main contribution term (6.19) and the additional terms (6.20) and (6.21) accordingly. Hence, to cope with the situation we adopt the following minimisation strategy in each resolution layer, which we call *alternating explicit scheme*: For a fixed number of iterations n, we first carry out $n/2$ iterations only with the term (6.19) and subsequently conduct the rest $n/2$ iterations with all terms, i.e. (6.19), (6.20) and (6.21), see Figure 6.14.

Since the omitted terms (6.20) and (6.21) are based on second-order derivatives which are usually responsible for the stagnation of the optimisation process these additional terms are not as influential as the main term (6.19) for the convergence. On this account, this actually offers us an option to select $\min(h_1^{-2}, h_2^{-2})$ times larger time step size for the first $n/2$ iterations and thereby computation time has been reduced by four orders of magnitude in our experiments. Moreover, as we will demonstrate in Section 6.4 the optimisation only with the simplified scheme shows reasonable results in most tests, which suggests that the simplified scheme can be interpreted as another way of optimisation strategy by excluding high frequency related terms for the hyperbolic type of energy functional such as (6.10) within the coarse-to-fine framework.

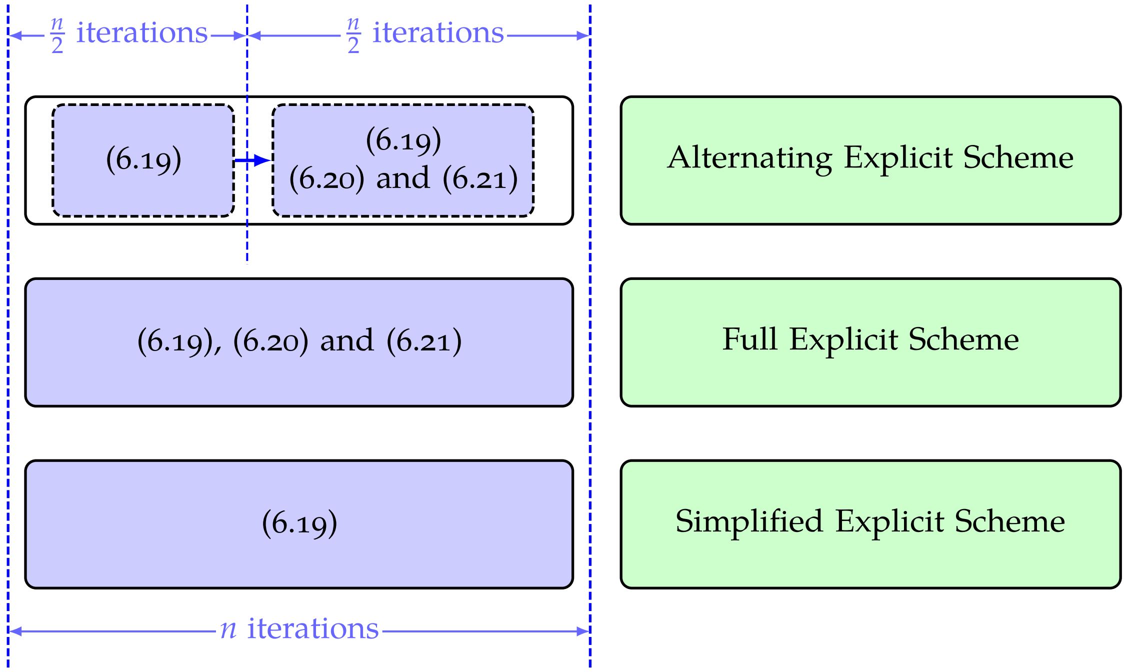

Figure 6.14. Comparison of the alternating explicit scheme with full and simplified schemes. In these schemes, the smoothness term contributions from (6.22) – (6.24) are always used.

6.4 Experimental Evaluation

In this section, we present our experimental evaluations on the Cartesian depth based variational perspective SfS model (6.10).

6.4.1 Test Images and Evaluation Metrics

For the assessment of our approach, we have used four synthetic images along with their ground truth data which are depicted in Figure 6.15. Moreover, these test images have been generated in such a way that they satisfy the model assumptions for (6.10), i.e. Lambertian surface reflectance with uniform albedo and illumination condition under the inverse square law.

The first image *Sombrero* in Figure 6.15(a) has been generated from the following parametric surface equation

$$Z(X,Y) = 0.5\,\frac{\sin(r(X,Y))}{r(X,Y)} + 1.7 \quad \text{with} \quad r(X,Y) = \sqrt{(10\,X)^2 + (10\,Y)^2} \tag{6.90}$$

and rendered according to the brightness equation (3.22) with uniform albedo $\rho = 1$. The size of the rendered image and the employed intrinsic parameters containing information on the focal length, the grid size as well as the principal point are listed in Table 6.2. For creating test images the *Stanford Bunny* and *Dragon* shown in Figure 6.15(b) and 6.15(c), we have used the open-source software Blender [37] and the 3-D models of the Stanford 3-D scanning repository [210]. Thereby, the information on the Z-buffer of the rendering path and the intrinsic parameters on the camera can be retrieved. As before, the rendering has been performed conforming to the brightness equation(3.22) and the size of the rendered image as well as intrinsic parameters are listed in Table 6.2. The last image *Suzanne* in Figure 6.15(d) has been obtained with the same procedure as before with the 3-D model provided by the software and the corresponding parameters are also given in Table 6.2. In addition, 8-bit greyscale quantisation has been employed to store all test images.

Table 6.2. Specifications of test images including intrinsic parameters.

	image size	focal length	grid size	principal point
Sombrero	256×256	$\mathtt{f} = 1$	$h_1 = h_2 = \frac{1}{200}$	$\boldsymbol{c} = (128, 128)^\top$
Stanford Bunny	256×256	$\mathtt{f} = 35$	$h_1 = \frac{1}{8}, h_2 = \frac{9}{128}$	$\boldsymbol{c} = (128, 128)^\top$
Dragon	256×256	$\mathtt{f} = 35$	$h_1 = \frac{1}{8}, h_2 = \frac{9}{128}$	$\boldsymbol{c} = (128, 128)^\top$
Suzanne	512×256	$\mathtt{f} = 35$	$h_1 = \frac{1}{16}, h_2 = \frac{9}{128}$	$\boldsymbol{c} = (256, 128)^\top$

Since the ground truth data is available for these synthetic images, we take two error measures into account as evaluation criteria: the first one with respect to the reconstructed surface and the second one with regard to the reprojected image. The first error measure we look into is the *relative surface error* (RSE) which represents how close the reconstructed surface $\mathcal{S}$ is to the ground truth one $\mathcal{S}^{\text{gt}}$ by

(a) Sombrero. (b) Stanford Bunny. (c) Dragon. (d) Suzanne.

Figure 6.15. Synthetic test images.

measuring a pointwise Euclidean distance between the two surfaces and comparing the measurement with that of the ground truth shape. This error metric is given by

$$\mathrm{RSE} = \frac{\sqrt{\sum_{\overline{\Omega}_i} \left|\mathcal{S}\left(x\left(\boldsymbol{i}\right)\right) - \mathcal{S}^{\mathrm{gt}}\left(x\left(\boldsymbol{i}\right)\right)\right|}}{\sqrt{\sum_{\overline{\Omega}_i} \left|\mathcal{S}^{\mathrm{gt}}\left(x\left(\boldsymbol{i}\right)\right)\right|}}\,. \tag{6.91}$$

It can be noted that the normalisation factor in (6.91) makes the error measure *relative* to the ground truth shape in contrast to an *absolute* type measure and useful for comparison between surfaces of different scales, which is often the case in computer vision. The second error measure we consider is the *relative image error* (RIE) which shows how close the reprojected image I is to the given input image I^{gt} by measuring the pointwise Euclidean distance between the two images and comparing the measurement with that of the input image. Hence, this error measure concerns the photometric aspect of the reprojected image and is defined as

$$\mathrm{RIE} = \frac{\sqrt{\sum_{\overline{\Omega}_i} \left|I\left(x\left(\boldsymbol{i}\right)\right) - I^{\mathrm{gt}}\left(x\left(\boldsymbol{i}\right)\right)\right|}}{\sqrt{\sum_{\overline{\Omega}_i} \left|I^{\mathrm{gt}}\left(x\left(\boldsymbol{i}\right)\right)\right|}}\,. \tag{6.92}$$

As in the case of the RSE in (6.91), in order to make a comparison feasible between images of different greyscales the normalisation in (6.92) is carried out with respect to the intensity of the input image.

6.4.2 Results on Synthetic Test Images

To keep the number of parameters minimal, we have selected the following predefined set of parameters, unless stated otherwise: a subsampling factor $\eta = 0.8$ for the coarse-to-fine approach, $n = 10^6$ solver iterations on each resolution level and a contrast parameter $\lambda = 10^{-3}$. Furthermore, the stated time step size τ in the different experiments refers to the simplified explicit scheme. For the case of the full explicit scheme, the time step size becomes $\min(h_1^2, h_2^2)$ times smaller.

For evaluating the reconstruction quality of the Cartesian Depth based perspective SfS algorithm, as a first experiment we have applied it to the aforementioned test images in Figure 6.15. Moreover, we investigate the performance between a quadratic and a subquadratic penalisers. The reconstruction results and reprojected images paired with the corresponding ground truth data are listed in Figure 6.17, 6.18, 6.19, and 6.20. The depth is visualised according to the colour map displayed in Figure 6.16, where red is encoded as near to the camera, blue as far, and green in between. Moreover, the surface error map is provided in Figure 6.21, where the intensity of red denotes error magnitudes above 1 % and white indicates error magnitudes below 1 %.

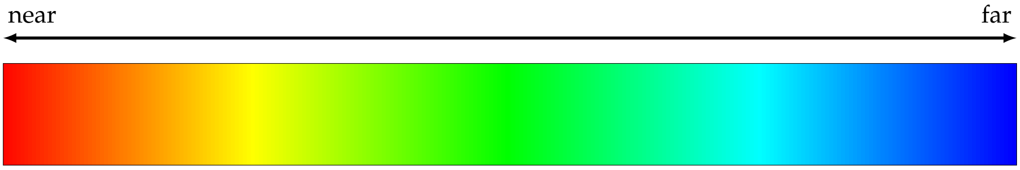

Figure 6.16. Colour-coded depth visualisation: Red indicates near to the camera, blue as far, and green in between.

As can be observed in Figure 6.17 – 6.20, the computed depth as well as the corresponding reprojected images are highly consistent with the ground truth data, which is also confirmed by the surface error maps in Figure 6.21. In fact, it shows only subtle discrepancy for a rather small area in each case except the *Sombrero*, which is not displayed because the complete error map belongs to the class of "under 1 %."

Concerning the comparison between a quadratic and a subquadratic penaliser, according to Table 6.3 the subquadratic regulariser (5.33) shows better performance on the reconstruction quality than that of quadratic one in terms of the previously defined error measures except the *Sombrero*, in which case a relatively smooth surface leads to the lowest RSE value.

Influence of Regularisation

In order to investigate the effect of the regularisation on the quality of the reconstruction and its reprojection, as a second experiment we have applied different amount of smoothness by changing the value of the regularisation parameter α for the test image *Sombrero* under the fixed parameter setting with $\tau = 0.001$ and $n = 10^4$. The graphical chart in Figure 6.22 illustrates how both error measures have behaved with respect to different values of the parameter α. As can be noticed, there appears a spike in the reprojection error (RIE) for a fairly modest amount of regularisation, which is, nevertheless, still under 3 %, but afterwards the value has

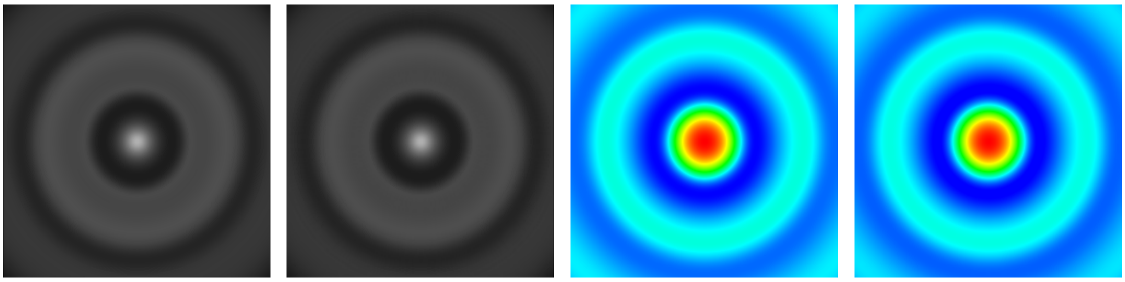

(a) Input image. (b) Reprojected image. (c) Ground truth depth. (d) Computed depth.

Figure 6.17. Results on *Sombrero*. Employed parameters are: $\alpha = 7.5 \times 10^{-5}$, $\tau = 10^{-2}$, $n = 10^6$.

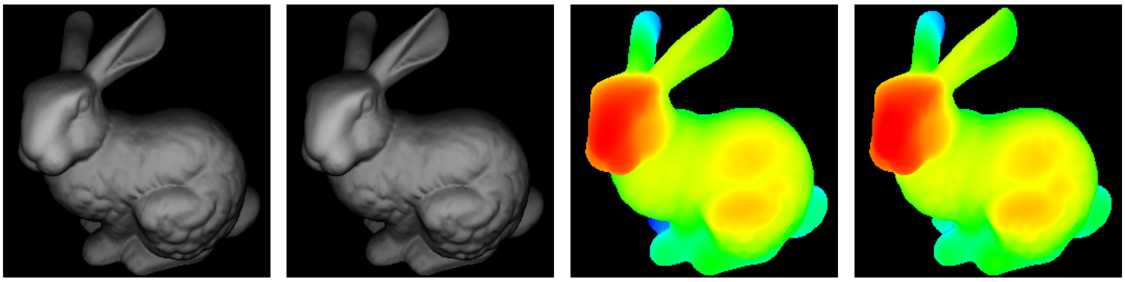

(a) Input image. (b) Reprojected image. (c) Ground truth depth. (d) Computed depth.

Figure 6.18. Results on *Stanford Bunny*. Employed parameters are: $\alpha = 7.5 \times 10^{-5}$, $\tau = 10^{-3}$, $n = 10^6$.

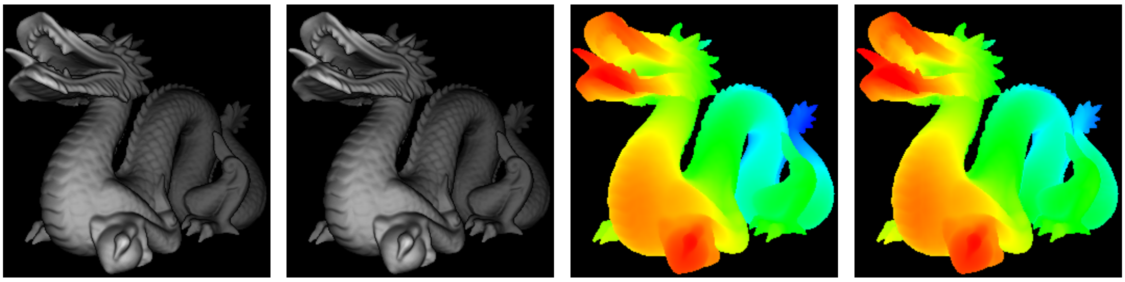

(a) Input image. (b) Reprojected image. (c) Ground truth depth. (d) Computed depth.

Figure 6.19. Results on *Dragon*. Employed parameters are: $\alpha = 7.5 \times 10^{-8}$, $\tau = 10^{-3}$, $n = 10^6$.

decreased abruptly and remained under 2 %. However, for a similar amount of regularisation, the actual reconstruction error RSE which is directly measured from the estimated surface is reduced by nearly three times from 4.4×10^{-2} to 1.7×10^{-2}. Given the fact that typical surfaces often exhibit a certain degree of local smoothness,

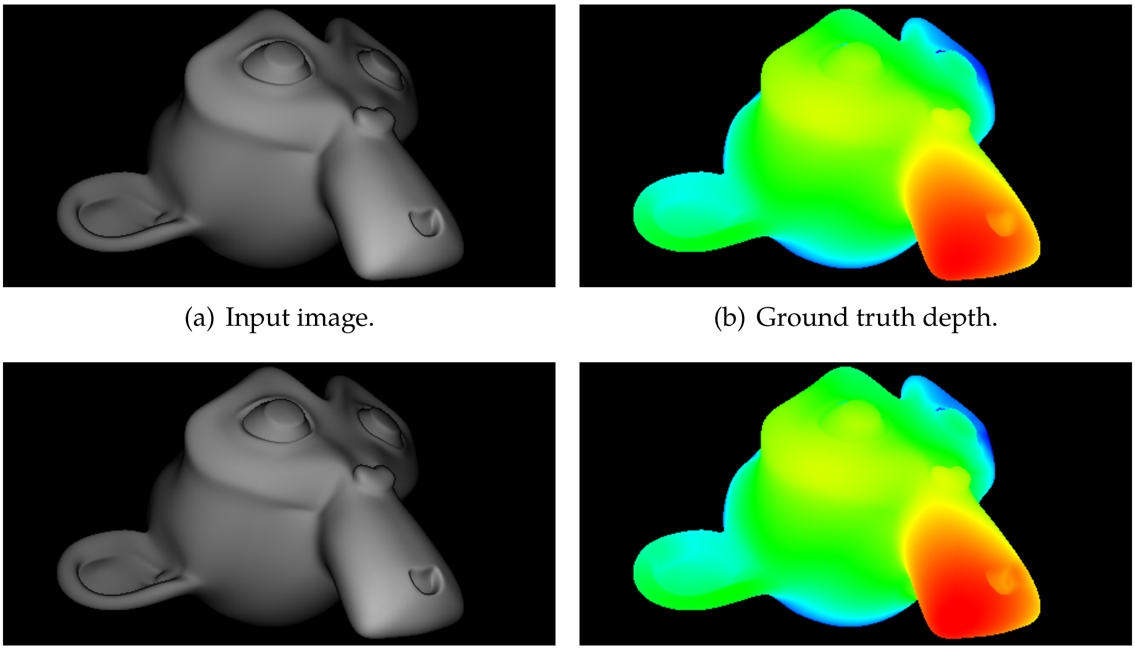
(a) Input image. (b) Ground truth depth.

(c) Reprojected image. (d) Computed depth.

Figure 6.20. Results on *Suzanne*. Employed parameters are: $\alpha = 10^{-7}$, $\tau = 10^{-3}$, $n = 10^{6}$.

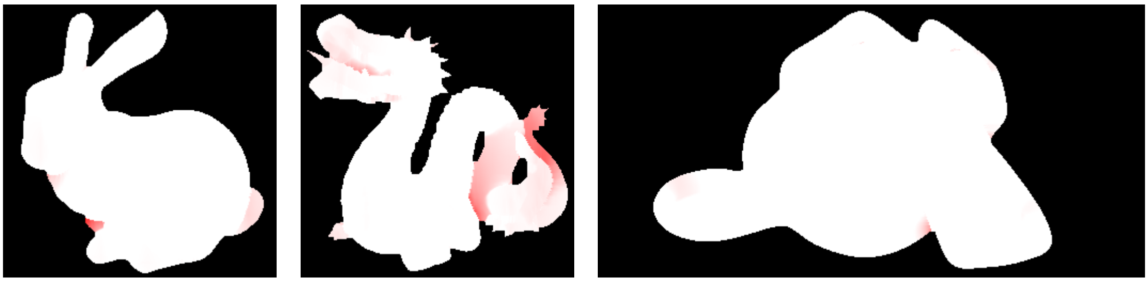
(a) Stanford Bunny. (b) Dragon. (c) Suzanne.

Figure 6.21. Surface error. Red indicates errors above 1 percent, where the intensity encodes error magnitudes. White denotes errors below 1 percent. The *Sombrero* is not shown, since the error is below 1 percent everywhere.

this outcome is not entirely surprising. This may also explain that a certain degree of regularisation has, in general, a positive effect on the quality of the estimation.

Independence of Initialisation

In Section 6.3.4, we have discussed the coarse-to-fine scheme along with the initialisation method for variational SfS. Since this type of hierarchical graduated optimisation

Table 6.3. Comparison of performance between quadratic and subquadratic penaliser. Best results for each test image are listed with boldface. Employed parameters are the same as in Figure 6.17, 6.18, 6.19 and 6.20.

	quadratic		subquadratic		
	RSE	RIE	RSE	RIE	runtime
Sombrero	**0.00208**	0.00694	0.00318	**0.00209**	29113s
Stanford Bunny	0.00546	0.00015	**0.00439**	**0.00007**	23969s
Dragon	**0.01376**	**0.00028**	**0.01376**	**0.00028**	25350s
Suzanne	0.00392	0.00011	**0.00251**	**0.00002**	48395s

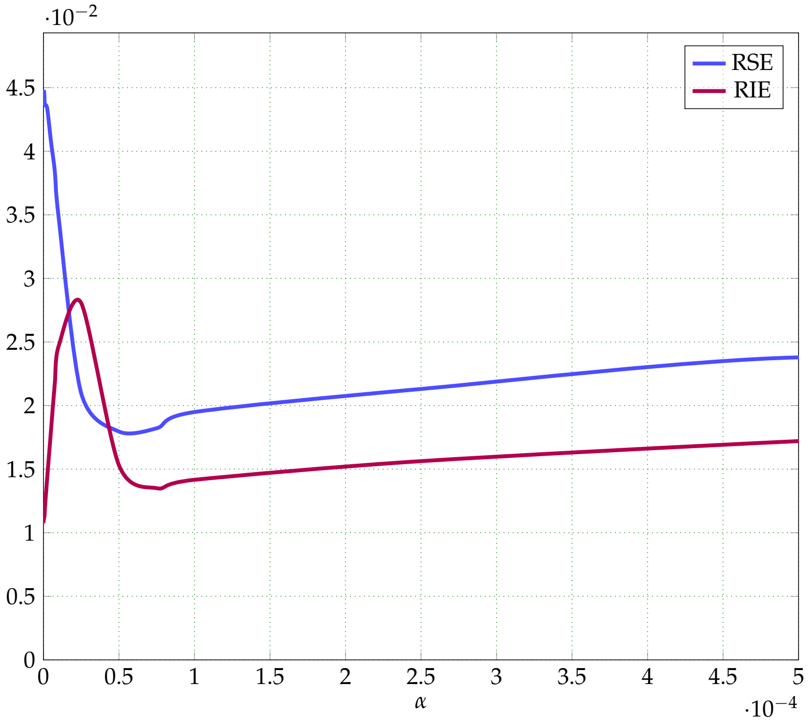

Figure 6.22. Influence of different amount of regularisation in terms of the surface related error (RSE) and the reprojection error (RIE) for the *Sombrero* in Figure 6.17.

strategy is a global strategy, it requires no specific knowledge of the initialisation [211]. To confirm this statement, as a third experiment we study the impact of the initialisation on the quality of the reconstruction as well as its reprojection. To this end, we have used the *Stanford Bunny* in Figure 6.15(b) whose ground truth depth belongs to the range $z \in [1, 2]$ and considered the following three initial surfaces as initialisations for our coarse-to-fine scheme: One is a plane with $z = 1$ which is relatively close to the ground truth data, another is also a plane with $z = 10$ which, however, is comparatively far away from the solution, and the other is the upper bound surface based on the discussions on (6.82) at the lowest resolution level. The results on the initial error and the one after $n = 10^6$ iterations are compared in Table 6.4.

As can be seen, there is a substantial difference between the two planes in terms of both error measures at the initial stage. After sufficient iterations, however, the initial gap has disappeared and surfaces of the same quality have been reconstructed from both planes with respect to the previously defined evaluation metrics, RSE and RIE. Apart from the surfaces with the planes, the upper bound initialisation from (6.82) has shown the same effect. Hence, this experiment shows that embedding the estimation process into a coarse-to-fine framework to avoid local minima for a highly non-convex energy functional is also useful to make the estimation less dependent on the initialisation. This is in full accordance with the continuation method [9, 10, 211].

Table 6.4. Impact of different initialisations on the reconstruction quality and reprojection accuracy for the *Stanford Bunny*. Employed parameters are: $\alpha = 7.5\times10^{-5}$, $\tau = 10^{-3}$, 10^6 iterations.

	initial error		after computation	
	RSE	RIE	RSE	RIE
plane ($z = 1$)	0.25804	1.63174	0.00439	0.00007
plane ($z = 10$)	6.41960	0.97373	0.00439	0.00007
based on (6.82)	0.37712	0.74363	0.00439	0.00007

Comparison of Numerical Schemes

In this experiment, we assess the performance of the three different numerical schemes that have been elaborated in Section 6.3.4: the alternating explicit scheme, the simplified explicit scheme, and the full explicit scheme, cf. Figure 6.14. To this end, we have conducted two experiments by applying the aforementioned three numerical schemes to downsampled versions of the test images in Figure 6.15: On the one hand, with the same stopping time which corresponds to "number of iterations × time step size", on the other hand with the same number of iterations. The final results of both studies are reported side by side in Table 6.5 and 6.6.

For the same stopping time test, the full explicit scheme shows superior quality to the other ones with respect to both error measures in most cases according to Table 6.5. Since the number of iterations is not predefined in this setting, the full explicit scheme must perform considerably more iterations than the other schemes to reach the same stopping time on account of the restricted time step size based on the discussions in Section 6.3.4. While this evidently helps to lower the error measures considering that more optimisation steps have been taken, it requires an enormous amount of runtime. Since the runtime of the full explicit scheme is up to four orders of magnitude higher than those of the other schemes even for such small size images, there are severe limitations in practice regarding the applicability to larger image sizes.

When it comes to the same number of iterations, the alternating scheme as well as the simplified one show clearly a better performance than the full scheme in most cases as presented in Table 6.6. This suggests that excluding the gradient related terms has turned out to be particularly rewarding not only for fast convergence but also for the minimisation itself. And yet, it does not lead to a considerable sacrifice of the quality.

Table 6.5. Comparison of different numerical schemes for equal numerical stopping time $t = 10$ with $t = n \times \tau$. Error measures and runtimes refer to smaller versions of the four test images. The same parameters are applied as in Figure 6.17 – 6.20 except for n, which is given by $n = t/\tau$.

	alternating scheme		simplified scheme		full scheme	
	RSE	RIE	RSE	RIE	RSE	RIE
Small Sombrero	0.01823	0.01920	0.01820	0.02048	**0.00785**	**0.00527**
(128×128)	(runtime: 30s)		(runtime: 15s)		(runtime: 178021s)	
Small Stanford Bunny	0.00659	0.00151	0.00667	0.00257	**0.00576**	**0.00097**
(128×128)	(runtime: 303s)		(runtime: 150s)		(runtime: 4278s)	
Small Dragon	0.01667	0.00267	0.01673	0.00620	**0.01526**	**0.00205**
(128×128)	(runtime: 308s)		(runtime: 149s)		(runtime: 4304s)	
Small Suzanne	**0.00899**	0.00514	0.01055	0.01909	0.01022	**0.00203**
(128×96)	(runtime: 223s)		(runtime: 111s)		(runtime: 2384s)	

Reconstruction with Inpainting

In this experiment, we investigate the inpainting capability of the smoothness term which is a clear advantage of variational methods in comparison to PDE-based approaches. To this end, using the *Stanford Bunny* in Figure 6.15(b) we have generated two degraded versions of the test image with corresponding confidence functions: a perforated version and a sliced one, as depicted in Figure 6.23(a) and 6.23(e) as well as the corresponding confidence functions in Figure 6.23(b) and 6.23(f), respectively. The estimated depth values and the reprojected images are visualised in Figure 6.23 and the corresponding error measures are given in Table 6.7. It can be observed that the degraded regions in the input data have been filled in by the smoothness term based on the information from adjacent data points and thereby no considerable

Table 6.6. Comparison of different numerical schemes for equal number of iterations. Results refer to the smaller versions of the four test images as in Table 6.5. The same parameters have been used as in Figure 6.17 – 6.20 except for n, which is given by $n = 10^7$.

	alternating scheme		simplified scheme		full scheme	
	RSE	RIE	RSE	RIE	RSE	RIE
Small Sombrero	0.02357	**0.00082**	0.02392	0.00659	**0.00358**	0.00319
Small Stanford Bunny	0.00390	**0.00001**	**0.00378**	0.00004	0.00489	0.00047
Small Dragon	0.00572	**0.00001**	**0.00562**	**0.00001**	0.00964	0.00170
Small Suzanne	**0.00319**	0.00002	0.00320	**0.00001**	0.00505	0.00056

differences have been made in the reconstruction when comparing both results with the ground truth data in Figure 6.18(c). The evaluation reported in Table 6.7 also verifies the quality of the reconstructions: All error measures are under 1 % and especially for the perforated case even the same RSE has been achieved as for the original version of the input image.

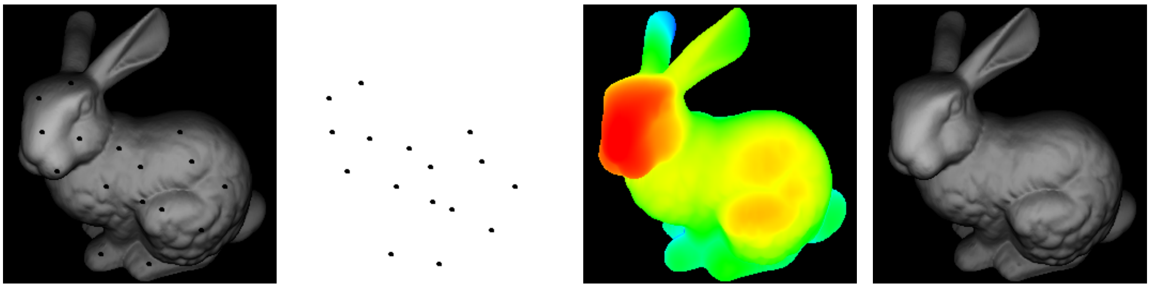

(a) Perforated version. (b) Confidence function. (c) Computed depth. (d) Reprojected image.

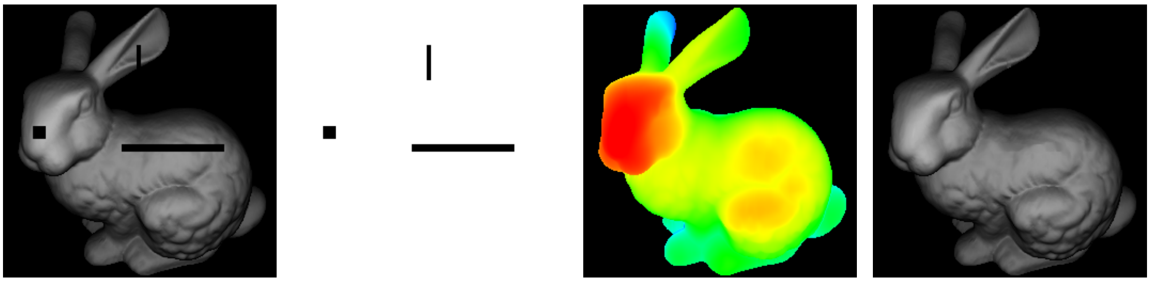

(e) Sliced version. (f) Confidence function. (g) Computed depth. (h) Reprojected image.

Figure 6.23. Experimental results on the deteriorated versions of the *Stanford Bunny* shown in Figure 6.15(b). The first row refers to the perforated version and the second to the sliced version. For both cases, employed parameters are: $\alpha = 7.5 \times 10^{-5}$, $\tau = 10^{-3}$, $n = 10^6$.

Table 6.7. Evaluation of the inpainting effect for degraded versions of the *Stanford Bunny*. Same parameters as in Figure 6.18, i.e. $\alpha = 7.5 \times 10^{-5}$, $\tau = 10^{-3}$, $n = 10^{6}$.

	perforated version Figure 6.23(a)	sliced version Figure 6.23(e)	original version Figure 6.15(b)
RSE	0.00439	0.00509	0.00439
RIE	0.00039	0.00249	0.00007

Comparison with PDE-based Approach

As a next experiment, we demonstrate the robustness of our variational method with respect to the noise by comparing the results with the PDE-based approach of Vogel *et al.* [259] in terms of the previously defined error measures. While the work by Vogel *et al.* [259] constitutes an extension to the baseline model by Prados and Faugeras [195] since it employs the Phong reflectance, we consider only a version with the Lambertian surface reflectance as well as the corresponding scheme which is essentially based on the efficient fast marching method that we have seen in Section 2.3.3. Moreover, we apply both algorithms to two images to demonstrate between advantages and disadvantages of each method: the one without noise and the other with noise. To this end, using the *Stanford Bunny* in Figure 6.15(b) we have added Gaussian noise with standard deviation $\sigma = 20$ for generating a noisy image. The outcomes from each case are reported in Table 6.8 and 6.9, respectively.

Concerning the scenario without noise, both methods have shown, in general, a superb performance, i.e. in most cases error values under 1 % with respect to both evaluation metrics. Nevertheless, when we take a closer look on Table 6.8 which is the test case without noise, the following underlying tendency of each method can be revealed: Whereas the PDE-based approach has shown better performance in terms of the surface related error (RSE), the variational method has obtained superior results with reference to the reprojection error (RIE). In fact, based on the discussions in Section 5.1.2 the role of each term in variational framework accounts for the phenomenon: The data term attempts to minimise the inconsistency of the photometric reprojection, which naturally leads to relatively lower image related error (RIE). However, at the same time the regulariser and the coarse-to-fine scheme necessarily induce some form of smoothness in the reconstruction, which is responsible for comparatively higher surface related error (RSE).

The previous situation turns completely around when it comes to noisy data, since our variational method can exploit not only the smoothness term but also the independence of the initialisation that we have observed in Table 6.4: (i) As we have seen in Section 5.4.3, the increased impact of the regulariser with a comparatively higher value of α can suppress the unreliable oscillations from noisy data, which makes possible to obtain a smooth surface, cf. the value α between Table 6.8 and 6.9. (ii) Concurrently, in contrast to the PDE-based approach by Vogel *et al.* [259] the hierarchical initialisation through the coarse-to-fine scheme does not have to rely entirely on the inaccurate information on the critical points of noisy data, which also makes the algorithm robust. Consequently, both effects make a sharp contrast in the reconstruction quality as presented in Table 6.9: While the RSE for the variational method lies in the range between 1 and 5 %, the same error measure for the PDE-based approach is much higher, i.e. 12 to 20 %. Besides the reported error measures, the computed depth of the *Stanford Bunny* by each method in Figure 6.24(c) and 6.24(d) supports the outcome of the error measures as well.

Table 6.8. Comparison between the Cartesian depth parametrised variational method and the PDE-based approach of Vogel *et al.* [259] with Lambertian reflectance model, which corresponds to the baseline model of Prados and Faugeras [195]. The same parameters are employed as in Figure 6.17 – 6.20.

	PDE-based approach Vogel *et al.* [259]		variational method Ju *et al.* [132]	
	RSE	RIE	RSE	RIE
Sombrero	**0.00301**	0.00495	0.00318	**0.00209**
Stanford Bunny	**0.00266**	0.00154	0.00439	**0.00007**
Dragon	**0.00422**	0.00255	0.01376	**0.00028**
Suzanne	0.00253	0.00082	**0.00251**	**0.00002**

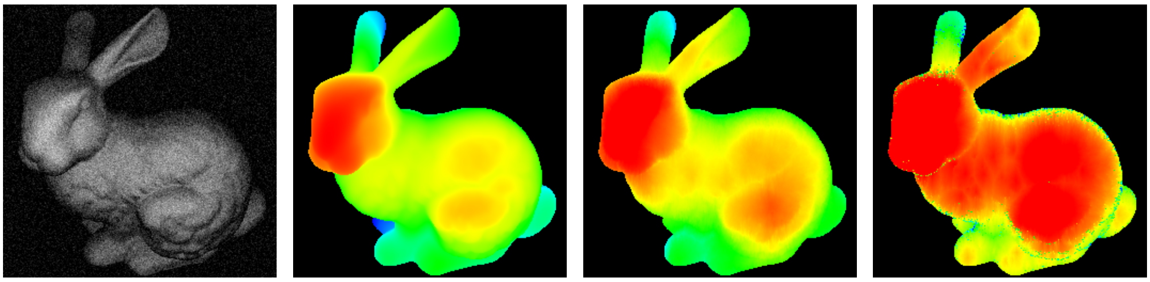
(a) Noisy input image. (b) Ground truth. (c) Variational method. (d) PDE-based method.

Figure 6.24. Computed depth for the noisy version of the *Stanford Bunny* (Gaussian noise with $\sigma = 20$). For our variational method, the employed parameters are: $\alpha = 1.0$, $\tau = 10^{-5}$, $n = 10^6$.

Table 6.9. Performance under noise. Comparison between our variational method and the PDE-based approach of Vogel *et al.* [259] with Lambertian reflectance model (= baseline model of Prados *et al.* [195]). Gaussian noise of standard deviation $\sigma = 20$. Error measures are given in terms of the relative surface error (RSE) and the relative image error (RIE). The applied parameters are as follows: *Sombrero* ($\alpha = 0.1$, $\tau = 10^{-5}$, $n = 10^{6}$), *Stanford Bunny* ($\alpha = 1.0$, $\tau = 10^{-5}$, $n = 10^{6}$), *Dragon* ($\alpha = 1.0$, $\tau = 10^{-5}$, $n = 10^{6}$), *Suzanne* ($\alpha = 1.0$, $\tau = 5 \times 10^{-6}$, $n = 10^{6}$).

	PDE-based approach Vogel *et al.* [259]		variational method Ju *et al.* [132]	
	RSE	RIE	RSE	RIE
Noisy Sombrero	0.19530	0.27254	**0.05118**	**0.13239**
Noisy Stanford Bunny	0.10973	0.17347	**0.03235**	**0.15279**
Noisy Dragon	0.12240	0.19409	**0.05395**	**0.18767**
Noisy Suzanne	0.12134	0.16783	**0.01256**	**0.14302**

6.4.3 Results on Real World Images

So far we have conducted all experiments with synthetic images that we have generated in Section 6.4.1. In order to investigate how the algorithm behaves with real world data, we use the real face images provided by Prados *et al.* [198] in this experiment. According to the authors, these photos were taken by a digital camera with a built-in flash in a relatively dark place, so that the assumptions made on the scene including the illumination as well as the light attenuation should not be severely violated. We have performed an experiment with two images, i.e. the one with closed eyes in Figure 6.25(a) and the other with open eyes in Figure 6.25(e). The employed intrinsic parameters are $\mathtt{f} = 5.8$ *mm* for the focal length and $h_1 = h_2 = 0.018$ *mm* for the grid size. The reconstruction results of the two real test images have been rendered from three different viewpoints and are shown in Figure 6.25. While for both test images we obtain visually realistic reconstructions, for the second image with open eyes in Figure 6.25(e) one can notice the inpainting effect on the eye region, where a confidence function has been defined in order to mask them out based on that the assumption on the Lambertian surface does not hold there.

6.5 Summary

In this chapter, we have proposed a novel variational model for perspective shape from shading by employing the Cartesian depth parametrisation. The established model is characterised by numerous attractive features that distinguishes it from other existing variational methods. Besides, it also has demonstrated good reconstruction

(a) Real test image 1. (b) View 1. (c) View 2. (d) View 3.

(e) Real test image 2. (f) View 1. (g) View 2. (h) View 3.

Figure 6.25. Reconstruction with real world images. Three different views are rendered based on the estimated depth. For both cases, employed parameters are: $\alpha = 7.5 \times 10^{-5}$, $\tau = 5 \times 10^{-3}$, $n = 2 \times 10^{5}$.

results for synthetic as well as real-world data which have even been corrupted, for instance, by noise. To deal with the resulting highly non-convex energy functional, we have developed a hierarchical graduated optimisation method by embedding an alternating explicit scheme into a coarse-to-fine framework. This makes the proposed algorithm robust with respect to the initialisation by not requiring any specific *a priori* information such as depth on critical points. At the same time, it leads to a far less computation time comparing with the case of a standard explicit scheme. Apart from aforementioned advantages on theoretical and practical aspects, our method can serve as a fundamental building block for perspective shape from shading in a variational framework. This offers the potential to combine with other reconstruction cues in computer vision such as stereo or multi-view stereopsis, see e.g. [161] the recent work of Maurer *et al.* at BMVC 2016.

CHAPTER 7

AN EFFICIENT LINEARISATION APPROACH

In the previous chapter, we have established a variational model for perspective shape from shading based on the Cartesian depth parametrisation instead of the radial depth based one in Chapter 5. In addition to the modelling side, we have also designed a hierarchical optimisation framework to minimise the resulting non-convex energy with the alternating explicit scheme. Although the aforementioned variational model retains many distinctive features as explained in Section 6.2.2, the employed multi-resolution based minimisation algorithm still suffers from the huge number of iterations for meaningful reconstructions due to the slow convergence of the explicit scheme. In particular, the limitation to small time step sizes brings various consecutive problems in practical applications: For high resolution images, the computation time based on the explicit scheme may increase drastically, which often turns out to be infeasible. Besides, an increased amount of regularisation for noisy or missing data entails a further drastic fall-off of the time step size, which makes the scheme exceedingly inefficient or impractical even for small images.

In this chapter, being aware of the aforementioned difficulties we introduce an efficient linearisation approach for our Cartesian depth based variational model [132] that we have studied in the previous chapter. To that end, we construct our numerical scheme in a way that it embeds a linear approximation based fixed point iteration with the upwind scheme [219] as well as the lagged diffusivity method [48, 254] into a Gauß-Newton type multi-resolution optimisation framework [9, 10, 36, 211]. This highly specialised scheme is, therefore, not only useful to minimise the underlying non-convex energy, but also able to respect the inherent hyperbolic properties of the data term, as well as to deal with the arising nonlinearity from the incremental computations [48, 254]. In addition, since our linearised scheme does not rely on a parameter of the numerical time step size any more, the reconstruction of high resolution images with a large amount of regularisation becomes feasible, which is particularly useful in the case of noisy data or data with missing information. Moreover, we make use of a numerical differentiation method for evaluating the derivatives expressions of the reflectance model in the data term during the linearisation process. Hence, the employed method can also be applied to the cases of advanced reflection models such as the Oren-Nayar model for rough surfaces [178, 179] and the Phong model for specular ones [189]. The considerable effort that we have made turns out to be well rewarded: On the one hand, a speedup by more than three orders of magnitude can be achieved when compared with the computation time of the alternating explicit scheme in [132] for the same synthetic test images. On the other hand, good reconstructions can be obtained within a reasonable runtime for noisy data sets, degraded images, and high resolution images.

This chapter is based on the paper of Maurer *et al.* [160] that was presented at GCPR and the structure is organised as follows: In Section 7.1, we describe our efficient linearisation approach called hyperbolic warping scheme by providing enough details to follow the idea for each building block. Then, we present comprehensive evaluation results of our algorithm in Section 7.2.

7.1 Hyperbolic Warping Strategy

In this section, we consider how to efficiently minimise the Cartesian depth based energy functional (6.10) that we have proposed in Chapter 6. As we have already discussed in Section 6.3, the hyperbolic nature of the data term (6.11) induced by the gradient ∇z has mainly caused difficulties in the efficient computation as well as the non-convexity. Hence, to overcome the situation we develop an efficient linearisation approach called *hyperbolic warping scheme* based on the work [48, 219, 247].

In order to construct the numerical scheme, we linearise the Euler-Lagrange equation (6.63) that is associated with the energy functional described by the upwind approximation in Section 6.3.2. Then, we derive our numerical scheme by making use of two nested fixed point iterations and an incremental computation within a coarse-to-fine framework inspired by the method of Brox *et al.* [48] for optical flow computation. While our linearisation approach is based on the three main components of Brox *et al.* [48], i.e. the two fixed point iterations, the incremental computation by means of the linearisation and the coarse-to-fine optimisation framework, the resulting scheme is to a large extent different due to the hyperbolic nature of our data term.

7.1.1 Fixed Point Iteration

In order to find a solution to the EL equation in (6.63), we introduce a fixed point iteration with respect to z by adopting a semi-implicit scheme for the contributions from the data term and an implicit scheme for the contributions from the smoothness term with the iteration index k. This yields the formulation

$$\begin{aligned} 0 \;=\; & c^{xy}\, E_D^{xyk+1} \left[E_D^{xyk}\right]_{z^{xyk}} + c^{x^-y}\, E_D^{x^-yk+1} \left[E_D^{x^-yk}\right]_{z^{xyk}} + c^{x^+y}\, E_D^{x^+yk+1} \left[E_D^{x^+yk}\right]_{z^{xyk}} \\ & + c^{xy^-}\, E_D^{xy^-k+1} \left[E_D^{xy^-k}\right]_{z^{xyk}} + c^{xy^+}\, E_D^{xy^+k+1} \left[E_D^{xy^+k}\right]_{z^{xyk}} \\ & + \alpha \left(\Psi'_{h_1^2} \left(\left(s^{xyk+1}\right)^2 \right) \left(z_{xx}\right)^{xyk+1} + 2\, \Psi'_{h_1 h_2} \left(\left(s^{xyk+1}\right)^2 \right) \left(z_{xy}\right)^{xyk+1} \right. \\ & \left. + \Psi'_{h_2^2} \left(\left(s^{xyk+1}\right)^2 \right) \left(z_{yy}\right)^{xyk+1} \right), \qquad (7.1) \end{aligned}$$

whose solution amounts to be z^{k+1}. Concerning the initialisation of z, the strategy discussed in (6.82) can be employed [132, 160]. Please note that the major sources of nonlinearity in (7.1) are comprised of E_D^{xyk+1} in the data term and the diffusivity functions $\Psi'_{h_{**}^2}$ with respect to its argument s^{xyk+1} in the smoothness term whose subscript is defined by

$$h_{**}^2 = \{h_1^2, h_1\, h_2, h_2^2\}\,. \qquad (7.2)$$

7.1.2 Incremental Computation and Linearisation

As a stepping stone to acquire the appropriate linear representation for the formulation in (7.1), we make use of the incremental computation method in [48, 254] by reformulating the expression z^{k+1} as

$$z^{k+1} = z^k + dz^k\,. \qquad (7.3)$$

This suggests that the new depth z^{k+1} at a time step $k+1$ can be computed as the sum of the known depth z^k from an old time step k and the unknown increment dz^k from the current computation.

We now turn to the nonlinearity of (7.1) with the incremental formulation (7.3) but deal with the contributions from the data term and the smoothness term separately: Taylor expansion for the data term and lagged diffusivity method [254] for the smoothness term.

Taylor Approximation for Data Term.

To resolve the nonlinearity of the data term, we make use of the Taylor approximation. To this end, we first substitute the incremental formulation (7.3) for z^{k+1} in (7.1). For the terms containing the time step $k+1$ in (7.1), i.e. E_D^{xyk+1} and $E_D^{x^\pm y^\pm k+1}$, by means of the superscript notations in Section 6.3.3 this corresponds to

$$\begin{aligned} E_D^{xyk+1} \;=\; & E_D \left(x, y, z^{xyk} + dz^{xyk}, z^{x^-yk} + dz^{x^-yk}, z^{x^+yk} + dz^{x^+yk}, \right. \\ & \left. z^{xy^-k} + dz^{xy^-k}, z^{xy^+k} + dz^{xy^+k} \right), \qquad (7.4) \end{aligned}$$

$$
\begin{aligned}
E_D^{x^-yk+1} \;=\; & E_D\Big(x-h_1, y, z^{x^-yk}+dz^{x^-yk}, z^{x^{-2}yk}+dz^{x^{-2}yk}, z^{x^+yk}+dz^{x^+yk}, \\
& \qquad z^{x^-y^-k}+dz^{x^-y^-k}, z^{x^-y^+k}+dz^{x^-y^+k}\Big)\,,
\end{aligned} \tag{7.5}
$$

$$
\begin{aligned}
E_D^{x^+yk+1} \;=\; & E_D\Big(x+h_1, y, z^{x^+yk}+dz^{x^+yk}, z^{xyk}+dz^{xyk}, z^{x^{+2}yk}+dz^{x^{+2}yk}, \\
& \qquad z^{x^+y^-k}+dz^{x^+y^-k}, z^{x^+y^+k}+dz^{x^+y^+k}\Big)\,,
\end{aligned} \tag{7.6}
$$

$$
\begin{aligned}
E_D^{xy^+k+1} \;=\; & E_D\Big(x, y+h_2, z^{xy^+k}+dz^{xy^+k}, z^{x^-y^+k}+dz^{x^-y^+k}, z^{x^+y^+k}+dz^{x^+y^+k}, \\
& \qquad z^{xyk}+dz^{xyk}, z^{xy^{+2}k}+dz^{xy^{+2}k}\Big)\,,
\end{aligned} \tag{7.7}
$$

$$
\begin{aligned}
E_D^{xy^-k+1} \;=\; & E_D\Big(x, y-h_2, z^{xy^-k}+dz^{xy^-k}, z^{x^-y^-k}+dz^{x^-y^-k}, z^{x^+y^-k}+dz^{x^+y^-k}, \\
& \qquad z^{xy^{-2}k}+dz^{xy^{-2}k}, z^{xyk}+dz^{xyk}\Big)\,,
\end{aligned} \tag{7.8}
$$

respectively, cf. (6.41), (6.47), (6.44), (6.50), and (6.53). Subsequently, by applying the first order Taylor expansion to the terms at a time step $k+1$ with respect to the corresponding terms at a time step k, one can obtain the expressions

$$
\begin{aligned}
E_D^{xyk+1} = & E_D^{xyk} + \Big[E_D^{xyk}\Big]_{z^{xyk}} dz^{xyk} + \Big[E_D^{xyk}\Big]_{z^{x^-yk}} dz^{x^-yk} \\
& + \Big[E_D^{xyk}\Big]_{z^{x^+yk}} dz^{x^+yk} + \Big[E_D^{xyk}\Big]_{z^{xy^-k}} dz^{xy^-k} + \Big[E_D^{xyk}\Big]_{z^{xy^+k}} dz^{xy^+k}\,,
\end{aligned} \tag{7.9}
$$

$$
\begin{aligned}
E_D^{x^-yk+1} = & E_D^{x^-yk} + \Big[E_D^{x^-yk}\Big]_{z^{xyk}} dz^{x^-yk} + \Big[E_D^{x^-yk}\Big]_{z^{x^{-2}yk}} dz^{x^{-2}yk} \\
& + \Big[E_D^{x^-yk}\Big]_{z^{xyk}} dz^{xyk} + \Big[E_D^{x^-yk}\Big]_{z^{x^-y^-k}} dz^{x^-y^-k} + \Big[E_D^{x^-yk}\Big]_{z^{x^-y^+k}} dz^{x^-y^+k}\,,
\end{aligned} \tag{7.10}
$$

$$
\begin{aligned}
E_D^{x^+yk+1} = & E_D^{x^+yk} + \Big[E_D^{x^+yk}\Big]_{z^{x^+yk}} dz^{x^+yk} + \Big[E_D^{x^+yk}\Big]_{z^{xyk}} dz^{xyk} \\
& + \Big[E_D^{x^+yk}\Big]_{z^{x^{+2}yk}} dz^{x^{+2}yk} + \Big[E_D^{x^+yk}\Big]_{z^{x^+y^-k}} dz^{x^+y^-k} + \Big[E_D^{x^+yk}\Big]_{z^{x^+y^+k}} dz^{x^+y^+k}\,,
\end{aligned} \tag{7.11}
$$

$$
\begin{aligned}
E_D^{xy^-k+1} = & E_D^{xy^-k} + \Big[E_D^{xy^-k}\Big]_{z^{xy^-k}} dz^{xy^-k} + \Big[E_D^{xy^-k}\Big]_{z^{x^-y^-k}} dz^{x^-y^-k} \\
& + \Big[E_D^{xy^-k}\Big]_{z^{x^+y^-k}} dz^{x^+y^-k} + \Big[E_D^{xy^-k}\Big]_{z^{xy^{-2}k}} dz^{xy^{-2}k} + \Big[E_D^{xy^-k}\Big]_{z^{xyk}} dz^{xyk}
\end{aligned} \tag{7.12}
$$

and

$$\begin{aligned} E_D^{xy^+k+1} &= E_D^{xy^+k} + \left[E_D^{xy^+k}\right]_{z^{xy^+k}} dz^{xy^+k} + \left[E_D^{xy^+k}\right]_{z^{x^-y^+k}} dz^{x^-y^+k} \\ &+ \left[E_D^{xy^+k}\right]_{z^{x^+y^+k}} dz^{x^+y^+k} + \left[E_D^{xy^+k}\right]_{z^{xyk}} dz^{xyk} + \left[E_D^{xy^+k}\right]_{z^{xy^{+2}k}} dz^{xy^{+2}k} , \end{aligned} \tag{7.13}$$

respectively.

Then, by plugging these approximations into the contributions from the data term in the optimality condition (7.1) and rearranging the resulting terms with respect to corresponding unknown dz depending on the central point of approximations, one can attain the form

$$\mathrm{EL}_D = e_D^{xyk}\, dz^{xyk} + \sum_{(\bar{x}\bar{y}) \in \mathcal{N}_D(xy)} e_D^{\bar{x}\bar{y}k}\, dz^{\bar{x}\bar{y}k} + r^{xyk} , \tag{7.14}$$

where e_D^{xyk} denotes the coefficient of dz^{xyk} given in Table 7.1, $(\bar{x}\bar{y}) \in \mathcal{N}_D(xy)$ represents the neighbouring positions of $(x, y)^\top$ for the data term where the approximations are performed. This corresponds to

$$\begin{aligned} (\bar{x}\bar{y}) \in \mathcal{N}_D(xy) = \{ & xy^{-2}, x^-y^-, xy^-, x^+y^-, x^{-2}y, x^-y, \\ & x^+y, x^{+2}y, x^-y^+, xy^+, x^+y^+, xy^{+2} \} . \end{aligned} \tag{7.15}$$

Moreover, $e_D^{\bar{x}\bar{y}k}$ depicts the coefficients of corresponding $dz^{\bar{x}\bar{y}k}$ that is also provided in Table 7.1, and r^{xyk} is for the rest terms that are not involved with the unknown dz^{**k}, which amounts to

$$\begin{aligned} r^{xyk} &= E_D^{xyk}\, c^{xy} \left[E_D^{xyk}\right]_{z^{xyk}} + E_D^{x^-yk}\, c^{x^-y} \left[E_D^{x^-yk}\right]_{z^{xyk}} + E_D^{x^+yk}\, c^{x^+y} \left[E_D^{x^+yk}\right]_{z^{xyk}} \\ &+ E_D^{xy^-k}\, c^{xy^-} \left[E_D^{xy^-k}\right]_{z^{xyk}} + E_D^{xy^+k}\, c^{xy^+} \left[E_D^{xy^+k}\right]_{z^{xyk}} . \end{aligned} \tag{7.16}$$

It should be noted that Table 7.1 only indicates the situation when all coefficients are fully occupied. However, this is not the case for the data term, since the employed upwind type approximation in Section 6.3.3 selects only one direction between the forward and the backward at the centre of the approximation for x- and y-direction, respectively. This necessarily makes one coefficient disappear in each direction, e.g. considering x-direction in (7.10) either $\left[E_D^{x^-yk}\right]_{z^{x^{-2}yk}}$ or $\left[E_D^{x^-yk}\right]_{z^{xyk}}$ must vanish owing to the aforementioned upwind property. In this context, the four coefficients at position $xy^{\pm 2}$ and $x^{\pm 2}y$ in Table 7.1 have no contributions: As an example, we consider the case at position $x^{-2}y$ in Table 7.1. The contribution of this case comes from the approximation at the central point x^-y, i.e. the selection between $\left[E_D^{x^-yk}\right]_{z^{x^{-2}yk}}$ and $\left[E_D^{x^-yk}\right]_{z^{xyk}}$ based on the upwind property. If the former term is chosen, the latter term becomes zero or if the latter term is chosen the former term becomes zero. In both cases, the multiplication of these two terms vanish. Since this property is valid for other positions, i.e. $x^{+2}y$, xy^{-2} and xy^{+2}, the assertion follows.

Table 7.1. The weight matrix based on the coefficients e_D^{xy} and $e_D^{\bar{x}\bar{y}k}$ of dz^{xyk} and $dz^{\bar{x}\bar{y}k}$ for the expression in (7.14) when it is fully occupied. The circled numbers refer to the expressions (7.9) – (7.13) from which the corresponding terms originate and thereby they share the same colour.

	$x-2h_1 =: x^{-2}$	$x-h_1 =: x^-$	x	$x+h_1 =: x^+$	$x+2h_1 =: x^{+2}$
$y+2h_2 =: y^{+2}$	0	0	$\left[E_D^{xy^+k}\right]_{z^{xy^{+2}k}} c^{xy^+} \left[E_D^{xy^+k}\right]_{z^{xyk}}$ ⑤	0	0
$y+h_2 =: y^+$	0	$\left[E_D^{x^-yk}\right]_{z^{x^-y^+k}} c^{x^-y} \left[E_D^{x^-yk}\right]_{z^{xyk}}$ ② $+\left[E_D^{xy^+k}\right]_{z^{x^-y^+k}} c^{xy^+} \left[E_D^{xy^+k}\right]_{z^{xyk}}$ ⑤	$\left[E_D^{xyk}\right]_{z^{xy^+k}} c^{xy} \left[E_D^{xyk}\right]_{z^{xyk}}$ ① $+\left[E_D^{xy^+k}\right]_{z^{xy^+k}} c^{xy^+} \left[E_D^{xy^+k}\right]_{z^{xyk}}$ ⑤	$\left[E_D^{x^+yk}\right]_{z^{x^+y^+k}} c^{x^+y} \left[E_D^{x^+yk}\right]_{z^{xyk}}$ ③ $+\left[E_D^{xy^+k}\right]_{z^{x^+y^+k}} c^{xy^+} \left[E_D^{xy^+k}\right]_{z^{xyk}}$ ⑤	0
y	$\left[E_D^{x^-yk}\right]_{z^{x^{-2}yk}} c^{x^-y} \left[E_D^{x^-yk}\right]_{z^{xyk}}$ ②	$\left[E_D^{xyk}\right]_{z^{x^-yk}} c^{xy} \left[E_D^{xyk}\right]_{z^{xyk}}$ ① $+\left[E_D^{x^-yk}\right]_{z^{x^-yk}} c^{x^-y} \left[E_D^{x^-yk}\right]_{z^{xyk}}$ ②	$\left[E_D^{xyk}\right]_{z^{xyk}} c^{xy} \left[E_D^{xyk}\right]_{z^{xyk}}$ ① $+\left[E_D^{x^-yk}\right]_{z^{xyk}} c^{x^-y} \left[E_D^{x^-yk}\right]_{z^{xyk}}$ ② $+\left[E_D^{x^+yk}\right]_{z^{xyk}} c^{x^+y} \left[E_D^{x^+yk}\right]_{z^{xyk}}$ ③ $+\left[E_D^{xy^-k}\right]_{z^{xyk}} c^{xy^-} \left[E_D^{xy^-k}\right]_{z^{xyk}}$ ④ $+\left[E_D^{xy^+k}\right]_{z^{xyk}} c^{xy^+} \left[E_D^{xy^+k}\right]_{z^{xyk}}$ ⑤	$\left[E_D^{xyk}\right]_{z^{x^+yk}} c^{xy} \left[E_D^{xyk}\right]_{z^{xyk}}$ ① $+\left[E_D^{x^+yk}\right]_{z^{x^+yk}} c^{x^+y} \left[E_D^{x^+yk}\right]_{z^{xyk}}$ ③	$\left[E_D^{x^+yk}\right]_{z^{x^{+2}yk}} c^{x^+y} \left[E_D^{x^+yk}\right]_{z^{xyk}}$ ③
$y-h_2 =: y^-$	0	$\left[E_D^{x^-yk}\right]_{z^{x^-y^-k}} c^{x^-y} \left[E_D^{x^-yk}\right]_{z^{xyk}}$ ② $+\left[E_D^{xy^-k}\right]_{z^{x^-y^-k}} c^{xy^-} \left[E_D^{xy^-k}\right]_{z^{xyk}}$ ④	$\left[E_D^{xyk}\right]_{z^{xy^-k}} c^{xy} \left[E_D^{xyk}\right]_{z^{xyk}}$ ① $+\left[E_D^{xy^-k}\right]_{z^{xy^-k}} c^{xy^-} \left[E_D^{xy^-k}\right]_{z^{xyk}}$ ④	$\left[E_D^{x^+yk}\right]_{z^{x^+y^-k}} c^{x^+y} \left[E_D^{x^+yk}\right]_{z^{xyk}}$ ③ $+\left[E_D^{xy^-k}\right]_{z^{x^+y^-k}} c^{xy^-} \left[E_D^{xy^-k}\right]_{z^{xyk}}$ ④	0
$y-2h_2 =: y^{-2}$	0	0	$\left[E_D^{xy^-k}\right]_{z^{x^+y^{-2}k}} c^{xy^-} \left[E_D^{xy^-k}\right]_{z^{xyk}}$ ④	0	0

Lagged Diffusivity Fixed Point Iteration for Smoothness Term.

For the contributions from the smoothness term, we also replace z^{k+1} with the incremental formulation (7.3) as performed for the data term. This turns the contributions from the smoothness term in (7.1) into

$$
\begin{aligned}
\mathrm{EL}_S = \alpha \Bigg(& \Psi'_{h_1^2}\left(\left(s^{xyk+1}\right)^2\right)\left((z_{xx})^{xyk} + (dz_{xx})^{xyk}\right) && (7.17)\\
&+ 2\,\Psi'_{h_1 h_2}\left(\left(s^{xyk+1}\right)^2\right)\left((z_{xy})^{xyk} + (dz_{xy})^{xyk}\right) + \Psi'_{h_2^2}\left(\left(s^{xyk+1}\right)^2\right)\left((z_{yy})^{xyk} + (dz_{yy})^{xyk}\right)\Bigg)
\end{aligned}
$$

where

$$
\begin{aligned}
\left(s^{xyk+1}\right)^2 \underset{(7.3)}{\overset{(6.62)}{=}} & \left((z_{xx})^{xyk} + (dz_{xx})^{xyk}\right)^2 && (7.18)\\
& + 2\left((z_{xy})^{xyk} + (dz_{xy})^{xyk}\right)^2 + \left((z_{yy})^{xyk} + (dz_{yy})^{xyk}\right)^2 .
\end{aligned}
$$

Since the curvature measure (7.18) described by the incremental formulation is contained as an argument of the diffusivity functions in (7.17), this also causes nonlinearity. To overcome the difficulty, we adopt the *lagged diffusivity* method [51, 253, 254] which is sometimes known as the *Kačanov* method [134]. The basic idea of this approach is that solving a nonlinear problem as a series of linear ones by means of the fixed point iteration [108, 254]. The method has been widely used to solve nonlinear problems arising in various field [90, 91, 135] including optical flow computations [48].

On this account, by introducing a second fixed point iteration with an iteration index n accompanied by the initialisation $dz^{xyk,n=0} = 0$ we apply the Kačanov method to the contributions from the smoothness term given in (7.17) and reformulate the derivative expressions as the corresponding ones in terms of the central point of approximations. This yields

$$\mathrm{EL}_S = \alpha \, \Psi'^{\,xykn}_{s} \left[z^{xykn+1} + dz^{xykn+1} \right] , \tag{7.19}$$

where $\Psi'^{\,xykn}_{s}$ denotes the diffusivity of a preceding time step n at the approximation point $(x, y)^\top$ given by

$$\begin{aligned} \Psi'^{\,xykn}_{s} := \Psi'_{h^4_{**}} \Bigg(& \left((z_{xx})^{xykn} + (dz_{xx})^{xykn} \right)^2 \\ & + 2 \left(\left(z_{xy}\right)^{xykn} + \left(dz_{xy}\right)^{xykn} \right)^2 + \left(\left(z_{yy}\right)^{xykn} + \left(dz_{yy}\right)^{xykn} \right)^2 \Bigg) . \end{aligned} \tag{7.20}$$

Please note that we use the bracket expressions $[\cdot]$ in (7.19) to stress that they are not the argument of $\Psi'^{\,xykn}_{s}$. Besides, because of the reformulation of the second derivative terms the diffusivity now involves 4-th order terms

$$h^4_{**} = \{ h_1^4 , h_1^2 h_2^2 , h_2^4 \} \tag{7.21}$$

instead of the second order ones in contrast to (7.17). Moreover, one can note that we make use of the term dz^{xykn} for the argument of the diffusivity function in (7.18) and dz^{xykn+1} for other smoothness term related contributions to enforce the lagged diffusivity. By following the notations in (7.14), this leads to

$$\begin{aligned} \mathrm{EL}_S = {} & \alpha \, \Psi'^{\,xykn}_{s} \left[z^{xykn+1} + dz^{xykn+1} \right] \\ & + \alpha \sum_{(\bar{x}\bar{y}) \in \mathcal{N}_S(xy)} \Psi'^{\,\bar{x}\bar{y}kn}_{s} \left[z^{\bar{x}\bar{y}kn+1} + dz^{\bar{x}\bar{y}kn+1} \right] , \end{aligned} \tag{7.22}$$

As in (7.19), the bracket expressions here also indicate that they are not the argument of $\Psi'^{\,xykn}_{s}$. For other notations, we follow the conventions from the data term. Therefore, $(\bar{x}\bar{y}) \in \mathcal{N}_S(xy)$ stands for the involved neighbouring positions of $(x, y)^\top$

for the approximation of the smoothness term as provided in Table 5.1. This corresponds to

$$\begin{aligned}(\tilde{x}\tilde{y}) \in \mathcal{N}_S(xy) = \{&x^{-2}y^{-2}, xy^{-2}, x^{+2}y^{-2}, xy^{-}, x^{-2}y, x^{-}y, \\ &x^{+}y, x^{+2}y, xy^{+}, x^{-2}y^{+2}, xy^{+2}, x^{+2}y^{+2}\} \,. \end{aligned} \tag{7.23}$$

Moreover, $\Psi'^{\tilde{x}\tilde{y}kn}_{s}$ denotes the corresponding diffusivity weight. It can be noticed from (7.22) that the nonlinearity with respect to its argument is not present any more since the diffusivity (7.20) has been already evaluated from the old time step n.

Once the nonlinear property in the smoothness term is sorted out, we combine both contributions from the data term and the smoothness term, i.e. (7.14) and (7.22). To this end, we also utilise dz^{kn+1} for the data term related contributions (7.14) in view of the employed lagged diffusivity for the smoothness term related ones (7.22). This yields

$$\begin{aligned} 0 = \mathrm{EL}_D + \mathrm{EL}_S \overset{(7.14)}{\underset{(7.22)}{=}} &\underbrace{e_D^{xyk}\, dz^{xykn+1} + \sum_{(\tilde{x}\tilde{y})\in\mathcal{N}_D(xy)} e_D^{\tilde{x}\tilde{y}k}\, dz^{\tilde{x}\tilde{y}kn+1} + r^{xyk}}_{\text{data term}} \\ &\underbrace{+\, \alpha\left(\Psi'^{xykn}_{s}\left[z^{xykn+1} + dz^{xykn+1}\right] + \sum_{(\tilde{x}\tilde{y})\in\mathcal{N}_S(xy)} \Psi'^{\tilde{x}\tilde{y}kn}_{s}\left[z^{\tilde{x}\tilde{y}kn+1} + dz^{\tilde{x}\tilde{y}kn+1}\right]\right)}_{\text{smoothness term}} . \end{aligned} \tag{7.24}$$

The full version of (7.24) with the linearised expressions of the data term is given by

$$\begin{aligned} 0 = \Big(&E_D^{xyk} + \left[E_D^{xyk}\right]_{z^{xyk}} dz^{xykn+1} + \left[E_D^{xyk}\right]_{z^{x^-yk}} dz^{x^-ykn+1} \\ &+ \left[E_D^{xyk}\right]_{z^{x^+yk}} dz^{x^+ykn+1} + \left[E_D^{xyk}\right]_{z^{xy^-k}} dz^{xy^-kn+1} \\ &+ \left[E_D^{xyk}\right]_{z^{xy^+k}} dz^{xy^+kn+1}\Big)\, c^{xy} \left[E_D^{xyk}\right]_{z^{xyk}} \end{aligned} \tag{7.25}$$

$$\begin{aligned} + \Big(&E_D^{x^-yk} + \left[E_D^{x^-yk}\right]_{z^{x^-yk}} dz^{x^-ykn+1} + \left[E_D^{x^-yk}\right]_{z^{x^{-2}yk}} dz^{x^{-2}ykn+1} \\ &+ \left[E_D^{x^-yk}\right]_{z^{xyk}} dz^{xykn+1} + \left[E_D^{x^-yk}\right]_{z^{x^-y^-k}} dz^{x^-y^-kn+1} \\ &+ \left[E_D^{x^-yk}\right]_{z^{x^-y^+k}} dz^{x^-y^+kn+1}\Big)\, c^{x^-y} \left[E_D^{x^-yk}\right]_{z^{xyk}} \end{aligned} \tag{7.26}$$

$$\begin{aligned} + \Big(&E_D^{x^+yk} + \left[E_D^{x^+yk}\right]_{z^{x^+yk}} dz^{x^+ykn+1} + \left[E_D^{x^+yk}\right]_{z^{xyk}} dz^{xykn+1} \\ &+ \left[E_D^{x^+yk}\right]_{z^{x^{+2}yk}} dz^{x^{+2}ykn+1} + \left[E_D^{x^+yk}\right]_{z^{x^+y^-k}} dz^{x^+y^-kn+1} \\ &+ \left[E_D^{x^+yk}\right]_{z^{x^+y^+k}} dz^{x^+y^+kn+1}\Big)\, c^{x^+y} \left[E_D^{x^+yk}\right]_{z^{xyk}} \end{aligned} \tag{7.27}$$

$$
\begin{aligned}
&+ \Big(E_D^{xy^-k} + \Big[E_D^{xy^-k}\Big]_{z^{xy^-k}} dz^{xy^-kn+1} + \Big[E_D^{xy^-k}\Big]_{z^{x^-y^-k}} dz^{x^-y^-kn+1} \\
&\quad + \Big[E_D^{xy^-k}\Big]_{z^{x^+y^-k}} dz^{x^+y^-kn+1} + \Big[E_D^{xy^-k}\Big]_{z^{xy^{-2}k}} dz^{xy^{-2}kn+1} \\
&\quad + \Big[E_D^{xy^-k}\Big]_{z^{xyk}} dz^{xykn+1}\Big) \, c^{xy^-} \Big[E_D^{xy^-k}\Big]_{z^{xyk}} \qquad (7.28) \\
&+ \Bigg(E_D^{xy^+k} + \Bigg[E_D^{xy^+k}\Bigg]_{z^{xy^+k}} dz^{xy^+kn+1} \quad + \Bigg[E_D^{xy^+k}\Bigg]_{z^{x^-y^+k}} dz^{x^-y^+kn+1} \\
&\quad + \Bigg[E_D^{xy^+k}\Bigg]_{z^{x^+y^+k}} dz^{x^+y^+kn+1} + \Bigg[E_D^{xy^+k}\Bigg]_{z^{xyk}} dz^{xykn+1} \\
&\quad + \Bigg[E_D^{xy^+k}\Bigg]_{z^{xy^{+2}k}} dz^{xy^{+2}kn+1}\Bigg) \, c^{xy^+} \Big[D^{xy^+k}\Big]_{z^{xyk}} \qquad (7.29) \\
&+ \alpha \Big({\Psi'}_{h_1^4}^{\,xykn} \Big[z^{xykn+1} + dz^{xykn+1}\Big] + 2\, {\Psi'}_{h_1^2 h_2^2}^{\,xykn} \Big[z^{xykn+1} + dz^{xykn+1}\Big] \\
&\quad + {\Psi'}_{h_2^4}^{\,xykn} \Big[z^{xykn+1} + dz^{xykn+1}\Big]\Big) \, . \qquad (7.30)
\end{aligned}
$$

One can note that the expressions in (7.25) – (7.29) came from the terms in (7.9) – (7.13), respectively.

Iterative Methods

To find a solution of (7.24), we consider iterative methods since a direct approach by inverting the system matrix constructed from (7.24) is, despite its sparsity, computationally expensive or even infeasible due to severe restrictions on resources based on its huge size $(nx \times ny)^2$, where nx and ny denote the number of pixels in x- and y-direction, respectively. In this respect, by reformulating the expression (7.24) as

$$
\begin{aligned}
0 = &\left(e_D^{xyk} + \alpha\, {\Psi'_s}^{xykn}\right) dz^{xykn+1} + \alpha\, {\Psi'_s}^{xykn} z^{xykn+1} + r^{xyk} \qquad (7.31) \\
&+ \sum_{(\bar{x}\bar{y}) \in \mathcal{N}_D(xy)} e_D^{\bar{x}\bar{y}k} dz^{\bar{x}\bar{y}kn+1} + \sum_{(\bar{x}\bar{y}) \in \mathcal{N}_S(xy)} {\Psi'_s}^{\bar{x}\bar{y}kn} \Big[z^{\bar{x}\bar{y}kn+1} + dz^{\bar{x}\bar{y}kn+1}\Big] \, ,
\end{aligned}
$$

at each iteration step we solve the following equation for the sought depth increment dz^{xykn+1}

$$
\begin{aligned}
0 &= \left(e_D^{xyk} + \alpha\, {\Psi'_s}^{xykn}\right) dz^{xykn+1} + \alpha\, {\Psi'_s}^{xykn} z^{xykn+1} + r^{xyk} + N_D + N_S \\
\Rightarrow \quad dz^{xykn+1} &= -\frac{\alpha\, {\Psi'_s}^{xykn} z^{xykn+1} + r^{xyk} + N_D + N_S}{e_D^{xyk} + \alpha\, {\Psi'_s}^{xykn}} := d\tilde{z}^{xykn+1} \, , \qquad (7.32)
\end{aligned}
$$

where

$$N_D = \sum_{(\bar{x}\bar{y}) \in \mathcal{N}_D^-(xy)} e_D^{\bar{x}\bar{y}k} \, dz^{\bar{x}\bar{y}kn+1} + \sum_{(\bar{x}\bar{y}) \in \mathcal{N}_D^+(xy)} e_D^{\bar{x}\bar{y}k} \, dz^{\bar{x}\bar{y}kn} \tag{7.33}$$

and

$$\begin{aligned} N_S = & \sum_{(\bar{x}\bar{y}) \in \mathcal{N}_S^-(xy)} {\Psi'}_s^{\bar{x}\bar{y}kn} \left[z^{\bar{x}\bar{y}kn+1} + dz^{\bar{x}\bar{y}kn+1} \right] \\ & + \sum_{(\bar{x}\bar{y}) \in \mathcal{N}_S^+(xy)} {\Psi'}_s^{\bar{x}\bar{y}kn} \left[z^{\bar{x}\bar{y}kn+1} + dz^{\bar{x}\bar{y}kn} \right] . \end{aligned} \tag{7.34}$$

In these expressions, $(\bar{x}\bar{y}) \in \mathcal{N}_{\{D,S\}}^-(xy)$ and $(\bar{x}\bar{y}) \in \mathcal{N}_{\{D,S\}}^+(xy)$ denote the set of neighbours that have been already updated and will be updated, respectively.

Since the neighbouring positions $(\bar{x}\bar{y}) \in \mathcal{N}_{\{D,S\}}^-(xy)$ in (7.33) and (7.34) have made use of the already updated values at time step $k, n+1$, this corresponds to the so-called *Gauß-Seidel* method [163, 221, 251] . In this case, the update rule is simply given by

$$dz^{xykn+1} = d\tilde{z}^{xykn+1} . \tag{7.35}$$

To further accelerate the convergence speed, we rewrite this update rule as

$$dz^{xykn+1} = dz^{xykn} + \left(d\tilde{z}^{xykn+1} - dz^{xykn} \right) \tag{7.36}$$

and introduce a relaxation factor ω to the particular direction $\left(d\tilde{z}^{xykn+1} - dz^{xykn} \right)$ that provides the information how the value dz^{xykn} have to be updated. This yields

$$\begin{aligned} & dz^{xykn+1} = dz^{xykn} + \omega \left(d\tilde{z}^{xykn+1} - dz^{xykn} \right) \\ \Leftrightarrow \quad & dz^{xykn+1} = (1-\omega) \, dz^{xykn} + \omega \, d\tilde{z}^{xykn+1} . \end{aligned} \tag{7.37}$$

When the relaxation factor ω is in the range $\omega \in (1,2)$, this method is called the *successive over-relaxation* (SOR) method [88, 275, 276]. One can note that this SOR method obtains a solution by extrapolating the Gauß-Seidel method (7.35), which has the form of a weighted average between the value dz^{xykn} at time step k, n and the already updated value $d\tilde{z}^{xykn+1}$ at time step $k, n+1$ by the Gauß-Seidel method. Moreover, the SOR method (7.37) can be reduced to the Gauß-Seidel method (7.35) when $\omega = 1$, as expected.

7.1.3 Coarse-to-fine Scheme

As the last building block for the hyperbolic warping strategy, we take advantage of the multi-scale optimisation framework in the spirit of the continuation method and graduated non-convexity as discussed in Section 6.3.4: The first fixed point iteration of (7.1) is embedded into a coarse-to-fine scheme as in [48, 132] to cope with the non-convexity of the approximated energy (6.35). This strategy helps not being trapped in local minima during the minimisation process and thereby leads to a minimiser in a global context, see Figure 6.13(a). To this end, we introduce two parameters: One is $\eta \in (0,1)$ that describes the downsampling factor between two consecutive resolution levels as in Figure 6.13(b), the other is κ for specifying the fixed point iteration numbers within one resolution layer. Then, the solution can be computed by only accumulating the increment at each level from coarsest to the original resolutions. This is given by

$$z_{(\ell=0)} = z_{(\ell_{\max})} + \sum_{m=0}^{\ell_{\max}} dz_{(\ell_{\max}-m)}\,, \tag{7.38}$$

where the subscript denotes the resolution level and $\ell_{\max}$ corresponds to the coarsest resolution level given by the downsampling factor $\eta^{\ell_{\max}}$, cf. Figure 7.1.

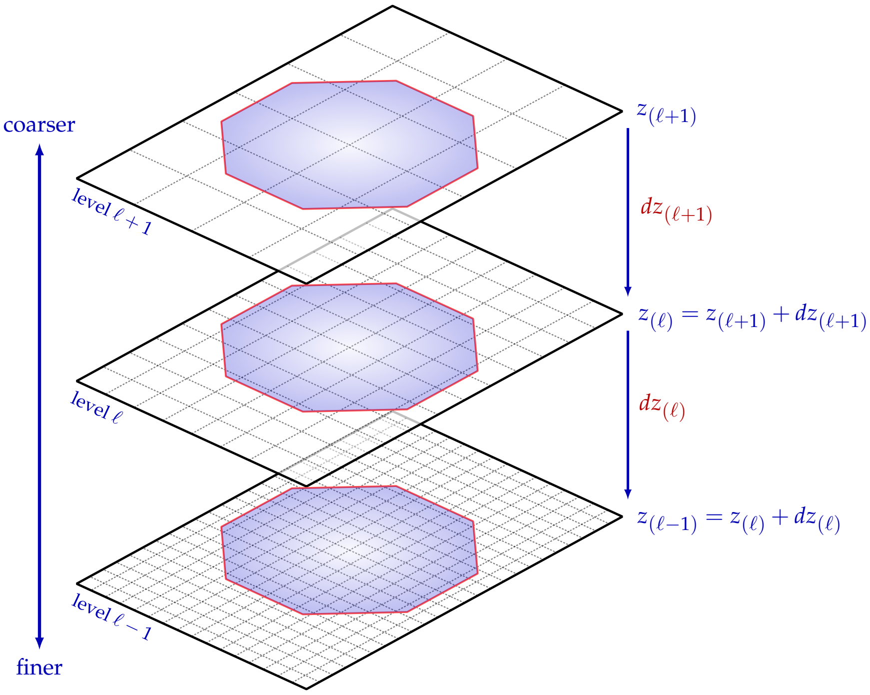

Figure 7.1. Coarse-to-fine scheme with incremental computation. The subscript denotes the resolution level.

7.1.4 Computation Method

As previously pointed out, for evaluating the linearised terms $E_D^{x^*y^*k+1}$ in (7.9), (7.10), (7.11), (7.12) and (7.13) the upwind type approximations in Section 6.3.2 are employed, cf. Line 5 in Algorithm 7.1. For computing the expressions $\left[E_D^{x^*y^*k}\right]_{z^{xyk}}$ in (7.1), we take numerical derivatives by inducing a predefined small amount of perturbations $\pm h_3$ on a current estimate of z^k and re-evaluate the corresponding terms. This procedure actually allows to apply the standard central difference scheme in differentiating $\left[E_D^{x^*y^*k}\right]$ with respect to z^{xyk} as follows:

$$\left[E_D^{xyk}\right]_{z^{xyk}} = \frac{E_D\left(\boldsymbol{x}, z^k(\boldsymbol{x}) + h_3\right) - E_D\left(\boldsymbol{x}, z^k(\boldsymbol{x}) - h_3\right)}{2\,h_3}, \tag{7.39}$$

$$\left[E_D^{x^-yk}\right]_{z^{xyk}} = \frac{E_D\left(\boldsymbol{x}-\boldsymbol{h}_1, z^k(\boldsymbol{x}-\boldsymbol{h}_1) + h_3\right) - E_D\left(\boldsymbol{x}-\boldsymbol{h}_1, z^k(\boldsymbol{x}-\boldsymbol{h}_1) - h_3\right)}{2\,h_3}, \tag{7.40}$$

$$\left[E_D^{x^+yk}\right]_{z^{xyk}} = \frac{E_D\left(\boldsymbol{x}+\boldsymbol{h}_1, z^k(\boldsymbol{x}+\boldsymbol{h}_1) + h_3\right) - E_D\left(\boldsymbol{x}+\boldsymbol{h}_1, z^k(\boldsymbol{x}+\boldsymbol{h}_1) - h_3\right)}{2\,h_3}, \tag{7.41}$$

$$\left[E_D^{xy^-k}\right]_{z^{xyk}} = \frac{E_D\left(\boldsymbol{x}-\boldsymbol{h}_2, z^k(\boldsymbol{x}-\boldsymbol{h}_2) + h_3\right) - E_D\left(\boldsymbol{x}-\boldsymbol{h}_2, z^k(\boldsymbol{x}-\boldsymbol{h}_2) - h_3\right)}{2\,h_3}, \tag{7.42}$$

and

$$\left[E_D^{xy^+k}\right]_{z^{xyk}} = \frac{E_D\left(\boldsymbol{x}+\boldsymbol{h}_2, z^k(\boldsymbol{x}+\boldsymbol{h}_2) + h_3\right) - E_D\left(\boldsymbol{x}+\boldsymbol{h}_2, z^k(\boldsymbol{x}+\boldsymbol{h}_2) - h_3\right)}{2\,h_3} \tag{7.43}$$

with the notations in (6.37), see Line 6 in Algorithm 7.1. One should note that the term B in the above expressions contains only selected upwind approximations. For solving the sparse linear system (7.31) efficiently, the SOR method in (7.37) is applied. Concerning the smoothness term, we have used the central difference method in the context of "first discretise then optimise" scheme as shown in Table 5.1, see Line 10 in Algorithm 7.1. The important building blocks for the computation method are compiled in Algorithm 7.1.

As previously indicated, this hyperbolic warping scheme allows to compute the depth map by accumulating only the increment at each resolution level on top of the initial depth at the coarsest layer by relying on the coarse-to-fine optimisation framework and the lagged diffusivity fixed point iteration. However, it may happen that erroneous increments from a suboptimal linear approximation could mislead the computation and thereby compromise the reconstruction quality. In order to prevent the situation, before adding the new increment to the depth map (Line 20 in Algorithm 7.1) we adopt an insurance policy in a way that the obtained increments during the fixed point iterations as well as SOR should stay within a predefined limit

dz_{limit} such that $|dz_\ell^{kn}| \leqslant dz_{\text{limit}}$. Otherwise, the increment is replaced with the closest values in the interval boundaries, see Line 14–17 in Algorithm 7.1.

Algorithm 7.1. A pseudocode of the hyperbolic warping scheme for variational perspective Shape from Shading.

```
   /* initialisation */
1  $i \longleftarrow 1, k \longleftarrow 1, n \longleftarrow 0, \ell \longleftarrow \ell_{\max}$
2  $z_\ell^k \longleftarrow$ initialise_$z$                                              /* (6.82) */

   /* coarse-to-fine scheme */
3  for $\ell = \ell_{\max}$ downto $0$ do

       /* fixed point iteration (7.1) at each level */
4      for $k = 1$ to $\kappa$ do
5          $E_D^{k+1} \leftarrow$ compute_Linearisation_in_DT $\left(z_\ell^k, E_D^k\right)$   /* (7.9) - (7.13) */
6          $\left[E_D^k\right]_{z_\ell^k} \leftarrow$ compute_Derivatives_in_DT $(z_\ell^k, h_3)$   /* (7.39) - (7.43) */

           /* lagged diffusivity fixed point iteration */
7          $dz_\ell^{kn} \longleftarrow 0$                          /* increment initialisation */
8          for $n = 0$ to $n_{\max}$ do
9              $e_D, r \longleftarrow$ compute_DT_Weights $\left(E_D^{k+1}, \left[E_D^k\right]_{z^k}\right)$        /* (7.31) */
10             $\Psi_s'^{kn} \longleftarrow$ compute_ST_Weight $\left(z_\ell^{kn}, dz_\ell^{kn}\right)$        /* Table 5.1 */

               /* SOR method for the linear system (7.31) */
11             for $i = 1$ to SOR_iteration_Number do
12                 $dz_\ell^{kni} \leftarrow$ SOR $\left(z_\ell^{kn}, dz_\ell^{kn}, \alpha, \omega, e_D, c, r, \Psi_s'^{kn}\right)$        /* (7.37) */

13             $dz_\ell^{kn} \longleftarrow dz_\ell^{kni}$

           /* for avoiding erroneous increments */
14         if $dz_\ell^{kn_{\max}} > dz_{limit}$ then
15             $dz_\ell^{kn_{\max}} \longleftarrow dz_{\text{limit}}$
16         if $dz_\ell^{kn_{\max}} < -dz_{limit}$ then
17             $dz_\ell^{kn_{\max}} \longleftarrow -dz_{\text{limit}}$

18         $z_\ell^{k+1} \longleftarrow z_\ell^k + dz_\ell^{kn_{\max}}$

19     $z_{\ell-1}^k \longleftarrow z_\ell^k$
```

7.2 Experimental Evaluation

In this section, we evaluate our hyperbolic warping algorithm that we have developed so far. For a fair comparison with the method without linearisation from the previous chapter, we take the same synthetic images in Figure 6.15 as well as the same error measures: the RSE in (6.91) that describes how close the estimated 3-D surface to the ground truth one and the RIE in (6.92) is. This indicates how well the reprojected image of the reconstructed surface matches the input image. Whereas our linearised algorithm involves several parameter values, they are mainly from solver related matters such as the number of iterations and thereby no fine-tuning process is required. Hence, we apply a predefined setting to the whole experiments: a downsampling factor $\eta = 0.9$, $\kappa = 5$ fixed point iterations per resolution, $n_{\max} = 9$ nonlinear update for lagged diffusivity fixed point iteration, 10 SOR iterations, a depth increment limit $dz_{\text{limit}} = 0.01$, $h_3 = 10^{-12}$ for numerical differentiation of E_D in the data term, a relaxation parameter $\omega = 1.8$ and a contrast parameter $\lambda = 10^{-3}$. Furthermore, the full confidence value one ($c = 1$) is assigned to the region for reconstruction but zero confidence is used at the background of the input images.

7.2.1 Impact of the Smoothness Term

One distinctive feature which distinguishes our hyperbolic warping scheme given in Algorithm 7.1 from the explicit scheme that we have seen in Chapter 6 is the feasibility of a large amount of regularisation. The freedom of choice with respect the amount of the smoothness α comes from the fact that our linearised algorithm is *not* influenced by the time step size τ any more to guarantee convergence, which actually makes a key difference compared with the explicit type schemes employed in (6.81), cf. Figure 6.14.

The first experiment concerns how the quality of reconstruction is affected as the regularisation parameter α grows progressively. The reprojected images of the corresponding estimations depending on the different values of α are displayed in Figure 7.2 along with the input image. The result demonstrates that a large degree of regularisation induces a strong smoothing effect on the reconstruction. This is supported by a rather flattened surface with not much details, as can be observed in Figure 7.2(d). It can be noted that the employed values of α in Figure 7.2(c) and 7.2(d) are much higher than the one used in Figure 6.18 or other ones in Section 6.4.2, all of which have used with the explicit scheme. The amount of regularisations used in Figure 7.2(c) and 7.2(d) would not be feasible with the explicit scheme. This property does not only play an important role when it comes to noisy data, but it also offers a possibility to determine the level of detail (LoD) [55] of the reconstruction.

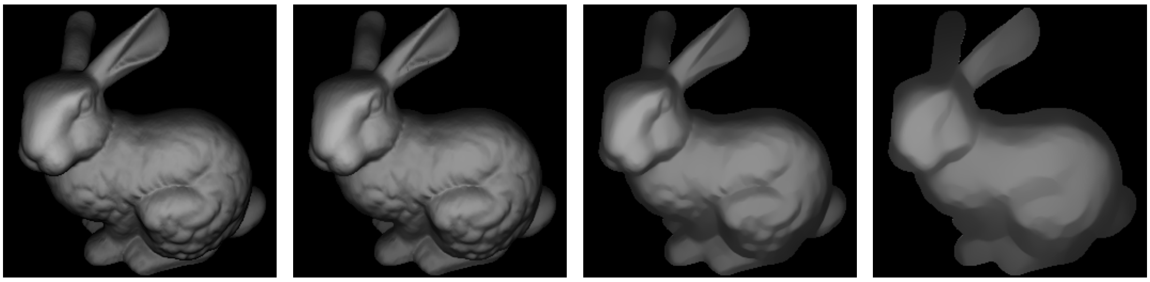

(a) Input image. (b) $\alpha = 1$. (c) $\alpha = 20$. (d) $\alpha = 100$.

Figure 7.2. Impact of the smoothness term subject to the different values of α for the *Stanford Bunny* test image.

7.2.2 Comparison with Other Methods

In this section, we compare our hyperbolic warping scheme with other methods: the PDE-based approach by Vogel *et al.* [259] with the Lambertian reflectance whose baseline model corresponds to the method of Prados and Faugeras [195] and our variational approach (explicit scheme) from the previous chapter. In order to explore different aspects of each method, i.e. strengths and weaknesses, not only the normal test images in Figure 6.15 but also corrupted versions containing Gaussian noise with $\sigma = 20$ are utilised for experiments and the computed error measures are compiled in Table 7.2.

With normal test images, both error measures of our linearised approach remain under 1 % (except in case of the *Dragon*), although the values are somewhat higher than those of other methods. The result also suggests that each method has its own advantages with respect to error measures: The PDE-based approach delivers better performance in term of the RSE, since it does not regularise the depth itself. Regarding the RIE, in contrast, the variational method [132] shows better quality considering that the penalisation is actually brought into effect on the data term in an attempt to neutralise the discrepancy between the input image and the reprojected one from the estimated depth.

Turning to the noisy data, however, it can be noticed that our linear approximation method outperforms the other approaches in both error measures. Besides, the outcome also indicates that both variational methods offer the distinct advantage of robustness against noise due to the regularisation. This is not the case for the PDE-based method that moreover rely on the singular points whether the data is noisy or not. This explains the substantially lower error values for both variational methods and comes to full agreement with the discussions in Section 6.4.2.

Moreover, the advantage of our linearised scheme is that it does not require a time step size as indicated in Section 7.2.1. Hence, contrary to the case of the alternating explicit scheme from the previous chapter no such a vast number of iterations is necessary for convergence. On this account, the severe restrictions on the choice of a relatively small amount of regularisations have been lifted. This supports the use of different values of α in Table 7.2 comparing with the explicit scheme, where the parameters have been optimised for the predefined iteration number $n = 10^6$.

Table 7.2. Comparison between our linearised approach and two other methods: the PDE-based method of Vogel *et al.* [259] and the alternating explicit scheme in Chapter 6. Error measures are given in terms of RSE and RIE for the four test images in Figure 6.15 as well as corresponding corrupted versions with Gaussian noise ($\sigma = 20$). The employed parameters of our approach are: *Sombrero* ($\alpha = 0.003$), *Stanford Bunny* ($\alpha = 0.08$), *Dragon* ($\alpha = 0.2$), *Suzanne* ($\alpha = 0.04$), *Noisy Sombrero* ($\alpha = 0.02$), *Noisy Stanford Bunny* ($\alpha = 3$), *Noisy Dragon* ($\alpha = 1$), *Noisy Suzanne* ($\alpha = 2$). For the method of Vogel *et al.* the same parameters have been utilised as in the original paper.

	Vogel *et al.* [259]		alternating explicit		hyperbolic warping	
	RSE	RIE	RSE	RIE	RSE	RIE
Sombrero	**0.00301**	0.00495	0.00318	**0.00209**	0.00768	0.00925
Stanford Bunny	**0.00266**	0.00154	0.00439	**0.00007**	0.00928	0.00327
Dragon	**0.00422**	0.00255	0.01376	**0.00028**	0.02904	0.02333
Suzanne	0.00253	0.00082	**0.00251**	**0.00002**	0.00696	0.00224
Noisy Sombrero	0.19530	0.27254	0.05118	0.13239	**0.01542**	**0.03851**
Noisy Stanford Bunny	0.10973	0.17347	0.03235	0.15279	**0.01359**	**0.12285**
Noisy Dragon	0.12240	0.19409	0.05395	0.18767	**0.03391**	**0.17732**
Noisy Suzanne	0.12134	0.16783	0.01256	0.14302	**0.00826**	**0.12038**

To show the value of the built-in smoothness term in variational methods, we further conduct an experiment with the noisy data by applying an extra pre- and post-processing step to the PDE-based method and our linearisation scheme, respectively. To this end, as a pre-processing step we adopt a total variation (TV)-based image denoising method [220] and for post-processing a depth smoothing technique by means of a second order smoothness term corresponding to our regulariser in (5.33). The outcome of this experiment is presented in Table 7.3. It shows the advantage of the built-in regularisation of variational methods by the fact that our linearised algorithm obtains better results even without the aforementioned steps while the quality of the reconstruction with the PDE-based method of Vogel *et al.* [259] has been considerably improved especially from a noise reduction process that had performed before the computation.

Table 7.3. Comparison of the methods between Vogel *et al.* [259] and our hyperbolic warping approach with noisy data by means of an additional pre-processing step (image denoising) or post-processing step (depth smoothing).

	Vogel *et al.* [259]			hyperbolic warping		
	original RSE	with pre-processing	with post-processing	original RSE	with pre-processing	with post-processing
Noisy Sombrero	0.19530	0.02008	0.19197	0.01542	0.01741	**0.01538**
Noisy Stanford Bunny	0.10973	0.01434	0.06164	0.01359	0.01470	**0.01357**
Noisy Dragon	0.12240	0.04623	0.08226	0.03391	**0.03322**	0.03390
Noisy Suzanne	0.12134	0.01245	0.06169	0.00826	0.00917	**0.00824**

7.2.3 Reconstruction with Inpainting

The experiment in this section investigates the inpainting functionality of the smoothness term (6.13). Whereas the same experiment has been performed in the previous chapter, an implicit restriction is imposed on domain size for inpainting due to the nature of the employed algorithm in the work: Since the explicit schemes inevitably require significantly more iterations to fill in large regions, which thereby takes huge amount of computation time, the domain size has been selected relatively small, cf. Figure 6.23.

However, our hyperbolic warping scheme can provide an inpainting result for comparatively large regions at marginal cost with respect to runtime. To confirm this statement, we run our algorithm with the degraded input image given in Figure 7.3(a), where the domain size for inpainting is substantially larger than those in the previous chapter and zero confidence ($c = 0$) is assigned to the region to be filled in. Based on the reprojected image in Figure 7.3(b), one can see that our scheme allows to obtain a high quality reconstruction even with a large fraction of missing information. This is also supported by the error measure (RSE = 0.00793), which is comparable to the case with complete data (RSE = 0.00696) according to Table 7.2. However, a moderate smoothing effect may be noticed at some inpainted regions, where the surface contains abrupt transitions of depth, e.g. the border between outer and inner part of the ear, the area between the heart-shaped nose and the mouth, and the upper part of the eyeball.

7.2.4 High-resolution Image

To demonstrate the main advantage of our linearised algorithm over other variational SfS methods with explicit schemes such as [131, 132], we make use of the high-resolution image *Blunderbuss Pete* in Figure 7.4(a) for reconstruction. Since the shortcoming of a very small time step size – which makes numerous iterations

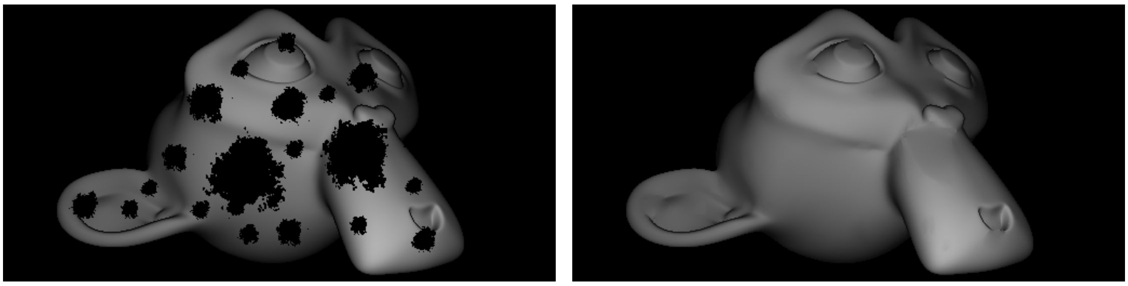

(a) Degraded input image.

(b) Reprojected image with $\alpha = 0.5$.

Figure 7.3. Inpainting experiment with the *Suzanne* image.

necessary for convergence in the explicit schemes – is overcome in our case, a speedup of three orders of magnitude with respect to runtime can be achieved for small size images as shown in Table 7.4. Moreover, a reconstruction can be attained with a reasonable computation time for the high-resolution image, which is obviously not the case with explicit schemes. When it comes to solely runtime, however, the PDE-based method shows clearly better performance, since the FM-based numerical scheme only needs to visit each point once and the overhead for the update process is marginal. This is actually the price that we have to pay when robustness of variational methods becomes essential part of an algorithm.

Apart from the reasonable computation time, the quality of reconstruction is still highly competitive when compared with that of the PDE-based approach: As shown in Figure 7.4(b), it is not easy to distinguish the reprojected image of our approach from the input image in Figure 7.4(a) without the difference plot provided in Figure 7.4(c) (RIE = 0.03414). Nevertheless, some difficulties may arise at wrinkles or folded regions with sudden changes of grey values for the reprojected image as well as at transition regions such as cloak around the legs, the knee and the torso for the reconstruction (RSE = 0.02930), cf. Figure 7.4(g) and 7.4(h). Although the method of Vogel *et al.* [259] shows a better performance in terms of the reprojection error (RIE = 0.00067), the reconstruction has, in general, similar error patterns, e.g. at the cloak, except some regions such as the knee and the torso (RSE = 0.01593).

7.3 Summary

In this chapter, we have developed an efficient numerical method for variational perspective SfS by means of a linearisation of the reflectance model. When compared with the standard explicit schemes, the proposed approach makes it possible to achieve a speedup by more than three orders of magnitude without significantly compromising the quality of the reconstruction. Aside from the speedup, a large amount of regularisation becomes feasible without considerably sacrificing the com-

Table 7.4. Comparison of runtime: Vogel *et al.* [259], alternating explicit scheme and hyperbolic warping approach.

	Vogel *et al.* [259]	alternating explicit	hyperbolic warping
Sombrero (256 × 256)	1s	29113s	17s
Stanford Bunny (256 × 256)	1s	23969s	11s
Dragon (256 × 256)	1s	25350s	12s
Suzanne (512 × 256)	2s	48395s	21s
Blunderbuss Pete (1080 × 1920)	33s	infeasible	340s

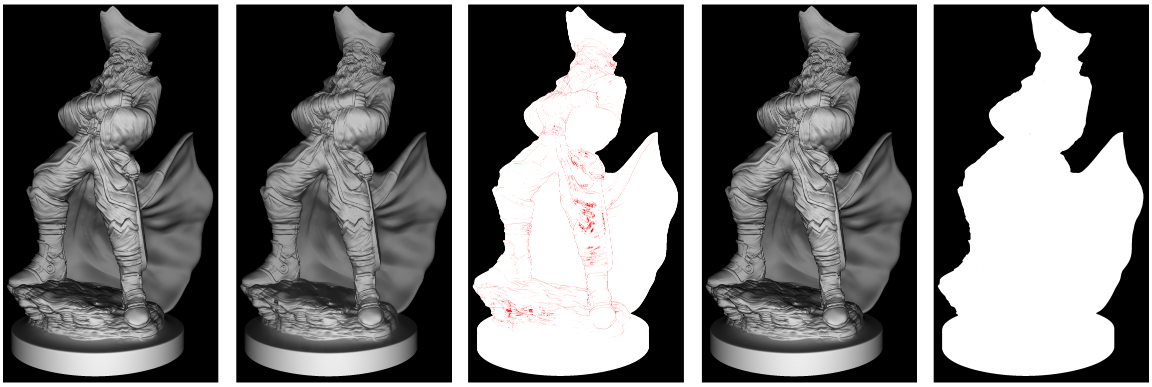

(a) Input image. (b) Reprojected image for our method. (c) Difference plot for Figure 7.4(b). (d) Reprojected image for PDE-based method. (e) Difference plot for Figure 7.4(d).

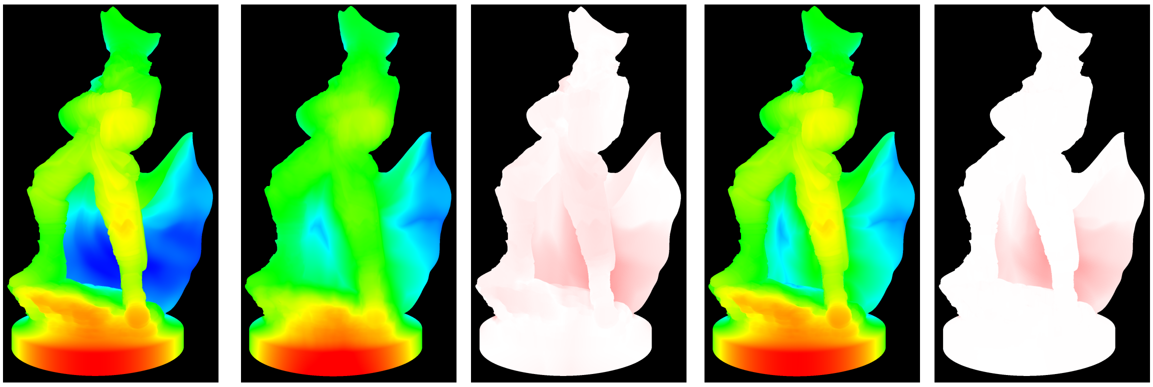

(f) Ground truth depth. (g) Our reconstruction. (h) Difference plot for Figure 7.4(g). (i) PDE-based reconstruction. (j) Difference plot for Figure 7.4(i).

Figure 7.4. Reprojected image and colour-coded depth map of the *Blunderbuss Pete* test image (3-D model by *BenDasie*). Red in difference plots indicates errors above 1 %, where the intensity encodes the error magnitude. White denotes errors below 1 %.

putation time. This feature is considered to be indispensable for the robustness of the algorithm, in particular, when it comes to corrupt data with noise or missing information. Furthermore, the employed numerical derivatives for the linearisation of the reflectance model can be extended to advanced reflection models in a straightforward way. Besides, the proposed strategy is highly versatile: it can be applied to other existing variational SfS models which are typically based on *explicit* schemes as the *de facto* standard, it can be combined with the aforementioned advanced reflectance models or it can be integrated as a building block for incorporating different depth cue modules such as stereo due to the Cartesian depth based parametrisation, see Maurer *et al.* BMVC 2016 [161]. As a consequence, the proposed numerical scheme is eligible as a promising candidate to become a standard tool in variational perspective SfS.

SUMMARY & OUTLOOK

The goal of this thesis has been set as to investigate perspective SfS from modelling and algorithmic viewpoints subject to the specified methods. In this chapter, we encapsulate our major contributions by emphasising *flexibility* and *efficiency* with respect to each approach: PDE-based methods and variational methods.

8.1 Summary of Contributions

Let us now summarise our contributions of each approach with respect to modelling and numerical viewpoints.

8.1.1 PDE-based Methods

When it comes to PDE-based methods, our primary concern has been to consider a *relaxed* assumption on the position of a point light source, i.e. the case of *not* being located at the optical centre of a camera.

Modelling Side

To this end, we first have derived our *generalised* brightness equation using the Lambertian reflectance model in Chapter 4. Furthermore, by employing the Oren-Nayar surface reflectance model [178] we have constructed a model that has the capability of *jointly* handling both more general illumination scenarios and non-Lambertian objects at the same time. The established models are described by HJEs in a spherical coordinate system such that critical points can be determined for the initialisation of the FM method.

Numerical Side

Aside from the flexibility of the modelling side, we have achieved the efficiency by customising the traditional FM method in a way that our adapted FM scheme satisfies special requirements for our model. This adaptation process leads naturally to the distinct features of our scheme: (i) In contrast to the traditional FM methods, our adapted FM scheme is able to deal with a general-type of HJEs by means of the Regula-Falsi method while the initial depth information identified by critical points is being propagated to the remaining computational domain. (ii) Furthermore, our scheme can also deal with the computation in a spherical system for the Cartesian input data. This interdependence requires the reevaluation at subpixel positions, which is resolved by incorporating bilinear interpolation. We have demonstrated the usability of our approach by applying it to real-world endoscopic test images.

8.1.2 Variational Methods

As far as variational methods are concerned, the prime subject has been to obtain a unified model containing all preferred features listed in Table 1.2 as well as a corresponding algorithm for minimising the associated energy.

Modelling Side

For variational methods, we first have derived a radial depth based variational model based on the brightness equation of Prados and Faugeras [195] in Chapter 5. Subsequently, by changing the parametrisation from the radial depth to a Cartesian one we have constructed a novel Cartesian depth based variational PSfS model in Chapter 6. When compared with existing variational models, our models have several noticeable features that stand out: (i) Our variational models are accompanied by an *edge-preserving* smoothness term. Hence, despite the regularisation effect, the employed subquadratic regulariser allows to preserve edges during the reconstruction, which is usually *not* the case for existing approaches, see Table 1.2. (ii) Our approaches have used the *correct* surface normal for the perspective SfS model instead of simply replacing with that of the orthographic one, e.g. Zhang *et al.* [278] and Wu *et al.* [270]. (iii) Moreover, our approaches belong to *direct* estimation methods because the established models are minimised with respect to the parametrised depth directly. Therefore, *no* further steps are required for reconstruction such as the integration of surface normals unlike most variational methods with two steps strategies [45, 89, 125]. (iv) Aside from the direct estimation, our model satisfies the integrability constraints per construction *without* requiring an additional term in comparison to usual variational methods, e.g. [1, 278]. (v) The confidence function in our model allows to rule out the corrupt data due possibly to noise or missing information and to fill in the information from the vicinity by taking advantage of the smoothness term. (vi) Since our Cartesian depth model is designed in a way that the reprojection error in the data term and the Cartesian depth in the smoothness term are penalised directly, the deviations of respective terms become photometrically and geometrically interpretable. (vii) Our model with the Cartesian depth parametrisation offers the full potential to be an individual module for being integrated with different cue methods, e.g. stereo [216], multi-view stereo [271, 273], or scene flow [24, 25], where the Cartesian depth becomes a common parametrisation.

Numerical Side

On the algorithmic side, we have developed a novel optimisation strategy in the light of the graduated non-convex approach [36]. Since our scheme contains an alternating explicit scheme based on the upwind discretisation [219] that is embedded into a coarse-to-fine optimisation framework, it can handle the arising *non-convex* energy by respecting the hyperbolic nature of the data term. During the optimisation process, the alternating explicit scheme can deal with the lagging property from the data term more efficiently than typical explicit schemes do, which leads to a considerable speedup. In addition, our scheme does *not* require any particular initialisation methods, e.g. PDE-based methods as in [1, 278]. We also have shown quality reconstructions as well as benefits of our numerical scheme with synthetic and real-world images.

Linearisation Methods. In order to further enhance the efficiency of our proposed optimisation strategy in variational methods, we have developed an efficient linearisation method called the *hyperbolic warping scheme* in Chapter 7. Inspired by the work of Brox *et al.* [48] that can handle both *non-convexity* and *nonlinearity* for optical flow computations, our scheme is constructed in a way that both difficulties and the hyperbolic nature of the data term are considered at the same time. To deal with the nonlinearity, we apply the Taylor approximation method to the data term by means of the lagged upwind discretisation and the lagged diffusivity fixed point iteration method [48, 254] to the smoothness term, respectively, after introducing an incremental computation [48, 254]. To resolve the non-convexity, the derived linearised approach is embedded into a graduated hierarchical optimisation scheme. The resulting scheme shows a speedup by more than a factor of three orders of magnitude when compared with the alternating explicit scheme. Furthermore, we have computed the arising derivatives numerically when linearising the reflectance model in the data term, which can be extended to advanced reflectance models in a straightforward way. Finally, our efficient linearised scheme does not suffer from the constraints on the relatively small time step size of the explicit scheme. Since the restrictions are lifted, our scheme is particularly beneficial in cases even when an explicit scheme is usually not feasible, e.g. for inpainting large missing parts or for encouraging a large amount of regularisation in view of severe noise. We have substantiated the advantages of our approach by applying it to a synthetic image containing large missing parts as well as to a high-resolution image.

8.2 Outlook

The present work can further be extended in some ways such that the quality of reconstructions could be improved.

In our variational and linearisation methods, only Lambertian reflectance model has been used. However, the Lambertian surface model sometimes cannot capture important properties of a surface appropriately especially when a surface contains significantly different properties than those of a matte surface, e.g. specular effect or roughness. In those cases, our framework can be extended to non-Lambertian reflectance models such as Phong or Oren-Nayar surface reflectance for better approximation of surface characteristics, which should be a straightforward extension.

Moreover, we have considered a subquadratic penaliser in variational methods. Although we have made use of a nonlinear edge-preserving regulariser, it has only isotropic effect on along and across edges. Therefore, an edge-enhancing anisotropic regulariser could also be considered for retaining important structures effectively. In this regard, Hafner *et al.* [106] have made use of the edge-enhancing regulariser of Perona and Malik [188] across the edges and the edge-preserving penaliser of Charbonnier *et al.* [54] along the edges, respectively, in the context of denoising and focus fusion.

Furthermore, SfS methods could be combined with different reconstruction modules that rely on texture information, e.g. stereo. In fact, the correspondence based reconstruction methods depend heavily on texture information, where SfS methods actually have disadvantages. Hence, we could make use of stereo methods in textured regions and SfS in texture-free areas for exploiting both advantages. Our recent work, i.e. Maurer *et al.* BMVC 2016 [161] which belongs to one of the very first work in this direction, shows highly promising results.

Another aspect for future work would be generalisations of assumptions on modelling components. Among others, most illumination scenarios in SfS have been usually limited to a point light source whose position must be known: it is positioned far away [61, 116], at the optical centre of a camera [6, 195, 259] or close to a camera. Apart from the light source, the albedo in the surface reflectance model is typically assumed to be uniform [61, 281]. Since these restrictions prevent SfS from being applied to more general settings, it is desirable to design an approach that can handle such cases. First approaches in this direction show promising results as well, see Maurer *et al.* BMVC 2016 [161].

In this context, spherical harmonics [58] turns out to be a useful tool for describing global illumination effect [26, 27, 28, 208]. Recently, Huang and Smith have applied the method to SfS for describing more complex illumination scenarios [124]. Moreover, Barron and Malik have used spherical harmonics in the intrinsic image problem [23, 103] for recovering scene properties by jointly estimating the reflectance, the illumination and the shape [20, 22]. However, most approaches are still restricted to a distant light source combined with Lambertian reflectance model under the orthographic camera projection [20, 22, 212, 218, 284]. Hence, it is natural to consider the perspective camera projection and non-Lambertian reflectance models for using spherical harmonic illuminations.

However, despite all the progress, real-world scenarios with uncontrolled settings remain still highly challenging, e.g. considering natural illumination [22, 128, 147, 184]. Therefore, it would be great when this work could encourage further contributions to open problems in the field.

REFERENCES

[1] A. Abdelrahim, H. Abdelmunim, J. Graham, and A. Farag. Novel variational approach for the perspective shape from shading problem using calibrated images. In *Proc. IEEE International Conference on Image Processing*, pages 2562–2566, 2013. (Cited on pages 7, 8, 9, 11, 121, 161, 162, 181, 220, 221, and 247).

[2] A. S. Abdelrahim. *Three-Dimensional Modeling of the Human Jaw/Teeth Using Optics and Statistics*. PhD thesis, Department of Electrical and Computer Engineering, University of Louisville, Louisville, Kentucky, USA, 2014. (Cited on pages 8 and 162).

[3] A. S. Abdelrahim, M. A. Abdelrahman, H. Abdelmunim, A. Farag, and M. Miller. Novel image-based 3D reconstruction of the human jaw using shape from shading and feature descriptors. In *Proc. British Machine Vision Conference*, pages 41.1–41.11, 2011. (Cited on page 1).

[4] S. Agarwal, Y. Furukawa, N. Snavely, I. Simon, B. Curless, S. M. Seitz, and R. Szeliski. Building rome in a day. *Communications of the ACM*, 54(10):105–112, 2011. (Cited on page 128).

[5] A. Agrawal, R. Raskar, and R. Chellappa. What is the range of surface reconstructions from a gradient field? In *Proc. European Conference on Computer Vision*, pages 578–591, 2006. (Cited on pages 130, 132, and 161).

[6] A. H. Ahmed and A. A. Farag. A new formulation for shape from shading for non-Lambertian surfaces. In *Proc. IEEE Conference on Computer Vision and Pattern Recognition*, pages 1817–1824, 2006. (Cited on pages 4, 10, 13, 19, 59, 66, 76, 78, 79, 81, 82, 84, 86, 87, 91, 92, 93, 102, 107, 115, and 222).

[7] A. H. Ahmed and A. A. Farag. Shape from shading under various imaging conditions. In *Proc. IEEE Conference on Computer Vision and Pattern Recognition*, pages 1–8, 2007. (Cited on pages 4, 76, and 160).

[8] A. H. Ahmed and A. A. Farag. Shape from shading for hybrid surfaces. In *Proc. IEEE International Conference on Image Processing*, pages 525–528, 2007. (Cited on page 160).

[9] J. C. Alexander and J. A. Yorke. The homotopy continuation method: numerically implementable topological procedures. *Transactions of the American Mathematical Society*, 242:271–284, 1978. (Cited on pages 11, 180, 191, and 199).

[10] E. L. Allgower and K. Georg. *Numerical Continuation Methods: An Introduction*. Springer, 1990. (Cited on pages 11, 180, 191, and 199).

[11] T. M. Apostol. *Calculus*. John Wiley and Sons, 1967. (Cited on page 24).

[12] V. I. Arnold. *Mathematical Methods of Classical Mechanics*. Springer, 1989. (Cited on page 20).

[13] M. Artin. *Algebra*. Prentice Hall, 1991. (Cited on page 99).

[14] G. Aubert and P. Kornprobst. *Mathematical Problems in Image Processing: Partial Differential Equations and the Calculus of Variations*. Springer, 2010. (Cited on pages 6, 19, and 24).

[15] G. Aubert and L. Vese. A variational method in image recovery. *SIAM Journal on Numerical Analysis*, 34(5):1948–1979, 1997. (Cited on pages 132 and 133).

[16] M. Bardi and I. Capuzzo-Dolcetta. *Optimal Control and Viscosity Solutions of Hamilton-Jacobi-Bellman Equations*. Birkhäuser, 2008. (Cited on pages 20, 26, 32, 36, 38, 42, and 85).

[17] G. Barles. *Solutions de viscosité des équations de Hamilton-Jacobi*. Springer, 1994. (Cited on pages 32 and 42).

[18] G. Barles. An introduction to the theory of viscosity solutions for first-order Hamilton-Jacobi equations and applications. In Y Achdou, G. Barles, H. Ishii, and G. L. Litvinov, editors, *Hamilton-Jacobi Equations: Approximations, Numerical Analysis and Applications*, pages 49–109. Springer, 2013. (Cited on page 25).

[19] J. T. Barron and J. Malik. High-frequency shape and albedo from shading using natural image statistics. In *Proc. IEEE Conference on Computer Vision and Pattern Recognition*, pages 2521–2528, 2011. (Cited on page 181).

[20] J. T. Barron and J. Malik. Shape, albedo, and illumination from a single image of an unknown object. In *Proc. IEEE Conference on Computer Vision and Pattern Recognition*, pages 334–341, 2012. (Cited on pages 181, 222, and 223).

[21] J. T. Barron and J. Malik. Color constancy, intrinsic images, and shape estimation. In *Proc. European Conference on Computer Vision*, pages 57–70, 2012. (Cited on page 181).

[22] J. T. Barron and J. Malik. Shape, illumination, and reflectance from shading. *IEEE Transactions on Pattern Analysis and Machine Intelligence*, 37(8):1670–1687, 2015. (Cited on pages 7, 222, and 223).

[23] H. G. Barrow and J. M. Tenenbaum. Recovering intrinsic scene characteristics from images. In Hanson A. and E. Riseman, editors, *Computer Vision Systems*, pages 3–26. Academic Press, 1978. (Cited on page 222).

[24] T. Basha, Y. Moses, and N. Kiryati. Multi-view scene flow estimation: A view centered variational approach. In *Proc. IEEE Conference on Computer Vision and Pattern Recognition*, pages 1506–1513, 2010. (Cited on pages 11, 160, and 221).

[25] T. Basha, Y. Moses, and N. Kiryati. Multi-view scene flow estimation: A view centered variational approach. *International Journal of Computer Vision*, 101(1): 6–21, 2013. (Cited on pages 11, 160, and 221).

[26] R. Basri and D. Jacobs. Lambertian reflectance and linear subspaces. In *Proc. IEEE International Conference on Computer Vision*, pages 383–390, 2001. (Cited on page 222).

[27] R. Basri and D. W. Jacobs. Lambertian reflectance and linear subspaces. *IEEE Transactions on Pattern Analysis and Machine Intelligence*, 25(2):218–233, 2003. (Cited on page 222).

[28] R. Basri, D. Jacobs, and I. Kemelmacher. Photometric stereo with general, unknown lighting. *International Journal of Computer Vision*, 72(3):239–257, 2007. (Cited on page 222).

[29] P. N. Belhumeur, D. J. Kriegman, and A. L. Yuille. The bas-relief ambiguity. In *Proc. IEEE Conference on Computer Vision and Pattern Recognition*, pages 1060–1066, 1997. (Cited on page 89).

[30] P. N. Belhumeur, D. J. Kriegman, and A. L. Yuille. The bas-relief ambiguity. *International Journal of Computer Vision*, 35(1):33–44, 1999. (Cited on page 89).

[31] R. Bellman. The theory of dynamic programming. *Bulletin of the American Mathematical Society*, 60(6):503–515, 1954. (Cited on pages 85 and 86).

[32] M. Bertero, T. A. Poggio, and V. Torre. Ill-posed problems in early vision. *Proceedings of the IEEE*, 76(8):869–889, 1988. (Cited on page 128).

[33] J. T. Betts. *Practical Methods for Optimal Control and Estimation Using Nonlinear Programming*. Society for Industrial and Applied Mathematics, 2010. (Cited on pages 138 and 165).

[34] G. L. Bilbro, W. E. Snyder, S. J. Garnier, and J. W. Gault. Mean field annealing: a formalism for constructing GNC-like algorithms. *IEEE Transactions on Neural Networks*, 3(1):131–138, 1992. (Cited on page 181).

[35] P. Billingsley. *Probability and Measure*. John Wiley and Sons, 1995. (Cited on page 40).

[36] A. Blake and A. Zisserman. *Visual reconstruction*. The MIT Press, 1987. (Cited on pages 181, 199, and 221).

[37] Blender. http://www.blender.org, (Last visited on 05/05/2015). (Cited on page 185).

[38] V. S. Borisov and S. Sorek. On monotonicity of difference schemes for computational physics. *SIAM Journal on Scientific Computing*, 25(5):1557–1584, 2004. (Cited on page 49).

[39] M. Born and E. Wolf. *Principles of Optics*. Cambridge University Press, 1999. (Cited on pages 44 and 56).

[40] A. G. Bors, E. R. Hancock, and R. C. Wilson. Terrain analysis using radar shape-from-shading. *IEEE Transactions on Pattern Analysis and Machine Intelligence*, 25 (8):974–992, 2003. (Cited on page 1).

[41] A. Bressan. Viscosity solutions of Hamilton-Jacobi equations and optimal control problems. http://www.math.psu.edu/bressan/PSPDF/HJ-lnotes.pdf, 2011. (Cited on pages 32 and 36).

[42] M. Breuß and Y. C. Ju. Shape from shading with specular highlights: Analysis of the Phong model. In *Proc. IEEE International Conference on Image Processing*, pages 9–12, 2011. (Cited on pages 13, 84, and 86).

[43] M. Breuß, E. Cristiani, J.-D. Durou, M. Falcone, and O. Vogel. Numerical algorithms for perspective shape from shading. *Kybernetika*, 46(2):207–225, 2010. (Cited on pages 48 and 181).

[44] M. Breuß, E. Cristiani, J.-D. Durou, M. Falcone, and O. Vogel. Perspective shape from shading: Ambiguity analysis and numerical approximations. *SIAM Journal on Imaging Sciences*, 5(1):311–342, 2012. (Cited on pages 3, 4, 48, 76, 91, 112, 121, and 166).

[45] M. J. Brooks and B. K. P. Horn. Shape and source from shading. In *Proc. International Joint Conference on Artificial Intelligence*, pages 932–936, 1985. (Cited on pages 8, 11, 131, 161, and 220).

[46] M. J. Brooks, W. Chojnacki, and R. Kozera. Impossible and ambiguous shading patterns. *International Journal of Computer Vision*, 7(2):119–126, 1992. (Cited on page 89).

[47] T. Brox and J. Malik. Large displacement optical flow: Descriptor matching in variational motion estimation. *IEEE Transactions on Pattern Analysis and Machine Intelligence*, 33(3):500–513, 2011. (Cited on page 181).

[48] T. Brox, A. Bruhn, N. Papenberg, and J. Weickert. High accuracy optical flow estimation based on a theory for warping. In *Proc. European Conference on Computer Vision*, pages 25–36, 2004. (Cited on pages 11, 15, 121, 128, 135, 181, 199, 200, 201, 205, 209, and 221).

[49] S. Bruvoll and M. Reimers. Spherical surface parameterization for perspective phape from shading. *Pattern Recognition Letters*, 33(1):33–40, 2012. (Cited on pages 4, 19, 102, and 160).

[50] M. P. D. Carmo. *Differential Geometry of Curves and Surfaces*. Prentice-Hall, 1976. (Cited on page 125).

[51] T. F. Chan and P. Mulet. On the convergence of the lagged diffusivity fixed point method in total variation image restoration. *SIAM Journal on Numerical Analysis*, 36(2):354–367, 1999. (Cited on pages 11, 15, and 205).

[52] T. F. Chan and L. A. Vese. Active contours without edges. *IEEE Transactions on Image Processing*, 10(2):266–277, 2001. (Cited on pages 121 and 128).

[53] P. Charbonnier, L. Blanc-Féraud, G. Aubert, and M. Barlaud. Two deterministic half-quadratic regularization algorithms for computed imaging. In *Proc. IEEE International Conference on Image Processing*, pages 168–172, 1994. (Cited on page 133).

[54] P. Charbonnier, L. Blanc-Féraud, G. Aubert, and M. Barlaud. Deterministic edge-preserving regularization in computed imaging. *IEEE Transactions on Image Processing*, 6(2):298–311, 1997. (Cited on pages 132, 133, and 222).

[55] J. H. Clark. Hierarchical geometric models for visible surface algorithms. *Communications of the ACM*, 19(10):547–554, 1976. (Cited on page 212).

[56] T. H. Cormen, C. E. Leiserson, R. L. Rivest, and C. Stein. *Introduction to Algorithms*. The MIT Press, 2009. (Cited on page 182).

[57] R. Courant. *Differential and Integral Calculus*. Interscience Publishers, Inc., 1959. (Cited on page 249).

[58] R. Courant and D. Hilbert. *Methods of Mathematical Physics*. Interscience Publishers, Inc., 1953. (Cited on pages 122, 123, 124, 126, 162, and 222).

[59] R. Courant and M. Isaacson, E. Rees. On the solution of nonlinear hyperbolic differential equations by finite differences. *Communications on Pure and Applied Mathematics*, 5(3):243–255, 1952. (Cited on page 85).

[60] F. Courteille, A. Crouzil, J.-D. Durou, and P. Gurdjos. Towards shape from shading under realistic photographic conditions. In *Proc. International Conference on Pattern Recognition*, pages 277–280, 2004. (Cited on pages 1, 3, 4, and 83).

[61] F. Courteille, A. Crouzil, J.-D. Durou, and P. Gurdjos. 3D-spline reconstruction using shape from shading: Spline from shading. *Image and Vision Computing*, 26(4):466–479, 2008. (Cited on pages 132 and 222).

[62] M. G. Crandall and P.-L. Lions. Condition d'unicité pour les solutions generalisées équations Hamilton-Jacobi de premier ordre. *Comptes Rendus de l'Académie des Sciences. Série I.*, 292(3):183–186, 1981. (Cited on page 39).

[63] M. G. Crandall and P.-L. Lions. Viscosity solutions of Hamilton-Jacobi equations. *Transactions of the American Mathematical Society*, 277(1):1–42, 1983. (Cited on pages 3, 10, 12, 19, 20, 25, 26, 32, 36, 39, 76, 102, 111, and 121).

[64] M. G. Crandall and P.-L. Lions. Two approximations of solutions of Hamilton-Jacobi equations. *Mathematics of Computation*, 43(167):1–19, 1984. (Cited on pages 3, 10, 12, 19, 20, 25, and 26).

[65] M. G. Crandall, L. C. Evans, and P.-L. Lions. Some properties of viscosity solutions of Hamilton-Jacobi equations. *Transactions of the American Mathematical Society*, 282(2):487–502, 1984. (Cited on pages 25, 32, and 39).

[66] M. G. Crandall, H. Ishii, and P.-L. Lions. User's guide to viscosity solutions of second order partial differential equations. *Bulletin of the American Mathematical Society*, 27(1):1–67, 1992. (Cited on page 25).

[67] E. Cristiani. *Fast Marching and Semi-Lagrangian Methods for Hamilton-Jacobi Equations with Applications*. PhD thesis, Department of Mathematics, SAPIENZA – Università di Roma, Rome, Italy, 2007. (Cited on pages 76, 85, 89, 112, and 121).

[68] E. Cristiani and M. Falcone. Fast semi-Lagrangian schemes for the eikonal equation and applications. *SIAM Journal on Numerical Analysis*, 45(5):1979–2011, 2007. (Cited on page 85).

[69] A. Crouzil, X. Descombes, and J.-D. Durou. A multiresolution approach for shape from shading coupling deterministic and stochastic optimization. *IEEE Transactions on Pattern Analysis and Machine Intelligence*, 25(11):1416–1421, 2003. (Cited on pages 129 and 130).

[70] P. Daniel and J.-D. Durou. From deterministic to stochastic methods for shape from shading. In *Proc. Asian Conference on Computer Vision*, pages 187–192, 2000. (Cited on page 129).

[71] K. Deguchi and T. Okatani. Shape reconstruction from an endoscope image by shape-from-shading technique for a point light source at the projection center. In *Proc. IEEE Workshop on Mathematical Methods in Biomedical Image Analysis*, pages 290–298, 1996. (Cited on pages 3 and 4).

[72] O. Demetz, M. Stoll, S. Volz, J. Weickert, and A. Bruhn. Learning brightness transfer functions for the joint recovery of illumination changes and optical flow. In *Proc. European Conference on Computer Vision*, pages 455–471, 2014. (Cited on pages 133, 135, and 181).

[73] E. W. Dijkstra. A note on two problems in connexion with graphs. *Numerische Mathematik*, 1(1):269–271, 1959. (Cited on page 44).

[74] Q. Y. Du, S. B. Chen, and T. Lin. An application of shape from shading. In *Proc. International Conference on Control, Automation, Robotics and Vision Conference*, pages 184–189, 2004. (Cited on page 1).

[75] P. Dupuis and J. Oliensis. Direct method for reconstructing shape from shading. In *Proc. IEEE Conference on Computer Vision and Pattern Recognition*, pages 453–458, 1992. (Cited on page 85).

[76] P. Dupuis and J. Oliensis. Shape from shading: Provably convergent algorithms and uniqueness results. In *Proc. European Conference on Computer Vision*, pages 259–268, 1994. (Cited on page 85).

[77] J.-D. Durou and F. Courteille. Integration of a normal field without boundary condition. In *Proc. International Workshop on Photometric Analysis For Computer Vision*, 2007. (Cited on page 138).

[78] J.-D. Durou and D. Piau. Ambiguous shape from shading with critical points. *Journal of Mathematical Imaging and Vision*, 12(2):99–108, 2000. (Cited on pages 3, 90, and 91).

[79] J.-D. Durou, M. Falcone, and M. Sagona. Numerical methods for shape-from-shading: A new survey with benchmarks. *Computer Vision and Image Understanding*, 109(1):22–43, 2008. (Cited on pages 1, 2, 3, 5, 9, 84, 87, 88, 94, 129, and 130).

[80] J.-D. Durou, J.-F. Aujol, and F. Courteille. Integrating the normal field of a surface in the presence of discontinuities. In *Proc. International Conference Energy Minimization Methods in Computer Vision and Pattern Recognition*, pages 261–273, 2009. (Cited on pages 130, 132, and 161).

[81] V. Estellers, J.-P. Thiran, and M. Gabrani. Surface reconstruction from microscopic images in optical lithography. *IEEE Transactions on Image Processing*, 23 (8):3560–3573, 2014. (Cited on pages 1 and 133).

[82] L. C. Evans. *Partial Differential Equations*. American Mathematical Society, 2010. (Cited on pages 20, 21, 22, 23, 24, 25, and 26).

[83] M. Falcone and R. Ferretti. *Semi-Lagrangian Approximation Schemes for Linear and Hamilton-Jacobi Equations*. Society for Industrial and Applied Mathematics, 2013. (Cited on page 85).

[84] H. Fassold, R. Danzl, K. Schindler, and Bischof. H. Reconstruction of archaeological finds using shape from stereo and shape from shading. In *Proc. Computer Vision Winter Workshop*, pages 21–30, 2004. (Cited on page 1).

[85] R. P. Feynman. *The Feynman Lectures on Physics*. Addison Wesley Longman, 1970. (Cited on page 45).

[86] D. J. Field. Relations between the statistics of natural images and the response properties of cortical cells. *Journal of the Optical Society of America A*, 4(12): 2379–2394, 1987. (Cited on page 7).

[87] D. A. Forsyth and J. Ponce. *Computer Vision : A Modern Approach*. Pearson, 2012. (Cited on page 1).

[88] S. P. Frankel. Convergence rates of iterative treatments of partial differential equations. *Mathematics of Computation*, 4(30):65–75, 1950. (Cited on page 208).

[89] R. T. Frankot and R. Chellappa. A method for enforcing integrability in shape from shading algorithms. *IEEE Transactions on Pattern Analysis and Machine Intelligence*, 10(4):439–451, 1988. (Cited on pages 5, 6, 8, 11, 85, 113, 121, 129, 130, 131, 161, and 220).

[90] S. Fučík, A. Kratochvíl, and J. Ečas. Kačanov-Galerkin method. *Commentationes Mathematicae Universitatis Carolinae*, 14(4):651–659, 1973. (Cited on page 205).

[91] S. Fučik, A. Kratochvíl, and J. Nečas. Kačanov's method and its application. *Revue Roumaine de Mathématiques Pures et Appliquées*, 20(8):907–916, 1975. (Cited on page 205).

[92] S. Galliani, M. Breuß, and Y. C. Ju. Fast and robust surface normal integration by a discrete eikonal equation. In *Proc. British Machine Vision Conference*, pages 106.1–106.11, 2012. (Cited on pages 49, 130, 132, and 161).

[93] S. Galliani, Y. C. Ju, M. Breuß, and A. Bruhn. Generalised perspective shape from shading in spherical coordinates. In *Proc. International Conference on Scale Space and Variational Methods in Computer Vision*, pages 222–233, 2013. (Cited on pages 4, 9, 13, 19, 87, 94, 101, and 115).

[94] Gastrolab. http://www.gastrolab.net, (Last visited on 05/05/2015). (Cited on page 115).

[95] I. M. Gelfand and S. V. Fomin. *Calculus of Variations*. Dover Publications, 2000. (Cited on pages 122 and 125).

[96] D. Geman and G. Reynolds. Constrained restoration and the recovery of discontinuities. *IEEE Transactions on Pattern Analysis and Machine Intelligence*, 14(3):367–383, 1992. (Cited on page 133).

[97] D. Geman and C. Yang. Nonlinear image recovery with half-quadratic regularization. *IEEE Transactions on Image Processing*, 4(7):932–946, 1995. (Cited on page 133).

[98] D. Gilbarg and N. S. Trudinger. *Elliptic Partial Differential Equations of Second Order*. Springer, 1977. (Cited on page 26).

[99] A. Gilchrist. *Seeing Black and White*. Oxford University Press, 2006. (Cited on page 1).

[100] F. Gozzi. Global regular solutions of second order Hamilton–Jacobi equations in Hilbert spaces with locally Lipschitz nonlinearities. *Journal of Mathematical Analysis and Applications*, 198(2):399–443, 1996. (Cited on page 20).

[101] F. Gozzi, E. Rouy, and A. Swiech. Second order Hamilton–Jacobi equations in Hilbert spaces and stochastic boundary control. *SIAM Journal on Control and Optimization*, 38(2):400–430, 2000. (Cited on page 20).

[102] B. Grieger. Shading under Titan's sky. *Planetary and Space Science*, 53(5):577–585, 2005. (Cited on page 1).

[103] R. Grosse, M. K. Johnson, E. H. Adelson, and W. T. Freeman. Ground truth dataset and baseline evaluations for intrinsic image algorithms. In *Proc. IEEE International Conference on Computer Vision*, pages 2335–2342, 2009. (Cited on page 222).

[104] J. Hadamard. Sur les problèmes aux dérivées partielles et leur signification physique. *Princeton University Bulletin*, 13:49–52, 1902. (Cited on page 24).

[105] J. Hadamard. *Lectures on Cauchy Problem in Linear Partial Differential Equations*. Yale University Press, 1923. (Cited on pages 24 and 38).

[106] D. Hafner, C. Schroers, and J. Weickert. Introducing maximal anisotropy into second order coupling models. In *Proc. German Conference on Pattern Recognition*, pages 79–90, 2015. (Cited on page 222).

[107] P. R. Halmos. *Measure Theory*. Springer, 1950. (Cited on page 40).

[108] W. Han, S. Jensen, and I. Shimansky. The kačanov method for some nonlinear problems. *Applied Numerical Mathematics*, 24(1):57–79, 1997. (Cited on page 205).

[109] R. Hartley and A. Zisserman. *Multiple View Geometry in Computer Vision*. Cambrdige University Press, 2004. (Cited on pages 60 and 62).

[110] J. J. Helmsen, E. G. Puckett, P. Colella, and M. Dorr. Two new methods for simulating photolithography development in 3d. In *Proc. SPIE*, pages 253–261, 1996. (Cited on pages 12 and 44).

[111] N. J. Higham and M. R. Dennis. *The Princeton companion to applied mathematics*. Princeton University Press, 2015. (Cited on pages 138 and 165).

[112] J.-B. Hiriart-Urruty and C. Lemaréchal. *Convex Analysis and Minimization Algorithms I*. Springer, 1996. (Cited on page 36).

[113] J.-B. Hiriart-Urruty and C. Lemaréchal. *Convex Analysis and Minimization Algorithms II*. Springer, 1996. (Cited on page 36).

[114] J.-B. Hiriart-Urruty and C. Lemaréchal. *Fundamentals of Convex Analysis*. Springer, 2004. (Cited on page 36).

[115] D. D. Holm. *Geometric Mechanics*. Imperial College Press, 2011. (Cited on pages 44 and 56).

[116] B. K. J. Horn. *Shape from Shading: A Method for Obtaining the Shape of a Smooth Opaque Object from One View*. PhD thesis, Department of Electrical Engineering, Massachusetts Institute of Technology, Cambridge, Massachusetts, USA, 1970. (Cited on pages 2, 3, 4, 5, 85, 113, and 222).

[117] B. K. J. Horn. Obtaining shape from shading information. In P. H. Winston, editor, *The Psychology of Computer Vision*, pages 15–155. McGraw-Hill, 1975. (Cited on page 3).

[118] B. K. P. Horn. *Robot Vision*. The MIT Press, 1986. (Cited on pages 62, 63, and 64).

[119] B. K. P. Horn and M. J. Brooks. The variational approach to shape from shading. *Computer Vision, Graphics, and Image Processing*, 33(2):174–208, 1986. (Cited on pages 6, 7, 121, 129, 130, 131, 132, and 161).

[120] B. K. P. Horn and M. J. Brooks. *Shape from Shading*. The MIT Press, 1989. (Cited on pages 3 and 158).

[121] B. K. P. Horn and B. G. Schunck. Determining optical flow. *Artificial Intelligence*, 17(1-3):185–203, 1981. (Cited on pages 121 and 128).

[122] B. K. P. Horn and R. W. Sjoberg. Calculating the reflectance map. *Applied Optics*, 18(11):1770–1779, 1979. (Cited on pages 63, 129, and 131).

[123] J. Huang and D. Mumford. Statistics of natural images and models. In *Proc. IEEE Conference on Computer Vision and Pattern Recognition*, pages 541–547, 1999. (Cited on page 7).

[124] R. Huang and W. A. P. Smith. Shape-from-shading under complex natural illumination. In *Proc. IEEE International Conference on Image Processing*, pages 13–16, 2011. (Cited on page 222).

[125] K. Ikeuchi and B. K. P. Horn. Numerical shape from shading and occluding boundaries. *Artificial Intelligence*, 17(1-3):141–184, 1981. (Cited on pages 6, 8, 11, 131, 161, and 220).

[126] H. Ishii. A simple direct proof of uniqueness for solutions of the Hamilton-Jacobi equations of eikonal type. *American Mathematical Society*, 100(2):247–251, 1987. (Cited on page 42).

[127] D. G. Jankowski and S. W. Squyres. Sources of error in planetary photoclinometry. *Journal of Geophysical Research*, 96(E4):20907–20922, 1991. (Cited on page 3).

[128] M. K. Johnson and E. H. Adelson. Shape estimation in natural illumination. In *Proc. IEEE Conference on Computer Vision and Pattern Recognition*, pages 2553–2560, 2011. (Cited on page 223).

[129] Y. C. Ju, M Breuß, A. Bruhn, and S. Galliani. Shape from shading for rough surfaces: Analysis of the Oren-Nayar model. In *Proc. British Machine Vision Conference*, pages 104.1–104.11, 2012. (Cited on pages 9, 13, and 86).

[130] Y. C. Ju, S. Tozza, M. Breuß, A. Bruhn, and A. Kleefeld. Generalised perspective shape from shading with Oren-Nayar reflectance. In *Proc. British Machine Vision Conference*, pages 42.1–42.11, 2013. (Cited on pages 4, 9, 13, 19, 87, and 94).

[131] Y. C. Ju, A. Bruhn, and M. Breuß. Variational perspective shape from shading. In *Proc. International Conference on Scale Space and Variational Methods in Computer Vision*, pages 538–550, 2015. (Cited on pages 5, 8, 9, 14, 121, 128, 129, 130, 131, 132, 133, 160, 162, 215, and 247).

[132] Y. C. Ju, D. Maurer, M. Breuß, and A. Bruhn. *Direct variational perspective shape from shading with Cartesian depth parametrisation*, pages 43–72. Springer, 2016. (Cited on pages 5, 8, 9, 14, 48, 128, 154, 158, 162, 166, 195, 196, 199, 200, 201, 209, 213, and 215).

[133] C. Y. Kao, S. Osher, and J. Qian. Lax-Friedrichs sweeping scheme for static Hamilton-Jacobi equations. *Journal of Computational Physics*, 196:367–391, 2004. (Cited on page 86).

[134] L. M. Kačanov. Variational methods of solution of plasticity problems. *Journal of Applied Mathematics and Mechanics*, 23(3):880–883, 1959. (Cited on page 205).

[135] J. Kačur, J. Nečas, J. Polák, and J. Souček. Convergence of a method for solving the magnetostatic field in nonlinear media. *Aplikace Matematiky*, 13(6):456–465, 1968. (Cited on page 205).

[136] R. Kimmel and A. M. Bruckstein. Tracking level sets by level sets: A method for solving the shape from shading problem. *Computer Vision and Image Understanding*, 62(1):47–58, 1995. (Cited on page 3).

[137] R. Kimmel and J. A. Sethian. Computing geodesic paths on manifolds. *Proceedings of the National Academy of Sciences*, 95(15):8431–8435, 1998. (Cited on page 4).

[138] R. Kimmel and J. A. Sethian. Optimal algorithm for shape from shading and path planning. *Journal of Mathematical Imaging and Vision*, 14(3):237–244, 2001. (Cited on pages 46 and 55).

[139] R. Kimmel, K. Siddiqi, B. B. Kimia, and A. M. Bruckstein. Shape from shading: Level set propagation and viscosity solutions. *International Journal of Computer Vision*, 16:107–133, 1995. (Cited on pages 3 and 4).

[140] S. Kirkpatrick, C. D. Gelatt, and M. P. Vecchi. Optimization by simulated annealing. *Science*, 220(4598):671–680, 1983. (Cited on page 181).

[141] D. A. Kleffner and V. S. Ramachandran. On the perception of shape from shading. *Perception and Psychophysics*, 52(1):18–36, 1992. (Cited on page 89).

[142] S. Koike. *A Beginner's Guide to the Theory of Viscosity Solutions*. The Mathematical Society of Japan, 2014. (Cited on pages 19, 24, 25, 26, 27, 32, and 42).

[143] R. Kozera. A note on existence and uniqueness in shape from shading. In *Proc. IEEE International Conference on Computer Vision*, pages 507–511, 1993. (Cited on page 89).

[144] R. Kozera. On complete integrals and uniqueness in shape from shading. *Applied Mathematics and Computation*, 73(1):1–37, 1995. (Cited on page 89).

[145] R. Kozera. Uniqueness in shape from shading revisited. *Journal of Mathematical Imaging and Vision*, 7(2):123–138, 1997. (Cited on page 89).

[146] S. N. Kružkov. Generalized solutions of the Hamilton-Jacobi equations of eikonal type. I. Formulation of the problems; existence, uniqueness and stability theorems; some properties of the solutions. *Mathematics of the USSR-Sbornik*, 27(3):406–446, 1975. (Cited on page 39).

[147] J. F. Lalonde, A. A. Efros, and S. G. Narasimhan. Estimating natural illumination from a single outdoor image. In *Proc. IEEE International Conference on Computer Vision*, pages 183–190, 2009. (Cited on page 223).

[148] J. H. Lambert. *Photometria, sive de Mensura et Gradibus Luminis, Colorum et Umbrae*. Eberhard Klett, 1760. (Cited on pages 4, 13, and 64).

[149] Y. G. Leclerc and A. F. Bobick. The direct computation of height from shading. In *Proc. IEEE Conference on Computer Vision and Pattern Recognition*, pages 552–558, 1991. (Cited on pages 6 and 129).

[150] K. M. Lee and C.-C. J. Kuo. Shape from shading with perspective projection. *Computer Vision, Graphics, and Image Processing: Image Understanding*, 59(2): 202–212, 1994. (Cited on page 7).

[151] K. M. Lee and C.-C. J. Kuo. Shape from shading with a generalized reflectance map model. *Computer Vision and Image Understanding*, 67(2):143–160, 1997. (Cited on page 7).

[152] R. J. LeVeque. *Numerical Methods for Conservation Laws*. Birkhäuser, 1992. (Cited on pages 25 and 49).

[153] R. J. LeVeque. *Finite Volume Methods for Hyperbolic Problems*. Cambridge University Press, 2002. (Cited on page 49).

[154] Q. Lin. *Enhancement, Extraction, and Visualization of 3D Volume Data*. PhD thesis, Linköping University, Linköping, Sweden, 2003. (Cited on page 49).

[155] P.-L. Lions. *Generalized Solutions of Hamilton-Jacobi Equations*. Pitman Publishing, 1982. (Cited on pages 20, 26, and 42).

[156] M. Lysaker, A. Lundervold, and X.-C. Tai. Noise removal using fourth-order partial differential equation with applications to medical magnetic resonance images in space and time. *IEEE Transactions on Image Processing*, 12(12):1579–1590, 2003. (Cited on page 133).

[157] D. Marr and E. Hildreth. Theory of edge detection. *Proceedings of the Royal Society of London B: Biological Sciences*, 207(1167):187–217, 1980. (Cited on page 133).

[158] J. Marroquin, S. Mitter, and T. Poggio. Probabilistic solution of ill-posed problems in computational vision. *Journal of the American Statistical Association*, 82(397):76–89, 1987. (Cited on page 128).

[159] S. Marschner and P. Shirley. *Fundamentals of Computer Graphics*. A K Peters/CRC Press, 2015. (Cited on page 66).

[160] D. Maurer, Y. C. Ju, M. Breuß, and A. Bruhn. An efficient linearisation approach for variational perspective shape from shading. In *Proc. German Conference on Pattern Recognition*, pages 249–261, 2015. (Cited on pages 5, 9, 14, 128, 200, and 201).

[161] D. Maurer, Y. C. Ju, M. Breuß, and A. Bruhn. Combining shape from shading and stereo: A variational approach for the joint estimation of depth, illumination and albedo. In *Proc. British Machine Vision Conference*, pages 76.1–76.14, 2016. (Cited on pages 12, 197, 218, and 222).

[162] R. Mecca, E. Rodolà, and D. Cremers. Analysis of surface parametrizations for modern photometric stereo modeling. In *Proc. International Conference on Quality Control by Artificial Vision*, 2015. (Cited on pages 121 and 160).

[163] A. Meister. *Numerik linearer Gleichungssysteme*. Springer, 2015. (Cited on page 208).

[164] H. Mobahi and J. W. Fisher. A theoretical analysis of optimization by Gaussian continuation. In *Proc. AAAI Conference on Artificial Intelligence*, pages 1205–1211, 2015. (Cited on page 181).

[165] H. Mobahi and J. W. Fisher. Coarse-to-fine minimization of some common nonconvexities. In *Proc. International Conference Energy Minimization Methods in Computer Vision and Pattern Recognition*, pages 71–84, 2015. (Cited on page 181).

[166] H. Mobahi, C. L. Zitnick, and M. Yi. Seeing through the blur. In *IEEE Conference on Computer Vision and Pattern Recognition*, pages 1736–1743, 2012. (Cited on page 181).

[167] P. Mountney, D. Stoyanov, and G. Z. Yang. Three-dimensional tissue deformation recovery and tracking. *IEEE Signal Processing Magazine*, 27(4):14–24, 2010. (Cited on page 1).

[168] D. Mumford and J. Shah. Optimal approximations by piecewise smooth functions and associated variational problems. *Communications on Pure and Applied Mathematics*, 42(5):577–685, 1989. (Cited on pages 121 and 128).

[169] S. K. Nayar. Shape recovery methods for visual inspection. In *Proc. IEEE Workshop on Applications of Computer Vision*, pages 136–145, 1992. (Cited on page 1).

[170] S. K. Nayar and M. Oren. Visual appearance of matte surfaces. *Science*, 267 (5201):1153–1156, 1995. (Cited on page 69).

[171] T. Okatani and K. Deguchi. Shape reconstruction from an endoscope image by shape from shading technique for a point light source at the projection center. *Computer Vision and Image Understanding*, 66(2):119–131, 1997. (Cited on pages 1, 3, 4, 63, 70, 71, and 115).

[172] T. Okatani and K. Deguchi. On the classification of singular points for the global shape from shading problem: A study of the constraints imposed by isophotes. In *Proc. Asian Conference on Computer Vision*, pages 48–55, 1998. (Cited on pages 3, 90, and 91).

[173] J. Oliensis. Shape from shading as a partially well-constrained problem. In *Proc. IEEE Conference on Computer Vision and Pattern Recognition*, pages 559–564, 1991. (Cited on pages 85, 89, 91, and 132).

[174] J. Oliensis. Shape from shading as a partially well-constrained problem. *Computer Vision, Graphics, and Image Processing: Image Understanding*, 54(2): 163–183, 1991. (Cited on pages 85, 89, 91, and 132).

[175] J. Oliensis and P. Dupuis. Direct method for reconstructing shape from shading. In *Proc. SPIE*, volume 1570, pages 116–128, 1991. (Cited on page 85).

[176] J. Oliensis and P. Dupuis. A global algorithm for shape from shading. In *Proc. IEEE International Conference on Computer Vision*, pages 692–701, 1993. (Cited on page 85).

[177] J. A. Oliensis. Uniqueness in shape from shading. *International Journal of Computer Vision*, 6(2):75–104, 1991. (Cited on pages 85, 89, and 91).

[178] M. Oren and S. Nayar. Generalization of the Lambertian model and implications for machine vision. *International Journal of Computer Vision*, 14(3):227–251, 1995. (Cited on pages 4, 12, 13, 65, 66, 67, 68, 69, 78, 200, and 219).

[179] M. Oren and S. K. Nayar. Diffuse reflectance from rough surfaces. In *Proc. IEEE Conference on Computer Vision and Pattern Recognition*, pages 763–764, 1993. (Cited on pages 4, 67, 78, and 200).

[180] M. Oren and S. K. Nayar. Seeing beyond Lambert's law. In *Proc. European Conference on Computer Vision*, pages 269–280, 1994. (Cited on pages 4 and 67).

[181] M. Oren and S. K. Nayar. Generalization of Lambert's reflectance model. In *Proc. International Conference and Exhibition on Computer Graphics and Interactive Techniques*, pages 239–246, 1994. (Cited on pages 4, 65, 66, and 67).

[182] S. Osher. A level set formulation for the solution of the Dirichlet problem for Hamilton-Jacobi equations. *SIAM Journal on Mathematical Analysis*, 24(5): 1145–1152, 1993. (Cited on pages 4, 10, 13, and 86).

[183] D. N. Ostrov. Viscosity solutions and convergence of monotone schemes for synthetic aperture radar shape-from-shading equations with discontinuous intensities. *SIAM Journal on Applied Mathematics*, 59(6):2060–2085, 1999. (Cited on page 1).

[184] G. Oxholm and K. Nishino. Shape and reflectance from natural illumination. In *Proc. European Conference on Computer Vision*, pages 528–541, 2012. (Cited on page 223).

[185] R. O'Hara and D. Barnes. A new shape from shading technique with application to Mars express HRSC images. *ISPRS Journal of Photogrammetry and Remote Sensing*, 67:27–34, 2012. (Cited on page 3).

[186] A. Pentland. Shape information from shading: A theory about human perception. In *Proc. IEEE International Conference on Computer Vision*, pages 404–413, 1988. (Cited on page 7).

[187] A. P. Pentland. Local shading analysis. *IEEE Transactions on Pattern Analysis and Machine Intelligence*, 6(2):170–187, 1984. (Cited on page 89).

[188] P. Perona and J. Malik. Scale-space and edge detection using anisotropic diffusion. *IEEE Transactions on Pattern Analysis and Machine Intelligence*, 12(7): 629–639, 1990. (Cited on page 222).

[189] B. T. Phong. Illumination for computer generated pictures. *Communications of the ACM*, 18(6):311–317, 1975. (Cited on pages 4, 12, 13, 65, 76, 93, and 200).

[190] Y. Pinchover and J. Rubinstein. *An Introduction to Partial Differential Equations*. Cambridge University Press, 2005. (Cited on page 22).

[191] T. Pock, D. Cremers, H. Bischof, and A. Chambolle. Global solutions of variational models with convex regularization. *SIAM Journal on Imaging Sciences*, 3(4):1122–1145, 2010. (Cited on page 132).

[192] T. Poggio, V. Torre, and C. Koch. Computational vision and regularization theory. *Nature*, 317(6035):314–319, 1985. (Cited on page 128).

[193] E. Prados. *Application of the theory of the viscosity solutions to the Shape From Shading problem*. PhD thesis, University of Nice Sophia Antipolis, Nice, France, 2004. (Cited on pages 4, 63, 64, 65, 75, 86, 87, 88, 90, and 91).

[194] E. Prados and O. Faugeras. Perspective shape from shading and viscosity solutions. In *Proc. IEEE International Conference on Computer Vision*, pages 826–831, 2003. (Cited on pages 3 and 4).

[195] E. Prados and O. Faugeras. Shape from shading: a well-posed problem? In *Proc. IEEE Conference on Computer Vision and Pattern Recognition*, pages 870–877, 2005. (Cited on pages 4, 10, 13, 14, 19, 59, 70, 71, 73, 76, 82, 84, 86, 87, 88, 89, 91, 93, 112, 115, 121, 130, 131, 154, 156, 160, 194, 195, 196, 213, 220, 222, and 247).

[196] E. Prados and O. D. Faugeras. Unifying approaches and removing unrealistic assumptions in shape from shading: Mathematics can help. In *Proc. European Conference on Computer Vision*, pages 141–154, 2004. (Cited on pages 4, 83, and 89).

[197] E. Prados, O. D. Faugeras, and E. Rouy. Shape from shading and viscosity solutions. In *Proc. European Conference on Computer Vision*, pages 790–804, 2002. (Cited on pages 82 and 83).

[198] E. Prados, F. Camilli, and O. Faugeras. A unifying and rigorous shape from shading method adapted to realistic data and applications. *Journal of Mathematical Imaging and Vision*, 25(3):307–328, 2006. (Cited on page 196).

[199] E. Prados, F. Camilli, and O. Faugeras. A viscosity solution method for shape-from-shading without image boundary data. *ESAIM: Mathematical Modelling and Numerical Analysis*, 40(2):393–412, 2006. (Cited on page 88).

[200] J. Qian, Y.-T. Zhang, and H.-K. Zhao. A fast sweeping method for static convex Hamilton–Jacobi equations. *Journal of Scientific Computing*, 31(1):237–271, 2007. (Cited on pages 10, 13, 86, and 94).

[201] Y. Quéau. *Reconstruction tridimensionnelle par stéréophotométrie*. PhD thesis, Université de Toulouse, Toulouse, France, 2015. (Cited on page 138).

[202] Y. Quéau and J.-D. Durou. Edge-preserving integration of a normal field: Weighted least-squares, TV and L^1 approaches. In *Proc. International Conference on Scale Space and Variational Methods in Computer Vision*, pages 576–588, 2015. (Cited on pages 130 and 138).

[203] H. Ragheb and E. R. Hancock. Surface normals and height from non-lambertian image data. In *Proc. International Symposium on 3D Data Processing, Visualization and Transmission*, pages 18–25, 2004. (Cited on page 4).

[204] H. Ragheb and E. R. Hancock. Surface radiance correction for shape from shading. *Pattern Recognition*, 38(10):1574–1595, 2005. (Cited on pages 4 and 115).

[205] M. A. Rajabi and J. A. R. Blais. Densification of digital terrain elevations using shape from shading with single satellite imagery. In *Proc. International Conference on Computational Science*, pages 3–12, 2001. (Cited on page 1).

[206] V. S. Ramachandran. Perception of shape from shading. *Nature*, 331(6152): 163–166, 1988. (Cited on page 89).

[207] V. S. Ramachandran. Perceiving shape from shading. *Scientific American*, 259 (2):76–83, 1988. (Cited on page 89).

[208] R. Ramamoorthi and P. Hanrahan. An efficient representation for irradiance environment maps. In *Proc. ACM Conference on Computer Graphics and Interactive Techniques*, pages 497–500, 2001. (Cited on page 222).

[209] J. Rauch. *Partial Differential Equations*. Springer, 1991. (Cited on page 20).

[210] The Stanford 3D Scanning Repository. http://graphics.stanford.edu/data/3Dscanrep/, (Last visited on 05/05/2015). (Cited on page 185).

[211] S. Richter and R. de Carlo. Continuation methods: Theory and applications. *IEEE Transactions on Circuits and Systems*, 30(6):347–352, 1983. (Cited on pages 11, 180, 182, 190, 191, and 199).

[212] S. R. Richter and S. Roth. Discriminative shape from shading in uncalibrated illumination. In *Proc. IEEE Conference on Computer Vision and Pattern Recognition*, pages 1128–1136, 2015. (Cited on page 223).

[213] R. F. Riesenfeld. Homogeneous coordinates and projective planes in computer graphics. *IEEE Computer Graphics and Applications*, 1(1):50–55, 1981. (Cited on page 60).

[214] T. Rindfleisch. Photometric method for lunar topography. *Photogrammetric Engineering*, 32(2):262–277, 1966. (Cited on pages 1 and 3).

[215] M. Rivera and J. L. Marroquin. Adaptive rest condition potentials: Second order edge-preserving regularization. In *Proc. European Conference on Computer Vision*, pages 113–127, 2002. (Cited on page 133).

[216] L. Robert and R. Deriche. Dense depth map reconstruction: A minimization and regularization approach which preserves discontinuities. In *Proc. European Conference on Computer Vision*, pages 439–451, 1996. (Cited on pages 11, 160, and 221).

[217] R. T. Rockafellar. *Convex Analysis*. Princeton University Press, 1970. (Cited on page 36).

[218] C. Rother, M. Kiefel, L. Zhang, B. Schölkopf, and P. V. Gehler. Recovering intrinsic images with a global sparsity prior on reflectance. In *Proc. Advances in Neural Information Processing Systems*, pages 765–773, 2011. (Cited on page 223).

[219] E. Rouy and A. Tourin. A viscosity solutions approach to shape-from-shading. *SIAM Journal on Numerical Analysis*, 29(3):867–884, 1992. (Cited on pages 3, 4, 7, 11, 12, 44, 46, 49, 55, 56, 76, 82, 83, 85, 86, 89, 90, 91, 112, 139, 199, 200, and 221).

[220] L. I. Rudin, S. Osher, and E. Fatemi. Nonlinear total variation based noise removal algorithms. *Physica D: Nonlinear Phenomena*, 60(1-4):259–268, 1992. (Cited on pages 121 and 214).

[221] Y. Saad. *Iterative Methods for Sparse Linear Systems*. Society for Industrial and Applied Mathematics, 2003. (Cited on page 208).

[222] X. Saint Raymond. *Elementary introduction to the theory of pseudodifferential operators*. CRC Press, 1991. (Cited on page 20).

[223] D. Samaras and D. Metaxas. Incorporating illumination constraints in deformable models for shape from shading and light direction estimation. *IEEE Transactions on Pattern Analysis and Machine Intelligence*, 25(2):247–264, 2003. (Cited on page 4).

[224] D. Schieborn. *Viscosity Solutions of Hamilton-Jacobi Equations of Eikonal Type on Ramified Spaces*. PhD thesis, Eberhard-Karls-Universität Tübingen, Tübingen, Germany, 2006. (Cited on page 26).

[225] R. Sedgewick and K. D. Wayne. *Algorithms*. Addison-Wesley, 2011. (Cited on pages 44 and 57).

[226] J. A. Sethian. Theory, algorithms, and applications of level set methods for propagating interfaces. *Acta Numerica*, 5:309–395, 1996. (Cited on pages 12, 39, and 44).

[227] J. A. Sethian. A fast marching level set method for monotonically advancing fronts. *Proceedings of the National Academy of Sciences*, 93(4):1591–1595, 1996. (Cited on pages 46 and 93).

[228] J. A. Sethian. Fast-marching level-set methods for three-dimensional photolithography development. In *Proc. SPIE*, pages 262–272, 1996. (Cited on page 85).

[229] J. A. Sethian. *Level Set Methods and Fast Marching Methods*. Cambridge University Press, 1999. (Cited on pages 7, 19, 44, 45, 46, 49, 55, 56, 57, 85, 111, and 113).

[230] J. A. Sethian. Fast marching methods. *SIAM Review*, 41(2):199–235, 1999. (Cited on pages 3, 44, and 49).

[231] W. A. Strauss. *Partial Differential Equations : An Introduction*. Wiley, 2008. (Cited on pages 22 and 49).

[232] D. Sun, S. Roth, and M. J. Black. Secrets of optical flow estimation and their principles. In *Proc. IEEE Conference on Computer Vision and Pattern Recognition*, pages 2432–2439, 2010. (Cited on page 181).

[233] R. Szeliski. Fast shape from shading. *Computer Vision, Graphics, and Image Processing: Image Understanding*, 53(2):129–153, 1991. (Cited on pages 128, 129, and 130).

[234] R. Szeliski. *Computer Vision: Algorithms and Applications*. Springer, 2010. (Cited on page 1).

[235] A. Tankus. *Perspective Shape-from-Shading*. PhD thesis, School of Computer Science, Tel-Aviv University, Tel Aviv, Israel, 2004. (Cited on page 3).

[236] A. Tankus, N. Sochen, and Y. Yeshurun. A new perspective [on] shape-from-shading. In *Proc. IEEE International Conference on Computer Vision*, pages 862–869, 2003. (Cited on pages 3, 4, and 19).

[237] A. Tankus, N. Sochen, and Y. Yeshurun. Perspective shape-from-shading by fast marching. In *Proc. IEEE Conference on Computer Vision and Pattern Recognition*, pages 43–49, 2004. (Cited on pages 1, 83, 85, and 160).

[238] A. Tankus, N. Sochen, and Y. Yeshurun. Shape-from-shading under perspective projection. *International Journal of Computer Vision*, 63(1):21–43, 2005. (Cited on pages 3, 115, and 247).

[239] S. Teboul, L. Blanc-Feraud, G. Aubert, and M. Barlaud. Variational approach for edge-preserving regularization using coupled PDEs. *IEEE Transactions on Image Processing*, 7(3):387–397, 1998. (Cited on page 133).

[240] D. Terzopoulos. Efficient multiresolution algorithms for computing lightness, shape-from-shading, and optical flow. In *Proc. of the Fourth National Conference on Artificial Intelligence*, pages 314–317, 1984. (Cited on page 181).

[241] D. Terzopoulos. Image analysis using multigrid relaxation methods. *IEEE Transactions on Pattern Analysis and Machine Intelligence*, 8(2):129–139, 1986. (Cited on page 181).

[242] W. B. Thompson, R. W. Fleming, S. H. Creem-Regehr, and J. K. Stefanucci. *Visual perception for computer graphics*. A K Peters/CRC Press, 2011. (Cited on page 89).

[243] A. N. Tikhonov. Solution of incorrectly formulated problems and the regularization method. *Doklady Akademii Nauk SSSR*, 4:1035–1038, 1963. (Cited on page 128).

[244] A. N. Tikhonov and V. Y. Arsenin. *Solutions of Ill-posed Problems*. V. H. Winston and Sons, 1977. (Cited on page 128).

[245] K. E. Torrance and E. M. Sparrow. Theory for off-specular reflection from roughened surfaces. *Journal of the Optical Society of America*, 57(9):1105–1114, 1967. (Cited on page 67).

[246] S. Tozza and M. Falcone. Analysis and approximation of some shape-from-shading models for non-Lambertian surfaces. *Journal of Mathematical Imaging and Vision*, 55(2):153–178, 2016. (Cited on page 85).

[247] P.-S. Tsai and M. Shah. Shape from shading using linear approximation. *Image Vision Computing*, 12(8):487–498, 1994. (Cited on pages 7, 11, 165, and 200).

[248] Y.-H. R. Tsai, L.-T. Cheng, S. Osher, and H.-K. Zhao. Fast sweeping algorithms for a class of Hamilton–Jacobi equations. *SIAM Journal on Numerical Analysis*, 41(2):673–694, 2003. (Cited on pages 10, 13, and 86).

[249] J. N. Tsitsiklis. Efficient algorithms for globally optimal trajectories. *IEEE Transactions on Automatic Control*, 40(9):1528–1538, 1995. (Cited on pages 12, 44, and 86).

[250] J. van Diggelen. A photometric investigation of the slopes and the heights of the ranges of hills in the maria of the moon. *Bulletin of the Astronomical Institutes of the Netherlands Numerische Mathematik*, 11(423):283–289, 1951. (Cited on page 3).

[251] R. S. Varga. *Matrix Iterative Analysis*. Springer, 2000. (Cited on page 208).

[252] L. Vese. *Problèmes variationnels et EDP pour l'analyse d'images et l'évolution de courbes*. PhD thesis, Université de Nice Sophia-Antipolis, Nice, France, 1996. (Cited on pages 132 and 133).

[253] C. R. Vogel. *Computational Methods for Inverse Problems*. Society for Industrial and Applied Mathematics, 2002. (Cited on pages 11, 15, and 205).

[254] C. R. Vogel and M. E. Oman. Iterative methods for total variation denoising. *SIAM Journal on Scientific Computing*, 17(1):227–238, 1996. (Cited on pages 11, 15, 199, 201, 205, and 221).

[255] O. Vogel. *Perspective Shape from Shading: Models, Algorithms, and Applications*. PhD thesis, Department of Computer Science, Saarland University, Saarbrücken, Germany, 2010. (Cited on pages 65, 87, and 88).

[256] O. Vogel and E. Cristiani. Numerical schemes for advanced reflectance models for shape from shading. In *Proc. IEEE International Conference on Image Processing*, pages 5–8, 2011. (Cited on pages 10, 13, 86, 87, and 112).

[257] O. Vogel, A. Bruhn, J. Weickert, and S. Didas. Direct shape-from-shading with adaptive higher order regularisation. In *Proc. International Conference on Scale Space and Variational Methods in Computer Vision*, pages 871–882, 2007. (Cited on pages 6, 128, 129, 130, 133, and 161).

[258] O. Vogel, M. Breuß, and W. Weickert. Perspective shape from shading with non-Lambertian reflectance. In *Proc. German Conference on Pattern Recognition*, pages 517–526, 2008. (Cited on pages 4, 8, 13, 59, 65, 76, 77, 78, 79, 82, 84, 86, 91, 92, 93, and 115).

[259] O. Vogel, M. Breuß, T. Leichtweis, and J. Weickert. Fast shape from shading for Phong-type surfaces. In *Proc. International Conference on Scale Space and Variational Methods in Computer Vision*, pages 733–744, 2009. (Cited on pages 19, 86, 87, 91, 111, 112, 194, 195, 196, 213, 214, 215, 216, 217, and 222).

[260] J. von Neumann and R. D. Richtmyer. A method for the numerical calculation of hydrodynamic shocks. *Journal of Applied Physics*, 21(3):232–237, 1950. (Cited on page 26).

[261] O. von Stryk and R. Bulirsch. Direct and indirect methods for trajectory optimization. *Annals of Operations Research*, 37(1):357–373, 1992. (Cited on pages 138 and 165).

[262] G. Wang, W. Su, and F. Gao. A specular shape from shading by fast marching method. *Procedia Engineering*, 24:192–196, 2011. (Cited on page 85).

[263] G. J. Ward. Measuring and modeling anisotropic reflection. In *Proc. ACM Annual Conference on Computer Graphics and Interactive Techniques*, pages 265–272, 1992. (Cited on page 4).

[264] A. J. Weir. *Lebesgue Integration and Measure*. Cambridge University Press, 1973. (Cited on page 40).

[265] L. Wilson, J. S. Hampton, and H. C. Balen. Photoclinometry of terrestrial and planetary surfaces. In *Proc. Lunar and Planetary Science Conference*, pages 912–913, 1985. (Cited on page 3).

[266] R. C. Wilson and E. R. Hancock. A radar reflectance model for terrain analysis using shape from shading. In *Proc. International Conference on Image Analysis and Processing*, pages 868–873, 1999. (Cited on page 1).

[267] L. B. Wolff. On the relative brightness of specular and diffuse reflection. In *IEEE Conference on Computer Vision and Pattern Recognition*, pages 369–376, 1994. (Cited on page 4).

[268] L. B. Wolff. Diffuse-reflectance model for smooth dielectric surfaces. *Journal of the Optical Society of America A*, 11(11):2956–2968, 1994. (Cited on page 4).

[269] L. B. Wolff, S. K. Nayar, and M. Oren. Improved diffuse reflection models for computer vision. *International Journal of Computer Vision*, 30(1):55–71, 1998. (Cited on page 4).

[270] C. Wu, S. Narasimhan, and B. Jaramaz. A multi-image shape-from-shading framework for near-lighting perspective endoscopes. *International Journal of Computer Vision*, 86(2):211–228, 2010. (Cited on pages 1, 5, 7, 8, 9, 10, 121, 128, 130, 158, 161, 162, 164, 181, 220, and 247).

[271] C. Wu, B. Wilburn, Y. Matsushita, and C. Theobalt. High-quality shape from multi-view stereo and shading under general illumination. In *Proc. IEEE Conference on Computer Vision and Pattern Recognition*, pages 969–976, 2011. (Cited on pages 11, 153, 160, and 221).

[272] C. Wu, M. Zollhöfer, M. Niessner, M. Stamminger, S. Izadi, and C. Theobalt. Real-time shading-based refinement for consumer depth cameras. *ACM Transactions on Graphics*, 33(6):200:1–200:10, 2014. (Cited on page 160).

[273] D. Xu, Q. Duan, J. Zheng, J. Zhang, J. Cai, and T.-J. Cham. Recovering surface details under general unknown illumination using shading and coarse multi-view stereo. In *Proc. IEEE Conference on Computer Vision and Pattern Recognition*, pages 1526–1533, 2014. (Cited on pages 11, 153, 160, and 221).

[274] M. Ye, R. M. Haralick, and L. G. Shapiro. Estimating piecewise-smooth optical flow with global matching and graduated optimization. *IEEE Transactions on Pattern Analysis and Machine Intelligence*, 25(12):1625–1630, 2003. (Cited on page 181).

[275] D. Young. *Iterative methods for solving partial difference equations of elliptic type*. PhD thesis, Department of Mathematics, Harvard University, Cambridge, Massachusetts, USA, 1950. (Cited on page 208).

[276] D. Young. Iterative methods for solving partial difference equations of elliptic type. *Transactions of the American Mathematical Society*, 76(1):92–111, 1954. (Cited on page 208).

[277] S. Y. Yuen, Y. Y. Tsui, and C. K. Chow. A fast marching formulation of perspective shape from shading under frontal illumination. *Pattern Recognition Letters*, 28(7):806–824, 2007. (Cited on page 247).

[278] L. Zhang, A. M. Yip, and C. L. Tan. Shape from shading based on Lax-Friedrichs fast sweeping and regularization techniques with applications to document image restoration. In *Proc. IEEE Conference on Computer Vision and Pattern Recognition*, pages 1–8, 2007. (Cited on pages 1, 6, 8, 9, 10, 11, 121, 129, 130, 158, 161, 162, 164, 181, 220, 221, and 247).

[279] L. Zhang, A. M. Yip, and C. L. Tan. A restoration framework for correcting photometric and geometric distortions in camera-based document images. In *Proc. IEEE International Conference on Computer Vision*, pages 1–8, 2007. (Cited on pages 1 and 158).

[280] L. Zhang, A. M. Yip, M. S. Brown, and C. L. Tan. A unified framework for document restoration using inpainting and shape-from-shading. *Pattern Recognition*, 42(11):2961–2978, 2009. (Cited on page 1).

[281] R. Zhang, P.-S. Tsai, J. E. Cryer, and M. Shah. Shape from shading: a survey. *IEEE Transactions on Pattern Analysis and Machine Intelligence*, 21(8):439–451, 1999. (Cited on pages 1, 2, 3, 6, 7, 84, 128, and 222).

[282] H. Zhao. A fast sweeping method for eikonal equations. *Mathematics of Computation*, 74(250):603–627, 2005. (Cited on pages 46 and 55).

[283] Q. Zheng and R. Chellappa. Estimation of illuminant direction, albedo, and shape from shading. *IEEE Transactions on Pattern Analysis and Machine Intelligence*, 13(7):680–702, 1991. (Cited on page 132).

[284] D. Zoran, D. Krishnan, J. Bento, and W. T. Freeman. Shape and illumination from shading using the generic viewpoint assumption. In *Proc. Advances in Neural Information Processing Systems*, pages 226–234, 2014. (Cited on page 223).

APPENDIX A

INTRINSIC PARAMETERS

In Chapter 3, we have derived the standard PDE-based perspective SfS models with Lambertian, Phong and Oren-Nayar surface reflectance in terms of image coordinates, i.e. (3.37), (3.49) and (3.71). Moreover, we have proposed and considered two variational models in Chapter 5 and 6, i.e. (5.32) and (6.10), along with their minimisation process in terms of image coordinates as well. However, the image is usually provided with pixel information and each coordinate system actually represents an image in a different way: a metric unit, e.g. *mm*, is used for image coordinates $(x, y)^\top$ and pixel indices for pixel coordinates $(i, j)^\top$, where the conversion factor from image to pixel coordinates corresponds to $1/h_1$ and $1/h_2$ in each direction, respectively. In this section, we deal with the radial depth based variational model (5.32) and the Cartesian depth based one (6.10) in terms of pixel coordinates to establish a connection between the two coordinate systems and its minimisation process. In this process, we take into account the intrinsic camera parameters including the principal point offset that we have discussed in Section 3.1.1. It should be noted that this transformation is compulsory and does not serve any specific purposes, e.g. exploiting the computational benefits or the different representations of the same information such as the spherical coordinates in Chapter 4.

In the SfS community, there are several ways to follow the convention irrespective of PDE-based or variational methods: The most common way is to make directly use of the metric values of x and y with pixel indices and corresponding grid sizes h_1 and h_2, e.g. [131, 195, 238, 270, 277]. One drawback of this method is a subsequent step that is required to take care of the principal point offset because it is usually not considered explicitly in the modelling. In this case, difficulties may arise in retrieving the correct information on intrinsic parameters such as grid sizes. In some cases, however, there can be also found work incorporating explicit modelling about the matter, e.g. either by means of the normalised variables according to the principal point offset [278] or using the camera calibration matrix as part of the projection matrix directly [1].

A.1 Coordinate Transformation

To express both models in terms of pixel coordinates, based on (3.7) we make use of the following transformation between image coordinates $\boldsymbol{x} = (x, y)^\top$ and pixel coordinates $\boldsymbol{i} = (i, j)^\top$

$$\begin{bmatrix} i \\ j \\ -1 \end{bmatrix} = K \frac{1}{\mathtt{f}} \begin{bmatrix} x \\ y \\ -\mathtt{f} \end{bmatrix} \Rightarrow \begin{bmatrix} x \\ y \\ -\mathtt{f} \end{bmatrix} = \mathtt{f}\, K^{-1} \begin{bmatrix} i \\ j \\ -1 \end{bmatrix}, \tag{A.1}$$

where h_1 and h_2 are grid spacing in each direction and K^{-1} is given by

$$K^{-1} = \begin{bmatrix} h_1/\mathtt{f} & 0 & -c_1\,(h_1/\mathtt{f}) \\ 0 & h_2/\mathtt{f} & -c_2\,(h_2/\mathtt{f}) \\ 0 & 0 & 1 \end{bmatrix} \tag{A.2}$$

with the principal point $(c_1, c_2)^\top$ given in terms of pixel coordinates. It can be noted that in contrast to (3.7) the sign of the third component in homogeneous coordinate representation is negative since the image plane is placed at $z = -\mathtt{f}$ as shown in Figure 6.1. By plugging (A.2) into (A.1), one can express the transformation from pixel coordinates to image coordinates as

$$\boldsymbol{x}\,(\boldsymbol{i}) = \begin{bmatrix} x(i) \\ y(j) \end{bmatrix} = \begin{bmatrix} h_1 & 0 \\ 0 & h_2 \end{bmatrix} \begin{bmatrix} i \\ j \end{bmatrix} - \begin{bmatrix} c_1\,h_1 \\ c_2\,h_2 \end{bmatrix}. \tag{A.3}$$

A.2 Standard PDE-based Models in Pixel Coordinates

Once we have the relationship (A.3) between the image and pixel coordinates, we can reformulate the aforementioned PDE-based perspective SfS models as the expressions in terms of pixel coordinates. For the Lambertian case, i.e. the brightness equation (3.36) with the Hamiltonian (3.37), this corresponds to

$$H_{\text{PF}}\,(\boldsymbol{x}, v\,(\boldsymbol{x}\,(\boldsymbol{i})), \nabla v\,(\boldsymbol{x}\,(\boldsymbol{i}))) = 0\,, \tag{A.4}$$

where

$$\begin{aligned} &H_{\text{PF}}\,(\boldsymbol{x}, v\,(\boldsymbol{x}\,(\boldsymbol{i})), \nabla v\,(\boldsymbol{x}\,(\boldsymbol{i}))) = \\ &\quad \frac{I\,(\boldsymbol{x}\,(\boldsymbol{i}))\;\mathtt{f}^2}{Q\,(\boldsymbol{x}\,(\boldsymbol{i}))} \sqrt{\mathtt{f}^2|\nabla v(\boldsymbol{x}\,(\boldsymbol{i}))|^2 + (\boldsymbol{x}\cdot\nabla v\,(\boldsymbol{x}\,(\boldsymbol{i})))^2 + Q\,(\boldsymbol{x}\,(\boldsymbol{i}))^2} - e^{-2\,v(\boldsymbol{x}(\boldsymbol{i}))}\,. \end{aligned} \tag{A.5}$$

In the same way, we can formulate the Phong brightness equation (3.48) associated with the Hamiltonian (3.49) and the term (3.50) in pixel coordinates. This yields

$$H_{\text{VBW}}\left(\boldsymbol{x}\left(\boldsymbol{i}\right), v\left(\boldsymbol{x}\left(\boldsymbol{i}\right)\right), \nabla v\left(\boldsymbol{x}\left(\boldsymbol{i}\right)\right)\right) = 0\,, \tag{A.6}$$

where

$$\begin{aligned} &H_{\text{VBW}}\left(\boldsymbol{x}\left(\boldsymbol{i}\right), v\left(\boldsymbol{x}\left(\boldsymbol{i}\right)\right), \nabla v\left(\boldsymbol{x}\left(\boldsymbol{i}\right)\right)\right) := \\ &J\left(\boldsymbol{x}\left(\boldsymbol{i}\right)\right)\, W\left(\boldsymbol{x}\left(\boldsymbol{i}\right)\right) - \kappa_d\, E_d\, e^{-2\,v(\boldsymbol{x}(\boldsymbol{i}))} - e^{-2\,v(\boldsymbol{x}(\boldsymbol{i}))} \frac{W\left(\boldsymbol{x}\left(\boldsymbol{i}\right)\right)\, \kappa_s\, E_s}{Q\left(\boldsymbol{x}\left(\boldsymbol{i}\right)\right)} \left(\frac{2\,Q\left(\boldsymbol{x}\left(\boldsymbol{i}\right)\right)^2}{W\left(\boldsymbol{x}\left(\boldsymbol{i}\right)\right)^2} - 1\right)^{\alpha} \end{aligned} \tag{A.7}$$

with

$$J\left(\boldsymbol{x}\left(\boldsymbol{i}\right)\right) = \left(I\left(\boldsymbol{x}\left(\boldsymbol{i}\right)\right) - \kappa_a\, I_a\right) \frac{\mathfrak{f}^2}{Q\left(\boldsymbol{x}\left(\boldsymbol{i}\right)\right)}\,. \tag{A.8}$$

The same procedure can be extended to the Oren-Nayar brightness equation (3.70) with the corresponding Hamiltonian (3.71) in a straightforward way. This gives

$$H_{\text{AF}}\left(\boldsymbol{x}\left(\boldsymbol{i}\right), v\left(\boldsymbol{x}\left(\boldsymbol{i}\right)\right), \nabla v\left(\boldsymbol{x}\left(\boldsymbol{i}\right)\right)\right) = 0\,, \tag{A.9}$$

where

$$\begin{aligned} &H_{\text{AF}}\left(\boldsymbol{x}\left(\boldsymbol{i}\right), v\left(\boldsymbol{x}\left(\boldsymbol{i}\right)\right), \nabla v\left(\boldsymbol{x}\left(\boldsymbol{i}\right)\right)\right) := \\ &\mathfrak{f}^2\, I\left(\boldsymbol{x}\left(\boldsymbol{i}\right)\right) \frac{M\left(\boldsymbol{x}\left(\boldsymbol{i}\right), \nabla v\left(\boldsymbol{x}\left(\boldsymbol{i}\right)\right)\right) + 1}{A\,\sqrt{M\left(\boldsymbol{x}\left(\boldsymbol{i}\right), \nabla v\left(\boldsymbol{x}\left(\boldsymbol{i}\right)\right)\right) + 1} + B\, M\left(\boldsymbol{x}\left(\boldsymbol{i}\right), \nabla v\left(\boldsymbol{x}\left(\boldsymbol{i}\right)\right)\right)} - e^{-2\,v(\boldsymbol{x}(\boldsymbol{i}))}\,. \end{aligned} \tag{A.10}$$

A.3 Variational Models in Pixel Coordinates

For variational methods, the principle remains the same. By making use of the established relationship (A.3) and change of variable theorem [57], we can reformulate the original energy functionals (5.32) and (6.10) which are expressed in terms of image coordinates as the one with pixel coordinates. This reads

$$E\left(v\left(\boldsymbol{x}\left(\boldsymbol{i}\right)\right)\right) = h \int_{\Omega_i} \underbrace{E_D\left(\boldsymbol{x}, v\left(\boldsymbol{x}\left(\boldsymbol{i}\right)\right), \nabla v\left(\boldsymbol{x}\left(\boldsymbol{i}\right)\right)\right)}_{\text{data term}} + \alpha\, \underbrace{E_S\left(D^2\, v\left(\boldsymbol{x}\left(\boldsymbol{i}\right)\right)\right)}_{\text{smoothness term}}\, \mathrm{d}\boldsymbol{i}\,, \tag{A.11}$$

and

$$E\left(z\left(\boldsymbol{x}\left(\boldsymbol{i}\right)\right)\right) = h \int_{\Omega_i} c\left(\boldsymbol{x}\left(\boldsymbol{i}\right)\right)\, \underbrace{E_D(\boldsymbol{x}\left(\boldsymbol{i}\right), z(\boldsymbol{x}\left(\boldsymbol{i}\right)), \nabla z(\boldsymbol{x}\left(\boldsymbol{i}\right)))}_{\text{data term}} + \alpha\, \underbrace{E_S(D^2\, z(\boldsymbol{x}\left(\boldsymbol{i}\right)))}_{\text{smoothness term}}\, \mathrm{d}\boldsymbol{i}\,, \tag{A.12}$$

where the defined pixel domain $\Omega_{\boldsymbol{i}}$ is obtained by the corresponding transformation $\Omega_{\boldsymbol{i}} = \boldsymbol{x}^{-1}(\Omega_{\boldsymbol{x}})$ and $h := h_1\, h_2$ denotes the conversion factor that comes from the effect of change of variables. By means of the determinant of the Jacobian J, this factor is given by

$$|\det\left(J\left(\boldsymbol{x}\left(\boldsymbol{i}\right)\right)\right)| = \left|\det\left(\begin{bmatrix} \dfrac{\partial x}{\partial i} & \dfrac{\partial y}{\partial i} \\ \dfrac{\partial x}{\partial j} & \dfrac{\partial y}{\partial j} \end{bmatrix}\right)\right| \overset{\text{(A.3)}}{=} \left|\det\left(\begin{bmatrix} h_1 & 0 \\ 0 & h_2 \end{bmatrix}\right)\right| = h_1\, h_2\,. \tag{A.13}$$

This result shows that the minimiser of the energy (A.11) and (A.12) in terms of pixel coordinates is not influenced by the coordinate transformation because the substitution factor is a constant and hence only leads to a global scaling of the energy.

A.4 Euler-Lagrange Equations in Pixel Coordinates

As we have derived the Euler-Lagrange equations in image coordinates, let us compute the associated Euler-Lagrange equations to (A.11) and (A.12) in pixel coordinates.

First, we consider the radial depth based model (A.11). Since the radial depth based model (5.32) in image coordinates has the same structure as (A.11) in pixel coordinates except the constant substitution factor $h = h_1\, h_2$, its associated Euler-Lagrange equation (5.55) in image coordinates has the same structure in pixel coordinates as well. This gives

$$\begin{aligned} 0 = &\left([E_D]_v - \frac{\partial}{\partial i}\, [E_D]_{v_i} - \frac{\partial}{\partial j}\, [E_D]_{v_j} \right) \\ &+ \alpha\, \left(\frac{\partial^2}{\partial i^2}\, [E_S]_{v_{ii}} + 2\, \frac{\partial^2}{\partial i \partial j}\, [E_S]_{v_{ij}} + \frac{\partial^2}{\partial j^2}\, [E_S]_{v_{jj}} \right) \end{aligned} \tag{A.14}$$

with boundary conditions

$$0 = \boldsymbol{n}^\top \begin{bmatrix} [E_D]_{v_i} - 2\,\alpha\, \dfrac{\partial}{\partial i}\, [\Psi'\left(s^2\right)\, v_{ii}] - 2\,\alpha\, \dfrac{\partial}{\partial j}\, [\Psi'\left(s^2\right)\, v_{ij}] \\ [E_D]_{v_j} - 2\,\alpha\, \dfrac{\partial}{\partial i}\, [\Psi'\left(s^2\right)\, v_{ij}] - 2\,\alpha\, \dfrac{\partial}{\partial j}\, [\Psi'\left(s^2\right)\, v_{jj}] \end{bmatrix} \tag{A.15}$$

and

$$\boldsymbol{n}_{\boldsymbol{i}}^\top \begin{bmatrix} v_{ii} \\ v_{ij} \end{bmatrix} = 0\,, \quad \boldsymbol{n}_{\boldsymbol{i}}^\top \begin{bmatrix} v_{ij} \\ v_{jj} \end{bmatrix} = 0\,, \tag{A.16}$$

where $\boldsymbol{n}_{\boldsymbol{i}} = (n_i, n_j)^\top$ stands for the outer normal vector.

Moreover, the same idea can also be extended to the Cartesian depth based model (A.12) in a straightforward way. Hence, based on the structure of the Euler-Lagrange equation (6.17) in image coordinates we obtain

$$\begin{aligned} 0 \;=\; & \left([c\,E_D]_z - \frac{\partial}{\partial i}\,[c\,E_D]_{z_i} - \frac{\partial}{\partial j}\,[c\,E_D]_{z_j} \right) \\ + \;\alpha\; & \left(\frac{\partial^2}{\partial i^2}\,[E_S]_{z_{ii}} + 2\,\frac{\partial^2}{\partial i\,\partial j}\,[E_S]_{z_{ij}} + \frac{\partial^2}{\partial j^2}\,[E_S]_{z_{jj}} \right) \end{aligned} \tag{A.17}$$

with the boundary condition

$$0 = \boldsymbol{n}_{\boldsymbol{i}}^\top \begin{bmatrix} [c\,E_D]_{z_i} - \alpha\,\frac{\partial}{\partial i}\left[\Psi'(s^2)\;z_{ii}\right] - \alpha\,\frac{\partial}{\partial j}\left[\Psi'(s^2)\;z_{ij}\right] \\ [c\,E_D]_{z_j} - \alpha\,\frac{\partial}{\partial i}\left[\Psi'(s^2)\;z_{ij}\right] - \alpha\,\frac{\partial}{\partial j}\left[\Psi'(s^2)\;z_{jj}\right] \end{bmatrix} \tag{A.18}$$

and

$$\boldsymbol{n}_{\boldsymbol{i}}^\top \begin{bmatrix} z_{ii} \\ z_{ij} \end{bmatrix} = 0\,, \quad \boldsymbol{n}_{\boldsymbol{i}}^\top \begin{bmatrix} z_{ij} \\ z_{jj} \end{bmatrix} = 0\,, \tag{A.19}$$

where $\boldsymbol{n}_{\boldsymbol{i}} = (n_i, n_j)^\top$ stands for the outer normal vector.

During the derivations of the Euler-Lagrange equations and their associated boundary conditions in pixel coordinates, i.e. (A.14) and (A.17) as well as (A.15) and (A.18), we have used the following relationships between derivatives in pixel and image coordinates based on (A.3)

$$\frac{\partial}{\partial i} = h_1\,\frac{\partial}{\partial x}\,, \quad \frac{\partial}{\partial j} = h_2\,\frac{\partial}{\partial y}\,, \quad \frac{\partial}{\partial z_i} = \frac{1}{h_1}\,\frac{\partial}{\partial z_x}\,, \quad \frac{\partial}{\partial z_j} = \frac{1}{h_2}\,\frac{\partial}{\partial z_y}\,, \tag{A.20}$$

$$\frac{\partial^2}{\partial i^2} = h_1^2\,\frac{\partial^2}{\partial x^2}\,, \quad \frac{\partial^2}{\partial i\,\partial j} = h_1\,h_2\,\frac{\partial^2}{\partial x\,\partial y}\,, \quad \frac{\partial^2}{\partial j^2} = h_2^2\,\frac{\partial^2}{\partial y^2}\,, \tag{A.21}$$

$$\frac{\partial}{\partial z_{ii}} = \frac{1}{h_1^2}\,\frac{\partial}{\partial z_{xx}}\,, \quad \frac{\partial}{\partial z_{ij}} = \frac{1}{h_1\,h_2}\,\frac{\partial}{\partial z_{xy}}\,, \quad \frac{\partial}{\partial z_{jj}} = \frac{1}{h_2^2}\,\frac{\partial}{\partial z_{yy}}\,. \tag{A.22}$$

The equivalence of the Euler-Lagrange equations with corresponding boundary conditions between two coordinate systems suggests that all derivations and statements in image coordinates remain still valid in pixel coordinates. Therefore, the implementation of the optimality condition which is derived in image coordinates can also be realised in pixel coordinates by means of the discretisation methods in Section 5.3.3 and 6.3.4 through the coordinate transform given in (A.3). However, it should be noted that first transforming pixel coordinates into image coordinates and subsequently conducting the minimisation process in image coordinates is conceptually the proper way.

APPENDIX B

PUBLICATIONS

B.1 Book Chapters

1. **Y. C. Ju**, D. Maurer, M. Breuß, A. Bruhn:
   Direct variational perspective shape from shading with Cartesian depth parametrisation.
   Perspectives in Shape Analysis - M. Breuß, A. Bruckstein, P. Maragos, S. Wuhrer (Eds.) Mathematics and Visualization, Springer, Berlin, 2016. *pp.* 43 – 72.

B.2 Conference Proceedings

2. D. Maurer, **Y. C. Ju**, M. Breuß, A. Bruhn:
   Combining Shape from Shading and Stereo: A Variational Approach for the Joint Estimation of Depth, Illumination and Albedo.
   In Proc. 27th British Machine Vision Conference (BMVC 2016, York, UK, September 19th-22th, 2016) - E. Hancock, W. Smith, R. Wilson (Eds.) pp. 76.1–76.14.

3. D. Maurer, **Y. C. Ju**, M. Breuß, A. Bruhn:
   An efficient linearisation approach for variational perspective shape from shading.
   In Proc. 37th German Conference on Pattern Recognition (GCPR 2015, Aachen, Germany, October 7th-9th, 2015) - B. Leibe, J. Gall, P. Gehler (Eds.)
   Lecture Notes in Computer Science, Springer, Berlin, 2015. *pp.* 249–261.

4. **Y. C. Ju**, M. Breuß, A. Bruhn:
   Variational perspective shape from shading.
   In Proc. 5th International Conference on Scale Space and Variational Methods in Computer Vision (SSVM 2015, Lège Cap Ferret, France, May 31th- June 4th, 2015) - J.-F. Aujol, M. Nikolova, N. Papadakis (Eds.)
   Lecture Notes in Computer Science, Springer, Berlin, 2015. *pp.* 538–550.

5. **Y. C. Ju**, S. Tozza, M. Breuß, A. Bruhn, A. Kleefeld:
   Generalised perspective shape from shading with Oren-Nayar reflectance.
   In Proc. 24*th British Machine Vision Conference* (*BMVC* 2013 - *Bristol, UK, September* 9*th*-13*th,* 2013) - *T. Burghardt, W. Mayol-Cuevas, M. Mirmehdi* (*Eds.*) *pp.* 42.1–42.11.

6. S. Galliani, **Y. C. Ju**, M. Breuß, A. Bruhn:
   Generalised perspective shape from shading in spherical coordinates.
   In Proc. 4*th International Conference on Scale Space and Variational Methods in Computer Vision* (*SSVM* 2013 - *Schloss Seggau, Graz region, Austria, June* 2*nd*-6*th,* 2013) - *A. Kuijper, K. Bredies, T. Pock, Horst Bischof* (*Eds.*)
   Lecture Notes in Computer Science, Springer, Berlin, 2013. *pp.* 222–233.

7. **Y. C. Ju**, M. Breuß, A. Bruhn, S. Galliani:
   Shape from Shading for Rough Surfaces: Analysis of the Oren-Nayar Model.
   In Proc. 23*rd British Machine Vision Conference* (*BMVC* 2012 - *Surrey, UK, September* 3*rd*-7*th,* 2012) - *R. Bowden, J. Collomosse, K. Mikolajczyk* (*Eds.*) *pp.* 104.1–140.11.

8. S. Galliani, M. Breuß, **Y. C. Ju**:
   Fast and Robust Surface Normal Integration by a Discrete Eikonal Equation.
   In Proc. 23*rd British Machine Vision Conference* (*BMVC* 2012 - *Surrey, UK, September* 3*rd*-7*th,* 2012) - *R. Bowden, J. Collomosse, K. Mikolajczyk* (*Eds.*) *pp.* 106.1–106.11.

9. M. Breuß, **Y. C. Ju**:
   Shape from Shading with Specular Highlights: Analysis of the Phong Model.
   In Proc. 18*th IEEE International Conference on Image Processing* (*ICIP* 2011 - *Brussels, Belgium, September* 11*th*-14*th,* 2011), *pp.* 9–12.

INDEX

ambiguity
  bas-relief 88
  convex/concave 89

bidirectional reflectance distribution function (BRDF) 63
boundary conditions
  Dirichlet 87
  Neumann 87
  state constraint 87

calculus of variations 122
camera calibration matrix 62
continuous viscosity solution 39, 43, 44
  viscosity subsolution 39, 44
  viscosity supersolution 39, 44
critical points 2, 84

Euler-Lagrange equations 122

fast marching (FM) method 44

Gauß-Seidel method 208
genealised solutions 25
generalised brightness equations 93
  Lambertian 101
  Oren-Nayar 106

Hamiltonian
  eikonal-type 23
  general-type 23
hyperbolic warping scheme 200

ill-posed 24
intrinsic parameters 62
inverse square law 70

Lagrangian 122

one-sided differentials 32
  subdifferential 32
  superdifferential 32
optimisation
  coarse-to-fine approach 180
  direct method 138
  first discretise then optimise 138
  first optimise then discretise 138
  graduated non-convexity 180
  indirect method 138

partial differential equation 20
  linear PDE 21
  nonlinear PDE 22
  order of a PDE 20
projection matrix 62

semi-differentials 32
Shape from Shading (SfS) 1
  perspective SfS (PSfS) 2
  variational PSfS 130
  variational SfS 129
singular points 2, 84
successive over-relaxation 208
surface reflectance
  Lambertian 64
  Oren-Nayar 67
  Phong 65

upwind scheme 46

vanishing viscosity method 26
variation 123

weak solutions 25
well-posedness 24